Istituto Universitario degli Studi Superiori di Pavia

Facoltà di Ingegneria

Computational modeling of coronary stenting: from image processing to clinical evaluation

by

Carolina Ferrazzano

A Thesis submitted in Fulfilment of the Requirements
for the Degree of Doctor in Philosophy in

Computational Mechanics and Advanced Materials
at Istituto Universitario degli Studi Superiori di Pavia, Italy

Ph.D. Program Coordinator: Prof. F. Auricchio

Supervisor:
Prof. F. Auricchio - Università degli Studi di Pavia
Co-supervisor:
Dr. M. Conti - Università degli Studi di Pavia

XXVI Ciclo (2010-2013)

Ad Armando

Acknowledgements

Four years ago I arrived in Pavia for the first time and my first impression was the too cold, wet and fog. But soon the comp-mech group made me feel at home. I would like to thank everyone for the constructive conversations and the nice moments in front of the sweets.
First, I would like to thank my Supervisor, Prof. Ferdinando Auricchio, for the given opportunity to study in this group, where I increased my skills and knowledges, for his great guidance and professional support in the development of this thesis.
I would like to thank Michele for his precious advises, friendly and support for this research study.
I have greatly appreciated the discussions with the Doctor Gregory Sgueglia; I acknowledge his helpful clarifications and useful comments.
Then, I thank all my lab-mates for their friendship: Andrea, Giuseppe, Adrien, Josef, Simone, Mauro, Eli, Elisa, Alessandro, Marco and Ako.
Special thanks to my colleagues, Anna and Chiara, and my flatmate, Mariella, for their nice conversations and friendship.
My deepest thanks go to my parents and my brother Angelo, for their constant encouragement to improve and step forward.
Last but not least, I would like to thank Armando for his smile and deep love.

Contents

Summary

CORONARY vessels are important arteries of cardiovascular system, which provide oxygenum and nutrient to the heart.
Coronary artery disease, which is the major cause of death in the Western countries, consists in the progressive growth of an atherosclerotic plaque inside the lumen with variable extension, known as *stenosis*, which narrows the vessel, impeding the normal blood flow and causing a cardiac attack.
In the clinical practice, percutaneous coronary intervention (PCI) has replaced the open-chest surgery, restoring the coronary lumen patency through mini-invasive intervention techniques, i.e., coronary stent deployed by the balloon inflation. Currently, there are not any predictive interventional techniques in the clinical practice, especially to support the procedural planning in the case of complex coronary lesions. In this scenario, an engineering tool able to support the pre-procedural planning could increase the intervention quality and the clinical outcomes.
Indeed, recent studies have highlighted the potential role of realistic computer-based simulations, such as structural finite element analysis (FEA), as a valuable support to the surgical planning of such percutaneous procedures.
Unfortunately, the link between the clinical practice and these engineering techniques is still limited to research test-cases. A key point to further promote such an interaction is to generate in a fast and effective manner the computational grids, i.e., meshes, to use in numerical simulations directly from angiographic images, acquired by X-Ray coronary angiography, which is the gold standard technique for the assessment of both location and severity of coronary artery stenosis.
Such computational models can offer, thus, objective measures of the generated coronary artery overcoming the limitations of the bi-dimensional images, i.e., stenosis degree, bifurcation angles, coronary lumen area and diameters. These analyses can be performed both before and after the PCI from sole two X-Ray single-plane angiographic images, providing to the surgeon important clinical informations.
Hence, the present study proposes a simple framework to generate three-dimensional (3D) FEA-suitable meshes of coronary bifurcations to use, virtually, in surgical intervention for specific coronary lesions treatment in order to predict the final results, improving the surgical planning.
The PCI performed in this study has allowed to analyse some FEA features in order to realize realistic and *patient-specific* numerical simulations. Particularly, the proposed analysis investigates the treatment of long coronary lesions, which is still a matter of debate among the community of interventional cardiologists.
Hence, the aim is to provide the surgeon a methodological approach to better understand the procedural techniques of the long lesions treatment used in the clinical

practice. In this scenario, the comparison of the results among different interventional techniques could allow to objectify the criterion of the better treatment to adopt for a patient-specific case from the medical images processing.

Sommario

Le coronarie sono importanti arterie del sistema cardiovascolare, che forniscono ossigeno e nutrimento al cuore. Le malattie cardiovascolari sono la principale causa di morte nei paesi occidentali; tra queste, la patologia riguardante il restringimento progressivo del lume coronarico, nota come stenosi coronarica, risulta essere quella più diffusa. Essa consiste nella crescita progressiva di una placca aterosclerotica ad estensione variabile che occlude il vaso arterioso, impedendo così al sangue di fluire normalmente all'interno dell'arteria, provocando un infarto cardiaco.
Nella pratica clinica, il ripristino della pervietà del lume vasale avviene attraverso interventi percutanei mediante l'uso di stent coronarici posizionati grazie all'espansione graduale di un palloncino. Non esistono tecniche preventive per supportare gli interventi percutanei dei vasi coronarici, soprattutto nel caso di lesioni aterosclerotiche diffuse e complesse. Diventa quindi necessario poter predire il risultato dell'intervento al fine di migliorare la qualità di uno specifico trattamento, pianificando così ogni tecnica chirurgica. In questo scenario, fornire al medico chirurgo uno strumento che possa rendere il suo operato più oggettivo, diventa indispensabile per migliorare sia la qualità di successo del suo intervento sia la qualità di vita del paziente.
Oggigiorno, metodi ingegneristici all'avanguardia attraverso l'uso di modelli e metodi computazionali agli elementi finiti stanno offrendo notevoli risultati attraverso l' implementazione opportuna di procedure numeriche che simulino interventi chirurgici realistici per il trattamento delle lesioni coronariche. Sfortunatamente, il link fra la pratica clinica e le tecniche ingegneristiche è ancora limitato. Un punto chiave per promuovere ulteriormente tale interazione è generare in modo veloce ed efficace modelli computazionali, ovvero mesh, da utilizzare nelle simulazioni numeriche direttamente da immagini monoplanari acquisite nella pratica clinica attraverso l'angiografia a raggi X, che costituisce oggi la tecnica *gold standard* per la localizzazione e misura delle stenosi coronariche.
Così, i modelli computazionali possono offrire misure oggettive del vaso costruito a partire dalle immagini mediche superando le limitazioni dovute alla loro bidimensionalità. L'oggetto 3D generato offre al medico informazioni cliniche importanti, come il grado di stenosi, angoli di biforcazione, area e diametri del lume vasale. Tali analisi possono essere effettuate sia prima che dopo l'intervento chirurgico a partire da sole due immagini angiografiche a raggi X.
Gli interventi chirurgici realizzati in questo studio di ricerca hanno permesso di analizzare aspetti dell'analisi agli elementi finiti al fine di realizzare simulazioni numeriche più realistiche e *ad hoc* per il paziente. In modo particolare si è analizzata una specifica tecnica di intervento per il trattamento delle lesioni coronariche lunghe. Le procedure di intervento clinico su tali patologie, più complicate e complesse, sono ancora poco chiare e poco conosciute dalla cardiologia interventistica.

In questo studio di ricerca si vuole fornire un metodo di approccio valido per una maggior comprensione delle possibili tecniche di intervento utilizzate dalla pratica clinica per il trattamento delle lesioni lunghe. In tal modo, il confronto dei risultati fra le diverse tecniche di intervento permetterà al medico interventista di oggettivare il criterio di scelta della migliore procedura clinica da adottare per uno specifico paziente a partire dall'elaborazione delle immagini angiografiche fornite direttamente dal medico.

Chapter 1

Introduction

Coronary artery disease, which is the main cause of death worldwide [1], is due to atherosclerotic lesions narrowing the arterial lumen, i.e., stenosis, and decreasing the blood supply to the heart muscle. Hence, such lesions constitute important index of the disease severity and many clinical decisions for the patient treatment depend on it. This chapter focuses on the coronary artery disease, from the diagnosis using several imaging techniques to the treatments performed in clinical practice.
After a brief description of the coronary anatomy and diseases, we discuss about the typical coronary treatments to understand because the stenting procedure is the main technique applied nowadays to restore the lumen artery patency. A short review of the angiographic medical techniques for coronary stenosis detection is presented to evaluate the imaging performance of each one. It worth noting that the medical images are the starting points for patient-specific simulations in computational mechanics. Then, we focus on the finite element analysis (FEA) simulations of coronary stenting which are investigated by the recent literature. Finally, the aim of the thesis is explained and its organization is summarized.

1.1 Coronary anatomy, physiology and pathology

Understanding the coronary artery anatomy and the physio-pathology is important to perform a detailed analysis of the angiographic images used for the image processing and the generation of 3D patient-specific models.
The cardiovascular system is composed of two main organs, i.e., the heart and the blood vessels (arteries, veins and capillaries), as depicted in Figure 1.1 (a).
The heart is a muscle that gives the impetus to the blood, relaxing (diastole) and contracting (systole) rhythmically and involuntarily. It has a conical shape, a base elongated upper and an apex directed slightly to the left; the base and its left part are inclined towards the vertebrae [2].
Such a muscle has four chambers, two superior atria and two inferior ventricles: the atria are the receiving chambers and the ventricles are the discarding chambers (see Figure 1.1 (b)). Every atria is separated by the respective ventricle through a valve, i.e., the bicuspid valve in the right part of the heart and the mitral valve in the left part one [3]. The pathway of the blood consists of a pulmonary and systemic circuit which operate simultaneously. De-oxygenated blood from the body flows via the *venae cavae* in the right atrium, which pumps it through the tricuspid valve in the right ventricle, whose subsequent contraction forces it out through the pulmonary valve into the pul-

monary arteries leading to the lungs. Meanwhile oxygenated blood returns from the lungs through the pulmonary veins into the left atrium, which pumps it through the mitral valve into the left ventricle, whose subsequent strong contraction forces it out through the aortic valve to the aorta leading to the systemic circulation [4].
During every cardiac cycle, the atria contract first, forcing the blood inside of their respective ventricles; then, the ventricles contract, forcing blood out to the heart. The arteries are the blood vessels that drive blood from the heart to the tissues, the veins lead the blood to the heart from the tissues and finally, the capillaries allow the exchanges between blood and tissue, and vice-versa. The arteries have a considerable blood pressure inside them, which decreases as the blood moves away from the heart due to the increase of the blood volume contained in the capillaries with respect to that contained in the aorta.
The heart is composed of three tunics from inside to outside: the endocardium, which has the same functions and the same structure of the arteries's endothelium detailed later in this section, and the myocardium, which is the hybrid muscle between smooth and striated. From the aortic valve of the heart, two small arteries emerge, i.e., the right coronary artery (RCA) and left coronary artery, as shown in Figure 1.2 (a), which are the artery vessel delivering the oxygen-rich blood to the myocardium. The progress of the RCA defines the border between the right atrium and right ventricle. This artery develops two branches down, the marginal branch left coronary artery and the anterior right coronary artery. The left coronary artery divides into the left circumflex artery (LCX), whose course defines the division between the left atrium and left ventricle, and the left anterior descending artery (LDA), which defines the boundary between the left and right ventricle. The LCX and the RDA pass behind the heart and join them, defining the atrio-ventricular limit. The coronary arteries which define the limit atrio-ventricular (right and left) and interventricular (anterior and posterior) are joined to ensure that, in the case of thrombus generation there is a vascularization everywhere [2]. The arteries are composed of three concentric layers or tunica, i.e., *intima*, *media* and *adventitia*, which are depicted in Figure 1.2 (b).

Tunica intima is the layer at contact with the blood and it is made of a single layer of endothelial cells embedded in extracellular matrix and an underlying thin basal lamina, which is also referred to as basement membrane, providing structural support to the arterial wall. Such a layer provides a non-thrombogenic surface so that the blood can flow through the artery without forming thrombus. The basal lamina contains non-fibrillar collagen types, adhesion molecules laminin, fibronectin, and other extracellular matrix molecules [5]. The coronary arteries contain a subendothelial layer of connective tissue and axially oriented smooth muscle cells [6]. It has been observed that the orientation of the collagen fibers in the subendothelial layer through the thickness it is not uniform but dispersed [7]. The intima is very thin, i.e., 0.05-0.1 mm, and its contribution to the mechanical properties in healthy young human arteries is not significant. Whereas, ageing and in the case of pathological conditions, the intima becomes thicker (0.2-0.4 mm) and stiffer, and develops a more complex and heterogeneous structure. These pathological changes are associated with alterations in the mechanical properties, which differ significantly from those of healthy arteries [8]. Finally, it is separated from the media by the internal elastic lamina, which is often considered to be part of its.

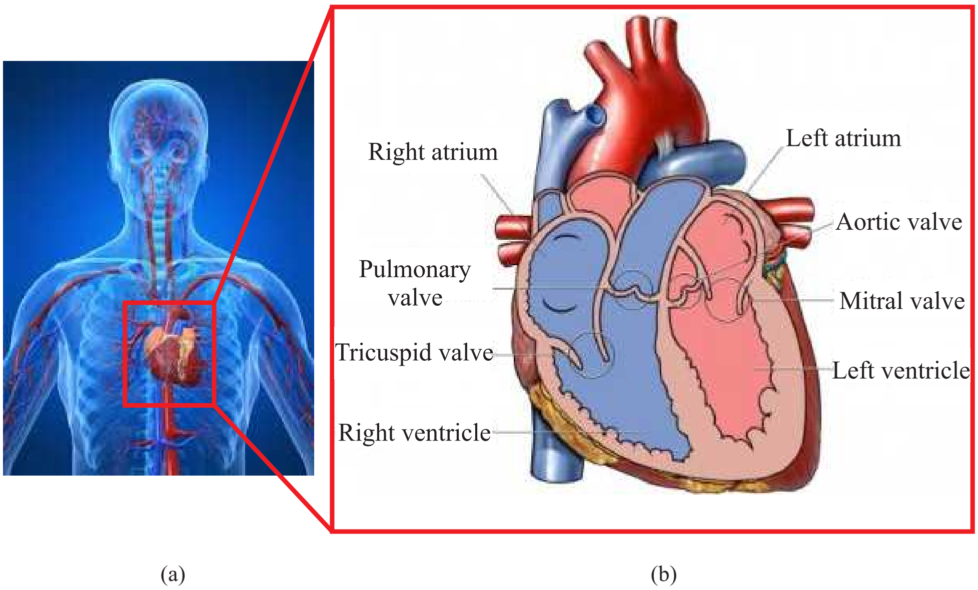

Figure 1.1 *Cardiovascular system: (a) heart, artery (red) and veins (blue) in the cardiovascular system; (b) the four chambers of the heart (figures are provided by web site http : //www.thirdage.com/).*

Tunica media is the middle and thickest layer of the artery, i.e, 0.1-0.5 mm, made of smooth muscle cells, elastin and collagen immersed into an aqueous ground substance containing proteoglycans, known as matrix. Such fibers are arranged in repetitive lamellar units separated by thin fenestrated sheets of elastin, forming concentric medial layers [9]. The thickness of such units is nearly independent of the radial location across the wall, but their number decrease as the distance from the heart increases, so that the lamellar units found absent in small muscular arteries. The laminated structure confers high strength to the media and explains how such a layer determines the mechanical properties of the whole vessel wall. In the media, collagen fibers are aligned along the the circumferential direction with a very little dispersion. This structural arrangement gives the media the ability to carry loads in the circumferential direction. Apparently, the distribution of collagen does not show changes in atherosclerotic arteries [10]. The media is separated from the adventitia by the external elastic lamina.

Tunica adventitia is the outermost layer of the artery and consists primarily of collagen fibers, elastin, nerves, fibroblasts, fibrocytes. The thickness size of the adventitia is thinner than the media, i.e., 0.25-0.40 mm. The adventitia is surrounded continuously by loose connective tissue, which often provides additional structural support. As for the intima, histological evidence have proven the dispersion of collagen fibers in the adventitial layer, which remains also in atherosclerotic arteries [10]. Collagen fibers tend to maintain an axial orientation and remain slack at low pressures, but as the pressure increases they straightened, reinforcing the arterial wall and preventing the over-stretching and the rupture of the artery [11].
The cardiovascular diseases are being addressed, as appropriate, through the prevention of risk factors, drug therapy and finally surgery. The healthy arteries of the heart are elastic and soft inside them (see Figures 1.3), having the important function of

providing blood, therefore oxygen, to the heart.

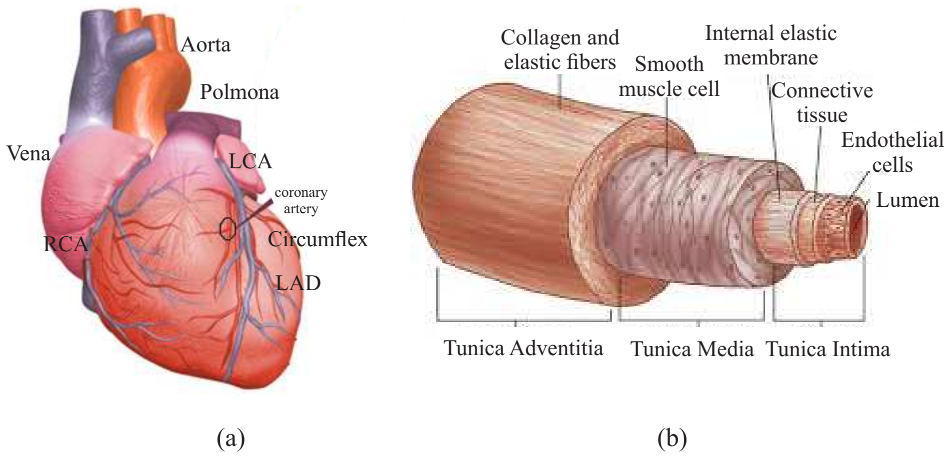

Figure 1.2 *Cardiovascular system: (a) main vessel of the heart, that are the aorta, the vena cava, pulmonary artery and coronary arteries, i.e., LAD (left anterior descending artery), LCA (left coronary artery) and Circumflex branch of left coronary artery (figures are provided by web site http : //www.healt − share.org); (b) structural organization and composition of the three different layers in the coronary vessel wall [12].*

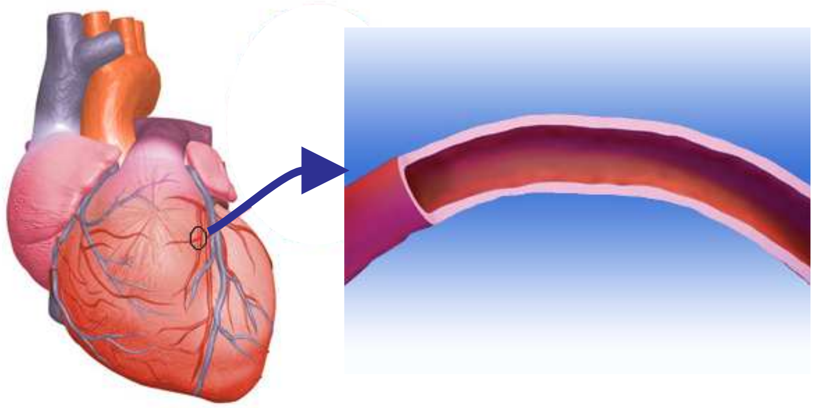

Figure 1.3 *Picture of an healthy coronary artery (figures are provided by web site http : //www.healt − share.org).*

The narrowing or obstruction of the artery, due to the tissue damage after the growth of atherosclerotic plaque, is known as stenosis. If such a disease is not treated by the medical point of view, it could bring the patient to a crisis condition, i.e., heart attack. In Figures 1.4 (a) and (b), it is possible to note the formation of an atherosclerotic plaque inside the lumen of the coronary artery, due to the accumulation of fats and lipids, which increase the thickness wall and decreasing the lumen diameter.

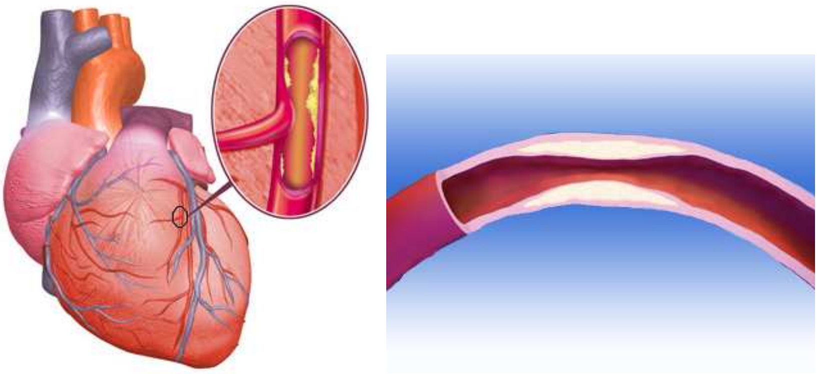

(a) (b)

Figure 1.4 *Picture of a coronary artery disease: (a - b) the occlusion of the coronary artery due to the atherosclerotic plaque (yellow color) could caused an heart attack.*

1.2 Coronary lesions and percutaneous treatments

The artery occlusion brings a quantity of oxygen and nutrients not sufficient for the proper functioning of the entire cardiac muscle [1]. Until the Seventies, the only possible way to restore the coronary lumen patency was represented by the bypass surgery: the circulation was restored by a bridge, consisting of an harvested vein usually from a leg, which bypassed the narrowing of the coronary artery obstruction. The technique of coronary artery bypass graft surgery, was later replaced by an intervention more effective, less invasive and expensive, i.e., the angioplasty transluminar percutaneous coronary angioplasty (PTCA). The PTCA consists in the insertion of a catheter with a small inflatable balloon inside the artery, which enlarges the stenotic artery, eliminating, thus, the plaque and allowing to restore the blood flow. Subsequently the expansion, the balloon is deflated and removed from the vessel [13].
However, after the intervention, the arterial wall lost its elasticity and flexibility, collapsing within the arterial lumen and making the stretch again occluded; such phenomenon is known as elastic recoil. To overcome such a problem, in the Nineties the technique of angioplasty has been increased by the installation of specific devices able to support the stenotic walls, i.e., the coronary stents (see Figure 1.5 (a)). A stent is a small expandable cage able to support the inside of the artery after its deployment.
The stenting procedure occurs simultaneous to the PTCA technique: the stent is deployed in the stenotic coronary artery by the use of a catheter introduced through percutaneous way (see Figure 1.5 (b)). The balloon expands the mesh of the stent and deploys it inside the inner coronary artery, as depicted in Figure 1.5 (c). Subsequently, the balloon is deflated, while the expanded stent remains in contact with the walls of the artery, avoiding, thus, the collapse of the vessel wall and, therefore, the elastic recoil problem (see Figure 1.5 (d)). Once the stent is placed, the cells of the arterial wall grow around the meshes of the device assuring further good placement. The introduction into clinical practice of the devices allowed to reduce the complications of this intervention, especially in cases of acute occlusion. The technological development in this area concerns the research and development of stents increasingly small and adaptable to different needs and situations [13]. Further, the introduction of drug eluting stents

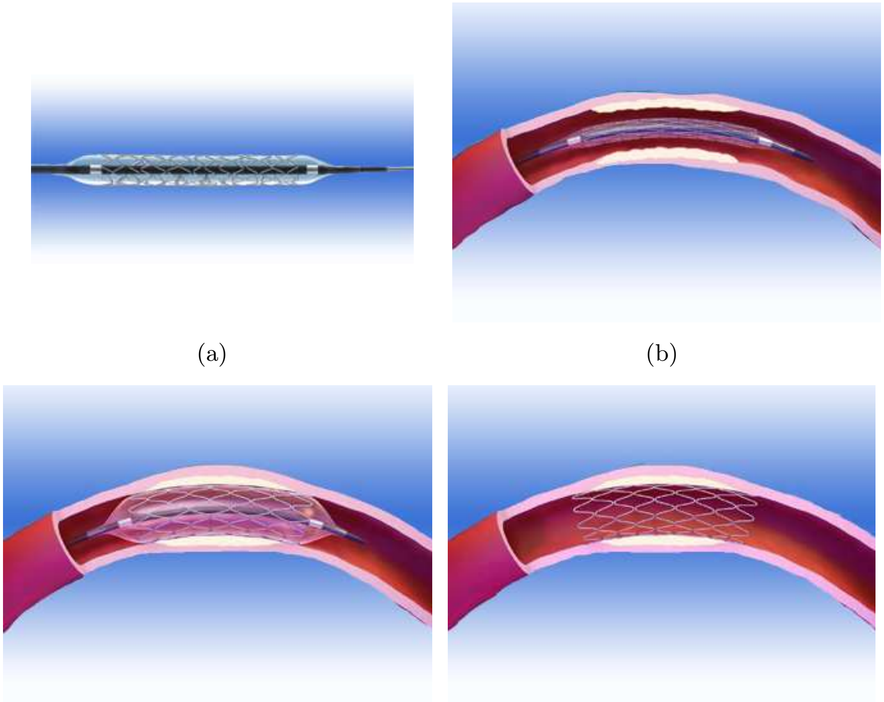

(a) (b) (c) (d)

Figure 1.5 Stenting procedure through the balloon expansion: (a) typica delivery system used in the clinical practice; (b) the system is placed inside the stenoted artery; (c) deployment of the stent; (d) at the end of the procedure, the stent restores the coronary lumen patency.

has provides significant reduction in the incidence of restenosis [14, 15].
However, despite the continuous advances in the interventional cardiology field, the treatment of complicated coronary lesions, i.e., stenosis in the bifurcation area of the coronary artery and diffused stenosis in the coronary lumen, continues to be associated with a lower procedural success rate and an higher complications and restenosis incidence [16, 17]. For this reason percutaneous treatments of such coronary lesions remain a challenge for interventional cardiology, both for technical aspects and long term clinical results [18, 19, 20]..
Hence, in this context, the introduction of a planning before the real intervention through the medical image elaboration and the predictive numerical surgery might improve the clinical outcome. The better way to promote such a procedure is to reproduce the numerical coronary interventions from patient-specific coronary artery models, which are generated through the analysis of the medical images acquired by the specific angiographic techniques, as discussed in the next section.

1.3 Coronary angiographic techniques

Medical image analysis has been introduced into clinical practice to quantify objectively vascular anatomy and mechanics of coronary artery, overcoming complicated and subjective interpretations of the anatomical data provided by the medical images.

This section focuses on the development of imaging tools for diagnostic aims, providing important anatomical features to support the decision of the physicians. Such tools provide also 3D virtual models from the elaboration of 2D medical images, which are the information vehicle in 3D modelling. The aim is to simplify the medical reporting and remove errors from subjective interpretation, offering great benefits in the phase of diagnosis and surgical planning.
Current imaging methods for coronary artery disease analysis can be classified as non-invasive, i.e., Computed Tomographic Angiography (CTA), Magnetic Resonance Imaging (MRI), and invasive methods, i.e., X-Ray Angiography, Intra-Vascular UltraSound (IVUS) and Optical Computed Tomography (OCT).
In the following, we review and describe these angiographic imaging techniques, which are used in clinical practice and in the computational science for 3D modelling.

1.3.1 Computerized Tomography Angiography

CTA is an X-Ray imaging modality where the X-Ray beam passes through the area of interest from several different angles using a spiral rotating tube and detector assembly (see Figure 1.6 (a)). The image scanning is synchronized with a contrast injection performed intravenously, using a technique called bolus tracking. Furthermore, such a biomedical instrumentation is composed of a workstation to elaborate the images: cross-sectional views are generated and then assembled for 3D model generation (see Figure 1.6 (b)).
In the last decade, the innovative multi-slice (or multidetector-array) CTA scanners have been introduced to acquire several tomographic slices in a single rotation, reducing the time of the image acquisition in few seconds. The main distinguishing feature is the extension of the detector arrays along the patient length [21].
In the case of relevant pathology analyses, such as the atherosclerotic plaques detection inside the lumen arteries, CTA images are often preferred by diagnosticians since they have high signal-to-noise ratio and good spatial resolution, providing, thus, accurate anatomical information of complex vascular lesions [22].
Particularly, in the coronary artery disease, CTA provides early and direct assessment of atherosclerotic plaques, identifying the plaque area, degree of stenosis and vessel wall morphology. Further, when associated with an intravenous contrast medium, such a technique is capable of identifying calcified and non-calcified lesions, distinguishing soft, intermediate and hard plaque. Such an imaging technique requires a heavy radiation exposure and is unable to image lesions with heavy calcium burden [23].

1.3.2 Magnetic Resonance Imaging

MRI of coronary arteries is the safest and the only fully non-invasive diagnostic method: any radiation exposure and damaging contrast [24]. Compared to CTA, MRI has higher temporal resolution and lower spatial resolution [21]. Recent developments make this technique capable of plaque characterization, including size, composition and inflammatory status, besides the ability of detecting micro-vascular obstruction.
However, although MRI angiography has generated promising data in recent trials, its long-image acquisition times, together with a limited contrast-to-noise ratio, hinder its

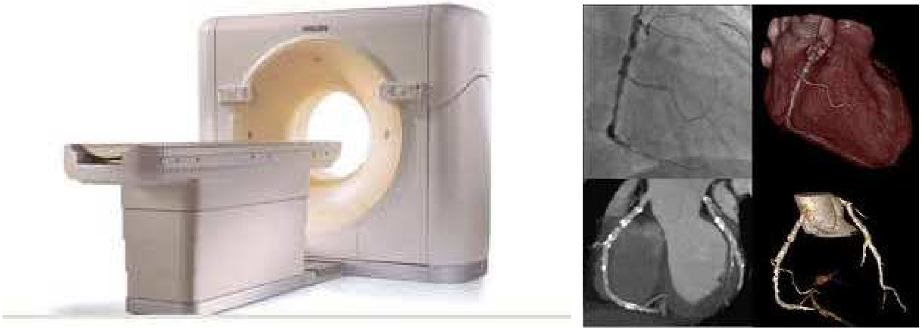

(a) (b)

Figure 1.6 *CTA angiographic images: (a) CT angiography composed of a circular tube having an X-Ray source and multidetectors-array and a mobile table; (b) the acquired image allow to explore the cardiovascular anatomy, i.e., the heart, the coronary arteries and the aorta vessel (figure are provided by the web site http : //www.viterborad.it/tac64.php).*

consistent application in clinical use [25]. A method to acquire better quality images and improve the signal-to-noise ratio is to associate MRI with a contrast medium injection, but this would nullify the non-invasiveness of this technique. Figures 1.7 (a) and (b) depict the reconstruction of the heart, the aortic valve and the coronary arteries, provided by the image elaboration of RMI images through the software Osirix [26]. A disadvantage of such a medical image technique is that the patients with metallic devices, such as pacemakers and coronary stents, cannot undergo MRI acquisition.

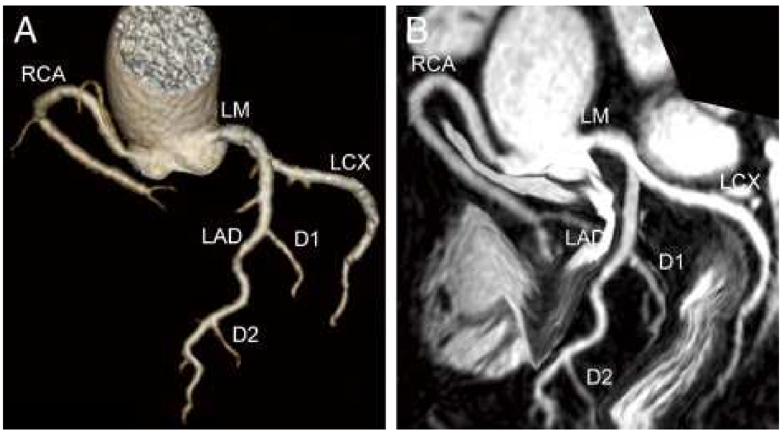

Figure 1.7 *3D coronary reconstruction from MRI angiography reported in [27]: on the left, the main coronary vessels of the heart, i.e., left coronary artery (LCA), left anterior descending artery (LDA), left main (LM), left circumflex artery (LCX), right coronary artery (RCA) and the secondary branches (Dn); on the right the angiographic image.*

1.3.3 X-Ray Angiography

X-Ray Angiography is the *gold standard* technique to detect the stenosis of the coronary arteries. This is traditionally done by injecting a radio-opaque contrast agent into the blood vessel, using X-Ray beam ionizing.

Such a technique involves the acquisition of a series of projection views through a C-arm, which performs a continuous rotation around the vessels of interest. The C-arm is composed of a source emitting the X-Rays beam and a flat detector to generate the angiographic images. The number of the projection views depends on the modal acquisition, that is on the rotational angle of the C-arm [28], as shown in Figure 1.8 (a). Angular views allow to obtain 2D angiography images, while a wider rotation of the instrument provides a complete angiographic images. Contrast between vessels and other tissues is achieved through the different absorption of X-Ray photons that characterizes the tissues: Figure 1.8 (b) illustrates an example of X-Ray angiographic image showing the coronary artery tree. Such a procedure is synchronized to the electrocardiography signal (ECG) and the contrast injection after the insertion of a catheter into the artery in order to increase the X-Ray attenuation properties of the blood and to acquire the image in specific cardiac phase [29].
Advanced X-Ray angiographic techniques allow to reconstruct coronary models from two projected views acquired in a monoplane or biplane system [28, 30]: in the first one the acquisition modality occurs with one source, where the two images are selected in two different cardiac cycle at the same cardiac phase, whereas the second one provides the two views simultaneously with the use of a double source.
Recently 3D rotational angiography has been introduced in diagnostic and clinical practice. This technique has the same physical principles of the 2D modality, with the possibility to have a rotational view of the structure in the human body [31] and thus a complete vision of the coronary arteries.
Nowadays, the X-Ray angiographic technique is commonly used to support both surgical and endovascular interventions and to estimate accurately the vascular size of the arteries. On the other hand, it is the most invasive of all angiographic modalities due to the use of ionizing radiation and contrast medium injection [32].

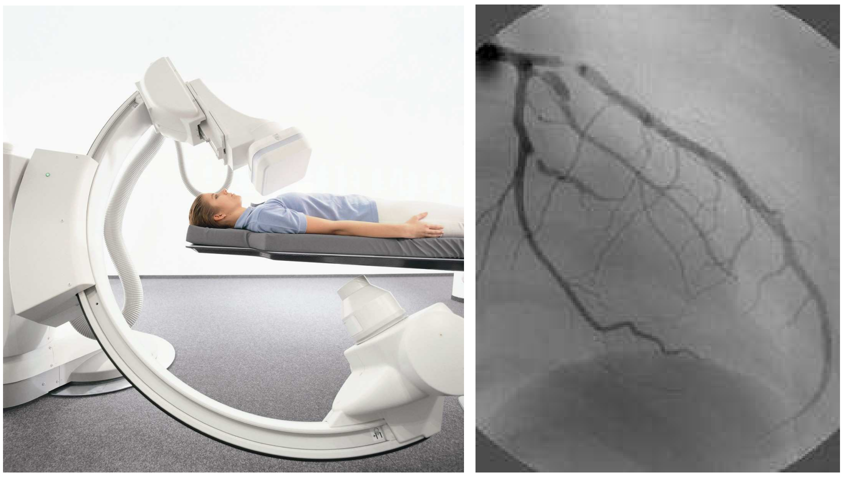

(a) (b)

Figure 1.8 *X-Ray angiographic image of coronary artery: (a) C-arm of the X-Ray angiography composed of a n X-Ray source and a flat detector for image acquisition; (b) 2D angiographic image to visualize the coronary artery tree (figures are kindly provided by Doctor G. A. Sgueglia).*

1.3.4 Intravascular Ultrasound Imaging

IVUS imaging provides the morphological information of coronary vessel wall, discerning the lumen and the outer vessel wall and providing accurate estimations both of their dimensions and of the plaque burden, as depicted in Figure 1.9.
The instrument is composed of an ultrasound transducer, mounted on a catheter of approximately 1 mm diameter passing through a standard guide-wire. The ultrasound transducer produces a 360 degrees real-time axial view by rotating the ultrasound beam rapidly around the axis of the catheter. Consecutive axial 2D images can be visualized separately or aligned and stacked longitudinally during the pullback of the ultrasound catheter to achieve the image volume and the comprehensive visualization of the vascular components [33].

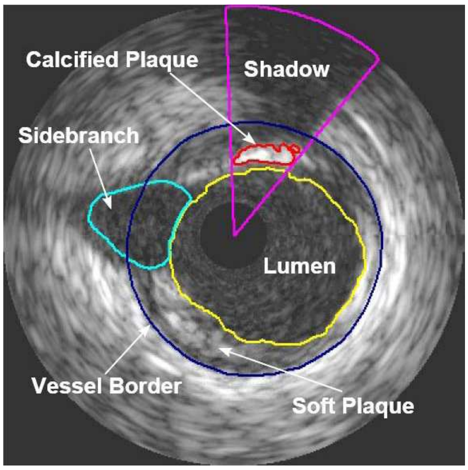

Figure 1.9 *IVUS images of coronary artery: the black circle in the middle of the image consists in the catheter where the transducer moves; coronary lumen is the dark area surrounding the catheter; calcified plaque, that blocks the ultrasound signal causing a dark shadow, is detected above the catheter; soft plaque is between the inside border of the vessel and the lumen; finally, the dark area left of the catheter is a side branch. (figure is provided by the web site http : //natcomp.liacs.nl).*

1.3.5 Optical Coherence Tomography

OCT is a recent invasive intravascular technology to detailed complex atherosclerotic lesions. As IVUS, it provides cross sectional images of vessels, as shown in Figure 1.10. Among the recent coronary imaging techniques, OCT has the high spatial resolution, about 10 times if compared to IVUS. This technology is able to identify the atherosclerotic plaques, the large lipid cores and to assess the coronary inflammation. OCT is able to detect the metal materials, identifying both stent and arterial wall. As a result of the excellent spatial resolution, stent struts are clearly defined. Besides invasiveness, main disadvantages of OCT are the limited penetration depth and the quite time consuming. Moreover, each coronary artery must be imaged separately making this technique unable to acquire an entire bifurcation in a single scan [34].

Despite several informations can be detected from different medical images described

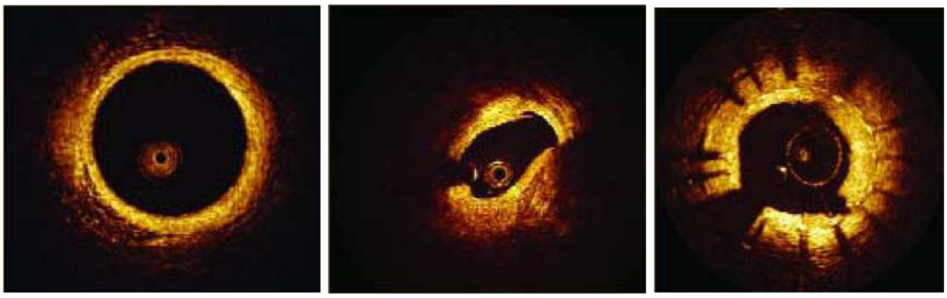

(a) (b) (c)

Figure 1.10 *OCT images of coronary artery cross sections: (a) normal artery; (b) stenotic artery with remarkable lumen narrowing; (c) cross sectional arterial view after stent implantation, where stent struts are clearly defined (figures are provided by the web site http : //surpassing.com/surpass − silicon − valley/equipment − oct.php).*

above, coronary imaging is still an open challenge for any medical operators, because coronary arteries are small (2-4 mm in diameter), tortuous, complex and continuously in motion. Besides ordinary requisites, such as complete diagnosis capability, accuracy and limited invasiveness, coronary imaging requires high temporal resolution to resolve the constant motion of the respiratory and the cardiac cycles, and high spatial resolution for the accurate imaging of very small vessels.
The state of the art about the 3D lumen coronary reconstruction is based on the projected views provided by X-Ray angiography [35]. Nevertheless, other tomographic and imaging systems such as CTA, MRI, IVUS and OCT have been developed in combination of the X-Ray coronary angiography [36]. Indeed, more complex studies such as image based structural simulations or fluid-structure interaction require other information for coronary models, i.e., arterial wall thickness, potential presence of atherosclerotic plaques and tissue properties characterization. These data cannot all be obtained via a single imaging technique. As a consequence, recently, several methods able to combine information coming from two different imaging techniques have been developed and proposed in the literature [37, 38], but they are not always available and not easy to implement. Further, the potential presence of medical devices in the vessels leads to other complications because current major imaging techniques cannot simultaneously detect both biological tissues and metallic objects [34].

1.4 Clinical applications: from image processing to numerical simulations

Much effort has been made over the last decade to reconstruct image-based models of coronary arteries to use in computational studies [39, 40]. In particular, a number of dedicated techniques and devices for stenting of bifurcation lesions are being developed [35, 41] from the 3D reconstruction of the anatomical geometry of the coronary vessel. Nowadays, X-Ray quantitative coronary angiography is the *gold standard* technique for both location and severity of coronary artery stenosis. This technique, widely available among interventional cardiologies, overcomes subjective visual estimation of lesion severity caused by high degree of the intra-observe variability presents in the traditional X-Ray angiography technique, providing objective quantification of the coronary artery

disease [42].
Nevertheless, this procedure has still bi-dimensional limitations due to the vessel overlap and foreshorting [43], which are of particular interest in the bifurcated coronary artery evaluation owing to their complex geometric configuration. Recently, advanced technologies evolving in 3D coronary artery modelling have been introduced from the X-Ray angiography technique, in particular in the case of complex lesions concern the bifurcated coronary arteries, i.e., CardioOp (Paieon, Rosh Ha'Ayin, Israel) and CAAS QCA 3D (Pie Medical, Maastricht, Netherlands) [43, 44, 45, 46].
On one hand, such innovative commercial software quantify accurately the coronary lumen disease overcoming these bi-dimensional limitations into clinical practice, on the other hand the resulting 3D coronary patient-specific models provide nowadays the information useful to generate mesh-grids models to use in finite element analysis (FEA). Indeed, recent studies have highlighted the potential role of realistic computer-based simulations based on coronary models derived directly from medical images, as a valuable support to the pre-procedural planning [20, 47, 48].
In particular, Mortier et al. [49] generated the coronary bifurcation model from three-dimensional (3D) geometrical information on the lumen of a left coronary tree, obtained by the rotational angiography using the dedicated Allura 3D-CA software[1]. In a similar manner, Morlacchi et al. [50] performed structural FEA of coronary stenting exploiting image-based reconstructions of the coronary bifurcation, which are created combining the information from conventional coronary angiography and computed tomographic angiography. Further, in the work proposed by Goubergrits et al. [51], the image-based coronary reconstruction, using the CAAS QCA 3D commercial software[2], stands out the usefulness of bifurcated artery models generated from the X-ray angiographic images to study the wall shear stress profiling in the coronary arteries.
Although these studies highlight the potentiality of realistic numerical simulations from image-based models, the link between the clinical practice and these engineering techniques is unfortunately still limited to research test-cases. In fact, even if several medical-imaging commercial workstations achieve the 3D coronary reconstruction, they are not able to build immediately FEA-suitable meshes, requiring thus *ad-hoc* implementation of outer hardware and software, as discussed by Goubergrits et al. [51] and Santis et al. [52], especially for 3D bifurcated coronary mesh models.
Given these considerations, it is clear that a key point to further promote the integration between clinical practice and the engineering tools is to generate in a fast and effective manner the computational grids directly from angiographic images used in the clinical practice [53], by-passing the coronary artery generation through these workstations.
Although, other angiographic imaging techniques, i.e., computed tomographic angiography (CTA), magnetic resonance angiography (RMA), intra-vascular ultrasound (IVUS), are investigates as alternative or in combination to the X-Ray angiography [36, 38], they are restricted to a limited number of patients and not many available in the clinical practice. Whereas, X-Ray angiography, which has been validated with respect to the CTA and RMA for coronary surface reconstruction and flow estimation [51], remains the current technique used in coronary artery diagnosis and treatment among the cardiologies.

[1] Philips Medical System Nederland B. V., Best, The Netherlands.http://www.healthcare.philips.com.

[2] Pie Medical, Maastricht, The Netherlands. http://www.piemedicalimaging.com.

1.5 Aim of the dissertation

Hence, the present study proposes a simple framework to generate 3D FEA-suitable meshes of coronary bifurcations from a given pair of X-Ray planar images to increase the integration and interaction between clinical practice and complex patient-specific computer based analyses.
In this context, we want offering a novel user-friendly tool, available also for the interventional cardiology, in order (i) to evaluate the bifurcated coronary morphologies and morphometries directly from medical images, (ii) to generate the patient-specific mesh models suitable for numerical analyses and (iii) to evaluate numerical stenting procedures from the image-based coronary models. In particular, this framework aims at providing the guidelines regarding long coronary lesions treatment in order to choose the optimal clinical procedure through the finite element analysis.
The flow chart in Figure 1.11 represents the methodological framework summarizing the computer-based procedure to support the surgical planning: in fact, several scenarios can be investigated through patient-specific numerical modelling and simulations, considering different geometries and materials and evaluating their performance in specific cases. The aim of this research focused on two main topics:

- providing an user-friendly tool for the elaboration of angiographic X-Ray images and 3D modelling generation;
- surgical simulations for the coronary lesions treatment through FEA.

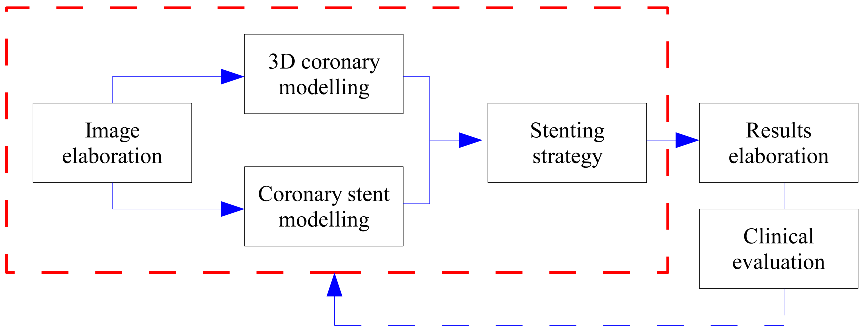

Figure 1.11 *Work-flow of the computational framework to evaluate the coronary stenting strategy performance from patient-specific coronary artery models: starting from medical images, we create both the geometrical model of the coronary artery and the stent to investigate, which are assembled to simulate the surgical intervention. The elaboration of results leads to the evaluation of the better stenting strategy to adopt for the specific treatment.*

In this study, X-Ray angiographic images have been chosen for 3D coronary computational modelling.
The X-Ray source and imaging detectors are on opposite sides of the patient's chest and freely move, under motorized control, around the patient who lies on the table while multiple images are taken quickly from different angles. To avoid subjective visual estimation of lesion severity due to the high degrees of intra-observer variability [54], we

propose a simple approach to quantify the medical images reading and to generate 3D meshes of coronary bifurcations for numerical analysis.

1.6 Organization of the dissertation

The dissertation is organized as follows:

- Chapter 2: Image processing and 3D modelling of bifurcated coronary arteries.
  Moving from the state of the art regarding the images-based coronary modelling, this chapter focuses on the description of a simple and novel framework for angiographic X-Ray images processing and the three-dimensional approach implemented to reconstruct the bifurcated coronary artery. The proposed approach represents a preliminary step toward the integration of clinical practice and numerical simulation through the generation in a fast and effective manner of the mesh grids directly from the medical images. Finally, validation testes are performed to verify and show the goodness of the image processing and reconstruction procedure implemented in the study.

- Chapter 3: Finite Element Analysis of bifurcated coronary artery.
  In this chapter, we move from the 3D modelling of the coronary artery to describe the analyses set-up done for the surgical coronary intervention to coronary stenosis treatment through the FEA. First of all, we describe the geometrical models assembled used for the numerical simulation, which are generated directly from medical images. Then, we go through material modelling and, in particular, we present the anisotropic constitutive equations adopted to describe the coronary vessel behaviour. Finally, a description of the considered boundary conditions is given and some aspects used for simulations are analyzed as well.

- Chapter 4: Numerical surgery for long coronary lesions treatment.
  Moving from the numerical and theoretical framework to simulate the coronary stenting simulation described in the previous chapter, two different strategies of percutaneous coronary interventions (PCIs) are virtually reproduced to anticipate surgical outcomes. Identifying the possible differences in the terms of coronary and stent stresses and strains due to the medical device implantation may allow to choose the better stenting strategies to adopt for a specific patient. Moreover, we have investigated also the impact of stenting procedure on the geometrical coronary profile, the apposition of the stent inside the coronary wall and the elastic recoil at the end of the stenting procedure.

- Chapter 5: Conclusions and future work.
  In the last chapter, the conclusions are highlighted to describe the aspects of the doctoral research. Moreover, further research developments are outlined.

Chapter 2

3D bifurcated coronary vessel modelling from medical images

Medical image analysis has been introduced into clinical practice to quantify objectively the anatomical geometry of the human body, overcoming complicated and subjective interpretations of the anatomical data provided by medical images.
Hence, the development of imaging tool might support and simplify the decision of the physicians and provide important anatomical features, removing errors from their interpretation and offering great benefits in the phase of diagnosis and surgical planning.
This chapter focuses on the approach of bifurcated coronary artery modelling from medical images both to compute important clinical features for planning interventional procedure and to obtain a 3D coronary mesh models to use in fluid-dynamic simulations or structural finite element analyses.
Hence, we move from a detailed description of the images-based coronary meshes modelling investigated by several Authors in the last years to the development of the novel framework performed in this research study.

2.1 Introduction

Nowadays, X-Ray quantitative coronary angiography is the *gold standard* technique for coronary stenosis detection. This technique, widely available among interventional cardiologies, overcomes subjective visual estimation of lesion severity caused by high degree of the intra-observe variability presents in the traditional X-Ray angiography technique, providing objective quantification of the coronary artery disease [42].
Nevertheless, this procedure has still bi-dimensional limitations due to the vessel overlap and foreshorting [43], which are of particular interest in the bifurcated coronary artery evaluation owing to their complex geometric configuration. Recently, advanced technologies evolving in 3D coronary artery modelling have been introduced from the X-Ray angiography technique, in particular in the case of complex lesions concern the bifurcated coronary arteries, i.e., CardioOp (Paieon, Rosh Ha'Ayin, Israel) and CAAS QCA 3D (Pie Medical, Maastricht, Netherlands) [43, 44, 45, 46]. On one hand, such innovative commercial software quantify accurately the coronary lumen disease overcoming these bi-dimensional limitations into clinical practice, on the other hand, the resulting 3D coronary patient-specific models provide nowadays the information useful to generate mesh-grids models to use in finite element analysis (FEA). Indeed, recent studies have highlighted the potential role of realistic computer-based simulations based

on coronary models derived directly from medical images, as a valuable support to the pre-procedural planning [20, 47, 48].
In the study of Antiga et al. [55], the arterial bifurcations has been reconstructed using only CTA images, proposing a fast, accurate and reproducible technique: the work develops a methodology able to build and analyze the 3D patient-specific models and to semi-automatically generate high quality hexahedral meshes.
Galassi et al. [45] have proposed a 3D reconstruction of coronary bifurcations based on 2D X-Ray angiographic images obtained in standard clinical tests. Their novel 3D reconstruction system well reproduced a solid model starting from biplanar angiographic images.
In particular, Mortier et al. [49] generated the coronary bifurcation model from three-dimensional (3D) geometrical information on the lumen of a left coronary tree, as shown in Figure 2.1 (a), obtained by the rotational angiography using the dedicated Allura 3D-CA software[1]. In a similar manner, Morlacchi et al. [50] performed structural FEA of coronary stenting exploiting image-based reconstructions of the coronary bifurcation, which are created combining the information from conventional coronary angiography and computed tomographic angiography (see Figure 2.1 (b)). Further, in the work proposed by Goubergrits et al. [51], the image-based coronary reconstruction, using the CAAS QCA 3D commercial software[2], stands out the usefulness of bifurcated artery models generated from the X-ray angiographic images to study the wall shear stress profiling in the coronary arteries.
Although these studies highlight the potentiality of realistic numerical simulations from image-based models, the link between the clinical practice and these engineering techniques is unfortunately still limited to research test-cases. In fact, even if several medical-imaging commercial workstations achieve the 3D coronary reconstruction [56, 57], they are not able to build immediately FEA-suitable meshes, requiring thus *ad-hoc* implementation of outer hardware and software, as discussed by Goubergrits et al. [51] and Santis et al. [52], especially for 3D bifurcated coronary mesh models.
Given these considerations, it is clear that a key point to further promote the integration between clinical practice and the engineering tools is to generate in a fast and effective manner the computational grids directly from angiographic images used in the clinical practice [53], by-passing the coronary artery generation through these workstations.
For example, Càrdenes et al. [38] have developed for the first time a method to combine CTA and X-Ray angiography for the reconstruction of bifurcated coronary artery to exam the pre- and post-operative conditions after stenting implant (see Figure 2.1 (b)). Limitations of this reconstruction technique are the assumption of circular cross section for the arteries and the limited information regarding the different composition of vascular tissues and the outer arterial wall shape.
In the study proposed by van der Giessen et al. [58], Authors presented another interesting framework that merges IVUS and CTA to derive 3D lumen and wall geometries, as depicted in Figure 2.1 (c), in which the relationship between wall shear stress and atherosclerosis has been investigated.
Recently, in the work of Tu et al. [36], new co-registration approach able to combine X-Ray angiography and IVUS/OCT imaging has been presented. This strategy allows

[1] Philips Medical System Nederland B. V., Best, The Netherlands.http://www.healthcare.philips.com.
[2] Pie Medical, Maastricht, The Netherlands. http://www.piemedicalimaging.com.

a straightforward and reliable solution for the assessment of the extent of coronary artery disease and the reconstruction of the coronary tree with lumen area and plaque size, but it is not routinely gated to the cardiac motion and in *vivo* validation has been limited.
Although, other angiographic imaging techniques, i.e., computed tomographic angiography (CTA), magnetic resonance angiography (RMA), intra-vascular ultrasound (IVUS), are investigates as alternative or in combination to the X-Ray angiography [36, 38], they are restricted to a limited number of patients and not many available in the clinical practice.
Whereas, X-Ray angiography, which has been validated with respect to the CTA and RMA for coronary surface reconstruction and flow estimation [51], remains the current technique used in coronary artery diagnosis and treatment among the cardiologies.
Hence, the present study proposes a simple framework to generate 3D FEA-suitable meshes of coronary bifurcations from a given pair of X-Ray planar images to increase the integration and interaction between clinical practice and complex patient-specific computer based analyses.
In this context, we want offering a novel user-friendly tool, available also for the interventional cardiology, in order to evaluate the bifurcated coronary morphologies and morphometries directly available to numerical analyses from medical images.

2.2 Coronary modelling: state of the art

In this section, we discuss about the current state of the art regarding the 3D coronary modelling from the medical images acquired be the X-Ray angiography technique.

2.2.1 X-Ray image-based coronary models

Several techniques have been developed in the last two decades for the 3D coronary models generation from X-Ray angiographic images. In the Appendix A, we detail an in-depth analysis regarding this angiographic technique from the early traditional methodology to the current innovative developments.
Such techniques can be assess from three kind of angiographic system detection: the monoplane [59, 60, 61, 62, 63], the biplane [59, 60, 64, 65, 66, 67] and the rotational system [31, 65, 68, 69, 70]. All these techniques are used within the ECG signal to correlate the images to the cardiac cycle.
The monoplane angiographic system was the first commonly used instrument for coronary intervention therapy, and the methods developed on a monoplane system can be used also for biplane and rotational angiographic systems: the differences among them consists in the acquisition modality of the projected views.
In the monoplane system, the angiographic images are acquired at different rotation angles: the projected views are selected at the same cardiac phase and in a different cardiac cycle. Whereas, in the biplane and rotational system the views are acquired by a double source and by a rotational modality, respectively. In the first two systems, two views are used for the 3D reconstruction, while in the third one more views are selected to compute the anatomical model. Then, the segmentation procedure is performed to detect the lumen contours, providing the necessary information about the

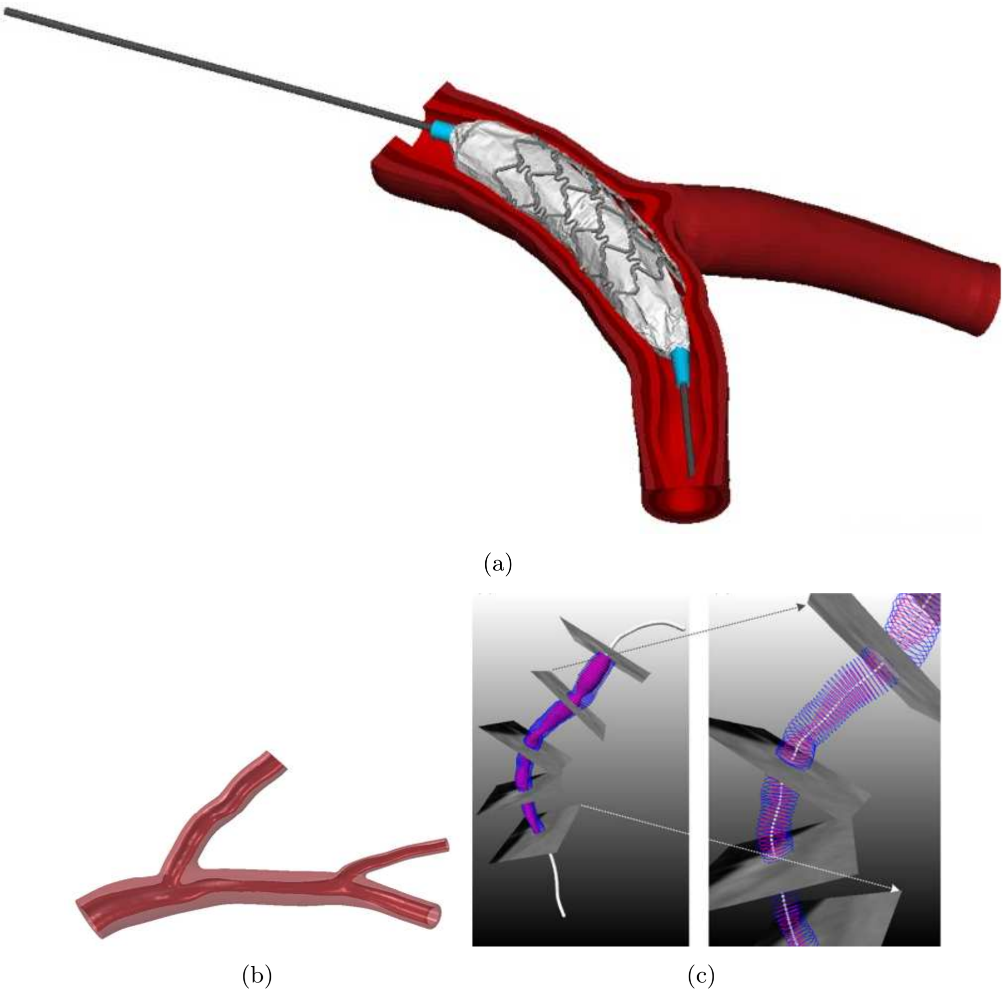

Figure 2.1 *3D coronary artery models from angiographic images: (a) vessel reconstruction reported in the study of Mortier et al. (2010 from X-Ray angiographic images; (b) coronary vessel generated in the study proposed by Càrdenes et al. (2011) from the CTA and X-Ray angiographic images and used also in the study of Morlacchi et al. [50]; (c) inner and outer cross-sections to coronary vessel reconstruction proposed by van der Giessen et al. (2010) combining the data provided by CTA and IVUS images.*

geometry of the coronary lumen for the 3D reconstruction procedure; an example of 2D segmentation procedure is depicted in Figure 2.2. However, accurate segmentation of arteries in multiple images is a crucial process and time consuming as well especially when a manual or iterative editing process is required.
In Moret et al. (1998) [71], a first quantitative analysis of 3D coronary modelling from two or more projections has been proposed, where a single projection is used to calculate the contour points of the vascular surface. The work is based on the knowledge of the standard radiographic projections, the landmarks placement, the vessel shape and the iterative identification of matching structures in two or more views.
In the work of Merle et al. (1998) [72], the 3D reconstruction of coronary tree is based on the contouring procedure of the two views, through a vessel tracking procedure, considering also the overlapping vessels. Final step consists in the matching of the vessels

between the two views. Such a matching procedure is based on the epi-polar theory proposed by Chen et al. [73].
The works of Chen et al. (2000) [73, 74] proposed an elegant method to generate accurately the entire coronary arterial tree based on two views, which are acquired from routine angiograms at arbitrary orientation and using a bi-planar imaging system.

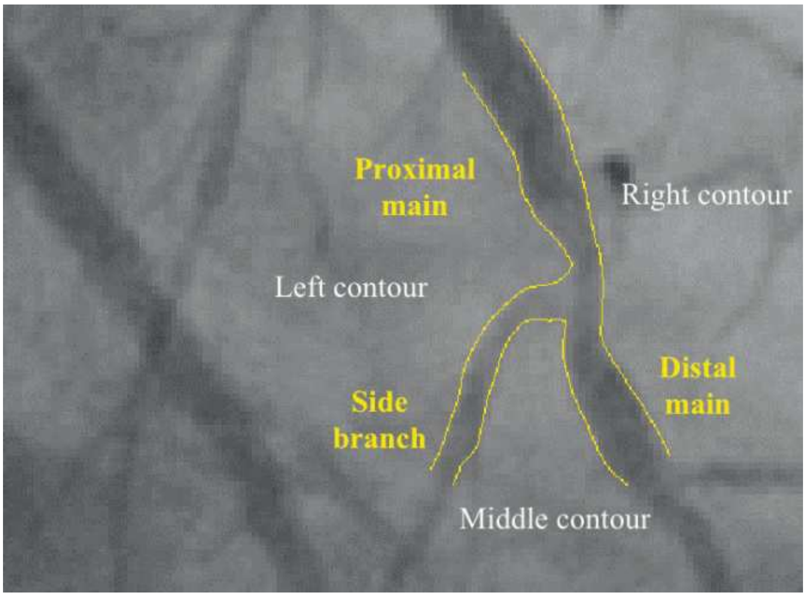

Figure 2.2 *An example of 2D segmentation procedure of the bifurcated coronary artery reported in the study of Rancharitar et al. [43].*

Such a procedure acquires a pair of angiograms associated with two different viewing angles. Each angiographic view is defined by the selected gantry orientation in terms of the left or right anterior oblique (RAO or LAO) angle and the caudal or cranial (CAUD or CRAN) angle with respect to the isocenter point to which the gantry arm rotates. The gantry information, accompanying the acquired images, is automatically recorded, including focal-spot to image-intensifier distance, field of view and gantry orientation. The work-flow for 3D modelling of the coronary arterial tree consists of four major steps: image acquisition, image segmentation, spatial correlation between the views and 3D reconstruction methodology. The segmentation procedure extracts the 2D geometrical features of the coronary lumen, like diameters, bifurcation points, directional vectors at individual bifurcations, centerlines. The spatial relationship between any two views can be characterized by a transformation in the forms of a rotation matrix R and a translation vector t with the 3D coordinate system defined in the X-Ray source or focal spot. By the use of the corresponding bifurcation points and vessel directional vectors identified from the pair of images, the transformation can be calculated to define the relative location and orientation of gantry systems associated with the two angiographic views. To compute the skeleton of the coronary arterial tree, the calculated transformation is used to establish the point correspondences between each pair of 2D vessel centerlines based on the epi-polar theory. Afterwards, a refinement process by the use of the minimization algorithm for segment-to-segment matching is performed. By the use of the correspondence relationship and transformation, the 3D morphologic struc-

tures of the coronary artery tree can be computed. The resultant lumen contours of the 3D vessel are modelled as a series of cross-sectional contours with the surfaces filled between every two consecutive contours calculated from the identified 2D diameters at the second step for the rendering of the approximated morphology of artery.
The image-based coronary modelling proposed in other studies [29, 44, 75, 76, 77, 78] follows a similar approach described previously. First, the two single-plane projected views are systematically studied and formulated; second, a non linear optimization method which takes the table movement and projection geometry into full account is proposed for the refinement of the 3D structure of the vessel skeletons; third, an accurate model is developed for the calculation of the contour points of the vascular surface. In such works the vessel features, i.e., centerlines, diameters, bifurcation points and direction vectors, have been extracted by a semi-automatic method.
Although much work has been done, the problem of precise reconstruction of coronary arteries from projection angiograms has not been solved satisfactorily, especially for bifurcated coronary arteries modelling [29].
The 3D coronary artery modelling depends highly on the information extracted from the segmentation procedure in a bi-dimensional analysis, which means to extract the vessel shape from the background of the grey-scale images.

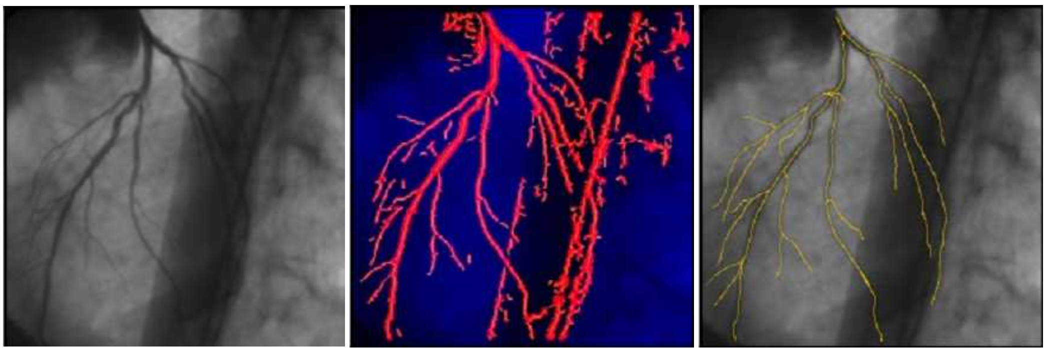

(a) (b) (c)

Figure 2.3 *3D coronary artery tree from two X-Ray biplane projected views reported in the study of Brien et al. [79]: (a) detailed view of original angiographic image; (b) segmentation to extract the coronary lumen area and to compute the centerline; (c) final centerline graph superimposed on the original angiographic image.*

All these procedure consists in semi-automatically contouring detection of the coronary lumen inside the medical image through a minimal amount of interaction: in fact the user identifies manually the courses of all major branches at the beginning of the procedure [79, 80, 81]; an example of the procedure is depicted in Figures 2.3.
Whereas, automatic segmentation are difficult to perform due to the presence of motion artefacts, contrast in-homogeneity and non-stationary background. Moreover the quality of the image could be also destroyed by low signal to noise ratio. For these reasons, the segmentation procedure is supported by an image enhancement to improve the image quality through filtering procedures.
The reconstruction techniques of coronary artery tree are developed with respect to the dataset typology of the angiographic images. The accessibility of the image data leads to take into account appropriate algorithms for the 3D reconstruction to connect the

boundary contours after the previous segmentation procedure [55, 82].
In the Appendix B, we report some techniques adopted for the elaboration of the medical angiographic images through an user-friendly and interactive environment with an high-level language, the software Matlab (The MathWorks Inc., Natick, MA, USA).

2.3 Framework for 3D coronary vessel modelling

Moving from such considerations, in this study we aim at defining a methodological framework, resembling the work-flow depicted in Figure 2.4. After images acquisition, two projected views are selected and then elaborated, first in an image processing and, then, in a specific 3D modelling procedures, which are implemented in Matlab (The MathWorks Inc., Natick, MA, USA).
The image processing consists in the image enhancement to improve the image quality and in the segmentation procedure for the coronary lumen contouring. The 3D coronary artery modelling (skeletoning) is generated from the 3D centerline reconstruction and the mean radii values computed thanks to the segmentation procedure. Finally, the algorithm generates automatically the vessel mesh model, computing also the main features of the bifurcated coronary artery, i.e., diameters, lumen area, bifurcation angles, stenosis degree. In the following we discuss each step of the work-flow. All the analyses presented in this study are performed off-line after the completion of angiographic study, through the use of an Intel Core 2 Duo CPU/3.23 of RAM, with a computational time of 4-5 minutes.

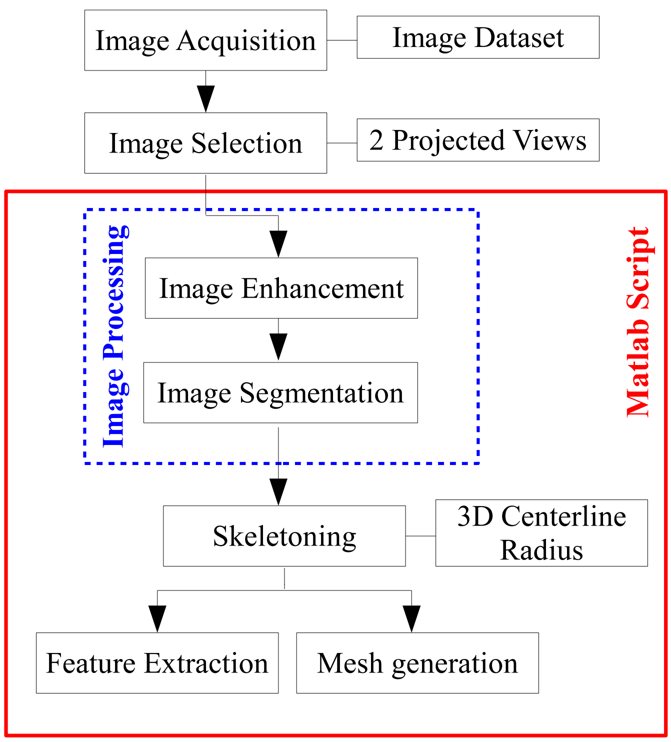

Figure 2.4 *Schematic work-flow of the 3D reconstruction procedure developed in this study.*

2.3.1 Image Acquisition

The input of the framework is a set of medical images, in DICOM format, acquired by X-Ray coronary angiography (General Electric, Schenectady, NY, U.S.A.). This technique consists in the radiologic visualisation of the coronary tree, thanks to contrast-dye injections performed through minimally-invasive catheterization. Usually, cine-angiographic sequences at 15 frames per second are acquired with the flat detector angles selected by the interventional cardiologist. Each frame of this sequence represents a projection of the coronary artery into a single-plane system. Moreover, the images are also correlated to the cardiac cycle by electrocardiographic gating [83]; this approach allows to reduce the artefacts due to the cardiac motion and facilitates the choice of different views at the same cardiac phase. Usually, the end-diastolic phase is preferred [63] because, in this specific time frame, the lumen is fully filled by the contrast-dye and thus it is easy to visualise [84].
During the image acquisition the table movement is minimised by an iso-centering procedure [85, 86]. Each image contains not only the patient's data but also the image acquisition settings, which include, among the others, focal-spot to image intensifier distance (SID), field of view (FOV), flat panel orientation, imager pixel spacing (IPS), and estimated radiographic magnification factor (ERMF). Other image metadata can be derived; for instance, the pixel spacing (PS) is computed as the ratio between IPS and ERMF for both views.
Each angiographic view is defined by the flat detector orientation in terms of the left or the right anterior oblique (LAO or RAO) angle and the caudal or cranial (CAUD or CRAN) angle with respect to the iso-center point. Moreover, the flat detector motion is characterised by constant SID and iso-center value in order to establish a pointwise correspondence between the two views [63, 74, 77].
In the obtained sequence of the angiographic images, the user manually selected the given projected view at the end-diastolic time, e.i., at the peak of the R wave of the ECG. The source send out interleaved pulses of X-Ray, which are partially absorbed by dense tissues in the subject and by radio-opaque dye that has been previously injected into the patient's coronary arteries. The intensifiers can be positioned to yield different projected views of the arterial structure in order to acquire the angiographic images; the user can analyze the image to obtain the appropriate views.

2.3.2 Quantitative coronary angiography in clinical practice

X-Ray quantitative coronary angiography (QCA) is the most commonly used imaging technique in clinical practice to assist coronary diagnosis and therapy. It involves injection of contrast agents into the artery followed by X-ray imaging in multiple planes and assessment of arterial lumen diameter.
The images generated by QCA suggest that atherosclerosis is a disease process, whereas it is actually diffusely distributed, where the wall thickness and plaque composition cannot be assessed. Moreover, the radiation exposure and the potential cause renal damage through use of contrast agent.
Even though several alternatives to X-Ray angiography have been developed, such as CTA, MRI, and 3D ultrasound, X-Ray angiography remains the gold standard for the diagnosis and treatment planning of coronary artery disease, due to its effective means of viewing the lumen and detecting the *stenosis*. In the following, we resume the limi-

tations in X-Ray angiography technique.

- A significant amount of 3D information, that describes the coronary arteries is lost by the 2D projection of the X-ray instrument. Indeed, quantitative analysis of coronary arterial diseases, such as atherosclerosis, aneurysm and arteriovenous malformation, often suffers from this intrinsic limitation.
- With the commonly used monoplane angiographic system, the physician can only obtain one angiogram from one angle of projection and it is very difficult for a novice physician to diagnose disease from limited angiograms. While the number of different projection angles may be increased, this approach leads to higher X-Ray exposure for both the patient and the physician and it also may result in adverse effects due to higher amounts of radiopaque contrast material.
- The imaging angle of the C-arm is restricted by the mechanics of the instrument. Even with advanced rotational angiographic systems, the physician cannot easily reach all the desired angles of projection.
- Overlapping and foreshortening commonly occur in 2D projections, only experienced physicians will be able to accurately correlate information from the separated projections, which will still be a subjective process.

In this context, 3D reconstruction of vessels from only two angiographic images is of great clinical and diagnostic interest as it can compensate for these limitations. A 3D visualization of coronary models can provide physicians an accurate inspection of the complex arterial network and quantitative assessment of vascular diseases in the space.

2.3.3 Image Selection

For the 3D coronary artery reconstruction, two projection views at the same cardiac phase are selected from the angiographic sequence with a constant CAUD/CRAN angle and varying LAO/RAO angle value; for instance, Figures 2.5 and 2.6 show an example of two pair of angiographic images regarding different coronary arteries anatomy having both a pixel resolution of 512x512 and an IPS of 0.3906 mm and 0.2875 mm, respectively.

In Figure 2.7 a schematic representation of the X-Ray angiography system is shown: the gantry or C-arm system, which included the flat detector, can rotate in different direction, from right to left position (RAO to LAO), from cranial to caudal position (CRAN to CAUD) with respect to the isocenter, which is a pivot point collocated virtually on the heart area of the human body. For the analysis a detailed workflow is reported in Figure 2.8 to describe the steps of the image processing: image enhancement and segmentation procedure. Such procedures consist in a series of steps, each of which handles some specific subtask.

2.3.4 Image Processing

Once the two views are selected, for each of them, it is necessary to enhance the image quality and to detect the edge contours of the lumen as described in the following subsections.

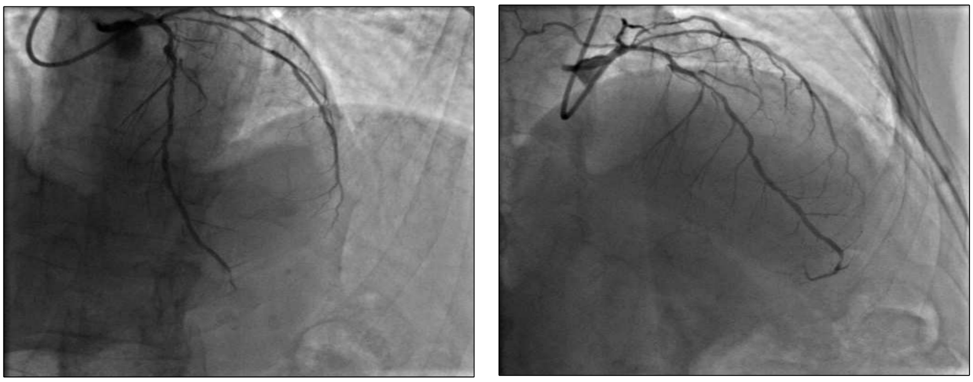

Figure 2.5 *X-Ray angiographic images: first (left) and second (right) view of the coronary tree, selected for the bifurcation model generation. In particular the images refer to the bifurcation between the left anterior descending artery and its septal branch.*

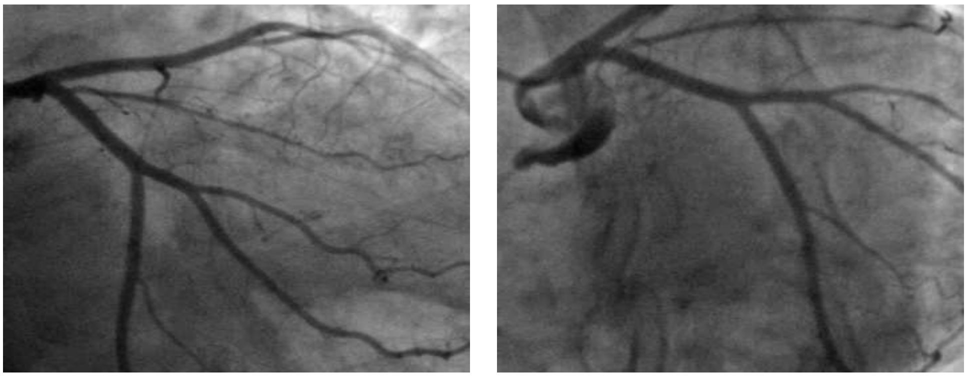

Figure 2.6 *X-Ray angiographic images: first (left) and second (right) view of the coronary tree, selected for the bifurcation model generation. In particular the images refer to the bifurcation between the left circumflex artery and its obtuse marginal branch.*

It is worth noting that the input of the image processing step consists in the two selected grey-scale images (scale 0-65535, 0 maps to black); each of them can be represented by a 2D function, *I(x,y)*, i.e., the function describing the intensity of the image in a given point, having *(x,y)* as coordinates.

Image Enhancement

The image enhancement is necessary to improve the quality of the digital image and to remove some artefacts; for instance, anatomical parts such as bone and muscle tissues within the patient's chest could appear as blood vessels at the local angiographic scale. The image enhancement is performed through the manipulation of the original image *I(x,y)* by the application of specific filters; in particular, in the present study, we apply a filtering strategy composed by the serial combination of the following filters[3]:

1. contrast enhancement;

2. noise removal and edge detection.

[3] All three mentioned filtering methods are already implemented within the Matlab Image Processing Toolbox.

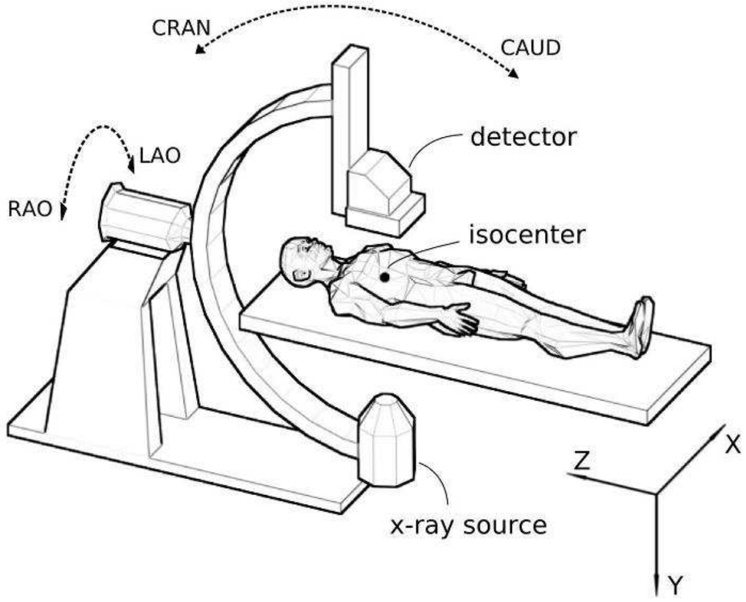

Figure 2.7 *Schematic representation of the X-Ray angiography system. Patient is positioned on the table for the angiographic image acquisition [28].*

Contrast enhancement.
A filtering operation is applied to adjust the intensity values and to exalt the image contrast of the two original images shown in Figures 2.5 and 2.6. This operation maps the values in the intensity image I to new values in I^c such that 1% of data is saturated at low and high intensities of I, increasing thus the contrast of the original image (see Appendix B).
Noise removal and edge detection.
Finally, once the noise is removed, we can detect the image edges, i.e., a set of connected pixels defining the boundary between two regions. Generally, the simplest method to find the edges is to compute the first-derivative of the image, i.e., the image gradient, and to define as edges, the points where the gradient value is maximum. Unfortunately, the only calculation of the gradient does not allow to discern correctly the pixels with a meaningful edge points. For this reason, we apply a filtering procedure consisting in the serial application of two filters: the gaussian and the laplacian filter. In fact, a valuable method to determine whether a value is significant or not is to compute the second-derivative of the image $I^w(x, y)$ by the laplacian operator $\bigtriangledown^2 I^w$, defining the edge points where its secondary derivative is equal to zero (the so-called, *zero-crossing* points). However, the laplacian generates noise into the image so it should be combined with a preliminary gaussian filter aimed at reducing the noise and at smoothing the image. The degree of blurring of the gaussian filetering is determined by the value of σ: in particular, the default value of sigma, i.e., 2, is adequate for the purposes of our study. Such a procedure is known as Laplacian of Gaussian (LoG) filtering [87, 88] (for more details see Appendix B). The result of the image processing with the application of such filters is depicted in Figures 2.9 (a) and (b); it is possible to note that the LoG filter generates a binary image with a thin edge points (see Figures 2.9 (c) and (d), Figures 2.10), forming some closed loop in the image, known as *spaghetti effect* [87].

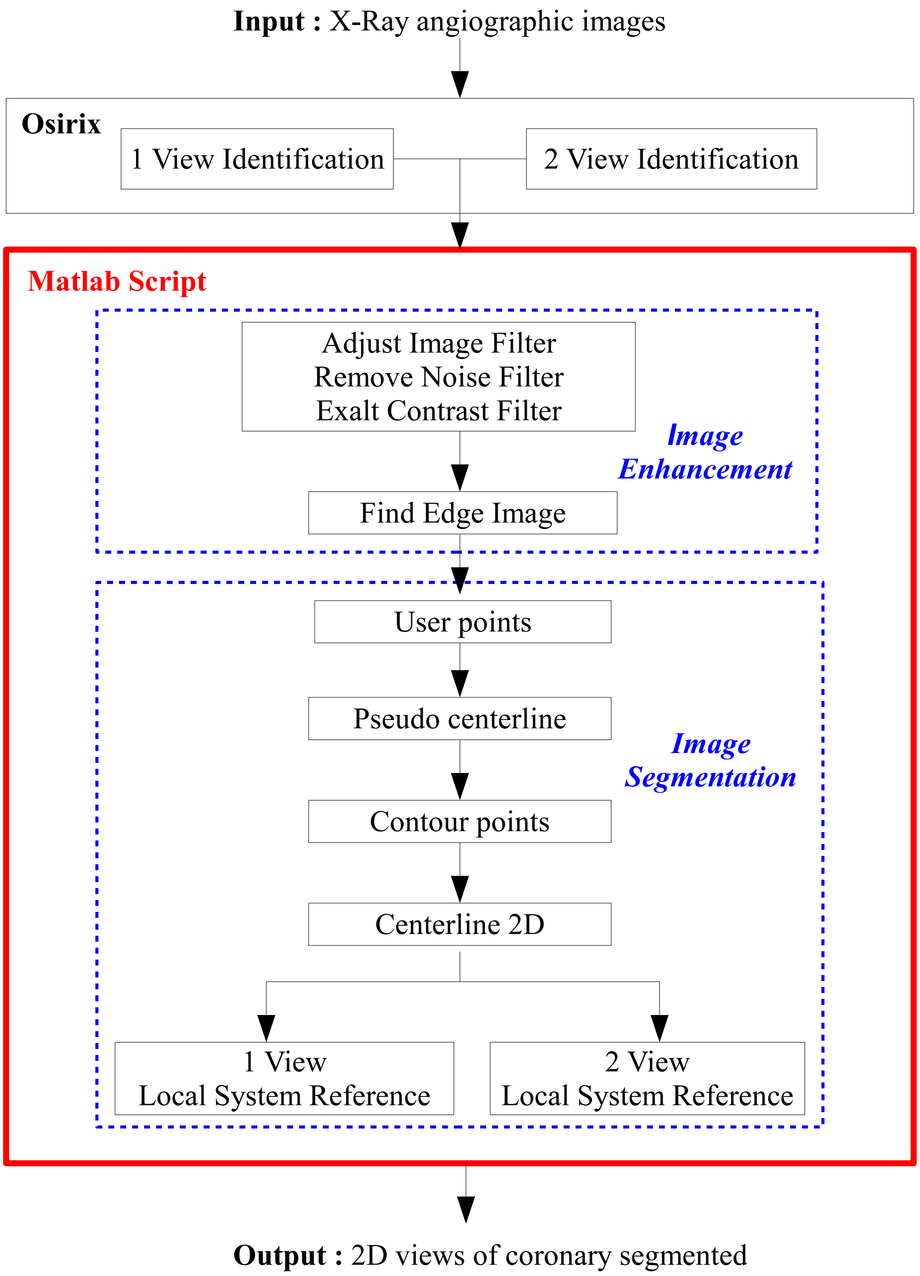

Figure 2.8 *Detailed workflow of the image processing and segmentation procedure from two selected angiographic views.*

Hence, the next step of the framework consists in the application of a segmentation procedure to discern the edges of the lumen contour, as described in the following subsection.

Image Segmentation

The procedure to assess the contour of the coronary lumen in both views is composed by three basic tasks:

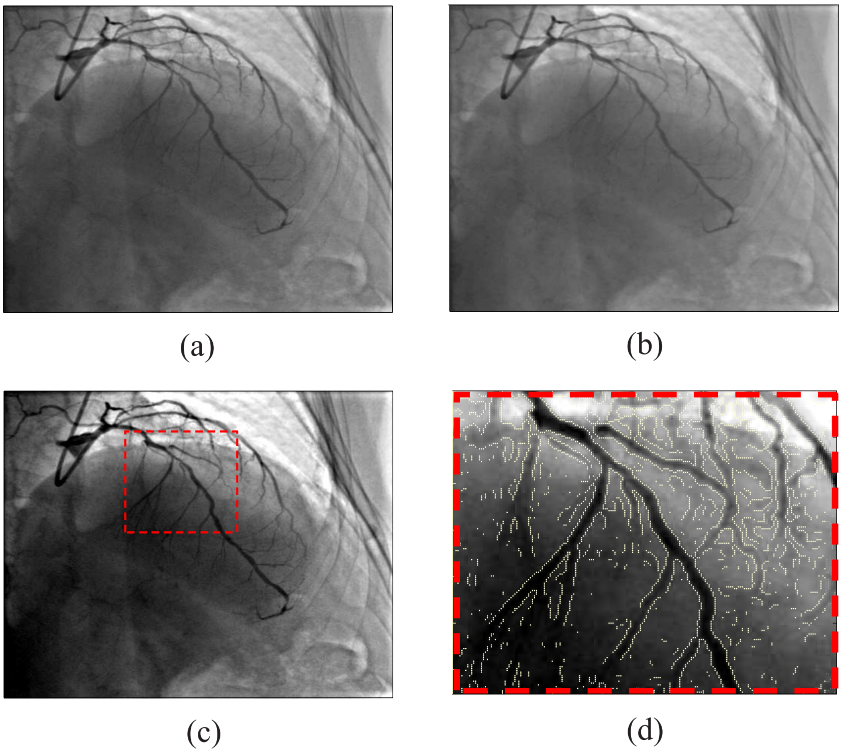

Figure 2.9 *Example of image processing: (a) the image refers to the second view of bifurcation between the left anterior descending artery and its septal branch; (b) image enhancement; (c) selected ROI; (d) edge detection, where the white dots correspond to the edges of the image.*

- identification of lumen contour and centerline;
- bi-dimensional analysis of the bifurcation coronary branches;
- bi-dimensional analysis of the bifurcation area.

Identification of lumen contour and centerline.
Our approach for the detection of both the contour and the centerline of the lumen is based on three main operations: i) identification of a pseudocenterline; ii) detection of the contour points; iii) determination of the centerline.
Once the region of interest (ROI) is selected and the edges are detected for both view (see Figure 2.11 (a)), an user-defined pseudocenterline is manually tracked inside the lumen to be segmented, both for the main and side branch of the coronary artery [31, 76, 89, 90]. The start and the end points of the pseudocenterline must correspond to two anatomical landmarks clearly visible in both views such as two points of bifurcation along coronary artery pattern. This selection constraint, coupled with an uniform re-sampling of both pseudo-centerlines, reduces the intra-operator bias introduced by the user choice.
To identify the lumen contour, we compute, for each i-th point P_i of the pseudocenterline, a line r crossing P_i and perpendicular to the segment $\overline{P_iP_{i+1}}$. Given r, we compute two distances, i.e., $D_1(E_k, P_i)$ and $D_2(E_k, r)$, for each edge point, E_k, as depicted in Figure 2.11 (b). D_1 and D_2 are used, through an appropriate weighting, to assess a pair of points, C_i, belonging to the lumen contour. Such a procedure classifies the edge

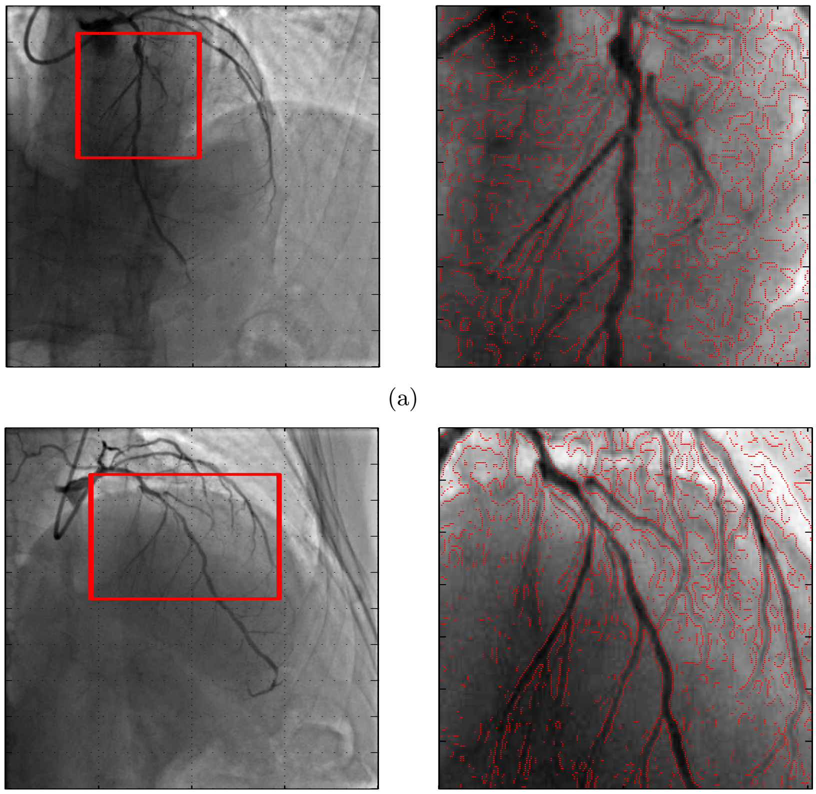

(a) (b)

Figure 2.10 *Edges detection of the angiographic images: the technique for the identification of the edges into the image are applied for the (a) first and (b) second view.*

points E_k based on the two distances, keeping for each pseudocenterline point only the two edge points which satisfy the criterion of minimum distance of both to the line r and point P_i. Finally, for each view, we define the i-th point of the"true" centerline as the mean point of C_i; consequently, each point of the centerline is now associated to a pair of lumen contour points, as depicted in Figure 2.11 (c).

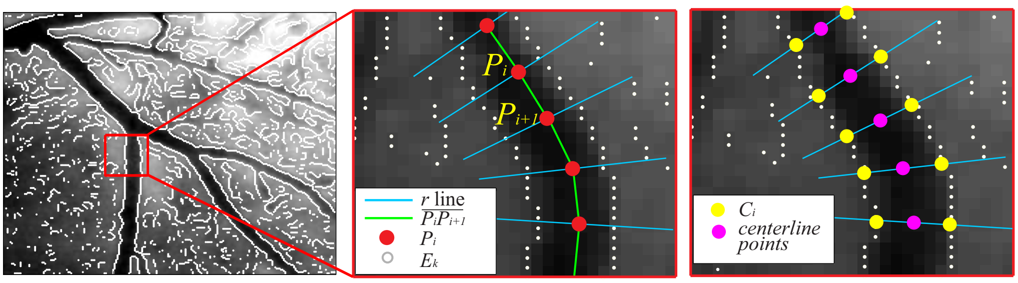

(a) (b) (c)

Figure 2.11 *Image processing and segmentation procedure: (a) image enhancement and edges (white) detections of a projected view; (b)-(c) lumen contouring (yellow) and centerline (magenta) computation from user-defined pseudocenterline points (red).*

Bi-dimensional analysis of the bifurcation coronary branches.

The definition of the bifurcation region requires the identification of two main points: 1) point of bifurcation (POB) defined as the point where all the centerlines of the branches meet [43]; 2) carina point defined as the point that appears interposed between the parallel origins of the main branch and the side branch [91].
For this purpose, we elaborate the centerlines and the contours of the main and secondary branch, previously detected, to compute: 1) the POB as the intersection of the centerlines of the two branches, i.e., the main and the secondary branches; 2) the carina point as mean point between the two closest points of main and side branch contours, as depicted in Figure 2.12 (a). Then, algorithm computes automatically the distance d between the POB and carina point to identify a confluence region inside the bifurcation area. Once these notable points and the distance d are defined, it is possible to discern the three different branches of the bifurcated coronary artery, i.e., the proximal main (PM), the distal main (DM) and the side branch (SB), and the so-called region of bifurcation (ROB) [43], as shown in Figure 2.12 (b). In Figures 2.13, we illustrate the results of such a procedure for the left anterior descending artery and its septal branch images.

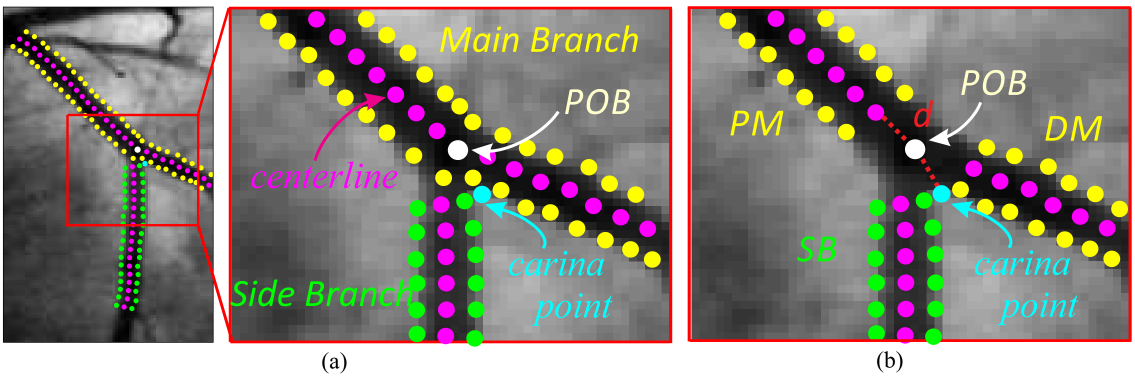

Figure 2.12 *Bi-dimensional analysis of bifurcation coronary branches and bifurcation area: (a) POB (white) and carina point (cyan) are identified in the view from bifurcated anatomical features; (b) once the distance d (red), between the POB and carina point, is computed, the PM (yellow), DM (yellow) and SB (green) contours and the respective centerlines (magenta) are detailed to discern the coronary branches to the ROB.*

Although this identification process, some possible artefact due to the overlap of the main on the secondary branch can be still present [43, 46, 92]. To reconstruct correctly the 3D model, it is necessary to know the mean radius value of the corresponding pair of contours between the two views; fictitious contours are considered in the hidden part of the secondary branch as described by the test-case depicted in Figure 2.14. Hence, from the inverted Y-like 3D model of Figure 2.14 (a), resembling the typical profile of a coronary bifurcation, two projected views, i.e., *view 1* and *view 2*, are generated as shown in Figures 2.14 (b) and (c). Given the PM, DM, and SB, it is possible to define, for each of the views, the height h_i, which is the distance between the PM boundary and the carina point (red dot). Then, if $h_1 \neq h_2$, there is an overlap; for example, in our case, $h_1 > h_2$, so part of the SB is hidden in the first view, consequently it is necessary to image here a fictitious contours, as a *quantity* weighted by the value $h_1 - h_2$ and having a radius values like to the corresponding pair of contours in the SB of the second

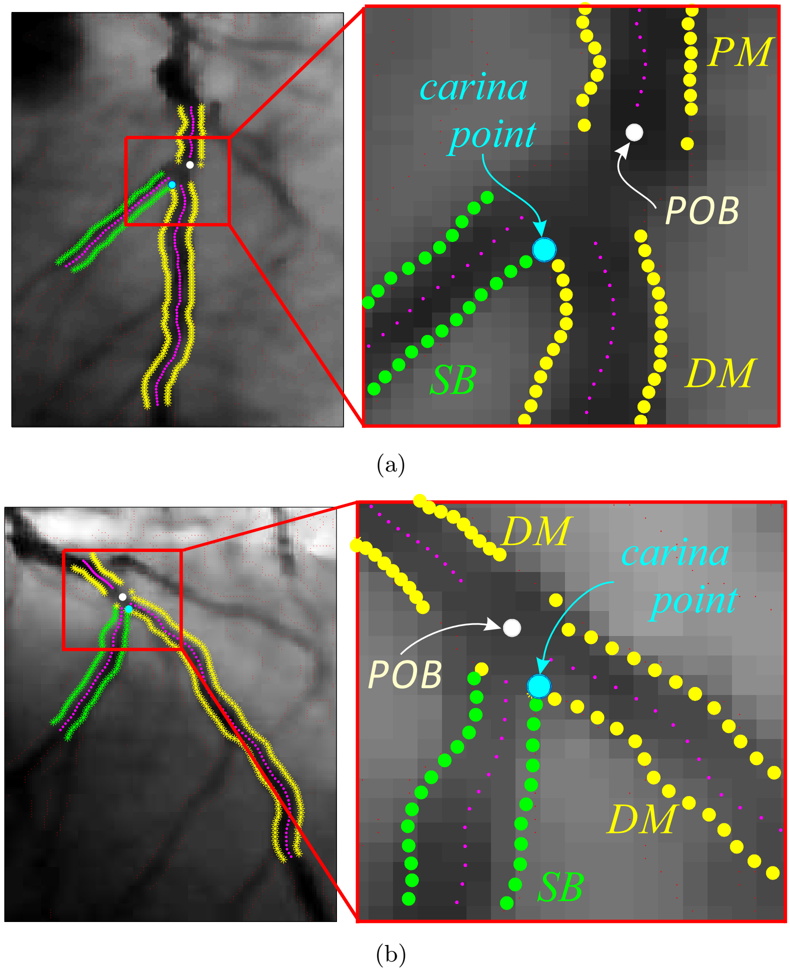

Figure 2.13 *Automatic procedure to compute bifurcation coronary features: (a) first and (b) second view indicates proximal main (PM) and distal main (DM) contours (yellow), side branch (SB) contour (green), centerline of the three branches (magenta), point of bifurcation (white) and carina point (cyan).*

view. These fictitious contours are then considered for the 3D reconstruction process.

Once contours of the coronary branches have been defined, we compute the external contour points in both views to reconstruct the vessel wall profile. Since the medical images contain no information about the vessel wall thickness, we adopt a reconstruction strategy considering an uniform wall thickness [93] in the non diseased region. At the location of the stenosis, we reconstruct the outer wall profile linearly interpolating the profile of the proximal and distal region as described in Figure 2.15. Unfortunately, this approach can lead to some undesired overlap between the outer DM and SB contours near the bifurcation, which can be avoided detecting and deleting these overlapping contour points for both the branches.

Bi-dimensional analysis of the bifurcation area.
The last step of the image segmentation consists in the definition of ROB contour

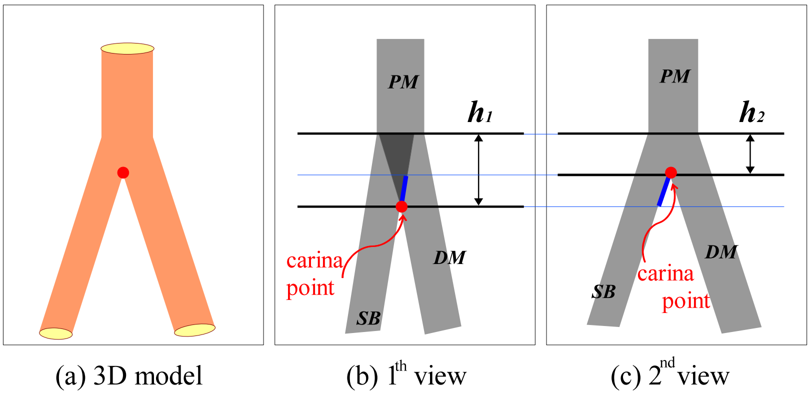

Figure 2.14 *Test-case representing the adopted approach to overcome the overlapping branch in the ROB: (a) inverted Y-like 3D model; (b - c) view 1 and view 2 of the 3D model and identification of branches and notable points to evaluate the hidden part due to the overlapping problem.*

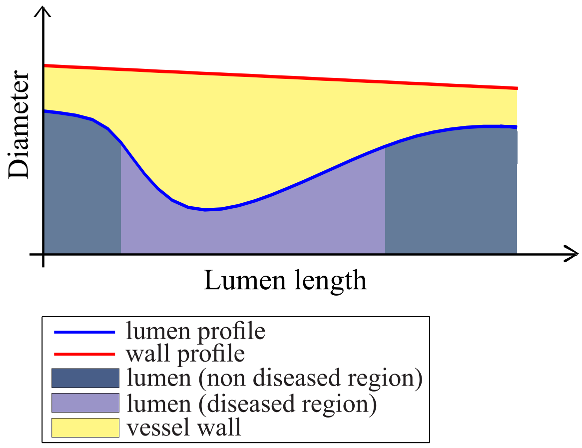

Figure 2.15 *Generation of the vessel wall: from the outer proximal and distal points of the healthy vessel's region, a linear interpolation is applied to compute the vessel wall.*

points. As described in Figure 2.16 (a), it is possible to identify three segments (pm_e, dm_e, sb_e) corresponding to ROB boundaries with respect to each branch.
The remaining boundaries are defined by three polynomial lines, l_A, l_B, and l_C shown in Figure 2.16 (b); these lines are built imposing appropriate Fent conditions at the ends derived from the corresponding contour points. Furthermore, given the ROB gravity center (GC) and the carina point, we can split the ROB with respect to branches as depicted in Figure 2.16 (c). Finally, we compute the external contour points of the ROB from a constant thickness value to determine the vessel wall of the ROB.

2.3.5 3D bifurcation coronary model reconstruction

In the previous sections, we have discussed how to retrieve all the necessary geometrical data of the bifurcation and its branches. In the following, we describe how we integrate this 2D information to create the corresponding 3D model. In particular, we aim at

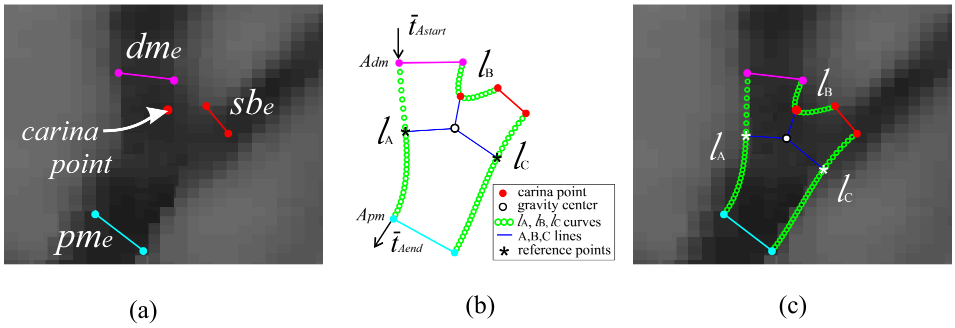

Figure 2.16 *2D ROB segmentation: (a) branch boundaries superimposed to the bifurcation; (b) polynomial curves defining the ROB contour; e.g., given the contour points, dm_A and pm_A, we impose the respective tangent vectors, $\bar{t}_{Astart}$ and $\bar{t}_{Aend}$, to build the curve l_A; the reference point is computed from the intersection between the A(C) line and the $l_A(l_C)$ curve. (c) Final result of the ROB segmentation superimposed to the original medical image.*

reconstructing the 3D profile of the centerline to be used as sweeping path of lumen cross-sections.
Given our working condition, which fixes one of the two rotation angles of the flat detector, e.g., CAUD/CRAN angle, we can consider the other rotation angle, e.g., RAO/LAO angle, as a measure of the relative rotation between the plane views around their intersecting axis as depicted in Figure 2.17. Then, we consider a local reference system (xyz) and a global reference system (XYZ); in particular, we assume that, for the first view, y is equal to zero while, for the second view, x is equal to zero. The definition of the two local views in the plane, shown in Figure 2.17 (a), reads as:

- x_1, z_1 for the first view;
- y_2, z_2 for the second view.

Furthermore, for the 3D reconstruction approach, we assume that the first and the second view in the global reference system $X_1Y_1Z_1$ and $X_2Y_2Z_2$, respectively, as follows:

$$\begin{cases} X_1, Y_1, Z_1 \\ x_1, 0, z_1 \end{cases} \tag{2.3.1}$$

$$\begin{cases} X_2, Y_2, Z_2 \\ 0, y_2, z_2 \end{cases} \tag{2.3.2}$$

From the reference system defined in 2.3.1 and 2.3.2 for the first and second view, respectively, the X-coordinate of the second view is imposed equal to zero, as shown in Figure 2.17 (b). If the first view is rotated of 90°with respect to the second view, then Y_1 is equal to zero, else $Y_1 \neq zero$. When the two views are not orthogonal the first view in $X_1Y_1Z_1$ is rotated of an angle α with respect to the plane X_1Z_1. In this case we defined $X_1'Y_1Z_1$, which differs of a theta angle (θ) with respect to the Y_2Z_2 plane ($\alpha = 90° - \theta$). If θ is equal to 90°then $X_1Y_1Z_1 \equiv X_1Z_1$ and $\alpha = 0$. Moreover, we assume the same Z-coordinates for both views.
As an example, we show in Figure 2.17 (b) the points P_1' and P_2 as the projections of the point P in the $X_1'Y_1Z_1$ and $X_2Y_2Z_2$, respectively. From such an example, we describe the steps of the 3D reconstruction procedure, which are:

1. 3D centerline reconstruction from two local views in XYZ reference system and θ angle value;
2. generation of the 3D cross-sections;
3. generation of the mesh.

In the first step, we take into account the projections of an i-th centerline point P_i to describe the 3D reconstruction of the centerline, as shown in Figure 2.17 (c). We assume P'_{i1} and P_{i2} as the projections of the point P_i in the first and second views, respectively; the views are not orthogonal and P'_{i1} is in $X'_1Y_1Z_1$. A geometrical approach is adopted to compute the coordinates (X_p, Y_p, Z_p) of the i-th point P_i from the information of the two projected views, neglecting the Z_p-coordinate, under the hypothesis of parallel X-ray beam; such an hypothesis is reasonable because we consider a small portion of the FOV. The X_p and Y_p coordinates are computed as follows:

$$\begin{aligned} X_p &= \overline{0a}, \overline{0a} = \overline{0b} - \overline{0c} \\ X_p &= \overline{0P}'_{i1} * cos(\alpha) - \overline{cP}'_{i1} * tan(\alpha) \end{aligned} \tag{2.3.3}$$

$$Y_p = \overline{oP_{i2}} \tag{2.3.4}$$

Equations 2.3.3 and 2.3.4 have been formulated from a simple geometrical approach, as highlighted in Figure 2.17 (c).

In the second step, the computed 3D centerline is used as a sweeping path for the creation of 3D coronary lumen profile. Then, we associate to each point of the 3D centerline, the mean radius value of both the inner and outer contours, which have been previously computed in the 2D analysis. Hence, from each point of the 3D centerline, which is considered as the center of a generic circle, and its mean radius, the algorithm computes automatically the inner and the outer circular cross-sections. While this sweeping procedure is used for the vessel branches, i.e., PM, DM and SB, we use the previous bi-dimensional analysis (see Figure 2.16) to reconstruct the 3D ROB by an automatic approach. For this purpose, we consider again the three extreme cross-sections of every branch, i.e., the PM_e, DM_e and SB_e, the 3D carina point and the gravity center (GC) of the ROB. The two reference points computed in the previous bi-dimensional analysis from the intersection of the A, C lines and the polynomial curves l_a and l_c, respectively (see Figure 2.16 (c)), allow to reconstruct the peanut-like section [46]. In the 3D analysis, the peanut-like section consists in a polynomial curve obtained through a proper tying of the two reference points and the two points belonging to the normal vector of the segment *(carina point, CG)*, as depicted in Figures 2.18 (a) and (b). After, the interpolation of the cross-sections is performed, discerning the 3D different regions in the bifurcation area, i.e., PM_B, DM_B, SB_B, as highlighted in Figure 2.18 (b) to complete the generation of the 3D bifurcation model.
Furthermore, to reconstruct the outer cross-sections of the ROB, we enlarge its inner cross-sections by an unique thickness value. At the end, we connect each region of the ROB (PM_B, DM_B, SB_B) with the respective coronary branches (PM, DM, SB); such a procedure is applied both for the inner and outer cross-sections, defining thus the new inner and outer boundaries of the vessel model to be connected for the generation of the hexahedral mesh. An example of such a computational grid, which is suitable

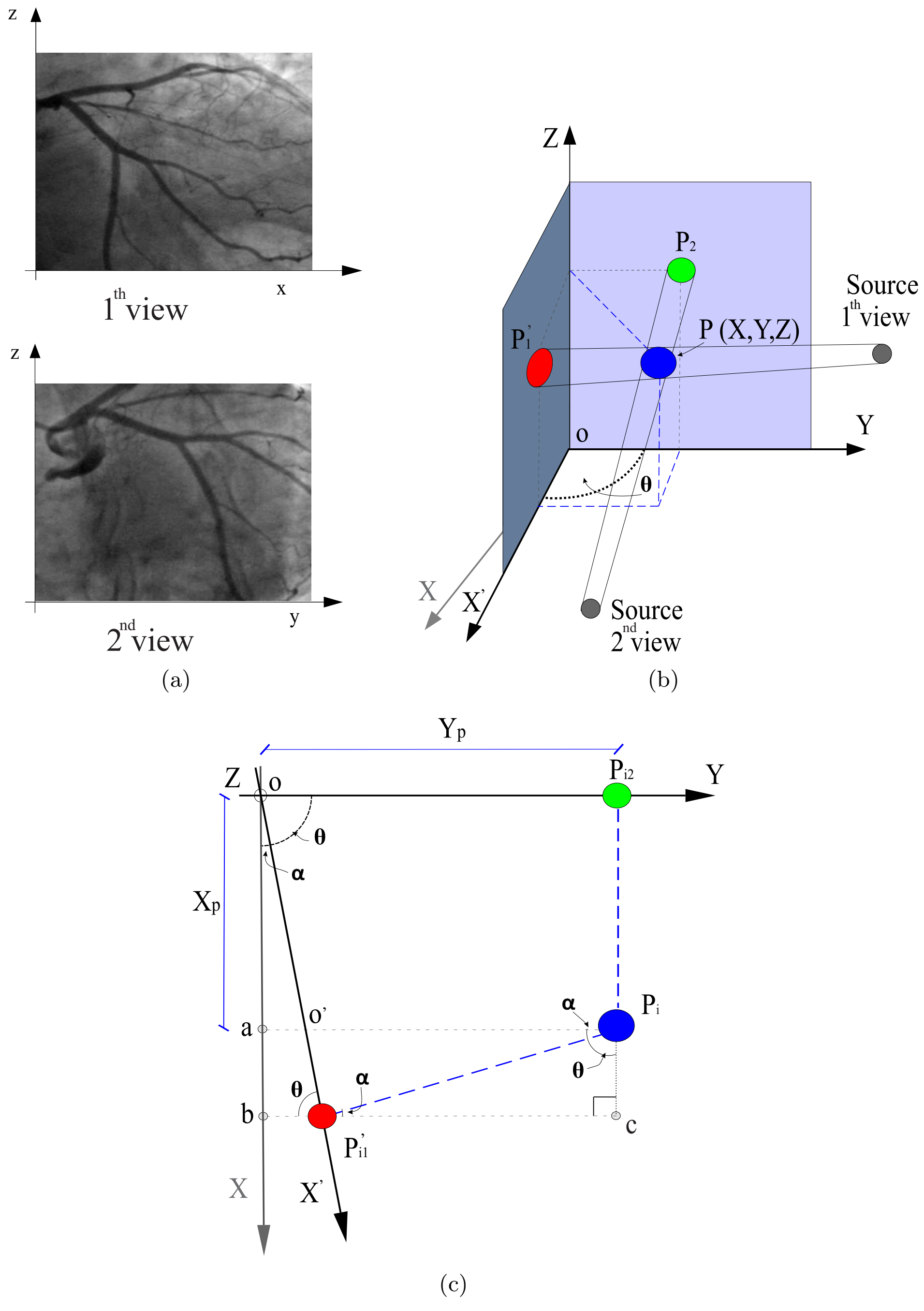

__Figure 2.17__ 3D reconstruction procedure: (a) local reference system of the first and second view; (b) global reference system of the two views for the 3D reconstruction of the point P from its projections, P_1' and P_2; (c) determination of the point's coordinates, $P(X_p, Y_p, Z_p)$, in a global reference system.

for FEA is depicted in Figure 2.18 (c).

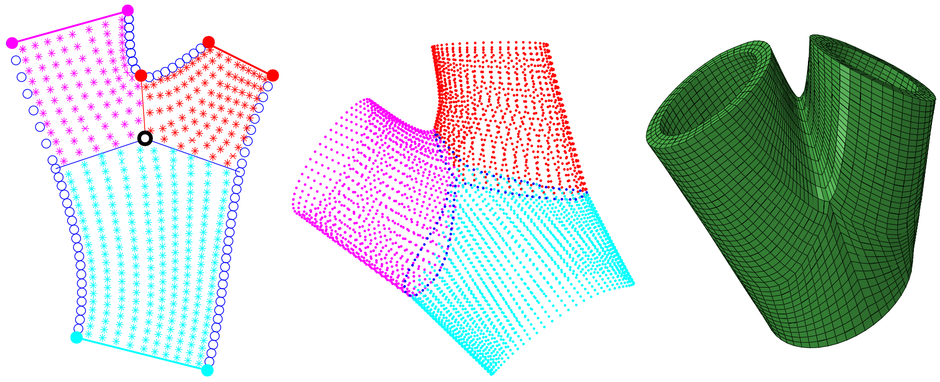

Figure 2.18 *3D ROB splitting: (a) 2D ROB segmentation; (b) 3D bifurcation cross-sections, i.e., proximal main PM_B (cyan), distal main DM_B (magenta), side branch SB_B (red), and peanut-like sections (blue dots); (c) hexahedral mesh of the ROB.*

2.4 Results

This section is divided in two subsections: in the first part, we present and discuss two validation tests to verify our framework; in the second part, we discuss the use of the framework to three real cases and in particular for the reconstruction of: i) left main coronary artery and its main side branch; ii) the left anterior descending coronary artery with a secondary branch; iii) bifurcation between the left main coronary artery and the left marginal artery before and after percutaneous intervention.

2.4.1 Validation test

Our framework can be basically decomposed in two main parts: (i) starting from the image processing of two planar projections of the same object, i.e., the coronary tree, we reconstruct the 3D centerline and assign to each point of its a mean radius value computed from the image segmentation of the two views; (ii) moving from the information obtained in the first part, we reconstruct the 3D inner and outer cross-sections of the coronary model to generate the corresponding FEA-suitable mesh. In order to verify the accuracy of our framework, in the following we discuss the results of two type of tests.
In the first test, we project the 3D CAD geometry of a known simple object to obtain the two views, which are then used as input of our framework to reconstruct the 3D model to be compared with the original one.
In the second test, given a STeroLitography (STL) representation of bifurcated vessels, we generate the 3D lumen profile through our framework from the 3D centerline points and the corresponding mean radii of the STL model; also in this case we compare the reconstructed model with the reference one for validation purposes.

3D reconstruction from two projected views

Using Rhinoceros, version 4.4 (McNell, Seattle, WA, USA), we create a simple CAD model resembling the typical trend of a stenotic lumen, as shown in Figure 2.19 (a).

Then, we generate two views based on the hyphothesis of parallel X-Ray beam from the 3D surface model with respect to five different scenarios of projection angles: 90°(orthogonal), 60°, 45°, 30°, and 20°(see Figure 2.19 (b)).
Finally, we use each set of views as input for our framework to reconstruct the 3D model, which is superimposed to the original one. To quantify the difference between the models, we use the *vmtksurfacedistance* module of VMTK library (`http://www.vmtk.org`), which computes the pointwise minimum distance of the reconstructed surface from the reference one, i.e., the original CAD model in our case (see Figure 2.19 (c)). The mean surface distance, I_d, is evaluated for every test case. As reported in Table 2.1, the results suggest good agreement between the reference surface and the reconstructed one because the mean error is lower than 0.1 mm for all the cases.
Similar results have been reported also in the study proposed by Goubergrits et al. [51], which demonstrated the efficacy of the bi-plane angiography-based reconstruction for the wall shear stress profiling of the coronary arteries with respect to the other imaging techniques.

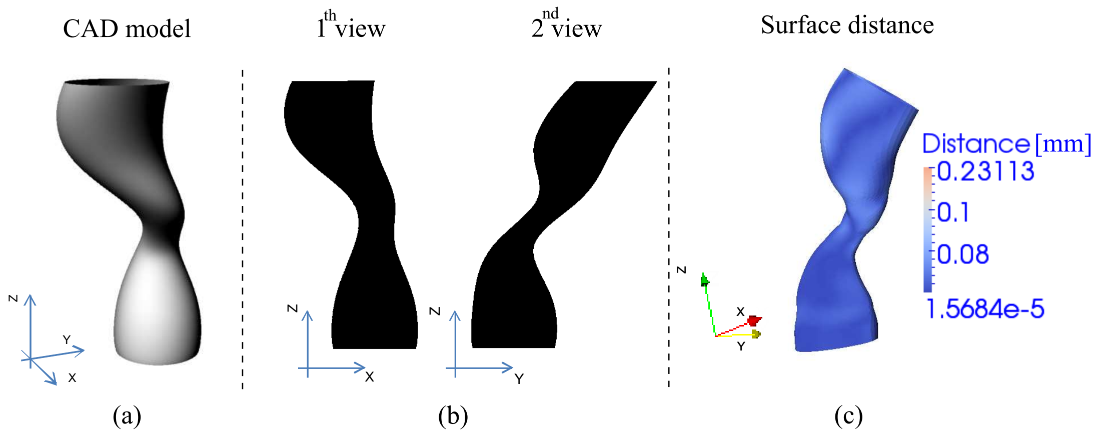

Figure 2.19 *3D reconstruction from two views: (a) CAD model generated in the software Rhinoceros from a known geometry; (b) two orthogonal views as projections of CAD model; (c) 3D reconstructed model superimposed to the CAD model to compute the surface distance.*

theta angle	Mean surface distance	norm L_2	norm L_∞
20°	0.0922 mm	$1.590 * 10^{-5}$ mm	0.2451 mm
30°	0.0913 mm	$1.587 * 10^{-5}$ mm	0.2392 mm
45°	0.0906 mm	$1.587 * 10^{-5}$ mm	0.2373 mm
60°	0.0902 mm	$1.584 * 10^{-5}$ mm	0.2362 mm
90°	0.0891 mm	$1.568 * 10^{-5}$ mm	0.2311 mm

Table 2.1 *Mean surface distance, norm L_2 and L_∞ computed from the comparison between the original model and that reconstructed through the elaboration of two views at theta angles.*

3D reconstruction from centerline and mean radii

For the second validation test, we consider three patient-specific artery models, depicted in Figure 2.20 (a), which are derived from the segmentation of Computed Tomography Angiography (CTA) images. The models are in STL format and for each of them, we compute the 3D centerline and the mean radius values by the *vmtkcenterlines* module available in the VMTK library.
Then we use this data as input for our framework computing the 3D model of each case (see Figure 2.20 (b)). Also in this case we superimpose the reconstructed model to the reference object (see Figure 2.20 (c)), measuring the surface distance between them. The results show the mean surface distance equal to 0.1996, 0.1823 and 0.1063 mm for the two carotid and coronary arteries, respectively, highlighting the effectiveness of the proposed approach also for this case. The results of such a comparison, depicted in Figure 2.20 (d), show the effectiveness of the proposed approach also for this case.

2.4.2 Application of the framework to real cases

In this section we describe the application of the proposed framework to three real cases analysing the angiographic images of three patients. The model generation has been supported by a dedicated Graphical User Interface (GUI), shown in Figure 2.21 and realised in the Matlab environment.
Such a GUI is composed of different graphical windows to allow user-interaction with the image processing applications and the 3D modelling tools, starting from the two angiographic images in DICOM format. Furthermore, the user can compute some clinical features of the 3D bifurcated coronary models, like the diameters, the lumen area and the bifurcation angles.

Figure 2.22 shows the segmentation procedure and 3D modelling results for two real cases: i) bifurcation between the left circumflex artery and its obtuse marginal branch (top), ii) bifurcation between the left anterior descending artery and a septal branch (bottom).
Both cases represent important branches of the left coronary artery system. While the first bifurcation is more relevant for clinical practice and percutaneous treatments; the second one is less relevant from this perspective but it is interesting for the generation of coronary artery models having atherosclerotic long lesions. As illustrated in Figures 2.22 and 2.23, the proposed approach provides an adequate lumen contouring for all the branches and the whole bifurcation area.
In particular, Figures 2.23 (a) and (b) show the diameters computed in both the views by three different operators and over-imposed to the lumen diameter profile provided by General Electric X-Ray angiographic workstation, which is considered as a reference. The results indicate an adequate accuracy of the performed elaboration; in fact, the average percentage error between the prediction of the proposed framework and the reference data is lower than 3% for both the views, while the intra-operator variability is lower than 0.1%.

We have also evaluated the quality of the generated meshes, adopting the equiangle skew parameter (Qeas) [52], which is a normalised measure of skewness, ranging from

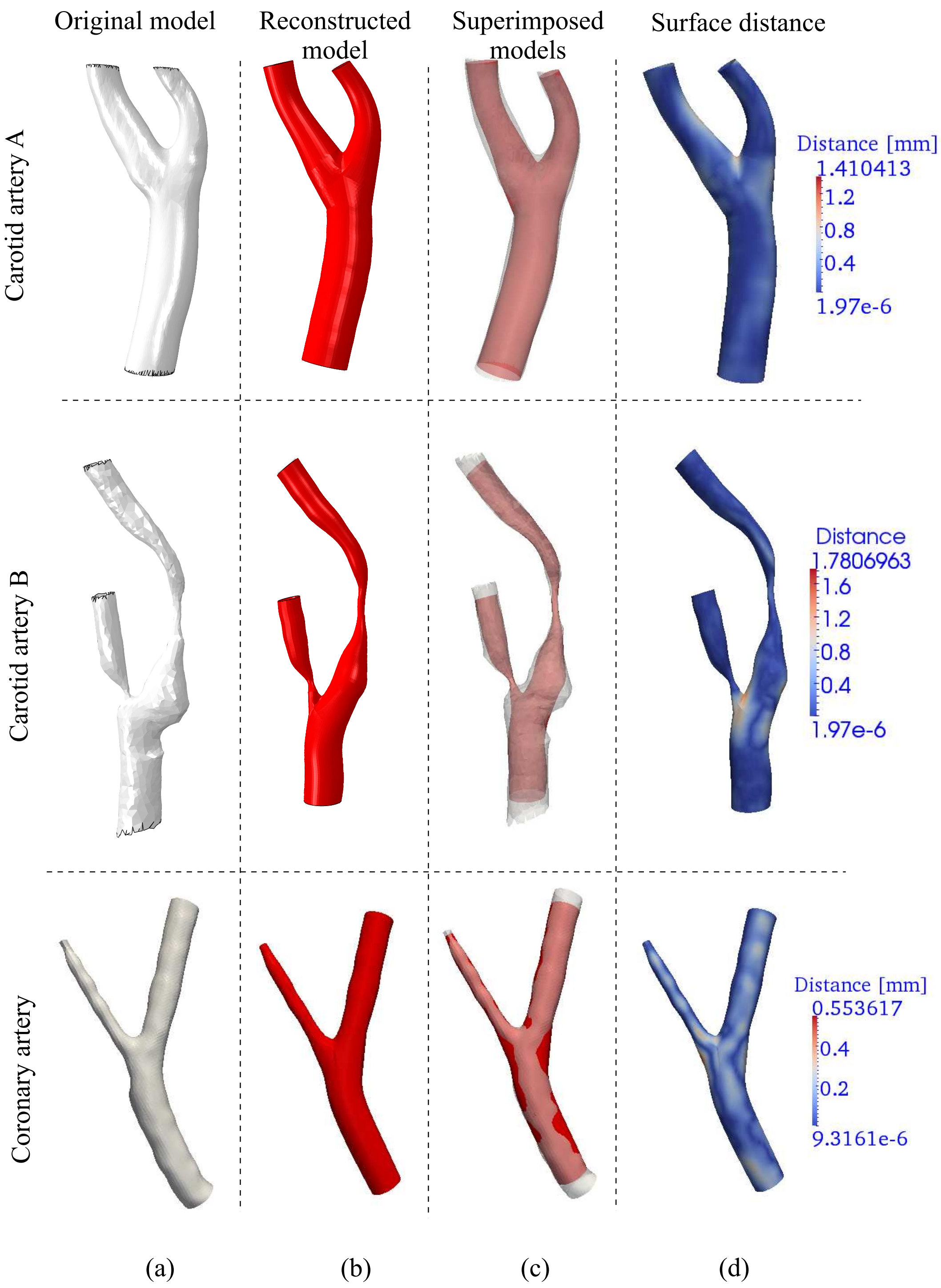

Figure 2.20 *3D reconstruction from centerline and mean radii from two patient-specific arteries: (a) original models (grey) in the STL format from the elaboration of volumetric data images; (b) reconstructed model (red) from the approach discusses above; (c) reconstructed model superimposed to the original model; (d) evaluation of the surface distance.*

0.0, i.e., perfect equiangular cell, to 1, i.e., maximal distorted cell. As reported in Table

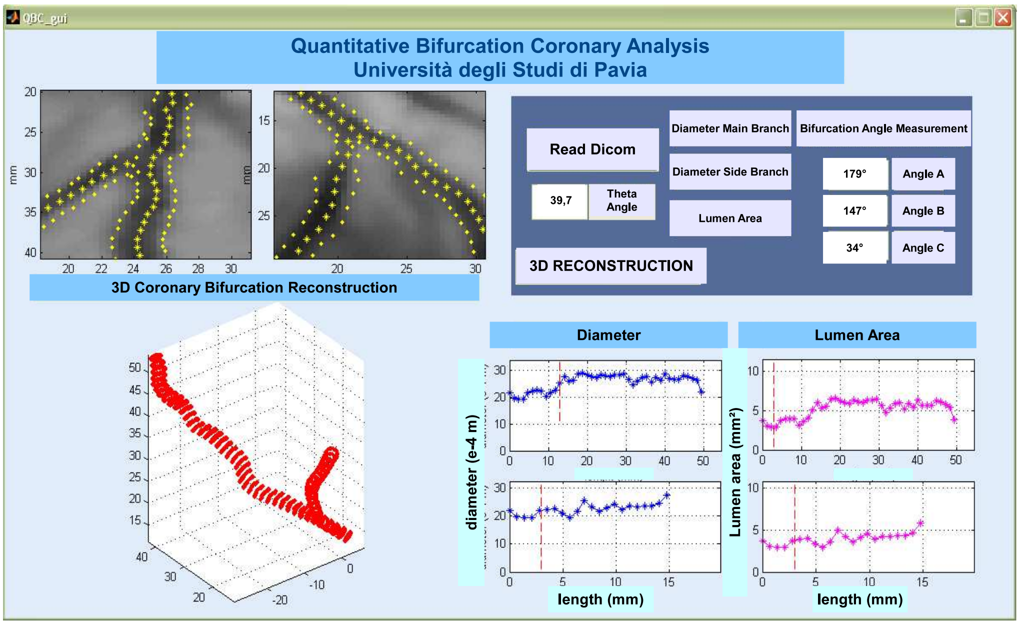

Figure 2.21 *Graphical User Interface (GUI) developed to allow a user-friendly interaction with the proposed framework. The GUI allows to visualise the 3D vessel model derived from the two views and the computed vascular features such as: i) lumen diameter and area for both the main and side branch; ii) the bifurcation angle between the different branches.*

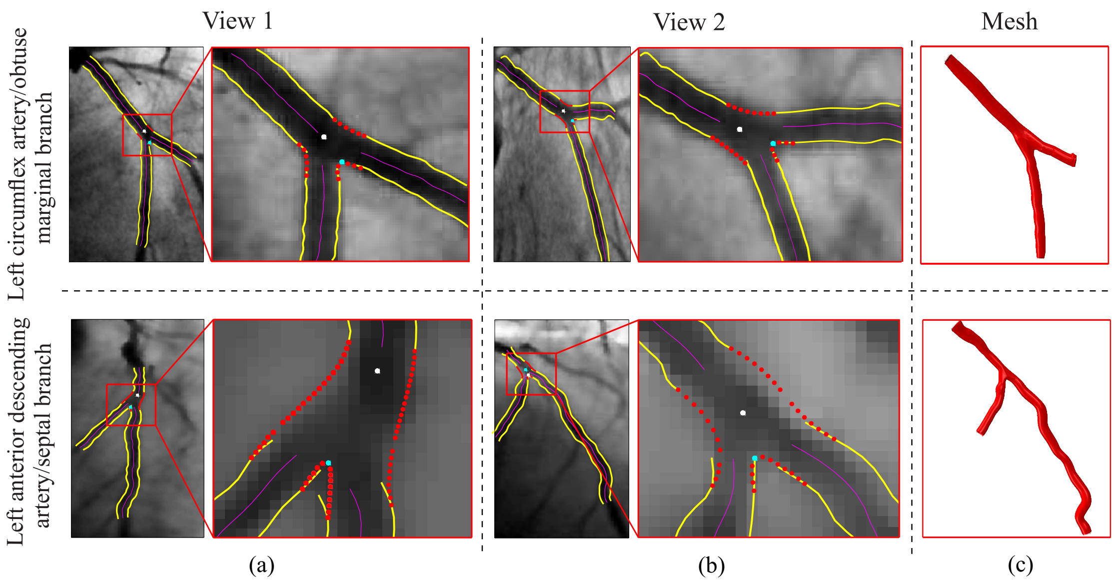

Figure 2.22 *Image processing and 3D model reconstruction of two different coronary arteries: (a)-(b) contours detection in both the views; (c) meshes of bifurcated coronary models generation for the numerical simulations.*

2.2 and 2.3, the quality of the generated hexahedral patient-specific meshes for both cases is satisfactory; in fact the greatest normalised measures of skewness (Qaes - Max) belong to the range of “good quality”.

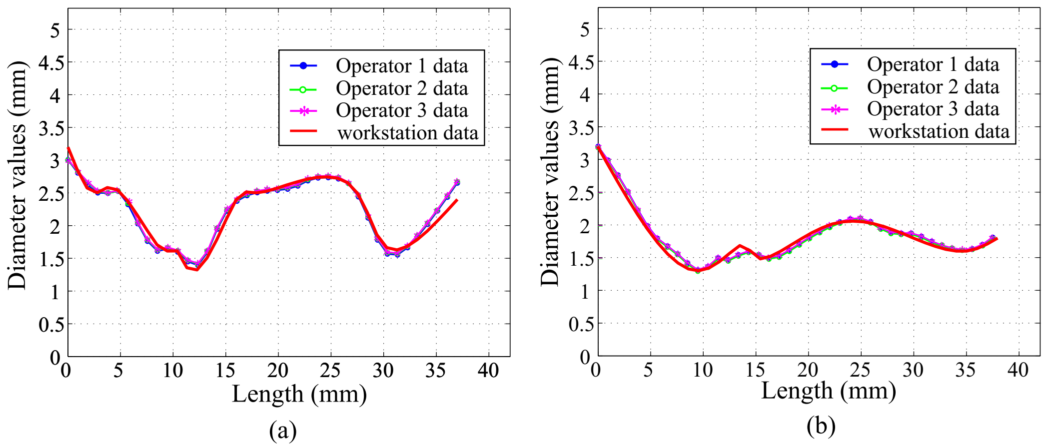

Figure 2.23 *Lumen diameter measurement of three different operators in the first (a) and second (b) view from our algorithm (blue, green, magenta), compared to those provided by General Electric X-Ray angiography (red). The values are referred to the main branch of the left anterior descending/septal branch bifurcation of Figure 2.22.*

Qeas	Quality	HEX 29,658	
		Elem	%
0.0 – 0.25	excellent	25,188	84,93
0.25 – 0.5	good	4,470	15,07
0.5 – 0.75	medium	0	0.0
0.75 – 1.0	poor	0	0.0
Max		0.30	

Table 2.2 *Mesh quality of the bifurcated coronary artery in the top of Figure 2.22 (c): the number of hexahedral elements (HEX-Elem) is divided in groups of similar mesh quality.*

Qeas	Quality	HEX 56,850	
		Elem	%
0.0 – 0.25	excellent	49,548	87,16
0.25 – 0.5	good	7,302	12,84
0.5 – 0.75	medium	0	0.0
0.75 – 1.0	poor	0	0.0
Max		0.37	

Table 2.3 *Mesh quality of the bifurcated coronary artery in the bottom of Figure 2.22 (c): the number of hexahedral elements (HEX-Elem) is divided in groups of similar mesh quality.*

We have also used the developed framework to assess the impact of percutaneous coronary intervention (PCI) on the vessel anatomy, comparing pre- and post-procedural images; in particular, we focused on the variation of the bifurcation angles among the

branches. In fact, PCI induces significant morphological changes especially in the bifurcation as demonstrated by the change of the angle between the distal main vessel and the side branch. Although the changes involving the bifurcation are supposed to cause hemodynamic effects [53], the clinical consequences are still unknown [35].
Hence, we have compared the pre- and post-procedural angiographic images (see Figure 2.24) of a patient who underwent a PCI targeting the bifurcation of the left circumflex artery with its obtuse marginal branch.
As depicted in Figures 2.24 (a) and (b), the profile of the lumen contours are changed due to the restoration of the lumen patency after the interventional procedure. This qualitative information is also confirmed by comparing the pre- and post-procedural lumen diameter variation shown in Figure 2.25.
The framework is also able to provide the angles between the branches, following the approach described by Wischgoll et al. [94], and to assess the stenosis degree. The severity of the stenosis degree is computed as

$$S = [1 - (D_{min}/D_{ref})^2] * 100\% \tag{2.4.1}$$

with D_{min} the minimum diameter and D_{ref} the reference diameter, i.e., healthy mean diameter of the coronary lumen [95] (see Table 2.4).

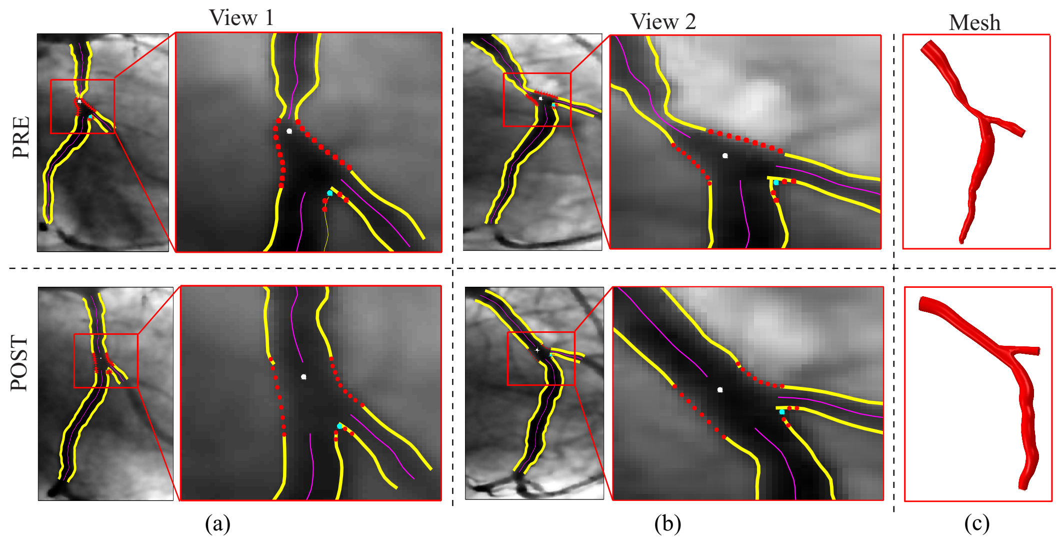

Figure 2.24 *Image segmentation and mesh generation of left coronary artery and left marginal artery before and after percutaneous coronary intervention.*

2.5 Discussion

In this study, we present a framework which is able to perform accurate geometrical analysis of the coronary bifurcation and to generate 3D computational grids, suitable for both structural finite element analysis (FEA) and Computational Fluid Dynamics (CFD) simulations, directly from two single-plane angiographic images. Consequently, the proposed work-flow integrates medical image analysis with the mesh generation, merging thus different levels of elaboration already proposed in literature but somehow

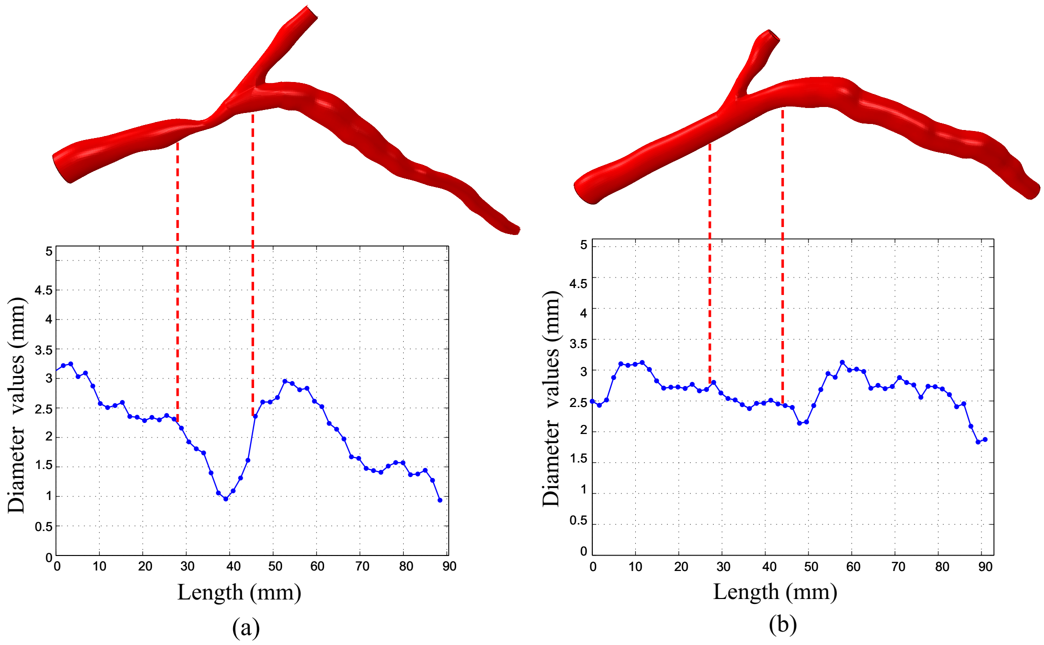

Figure 2.25 *3D reconstruction of bifurcation coronary artery before (a) and after (b) the percutaneous coronary intervention. Diameter profile is associated to the respective coronary reconstruction, highlighting the stenosis area in (a) with red line.*

Patient	A	B	C	Stenosis degree
PRE	152°	38°	170°	77%
POST	173°	13°	174°	-

Table 2.4 *Bifurcation angles (A, B, C) and stenosis degree computed before (PRE) and after (POST) percutaneous coronary intervention. European Bifurcation Club (http://www.bifurc.net) labels such angles as follows: A is the angle between the proximal main vessel and the side branch; B is the angle between the distal main vessel and the side branch; C is the angle between the proximal and distal main vessel.*

not fully linked each other, as discussed in the following.
There are many studies addressing the reconstruction of 3D coronary lumen profile from two single, or bi-plane, projected X-Ray angiographic views. For instance, several works [77, 96, 97] are based on the epipolar theory proposed by Chen and Carroll. [74], which allow to vary arbitrarily the LAO/RAO and the CAUD/CRAN angle [28], with a minimum shift of 30°. The approach proposed in these works is characterized by two fundamental steps: i) the image enhancement and segmentation of the acquired views to compute the corresponding 2D centerlines; ii) back-projection of the computed 2D centerlines through mathematical relations (epipolar theory) to reconstruct the 3D profile of the coronary tree. It is worth mentioning also the contribution of Zifan et al. [98], which reconstruct the 3D centerlines of the coronary tree from X-Ray angiogram images, obtained from one single rotational acquisition, through a method based on genetic algorithms. All these studies limit their investigation to the generation of 3D vessel centerline missing thus the step of mesh generation.
On the other hand, there are also several studies using the 3D centerline and some

other information, e.g., vessel diameter profile, to reconstruct computational grids. For instance, Santis et al. [52] propose a semi-automatic methodology for patient-specific reconstruction and structured meshing of coronary. The input data of their framework is a VRML file, containing already segmented 3D geometry, as differently oriented circular sections lined-up along the centerline; such an input data is the result of an image elaboration performed by the Allura 3D-CA workstation software. Starting from a similar input data, Mortier et al. [49] perform FEA stenting simulations using 3D patient-specific structured mesh of left coronary artery bifurcation. More recently, Morlacchi et al. [50] investigate numerical simulations of stenting using patient-specific coronary models based on the 3D reconstruction provided by the study of Càrdanes et al. [38], which propose a method combining two imaging techniques, i.e., the computed tomography and X-Ray coronary angiography.
Nevertheless, it is also necessary to underline that, although there are different commercially available solutions, the generation of 3D analysis-suitable vessel models is not always available, requiring, thus, *ad hoc* hardware and software implementation, as discussed by Goubergrits et al. [51] and Santis et al. [52].
Given such a consideration, our study proposes a simple methodology of 3D patient-specific coronary modelling from angiographic images, which may be exploited also for CFD studies [99] because it accurately reproduces the coronary lumen.

Chapter 3

Simulation of percutaneous coronarary intervention: analysis set-up

In this chapter, a finite element analysis (FEA) stenting procedure, considering the insertion of a folded balloon and a catheter over a guide wire, is proposed to perform the stent deployment in bifurcated patient-specific coronary vessel models.
We developed a methodological framework to provide the surgeon the essential clinical features as guidelines for percutaneous coronary interventions directly from angiographic image processing towards virtual surgical simulations.

3.1 Introduction

The stenting procedure has the goal to restore the lumen patency of occluded artery. Numerous computational studies have been carried out to investigate both the expansion and mechanical behaviour of different stent designs and the stress state and associated injury induced by stent placement [14, 47, 49, 50]. These analyses are important factors to consider because they contribute to the complex reaction processes that lead to the vessel restenosis.
An ideal stent design should, therefore, avoid tissue damage as much as possible and minimize the induced stresses, while providing sufficient radial support.
In the following, we describe the main steps of the percutaneous coronary intervention. In the clinical practice, the stenting procedure consists in five different steps:

- guide wire insertion;
- stent/balloon movement over the guide wire;
- balloon inflation and following stent deployment;
- balloon deflation;
- balloon and guide wire removal.

In the methodology developed in this study, the first and the last steps have been ignored in order to focus only on the stent insertion and deployment. The balloon deflation, instead, has to be taken into account since provides additional information such as the radial strength of the stent under the elastic recoil of the vessel walls. The balloon expandable Xience-Prime stent (Abbott Vascular, Santa Clara, CA, USA) has been chosen for the insertion and deployment in coronary arteries due to its popularity among the clinical practice for coronary long lesions (see Figure 3.1).

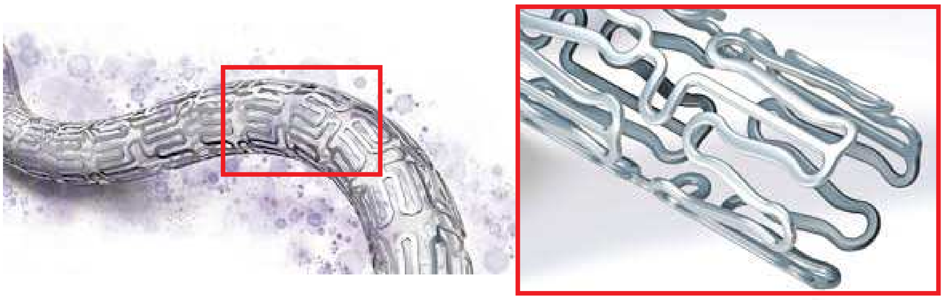

Figure 3.1 *Xience Prime: family of everolimus eluting coronary stent systems, indicated for improving coronary luminal diameter in patients with symptomatic heart disease due to de novo native coronary artery lesions, having long coronary lesions (figures provided by site web* $http://www.abbottvascular.com/us/xience - v.html$*).*

3.2 Materials and Methods

A finite element analysis requires both geometry and material properties both of the stent and of the blood vessel and appropriate loading conditions to simulate the stenting procedure.
Following, we describe the components of the numerical analyses implemented in this study to simulate the surgical procedure, considering two stenoted coronary arteries, i.e., the left anterior descending artery and its septal branch (LDA) and the left coronary artery (LCA), belonging to two different patients.

3.2.1 Coronary artery model

Geometrical modelling

Each 3D patient-specific coronary model has been reconstructed from two single-plane X-Ray angiographic views, which have been acquired by the General Electric X-Ray angiography (General Electric, Schenectady, NY, U.S.A.). Every angographic view is defined by the flat detector orientation in terms of the left or the right anterior oblique (LAO or RAO) angle and the caudal or cranial (CAUD or CRAN) angle with respect to the iso-center point, where the C-arm of the angiography rotates.
Once the two images are selected, they are elaborated in Matlab, through the framework developed in this study and detailed in *Chapter 2*. The image processing consists in the image enhancement procedure to improve the image quality and in the segmentation procedure to detect the lumen contours and the centerline points. The results of the two elaborated images performed for both the patients are depicted in Figures 3.2 (a) and (b) and Figures 3.3 (a) and (b).
Each 3D centerline is generated from the two centerlines computed by the segmentation procedure of the two views, and, then, used as a path for the generation of 3D coronary lumen profile: to each point of the three-dimensional centerline, we associate

the mean radius value computed from the two segmented views to generate the inner lumen through the cross-sections reconstruction. To create the vessel wall, the outer cross-sections are computed by the enlargement of the inner sections from a mean vessel thickness value, which is provided by Holzapfel et al. [93] (see Figure 3.2 (c) and Figure 3.3 (c)). Then, the fully hexahedral-element mesh is generated by connecting appropriately the inner and outer boundaries of the coronary model, as depicted in Figure 3.2 (d) and Figure 3.3 (d).

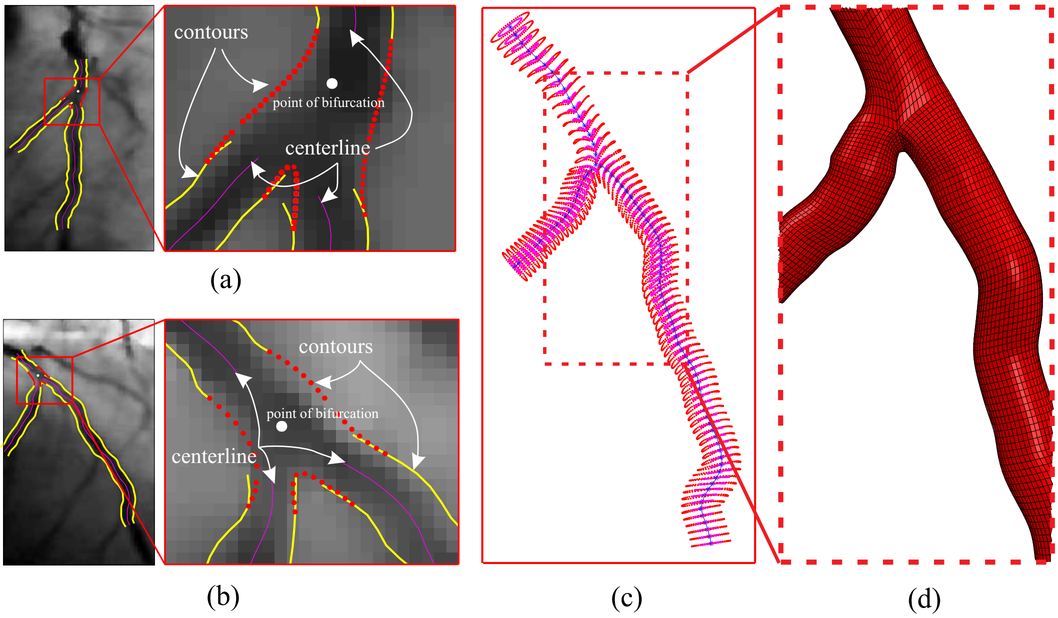

Figure 3.2 *Coronary artery generation: (a - b) image processing, i.e., image enhancement and segmentation procedures for both the projected views; (c) 3D coronary vessel modelling: centerline of the branches (blue), outer cross-sections (red) generated from the enlargement of the inner cross-sections (magenta); (d) hexahedral-element mesh of the bifurcated coronary model for the numerical simulations.*

Both the coronary arteries have diffuse stenosis along the main vessel. In this study, to describe the bio-mechanics of the coronary artery, we refer to the constitutive model reported in the next Section 3.2.1, considering an heterogeneous and anisotropic material fibers-reinforced. The material coefficients for the three layers are summarized in Table C.2 of the following section.

Material modelling

The coronary artery wall is composed of three layers (*intima*, *media* and *adventitia*) having different composition and collagen fibers organization, which confer to the coronary wall an anisotropic mechanical behaviour [100, 101]. In this study, to account such a behaviour, we refer to the model proposed by the work of Gasser et al. [7], which considers the fibers symmetrically oriented with respect to the circumferential direction. This model introduces a constitutive law derived from the strain energy function Ψ, and for incompressible and anisotropic models Ψ is split into an isotropic

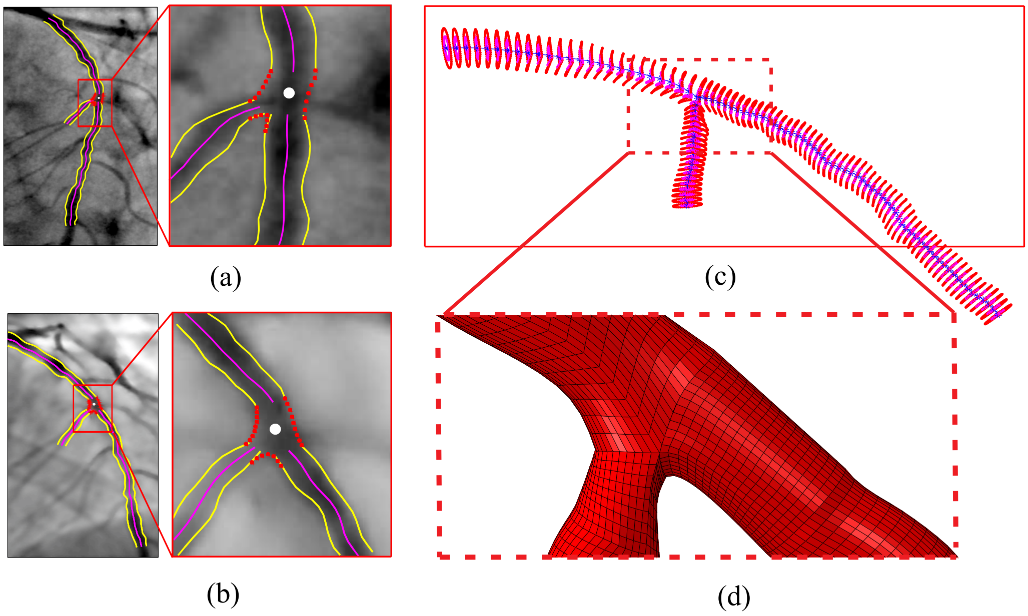

Figure 3.3 *Coronary artery generation: (a - b) image processing, i.e., image enhancement and segmentation procedures for both the projected views; (c) 3D coronary vessel modelling: centerline of the branches (blue), outer cross-sections (red) generated from the enlargement of the inner cross-sections (magenta); (d) hexahedral-element mesh of the bifurcated coronary model for the numerical simulations.*

part, Ψ_{iso} associated to the elastin matrix, and an anisotropic part Ψ_{aniso} associated to the collagen fibers embedded in the matrix:

$$\Psi = \Psi_{iso} + \Psi_{aniso} \tag{3.2.1}$$

The two terms are particularized as follows:

$$\Psi_{iso} = \frac{\mu}{2}(I_1 - 3), \tag{3.2.2}$$

$$\Psi_{aniso} = \frac{k_1}{2k_2} \sum_{i=4,6} \left\{ \exp\left[k_2(\kappa I_1 + (1-3\kappa)I_i - 1)^2\right] - 1 \right\} \tag{3.2.3}$$

where μ is the shear modulus of the matrix, $I_1 = \mathrm{tr}\boldsymbol{C}$ is the first invariant of the right Cauchy-Green strain tensor $\mathbf{C}$, and $I_4 = \boldsymbol{C} : \boldsymbol{a}_0^1 \otimes \boldsymbol{a}_0^1$, $I_6 = \boldsymbol{C} : \boldsymbol{a}_0^2 \otimes \boldsymbol{a}_0^2$ are the fourth invariants associated to the two-fiber families, with $\boldsymbol{a}_0^1 = [cos\beta^1, sin\beta^1, 0]$ and $\boldsymbol{a}_0^2 = [cos\beta^2, sin\beta^2, 0]$ the unit vectors which denote the orientation of each fibers family in the reference configuration, with $\beta^1 = -\beta^2 = \beta$ the fiber orientation angle with respect to the circumferential direction. The non-negative parameters k_1 and k_2 are the stress-like and the dimensionless parameter, respectively, and $\kappa \in [0, 1/3]$ is the fiber distribution parameter.
For anisotropic hyperelastic models, we assign an appropriate local reference system for each element of the coronary vessel mesh to define the relative fibers orientation, as

required by Abaqus [102].
Since a multi-layer structure of the arterial wall has been considered, we have computed both the set of parameters (μ, k_1, k_2, κ and β) for each layer, minimizing an objective function as described in Auricchio et al. [102], and the mean square root error (RMSE), which is proposed in [93] to evaluated the fittings quality. The experimental data used for the calibrations refer to the uni-axial tensile tests of the IX specimen coronary arteries reported in the work of Holzapfel et al. [93] for every layer. For the details of the coronary artery material modelling, we propose the Appendix C: the results of the fitting procedure and the parameters used in this study are depicted in Figure C.3 and listed in Table C.2.

3.2.2 Stent model

The investigated coronary drug-eluting stent selected for this study is the Xience Prime, crimped on a tri-folded balloon, which are a nominal length of 38 mm and a nominal diameter of 3 mm. The stent geometry was reconstructed in an image processing software, Osirix from the volumetric data of the images acquired by micro-CT imaging (see Figure 3.4 (a)). The voxel pitch of the scans was 1 microm allowing an accurate assessment of stent dimension for a correct 3D reconstruction of the stent in a StereoLiTography (STL) file. Such a format describes a three dimensional object whose surface geometry has been discretized into triangles, each of them has coordinates X, Y and Z to vertices and an index to describe the orientation of the surface normal.
Owning these parameters and using the repeating unit geometry of the stent design, solid models of the full stent can be generated. A planar geometry of the unrolled stent has been accurately drawn with Rhinoceros 4.0[1] (Figure 3.4 (b)), a NURBS-based 3D modeling tool used for industrial design, and then meshed in ABAQUS (Dassault Systemes, Abaqus Inc., Rhode Island, USA), as proposed in the study of Auricchio et al. [103] and shown in Figure 3.4 (c). The stent geometry discretization resulted in a highly regular mesh of about 8-node cubic elements with reduced integration. The inner and outer diameter of the crimped stent are 1.2 and 1.35 mm, respectively, and the resulting strut thickness of 0.15 mm is also confirmed by the manufacturer.
The Xience stent is manufactured by Cobaltum-Cromium material (CoCr). The elastoplastic behaviour of this material wa described through a Von Mises-Hill plasticity model with isotropic hardening. The Young's modulus, the Poisson's ratio and the density have been imposed to be 233 GPa, 0.35 and 8800 g/cm^3, respectively. Other parameters are the yield stress of 404 MPa, the ultimate stress of 930 MPa and the ultimate deformation of 0.0448 [104]
The stent geometry was meshed with linear eight-node hexahedral elements with reduced integration (C3D8R) using the preprocessing capabilities within ABAQUS-CAE, where the regions of the stent geometry subjected to minor deformations during the stent expansion were meshed with larger elements.

[1]McNeel & Associates, Indianapolis, USA

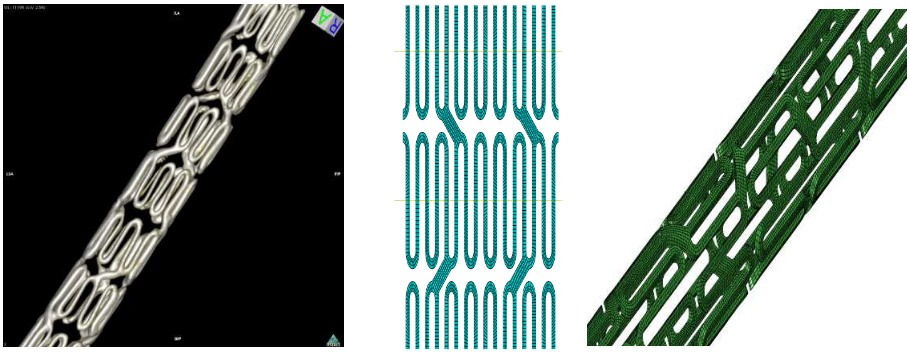

(a) (b) (c)

Figure 3.4 *An example of stent reconstruction: (a) view of the STL stent from micro-CT image; (b) planar mesh stent from ABAQUS and (c) ABAQUS view of the stent model.*

3.2.3 Balloon model

Although several numerical studies dedicated to balloon expandable stents and balloon angioplasty can be found in literature, only the studies of De Beule et al. [105] and Mortier et al. [49, 106] have included in their computational analyses the balloon itself in its actual folded shape and with an appropriate material description. While, in the other studies the balloon is discarded from the analysis and replaced with a uniform pressure distribution or the balloon is simulated as a non-folded cylinder.
In this study a realistic and validated model is developed to study the expansion of folded angioplasty balloons based on the manufacturer compliance chart. Subsequently, different expansion modelling strategies are studied and compared to perform the balloon expandable coronary stent. Such an analysis considers the main balloon features, which are the folding pattern, the overall dimensions, i.e., length, diameter, and the material properties.
The geometry and the size of the folded balloon model are provided thanks to the high resolution of the images, which are acquired with the micro-CT, as shown in Figure 3.5 (a). Such images are analyzed and elaborated with an image processing tool, i.e., ImageJ, and then the whole balloon model is reconstructed using both a Matlab script and ABAQUS/CAE, as depicted in Figures 3.5 (b) and (c). To discretize the balloon mesh, a membrane elements with a specific thickness has been used. The balloon used in this study is a semi-compliant balloon, having a nylon-based material.
The literature has allowed to perform the constitutive model of the balloon having approximatively a similar behaviour with respect to the compliance chart of the delivery system, i.e., the pressure/diameter relationship, which is provided by the manufacturer data. Hence, we have supposed the mechanical properties of the balloon having an hyperelastic (neo-hooke) behaviour, which is described by a polynomial strain energy function of the first order, $\psi = C_{10}(I_1 - 3)$ with C_{10} material constant and I_1 invariant of the left Cauchy-Green deformation tensor; we assume the material coefficients C_{10} equal to 65 MPa and the density of 1350 g/cm^3. Moreover, different thickness value of the membrane elements are considered to compare the possible different results in terms of pressure-diameter relationship.
Finally, the trifolded balloon geometry was meshed with three-node triangular membrane elements with reduced integration (M3D3R) using the preprocessing capabilities

within ABAQUS-CAE.

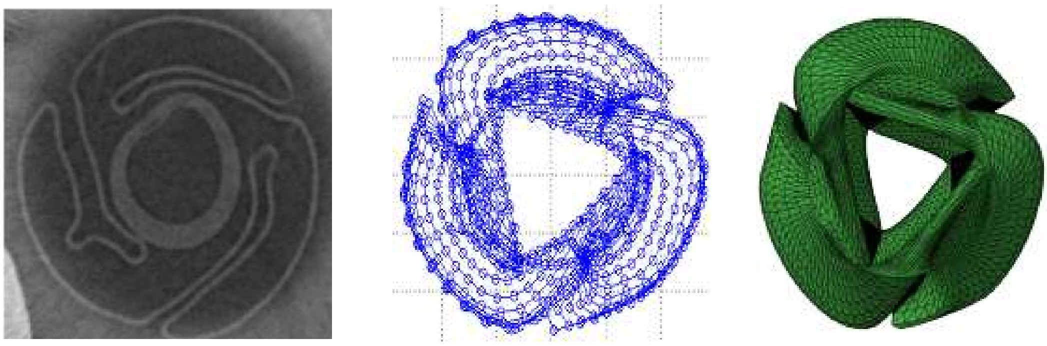

(a) (b) (c)

Figure 3.5 *Balloon reconstruction from image: (a) micro-CT image of the tri-folded balloon section; (b) MATLAB and (c) ABAQUS view of the balloon section end; from its folded configuration, the balloon rotates itself ending in circular tip.*

3.2.4 Catheter, Tip, Guide wire models

The catheter is a tube placed inside the balloon connected with the two short tubular tips, which have a conical shape in the distal direction and a cylindrical shape in the proximal one, as shown in Figure 3.6 (a). The length of the catheter is equal to the balloon one and the diameter is equal to 0.22 mm.

The length of the both tips are assumed to be 1 mm and inner diameter is 0.22 mm, the same as the diameter of the catheter tube because they are connected. The cylindrical tip outer diameter measures as the balloon end diameter, i.e., 0.6 mm. The conical tip outer diameter, instead, decreases from the balloon end diameter to 0.36 mm.

The guide wire acts as a determining instance of the delivery system because it represents the rail on which the balloon/stent travels. Its geometry has been generated from a smooth interpolation of the coronary vessel centerline: for each of the centerline points, considering a diameter of 0.1 mm, we have created the sections by an appropriated sweeping procedure. The guide wire has been modelled as a cylinder running through the catheter and the tips i.e., the catheter shaft, acting as the track for the movement of the entire stent/balloon device (see Figure 3.6 (b)). The diameter of the guide wire is assumed to be 0.13 mm, whereas its length depends on the coronary artery one.

Polyethylene is the material considered for the catheter and tips models. Hence, they are assumed to behave a linear elastic behaviour, with a elastic module E=1000 MPa, Poisson's module $\nu = 0.4$ and density = 940 Kg/m^3. The guide wire, which is in nitinol material, has been modelled as a rigid body in this numerical analysis and, thus, any material is required in this case.

The catheter and the tips have been discretized in four-node doubly curved thick shell with reduced integration (S4R), while the guidewire has been modelled with four-node bilinear rigid quadrilateral elements (R3D4).

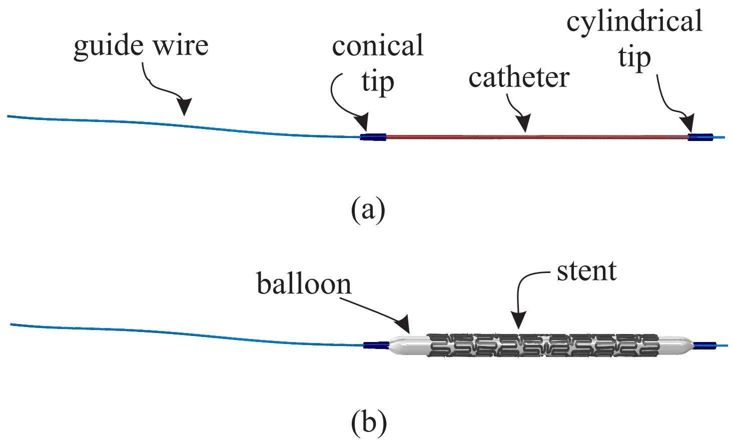

Figure 3.6 *Delivery system components: (a) catheter (red color), guide wire (cyan color) and two tips (blue color); (b) balloon and stent model.*

3.2.5 Boundary conditions

The numerical simulation of coronary stenting is performed assembling all the components of the delivery system and the patient-specific coronary model. The whole simulation representing the stenting procedure is composed of two main analyses, which are performed in a cylindrical reference system:

- analysis 1: insertion of the stent/balloon in the coronary artery;
- analysis 2: deployment of the stent from the balloon inflation/deflation.

Analysis 1.

All the components of the delivery system are considered to perform this analysis, except the tips to simplify the numerical simulation. Furthermore, a reduced coronary artery model, which is modelled as rigid part, is taken into account to assure the correct position of the delivery system into the vessel; such model is constrained to a reference point, wherein all the translational degrees are stopped. To allow a synergy movement among the components of the delivery system, appropriated Multi Point Constraint (MPC) are considered.
Following, we describe every MPC used in this study, i.e., the *MPC-Link-stent* and the *MPC-beam-balloon/catheter*.
MPC-Link-stent: in every extremity of the stent, a number of nodes are selected and a reference point (RP) is computed as mass center of its; then, nodes are linked to the RP;
MPC-beam-balloon/catheter: also the both extremities of the balloon and catheter sections are linked to the other RPs. Such constrains allows both the balloon/catheter movement and the movement of the stent within the other component along the guide-wire during the insertion of the delivery system.

Analysis 2.

The stent deployment in the coronary artery through the balloon expansion is simulated. Once the *Analysis 1* is terminated, sole the deformed parts of the balloon and the stent are imported, which are assembled with the coronary vessel mesh. Moreover, the stress state of the previous analysis are update as initial state with the option *Predefined Field* presented in *Abaqus Manager*, both for the balloon and stent models. An increasing uniform pressure starting from 0 N/mm^2 up to 1.824 N/mm^2 on the inner surface of the tri-folded balloon has been applied[2]. The *MPC-Link-balloon*: in the both ends of the balloon prevents the balloon movement and shortening, but allowing its expansion. Boundary conditions have been then applied to the ends of all branches from cylindrical reference system: all the translational degrees of freedom have been constrained to avoid rigid body motion.
Resuming, we have imposed at the nodes of both balloon extremities a boundary condition such that the displacement in the principal direction is equal to zero, while the stent model is left free at the balloon expansion. The balloon inflation is allowed by the application of an uniform pressure.

3.3 Early simulation experience: one long stent deployment

In this section we describe the numerical stenting procedure performed through the FEA, simulating the real stenting procedure which is done in the clinical practice. As mentioned previously, the whole numerical simulation is composed of two analyses and each of them is composed of two main steps:

Analysis 1

- crimping;
- insertion.

Analysis 2

- deployment;
- balloon deflation.

The numerical simulation have been performed using ABAQUS/Explicit (Dassault Systemes Simulia Corp., RI, USA) due to the high non-linearity of the procedure, as described in Gastaldi et al. [47], which is mainly caused by the non linear material behaviour and complex contact conditions. Inertia was assumed to have a negligible impact on both the stent expansion and the balloon inflation, hence the procedures have been modelled as quasi-static processes [107]. Generally in a quasi-static analysis to produce smooth changes in terms of velocity and acceleration, the application of the smooth loading is required.
To verify the quasi-static hypothesis, it was necessary to control the dynamic of the expansion by maintaining the ratio between kinetic energy and internal energy of the system under 5-10% during the entire simulation, so to assure that the inertial forces

[2]The value of the pressure is provided by the manufactured data.

remained insignificant. In order to achieve this goal, adequate time step and load application rates were applied while an element-by-element stable time increment estimate, coupled with a "variable mass scaling technique", reduced the computational cost of each simulation. Contact between the parts of the model were defined according to the general contact algorithm available in Abaqus/Explicit that enforces contact constraints using a penalty contact method, which searches for node-into-face and edge-into-edge penetrations in the current configuration.
Hence, friction has been included in the simulations by means of a Coulomb friction model with a static friction coefficient of 0.2 (valid for both nylon-nylon and nylon-steel interactions under clean conditions).
Different simulation time steps have been chosen. The stent has been, indeed, crimped in 0.001 seconds, since presents negligible dynamic effects while for the insertion step has been selected faster simulation time, 0.01 seconds. The deployment and the balloon deflation steps have, instead, been chosen to last 0.01 seconds. The analyses could not be faster since the inertial forces became dominant.
The time period of the quasi-static stent expansion process has been decreased with the aim at reducing the computational time. The main problem is that as the event is accelerated, the presence of inertial forces may modify the response of the system. Energies have been monitored during the stent expansion in order to assure that the inertial forces were acceptable. During most of the expansion process, the ratio of kinetic to internal energy of the whole model was less than 5-10%. Only during the short transition period between the crimped and the expanded state the ratio was slightly higher and a maximum of 10-20% has been reached.

3.3.1 Analysis 1: crimping and insertion

Crimping. This is the process in which the stent is crimped on the balloon to achieve its crimped configuration. Such a procedure is simulated by applying an increasing pressure on outer surface of the stent and, at the same time, on the inner surface of the balloon. The pressure applied on the stent starts from 0 N/mm^2 and reaches 0.25 N/mm^2 in order to reduce the stent diameter, whereas the pressure on the balloon varies in a very small range (0-0.0005 N/mm^2) to partially unfold the balloon without transferring the load to the stent (see Figures 4.4 (a) and (b)).
During the crimping step, both the balloon and catheter extremity have been constrained to prevent the movement and the shortening problems. The superelastic properties of the guide wire during the crimping and the insertion step has been neglected because the guide wire deformations are supposed to be small; this is the reason to have implemented the guide wire as 3D rigid part instead of 3D deformable part and all the translational and rotational degrees of freedom of its reference point has been constrained.

Insertion. This step has been simulated by enforcing a displacement at the proximal end of the catheter shaft to reach the stenotic region. To applied this displacement all the nodes of the proximal face of the balloon/catheter have been linked through multipoint constraint (MPC-Link-tip). The multipoint constraint allows the motion of the slave nodes of a region to the motion of a single point. An additional equal displacement boundary condition and an equal multipoint constraint, have been imposed to the proximal stent end (MPC-Link-stent). Without this condition, it was impossible to adequately position the stent because sliding occurred between the balloon membrane and the inner stent surface. This sliding is due to insufficient frictional forces, although a pressure has been applied to the outer stent surface, prior to and during the insertion to mimic the stent fixation after crimping. Figure 3.7 (a)-(b)-(c) illustrates the result of the insertion procedure of the device in the region of interest.

3.3.2 Analysis 2: inflation and deflation

Deployment. In order to simulate the inflation of the inserted stent/balloon system, a model based on the results achieved in the insertion step has been developed. The multipoint constraint applied in the insertion step prevents the stent to deploy since each slave nodes is rigidly linked to the control point. Therefore the analysis could not be done with a unique simulation, since the multipoint constraint could not be inactivated before the last step. For this reason all the parts, except the guide wire, have been imported from the insertion step in their deformed shape. The guide wire has been, instead, edited ex novo as a 3D deformable part and fixed at both ends since the guide wire, in the deployment step, undergoes higher deformations. The simulation of the free expansion of the stent has been achieved by imposing a linear increasing pressure starting from 0 N/mm^2 up to 1.824 N/mm^2, as indicated by manufacturing data, which is applied uniformly on the inner surface of the trifolded balloon (see Figure 3.7 (d)). While importing the stent and the balloon from the insertion step, their state of stress has to be taken into account. Thanks to the *Predefined Field Manager* of the *Load module* in ABAQUS, all the stresses can be applied back to the parts imported.

Deflation. As previously stated, the balloon deflation has been included in the FEA to study the stent recoil due both to the stent material and to the pressure imposed by the elastic recoil of the vessel walls. In order to simulate the balloon deflation stage, a linear decreasing pressure has been applied starting from 1.824 N/mm^2 down to 0 N/mm^2 applied uniformly on the inner surface of the trifolded balloon. Figures 3.7 (e) and (f) illustrate the result of the balloon deflation and the placement procedures of the metallic stent inside the coronary wall. The same stenting procedure through the numerical techniques has been performed for the bifurcated coronary artery (LCA), as depicted in Figures 3.8.

3.4 Numerical simulations aspects

In this section, we describe the main computational characteristics used in the numerical analysis to simulate virtually the surgical intervention to evaluate the guideline of the stenting performance for the long coronary lesions treatment. Several aspects have been taken into account to perform this procedure, which appears complex and delicate in FEA issues.

3.4.1 Quasi-static Abaqus/Explicit analysis and kinetic-internal energy ratio

All the steps modelled in our simulations have been performed in a quasi-static analysis using Abaqus/Explicit as finite element solver, providing also a stable general contact

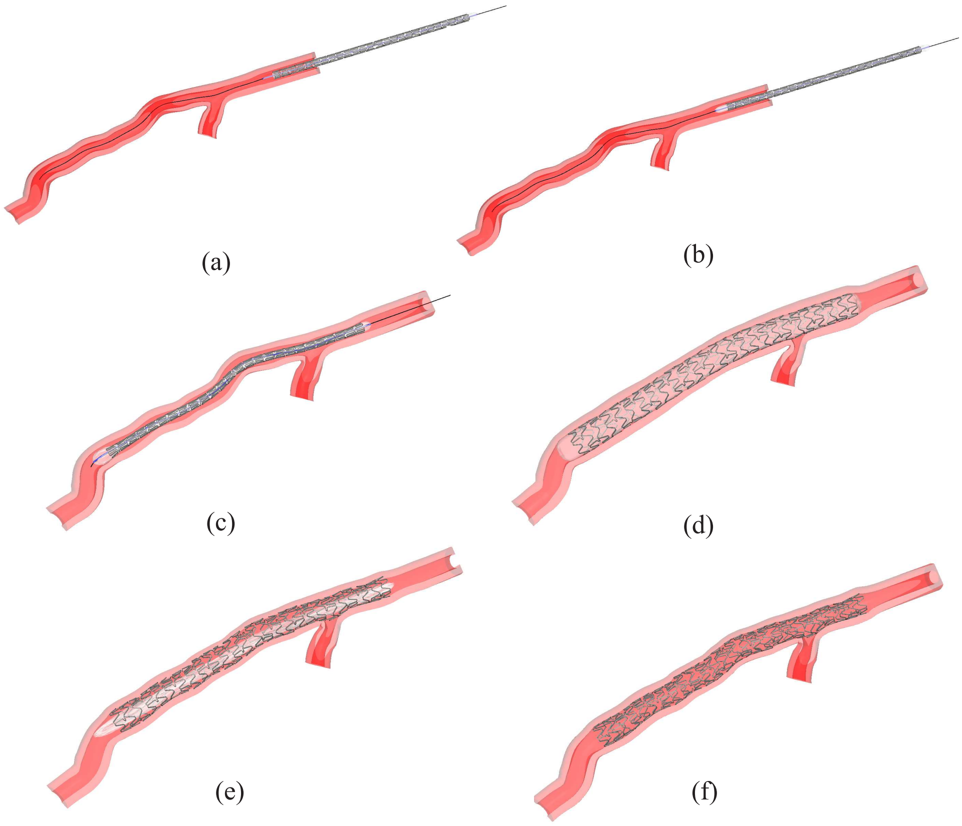

Figure 3.7 *Stenting procedure of the long stent: (a) initial configuration; (b) crimping procedure of the stent; (c) final position of the catheter and stent/balloon after the insertion procedure; (d) configuration at the maximum expansion of the balloon, pressure reachs 1.824 MPa; (e) deflation of the balloon at the pressure of 0 MPa; (f) final configuration of the stent inside the coronary vessel.*

algorithm.
To model quasi-static events requires some considerations: in fact, modelling the process in its natural time period is computationally impracticable because a lot of time incrementation would be required. To solve such an inconvenience, we can increase artificially the speed of the process increasing in this case the material density. Hence, an appropriate semi-automatic mass-scaling of the models used in the simulation is applied to govern the stable time increment [108].
To ensure that the inertia forces are neglected during all the process, we have monitored the kinetic (ALLKE) and internal (ALLIE) energies to verify the condition of quasi-static regime, i.e., the ratio between these energies (ALLKE/ALLIE) has to be lower than the threshold of 5-10%.
Further, we have performed preliminary numerical tests to assess the impact of time step on such an energies ratio and on computed values, varying the time step values, i.e., 0.001 s (T1), 0.01 s (T2) and 0.1 s (T3). The results in Figures 3.9 (a) and (b) show the ratio ALLKE/ALLIE of the stent and balloon model, respectively, to perform the process at the different simulation times. We can note similar profiles at the different simulation times, except for the initial instants due to the initial contact between the

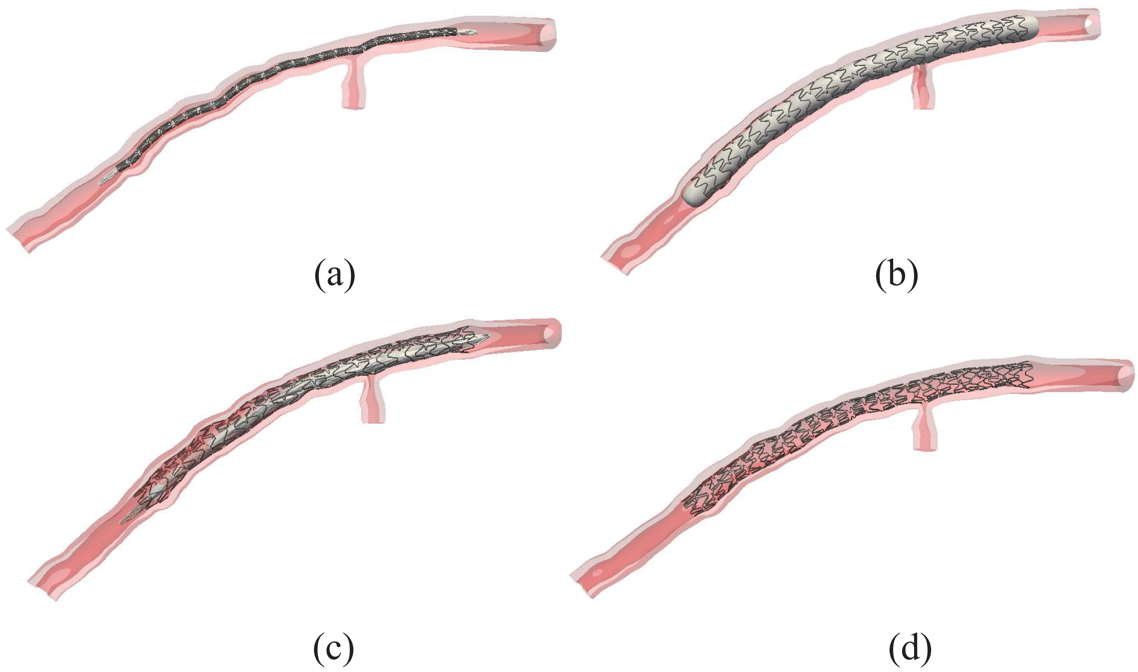

Figure 3.8 *Stenting procedure of the long stent: (a) stent crimped and inserted in the coronary lumen; (b) configuration at the maximum expansion of the balloon, pressure reachs 1.824 MPa; (c) deflation of the balloon at the pressure of 0 MPa; (d) final configuration of the stent inside the coronary vessel.*

stent and balloon model.
In Figures 3.10 (a) and (b), we show the ALLKE/ALLIE ratio of the vessel/stent for the two stenting strategies adopted in our study regarding the stent deployment analysis. The initial peak of the energies ratio at beginning of every step is due to te contact between the vessel and the (see ALLKE/ALLIE ratio - vessel in Figure 3.10) and to the stent/balloon contact (see ALLKE/ALLIE ratio - stent Figure 3.10). Such a transient zone can be neglected because it has a limited impact on the computed results.

3.4.2 Crimping

Crimping has been implemented in the simulation before the insertion of a stenting system both to simulate the real stent configuration and to enable a uniform movement of the entire structure. Indeed comparing the STL geometry of the stent generated from micro-CT images and its CAD mode, we can note differences in the diameters measurements. The diameter value of the crimped configuration of the STL model is lower than CAD model, as shown in Figure 3.11.

3.4.3 Compliant Chart

To validate the mechanical behaviour of the balloon/stent, we have computed its resultant pressure/diameter relationship through the balloon expansion, which enlarges the stent strut, and compared the numerical results with respect to the manufacturing

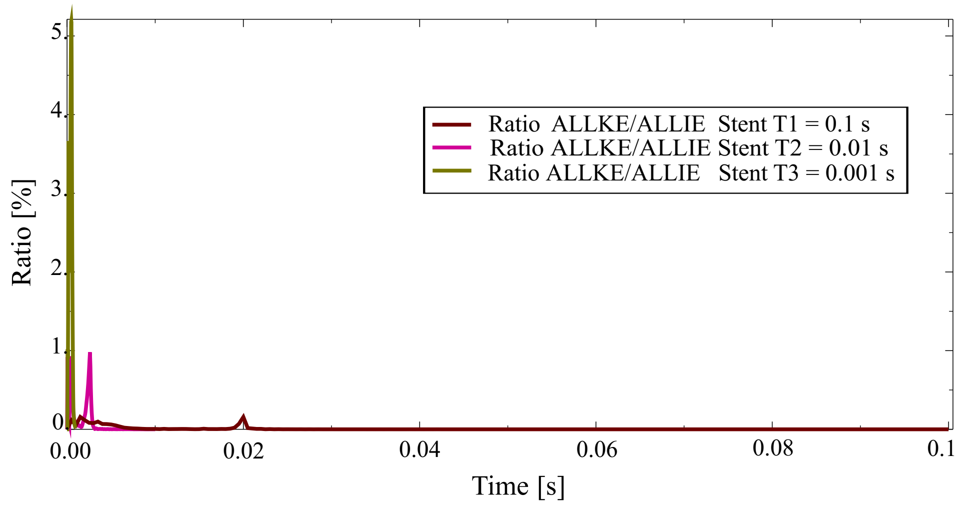

(a)

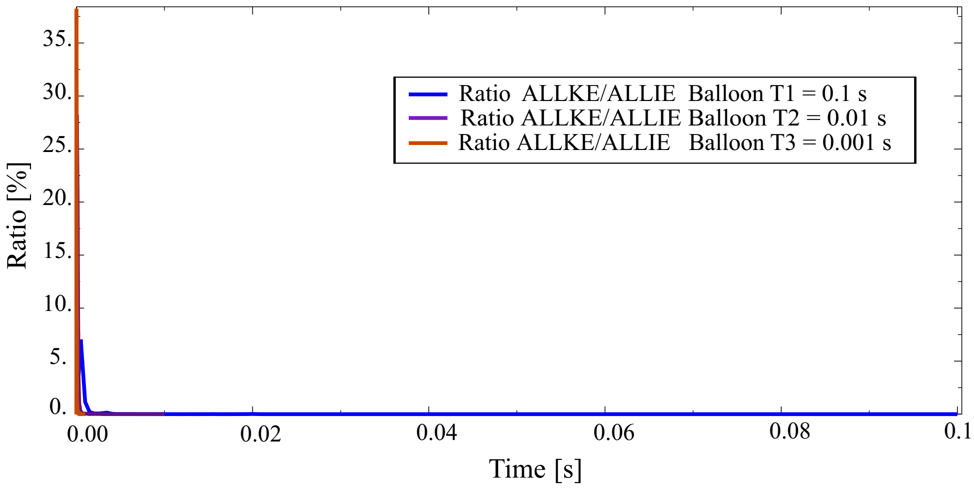

(b)

Figure 3.9 *Ratio between the kinetic and internal energies: (a - b) ALLKE/ALLIE ratio for stent and the balloon model at the balloon/stent expansion to compare the results at the different simulation times.*

data provided by the Abbott company.
This results show a good approximation with respect to the manufacturing data, as shown in Figure 3.12 (a): the balloon model demonstrates realistic deformations under different pressure values. The maximum percentage difference between our result and the CC provided by manufacturing data is lower than 3%; hence, such a result seems to justify the choice of the balloon constitutive modeling. This experimental result is showed for a time (T) equal to 0.01 seconds, applying the pressure in a *smooth way*. In Figure 3.12 (b), we show the ratio between the kinetic (ALLKE) and internal (ALLIE) energy of the stent and the balloon model: every computed ratio is lower than 5-10%, verifying, thus, the quasi-static regime of the simulation.

As shown in Figure 3.12 (a), at the pressure of 0.2 MPa, the balloon is already unfolded but is still in a transient state. The numerical results both for the pressure values be-

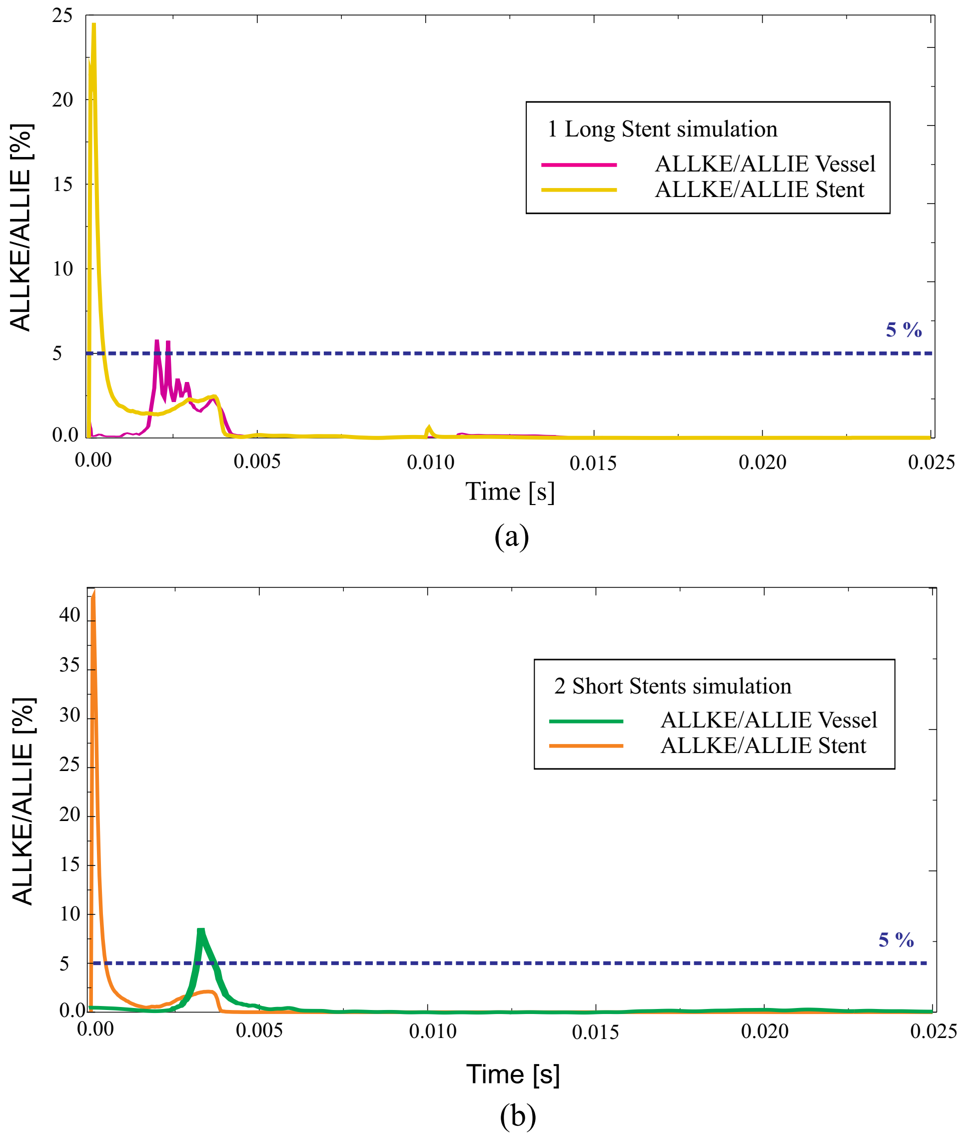

Figure 3.10 *Ratio between the kinetic and internal energies: (a) ALLKE/ALLIE ratio for stent and vessel during the simulation of the one long stent; (b) ALLKE/ALLIE ratio for stent and vessel during the simulation of the distal short stent.*

tween 0.8 and 1 MPa and high pressures range have a good approximation with respect to those provided by the manufactured data. However, for intermediate pressure values, the obtained results underestimate the experimentally data; this is probably due to the hyperelastic material behaviour which has been assigned to the balloon membrane. In Figure 3.13, we show the main time steps of the balloon inflation to evaluate the compliance chart.

In this study, we have evaluated two further analyses: (i) the way to apply mode the pressure load through two different loading amplitudes, i.e., smooth versus linear amplitude and (ii) the influence of the thickness balloon size, which are described in the next subsection.

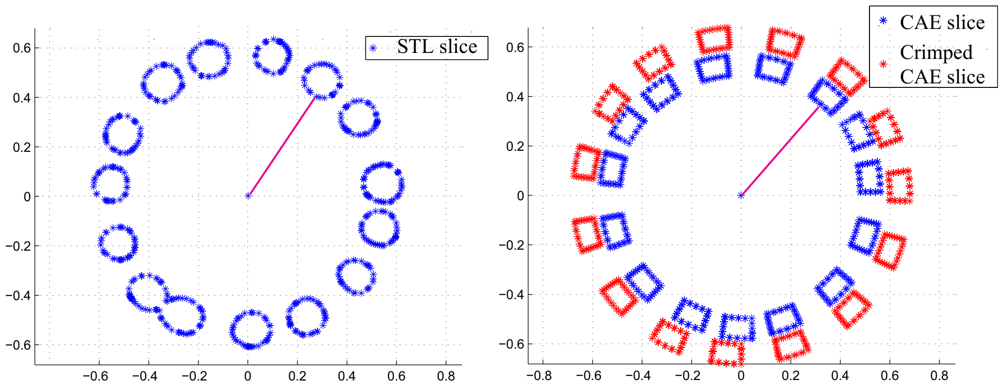

(a) (b)

Figure 3.11 *Crimping procedure result: (a) MATLAB slice of the STL model reconstructed directly from the micro-CT images; (b) MATLAB slice of the CAE model reconstructed from Abaqus/CAE (red) and the crimped CAE model after the crimping procedure (blue) that reachs the real stent diameter value.*

3.4.4 Loading Amplitude

Linear vs smooth amplitude curves.

Generally, for accuracy and efficiency, quasi-static analyses require the application of a loading that is as smooth as possible. Applying the load in the smoothest possible manner requires that the acceleration changes only in a small amount from one increment to the next. If the acceleration is smooth than the changes in velocity and displacement are also smooth. In Figure 3.14 (a), the results of the two simulations at different loading amplitude are depicted: the pressure-diameter relationship in both the cases show the same behaviour with respect to the manufactured data.

Comparison of different membrane thickness size.

Two different size of the balloon thickness have been considered to know the possible influence of the membrane size (0.03 mm vs 0.02 mm) with respect to the compliance chart. Hence, we have compared the results for two thickness values, i.e., 0.03 mm versus 0.02 mm. As depicted in Figure 3.14 (b), the obtained results are very different: in fact, for the smaller membrane thickness, i.e., 0.02 mm, the computed diameters to the relative pressure values exceed the manufactured data results. Such an analysis has been evaluated in the case of smooth load application. Whereas, evaluating the same analysis with the load applied in linear way, the results change approximating better the manufactured data, as depicted in Figure 3.14 (c).
We conclude that both the application of different loading amplitude and different balloon thickness size influence the final result in terms of compliance chart. In this study, we have preferred choosing a membrane thickness of 0.03 mm and applying a smooth loading amplitude, for the reasons described in previous Sections.

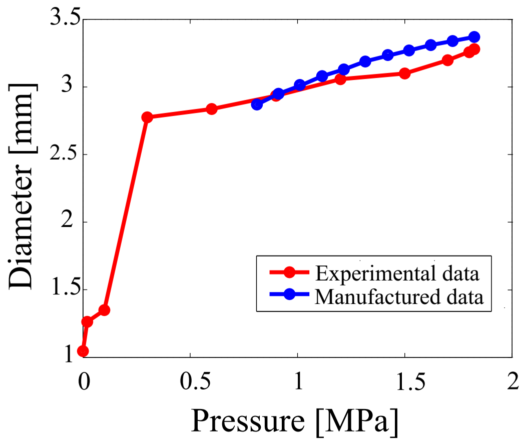

(a)

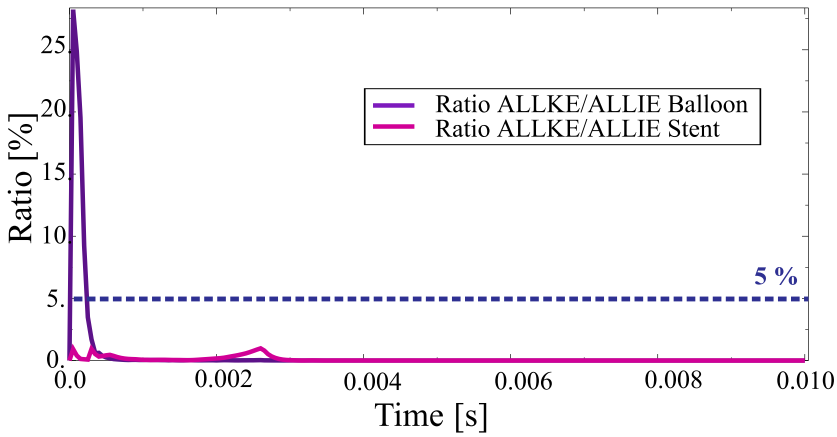

(b)

Figure 3.12 *Compliance chart of the balloon/stent: (a) the diameter-pressure relationship of the experimental data (red) compared to that manufactured data; (b) ratio between the kinetic (ALLKE) and the internal (ALLIE) energy of the balloon/stent model to verify the quasi-static regime of the analysis.*

3.4.5 Predefined field

When importing the models from a step to the other, all the solicitation levels, i.e. the stress and the strain values, can be applied back to the parts imported and taken into account for the next steps through the *Predefined Field Manager* of the ABAQUS *Load module*. If no initial conditions are specified, Abaqus/Explicit will assume that the all parts are in unloaded state.
Precisely, when the entire simulation is divided in two or more steps due to several motivations, as for example the computational time, in the step next to the first one, we can use the *Predefined field* tool (PF) to consider the stress and the strain values in the successful step to get continuity at the all numerical procedures of the simulation. In this study, we have considered two test-cases, i.e., the *Predefined field* as the initial state and the same condition without such a state; hence, we have compared the simulations to evaluate possible differences between them. This allows to understand if the

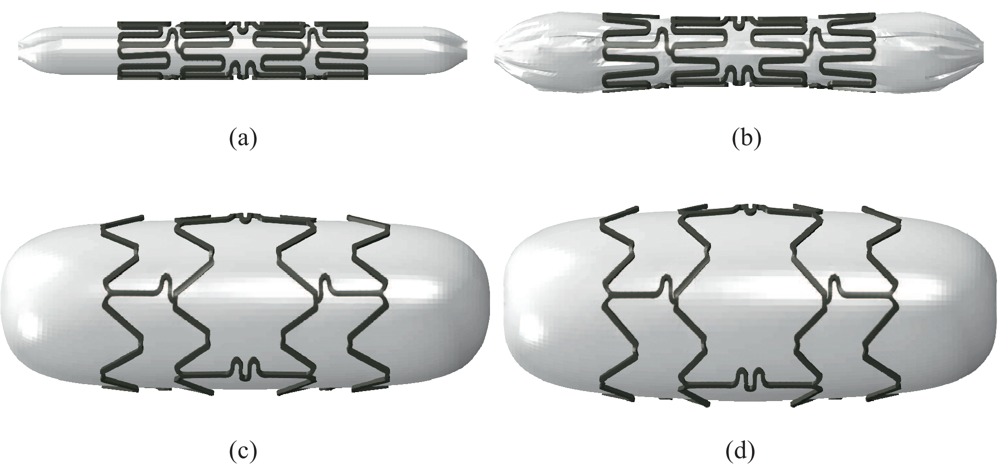

Figure 3.13 *Numerical simulation of the free balloon expansion in different time steps: (a) initial state (T=0 s, P=0 MPa); (b) the balloon begins to be unfolded (T=0.002 s, P=0.6 MPa); (c) in a few time the balloon is already unfolded (T=0.009 s, P=1.3 MPa); the balloon is at the maximum expansion (T=0.01 s, P=1.824 MPa).*

PF influences the next numerical procedure: such a condition could be interested and useful in some situations.
Hence, once the first step, i.e., the stent crimping and insertion, has been concluded, two next different numerical analyses about the stent deployment have been compared. The results are showed in the next Section (see Section 3.5).

3.4.6 Viscous Pressure

The viscous pressure application is the way to damp out quickly the dynamic effects due to the kinetic energy associated with the structure's motion, reaching, thus, the quasi-static equilibrium in a minimal number of increments.
Using the viscous pressure means applying a damping at the external surface of the body of interest, i.e., an effect that reduces the oscillations amplitude of the structure of interest The viscous pressure is defined as 1-2% of the quantity $c_v = -\rho * c_d$, with $c_d = \sqrt[2]{E/\rho}$ the wave speed of the material, E is the young modulus and ρ is the density of the material. The effect of the load is to absorb the pressure waves which cross the free surface of the model, thus, avoiding the reflection of the energy that generates strong dynamic effects on the model.
Hence, we have computed the viscous pressure of the vessel, considering a young modulus of 300 KPa and a density of $1.256 * 10^{-9} tonn/mm^3$, while for the stent 233 GPa and $8.8 * 10^{-9} tonn/mm^3$ as young modulus and density, respectively. The two viscous pressures have been applied to the respective external surfaces of the models.

3.5 Results and Discussion

In the following, we analyse the numerical outcomes of the two stenoted coronary arteries (LAD and LCA) to evaluate the impact of the long stent deployment with respect to different aspects of clinical interest, such as the stent/arterial solicitation level, i.e.,

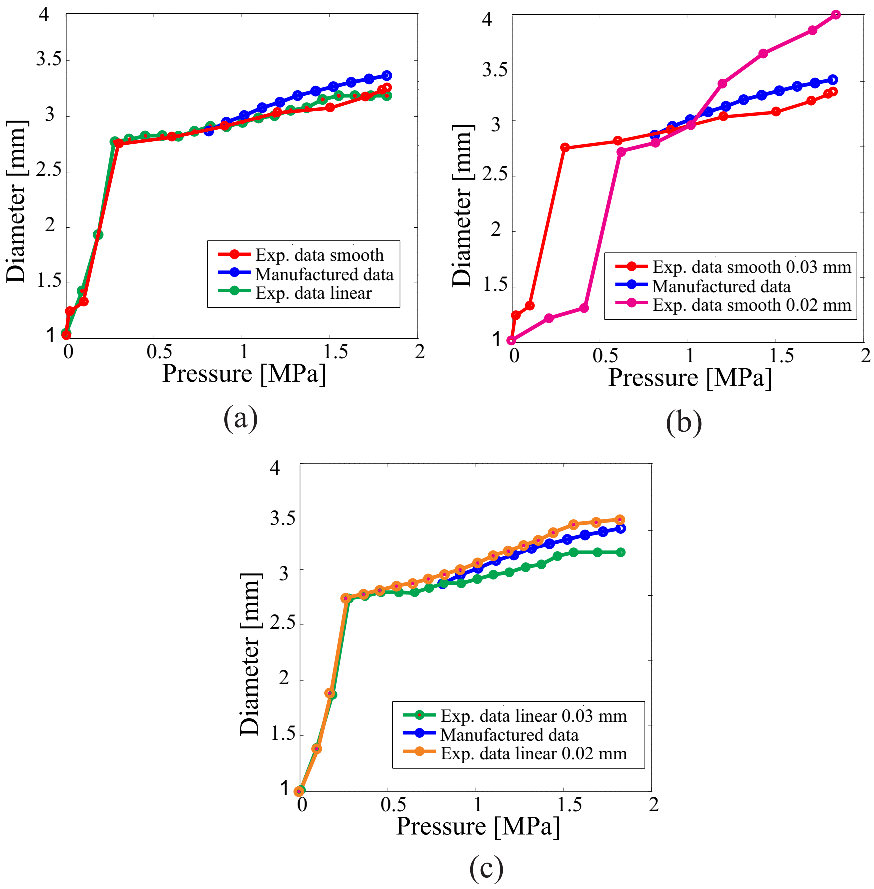

Figure 3.14 *Compliance chart of the balloon/stent: (a) evaluation of the diameter-pressure relationship between the procedures at different loading amplitude, i.e., smooth versus linear; (b) comparison of the procedure at the same loading amplitude, i.e., smooth, and different membrane thickness of the balloon, i.e., 0.03 mm versus 0.02 mm; (c) in this case, the linear amplitude of the load is shown at different membrane thickness of the balloon.*

the stress and strain values, and the post-stenting anatomical changes.

3.5.1 Evaluation of stress and strain

Coronary vessel. The main stress imposed by stent on the coronary artery is due to its radial expansion during the balloon inflation. Hence, for the stress distribution analyses of the coronary vessel, we consider the maximum principal stress, which is in circumferential direction. The stress results showed in this section refer to the anisotropic and heterogeneous mechanical behaviour of the coronary vessel from the material coefficients illustrated in Table C.2.

We taken into account two main moments of the numerical simulation, i.e., at the maximum balloon expansion and at the end of the stenting procedure. The coronary stress results of the coronary artery shown in Figure 3.2 are depicted in Figure 3.15: we show the arterial solicitation level in two test-cases, as anticipated in the subsection 3.4.5, i.e., with and without the *Predefined Field* as initial state. The two considered test-cases have been performed with the same first numerical analysis (stent crimping

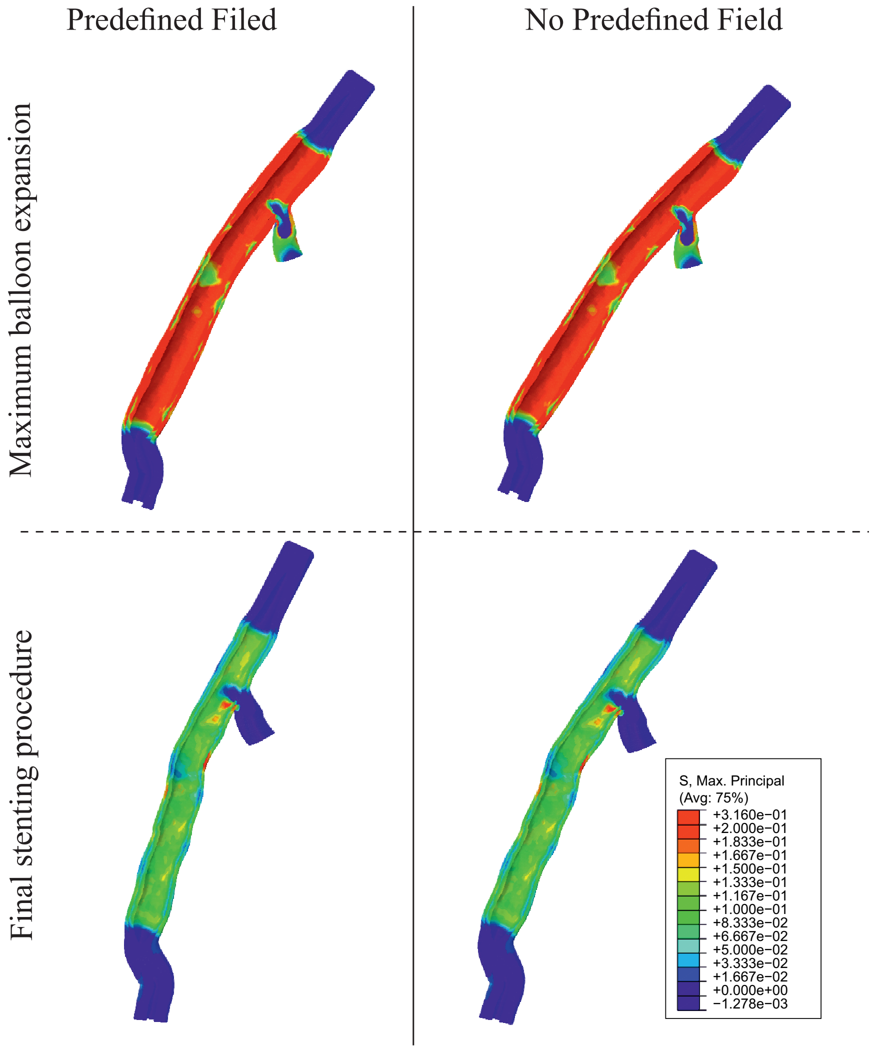

Figure 3.15 *LAD maximum principal stresses computed for two test-cases of stent deployment: at the maximum balloon expansion and at the end of the stenting procedure similar results are computed.*

and insertion) and different last analysis regarding the stent deployment. As showed in Figures 3.15 and illustrated in Figures 3.16, the difference between the two test-cases are very small. We have computed an mean error value lower the 0.01% in both the main moments, i.e., the maximum balloon expansion and the final stenting procedure. In particular, the 99% of the discretized coronary volume at the end of the stenting procedure have a stress value lower than about 0.15 MPa and the maximum value of the stress reaches the value of about 0.22 MPa, which is concentrated nearby the bifurcation area and in the extremity of the coronary vessel. Results suggest that the two procedures are equivalent in terms of coronary vessel stress.

In Figure 3.17, we show the stress results of the LCA computed at the maximum balloon expansion and at the end of the stenting procedure in the case of not-application of the *PF*. In this case high stress values have been computed: at the maximum balloon expansion the stress reaches the value of 4 MPa, while at the end of the simulation the value of 0.5 MPa. Once the stent has been deployed, stresses distribution is partially

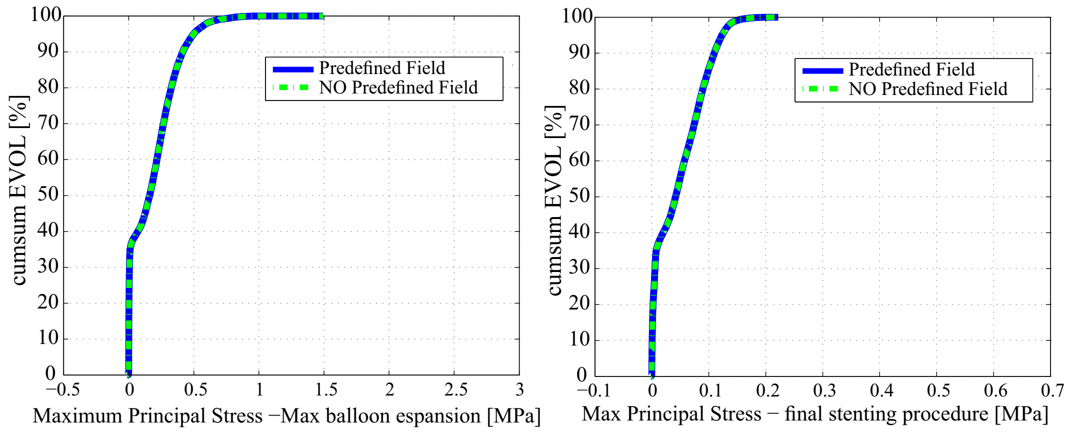

(a) (b)

Numerical analysis	Stress values	Maximum balloon expansion	Final stenting procedure
Vessel stress Predefined Field	Max	1.487 MPa	0.214 MPa
	< 99 %	0.695 MPa	0.152 MPa
Vessel stress NO Predefined Field	Max	1.486 MPa	0.213 MPa
	< 99 %	0.693 MPa	0.152 MPa

(c)

Figure 3.16 *Comparison of the numerical results for the stented coronary artery model in the two test-cases: (a - b) Von Mises stresses at the maximum balloon expansion and at te end of the stenting procedure; (c) table to summarize the maximum stress values and the stress value of 99% of the coronary volume elements.*

homogeneous along the coronary vessel; maybe, the bio-mechanical response depends on the initial geometry of the bifurcated coronary artery.
Generally, high values of stress can cause injuries in the inner of the coronary artery and considering the ultimate stress value of the coronary artery approximatively equal to 1-2 MPa, the stress values computed in the last stenting procedure are critical during the stenting procedure [107].

Stent. In this study, we have also evaluated the Von Mises stress and the plastic equivalent strain (PEEQ)[3] values of the stent at the end of the stenting procedure.
For the numerical simulation of Figure 3.7, Von Mises stresses distribution is homogeneous enough for the whole stent structure and the maximum value computed is located both in the inner curvature of the stent bending and in the conjunction point of the stent ring and intra-ring connectors, reaching the maximum value of 834 MPa, while the 99% of the discretized stent volume have a stress value lower than about 595 MPa

[3]Scalar representation of the amount of plastic strains that the stent suffers during the balloon expansion, providing structural support to the arterial wall and preventing its immediate recoil.

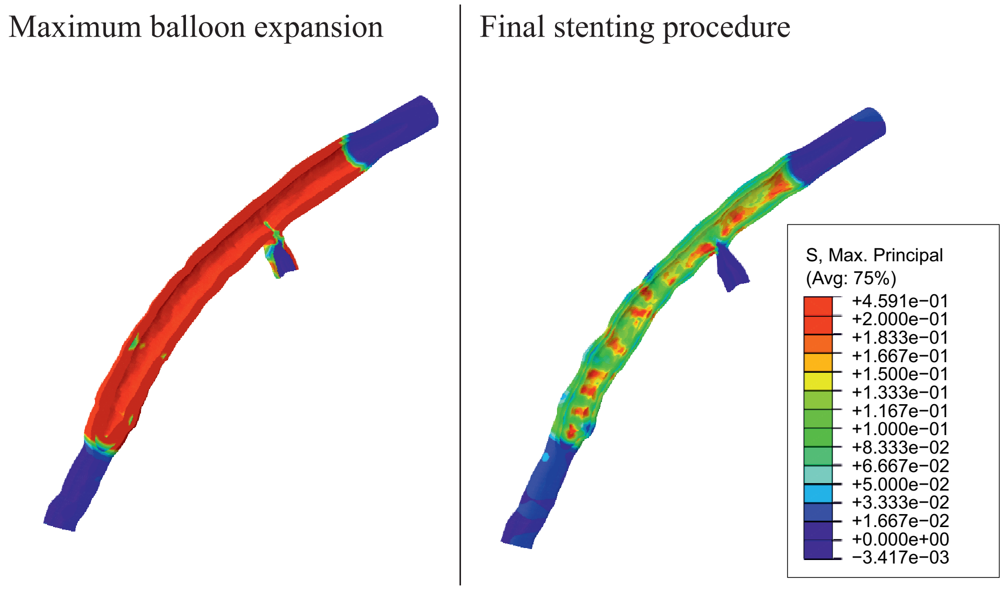

Figure 3.17 *LCA maximum principal stresses computed of the left coronary artery at the maximum balloon expansion and at the end of the stenting procedure: the values are higher than those computed in the case of the left coronary artery (see Figure 3.15).*

(see Figures 3.18 (a)).
The PEEQ values show that the inelastic behaviour is more concentrated in the bending of each stent strut. Figure 3.18 (b) highlight the maximum PEEQ value of 0.45, which is near to the ultimate tensile strain at the break of the considered material (CrCo), i.e., 0.448 [50].
In both the test-cases, the results of the stent stress and strain values are similar, with a mean error value lower the 0.01%, as shown in Figure 3.18 (c). Finally, we can conclude that the use of an initial conditions derived from the final stress and strain values on the previous analysis with respect to the next procedures provides the same results in this study in terms of artery/stent solicitation level.
In Figure 3.19, we report the Von Mises stress and PEEQ computed for the stenting procedure performed in the stenoted LCA. Also in this case the stress distribution is homogeneous enough for the whole stent structure and the maximum value computed is located both in the inner curvature of the stent bending and in the conjunction point of the stent ring and intra-ring connectors, reaching the maximum value of 843 MPa, while the 99% of the discretized stent volume have a stress value lower than about 592 MPa.

3.5.2 Anatomical changes

The stenting implant induces some important changes on the vascular anatomy [106]: arterial straightening, lumen diameter, bifurcation angles.

Arterial straightening.
Arterial straightening is a clinically-relevant issue because it is considered a reliable predictor of post-operative adverse cardiac events [109] and restenosis intrastent due to

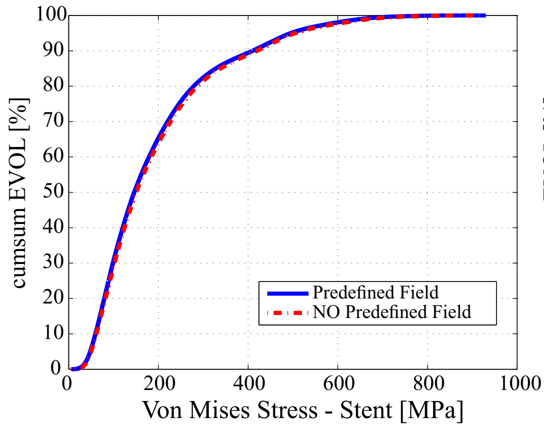

(a)

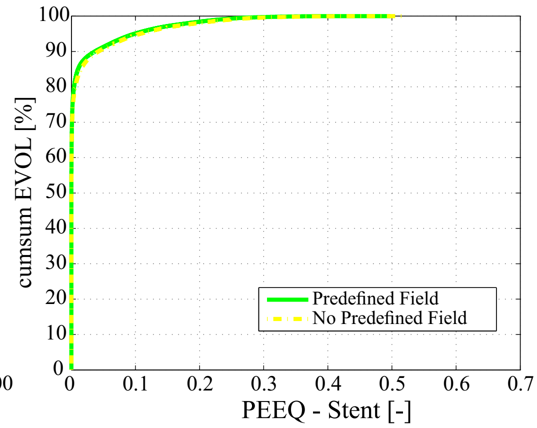

(b)

Numerical analysis	values	Von Mises Stress	PEEQ
Predefined Field	Max	835 MPa	0.45
	< 99 %	595 MPa	0.20
NO Predefined Field	Max	834 MPa	0.45
	< 99 %	595 MPa	0.20

(c)

Figure 3.18 *Numerical results of the stent model in the LAD at the end of the stenting procedure to compare the two test-cases: (a) Von Mises stress values; (b) PEEQ values; (c) stress and strain values of the 99% of the stent volume elements.*

Numerical analysis	values	Von Mises Stress	PEEQ
Stent LCA patient	Max	843 MPa	0.42
	< 99 %	592 MPa	0.20

Figure 3.19 *Numerical results of the stent model in the LCA at the end of the stenting procedure to compare the two clinical procedures.*

the alteration of the wall shear stress [110]. Moreover, such an anatomical change as an indirect measure of the stent flexibility, which has been for this reason investigated by several numerical studies [49, 111]. Given such considerations, we have also evaluated the post-stenting arterial straightening on our study following the approach proposed by previous studies [50, 112], which suggest to evaluate this effect through the comparison of the pre- and post-operative tortuosity index.
The lumen tortuosity index (T) is defined as:

Patient	A	B	C	Stenosis degree
PRE	173°	54°	133°	55%
POST	142°	42°	176°	-

Table 3.1 *Bifurcation angles (A, B, C) and stenosis degree computed before (PRE) and after (POST) percutaneous coronary intervention.*

$$T = L/L' - 1 \tag{3.5.1}$$

with L, the centerline length, and L', the distance between the extreme points of the vessel [113]; the centerline is computed through the *vmtkcenterlines* module of VMTK library (http://www.vmtk.org). In this study, the tortuosity index changes from 0.0574 to 0.0339 (-41%) for the coronary artery shown in Figure 3.20 (a), and from 0.0424 to 0.0353 (-20%) for the coronary artery shown in Figure 3.21 (a). Similar results are highlighted qualitatively in the study of Mortier et al. [49], which compared the initial and the final configuration of the coronary lumen profile after the stenting procedure. The measure of the tortuosity index is reported also in the recent study of Morlacchi et al. [50], where the change of the tortuosity index is about 20-30%. Hence, we conclude that the tortuosity value after the stenting procedure depends also by the initial tortuosity of the coronary vessel.

Coronary diameter, lumen area and bifurcation angle degree.
We have evaluated also the change of the coronary configuration with respect to the initial geometrical anatomy and the patency restoration of the coronary artery comparing the initial and the final lumen coronary diameters, the lumen area and the bifurcated angle degree of the two stented coronary arteries. Such results have been performed in the case without the initial state derived from the next first analysis. Figures 3.20 and 3.21 show the tortuosity change of the coronary artery profile and the coronary patency recovery after the stenting procedure through the coronary diameters analysis.
The framework adopted in our study computes also the lumen area of the coronary lumen before and after the stenting procedure. In the lumen The angles between the branches have been computed following the approach described by Wischgoll et al. [94], and the stenosis degree following the formulation shown in the Section 2.4.2 of *Chapter 2*. These values are illustrated in Tables 3.1 and 3.2 for both the coronary arteries. Such measured values are important clinical features for the pre-operative planning in order to predict the patient outcomes, improving the stenting procedure by adopting the better strategy for a specific patient.

3.5.3 Evaluation of the stenting procedure from post-operative images

In order to qualitatively assess the reliability of the computed post-stenting stent/vessel configuration, we have overlapped the outcome of numerical analysis with the angiographic images of the coronary artery acquired after a real percutaneous coronary intervention, as recently proposed by Morlacchi et al. [50].

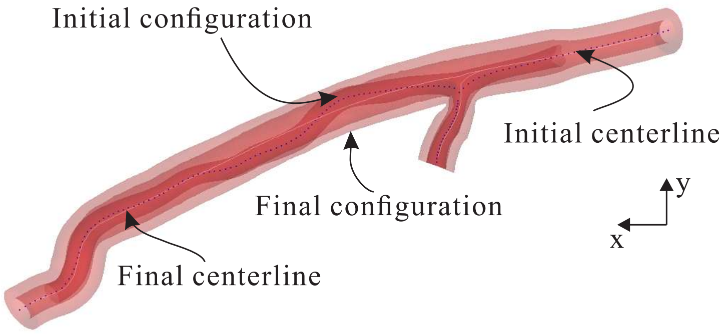

(a)

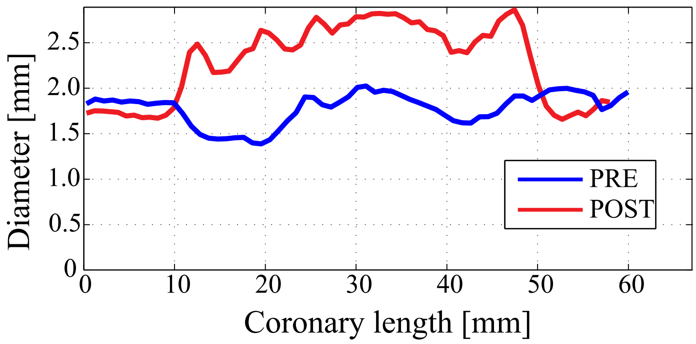

(b)

Figure 3.20 *Results of coronary configuration (LDA) before and after the stenting procedure: (a) coronary lumen profile and relative centerlines; (b) diameter values of the coronary artery.*

For this purpose, using the available pre- and post-operative angiographic images of the intervention, we have considered the case of another patient having a long coronary lesion as highlighted in Figure 3.23 (a) and treated with one long stent as illustrated in Figures 3.23 (b) and (c), showing the angiographic images at the maximum balloon expansion and at the end of the stenting procedure, respectively.
Starting from these pre-operative angiography, we have reconstructed the 3D patient-specific coronary model; then, following the procedure previously described, we have performed the simulation of the one long stent implant. As depicted in Figures 3.23 (d), (e) and (f), we can observe a satisfactory qualitative matching between the image and 3D models, even if the distal part of the 3D models are slightly dislocated with respect to the angiographic image in Figure 3.23 (f). This issue could be due to the dif-

Patient	A	B	C	Stenosis degree
PRE	175°	24°	151°	63%
$POST$	176°	20°	164°	-

Table 3.2 *Bifurcation angles (A, B, C) and stenosis degree computed before (PRE) and after (POST) percutaneous coronary intervention.*

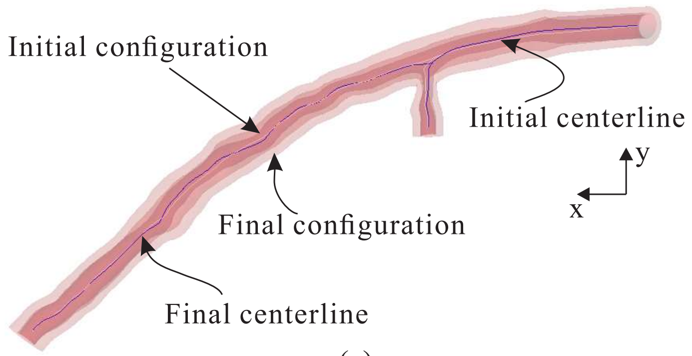

(a)

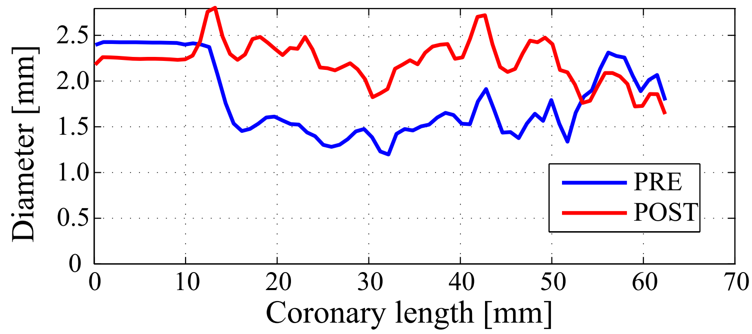

(b)

Figure 3.21 *Results of coronary configuration (LCA) before and after the stenting procedure: (a) coronary lumen profile and relative centerlines; (b) diameter values of the coronary artery.*

ferent objects in comparison, i.e., the 2D image view and the 3D models. However, we have compared the mean diameter values between the coronary lumen in the projected view and the coronary vessel model after the stenting procedure. The difference (mean error) between the numerical prediction and the post-operative outcome, as shown in Figure 3.24, keeps lower than 0.1%; this result supports the reliability of the proposed numerical study.

3.5.4 Anisotropic vs isotropic vessel material

In this study, we want to compare the coronary stress results after the stenting procedure at different material properties, i.e., isotropic versus anisotropic.
The isotropic material coefficients of the coronary vessel model has been computed through a polynomial strain energy function of the sixth order, which is carried out with respect to the experimental data of the coronary artery's IX specimen provided by Holzapfel et al. [93]. It worth noting that we have implemented an isotropic constitutive model from the same experimental data which allowed to obtain the parameters used to describe the anisotropic behaviour of the coronary vessel (see Appendix C).
The results of the fitting procedure are based on the experimental curves obtained as mean between the circumferential and axial curves, as reported in Figure C.2, and the obtained material parameters are listed in Table C.1. Also in this study, to reproduce

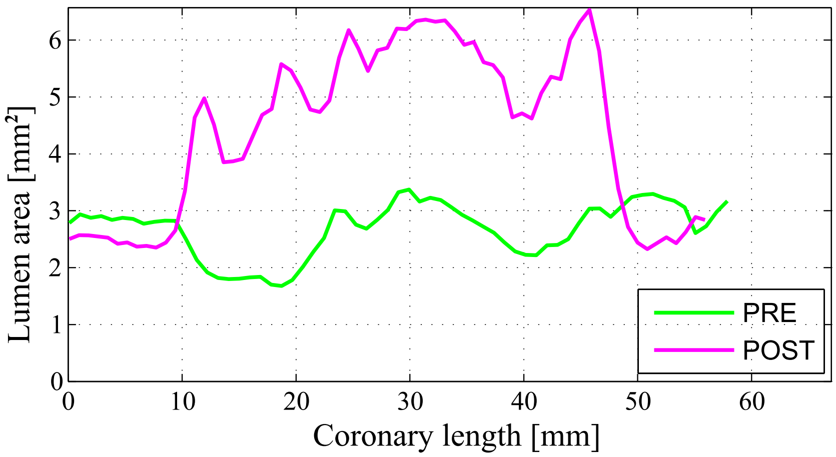

(a)

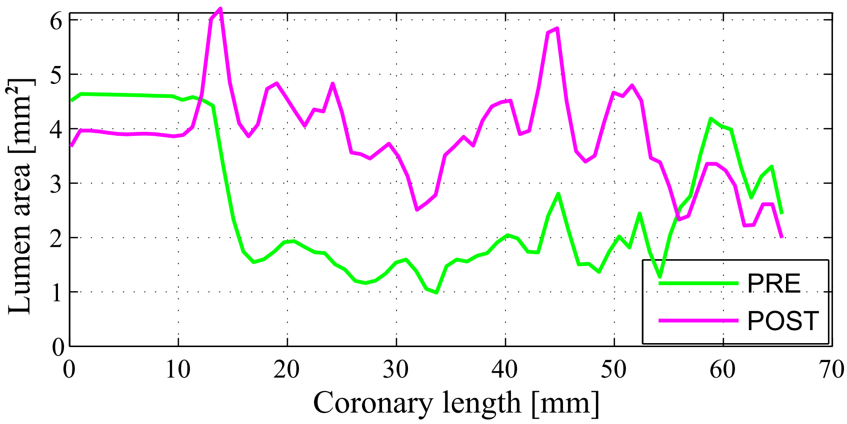

(b)

Figure 3.22 *Results of coronary configuration before and after the stenting procedure: (a) coronary lumen area of the LAD; (b) coronary lumen area of the LCA.*

the isotropic behaviour of the coronary artery, we have computed the mean square root error (RMSE) [93] in order to evaluated the fittings quality: 0.0034, 0.000945 and 0.0044, for the intima, media and adventitia layers, respectively.
The comparison between the different material properties assigned to the coronary vessel are depicted in Figure 3.25 and illustrated in Table 3.3.
We report the maximum principal stress values at the maximum balloon expansion and at the end of the stenting procedure for both the cases: the 99% of the coronary mesh volume elements have a stress value lower than 1.7 MPa for the isotropic vessel material versus the 0.7 MPa computed for anisotropic vessel one at the maximum balloon expansion; whereas, at the end of the procedure the computed results show that the 99% of the volume elements have stress values lower than 0.33 MPa versus the value of 0.15 MPa computed in the case of anisotropic material. Hence, the comparison between the two mechanical behaviour show a difference of 40-50%.
We show in Figures 3.26 the results in terms of coronary vessel stresses at the end of the stenting procedure: the stresses distribution in the case of isotropic material is inhomogeneous along the inner vessel wall, reaching a peak value of 0.33 MPa against

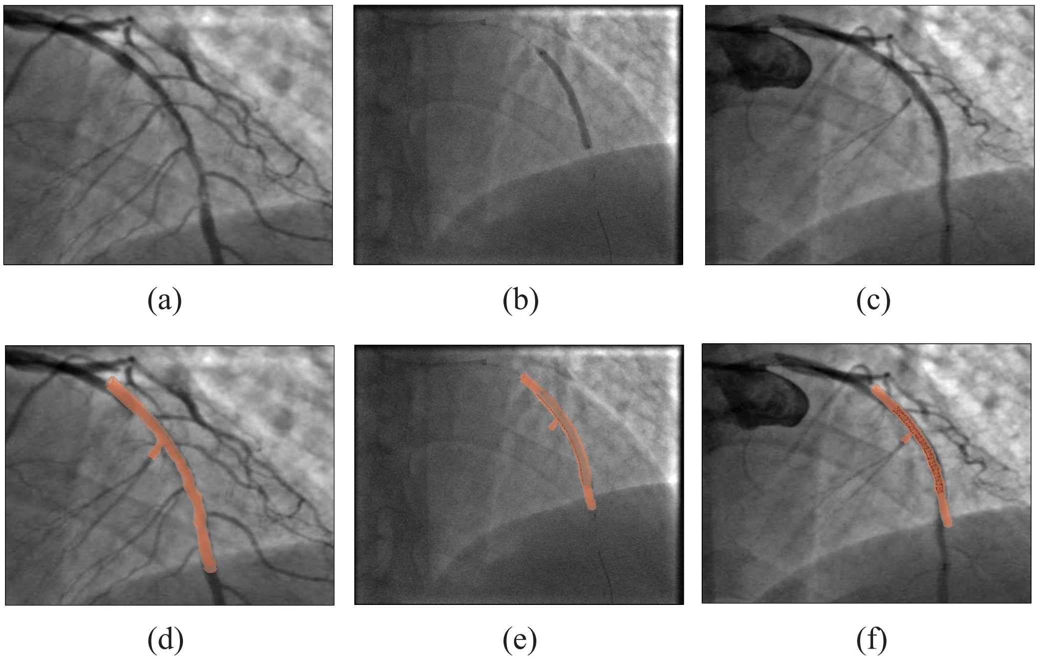

Figure 3.23 *Coronary long lesion treatment: (a) angiographic view before the percutaneous coronary intervention; (b) image agiographic view at the instant of the maximum balloon expansion; (c) image agiographic view after the stenting implant; (d) 3D coronary model superimposed to the angiographic view; (e) visualization of the balloon model at the maximum expansion of the numerical simulation superimposed to the image from a matching viewpoint; (f) final configuration of the vessel and the stent at the end of the stenting procedure superimposed to the image from a matching viewpoint.*

the value of 0.21 MPa in the case of anisotropic material.

Finally, we conclude that the implementation of the anisotropic material provides

Analysis	Stress	Max balloon expansion	Final procedure
Vessel	Max	2.6 MPa	0.70 MPa
ISOTROPIC	$< 99\%$	1.7 MPa	0.33 MPa
Vessel	Max	1.486 MPa	0.213 MPa
ANISOTROPIC	$< 99\%$	0.693 MPa	0.152 MPa

Table 3.3 *Maximum principal stress values for isotropic and anisotropic material: (i) at the maximum balloon inflation and (ii) at the end of the stenting procedure; we illustrate the maximum coronary stress and the coronary stresses lower the 99% of the vessel volume elements.*

a mechanical behaviour stiffer than that isotropic, highlighting the restriction of the isotropic material employment with respect to that anisotropic, which is the real mechanical behaviour of the coronary arteries, as described in the Section 1.1 of *Chapter 1*.

Further, we note that also isotropic coronary artery presents stresses pre-dominantly aligned in the circumferential direction. We may speculate that this result is due to the greater extensibility in the radial direction than in the circumferential one of the fiber-reinforced arteries. This aspect leads also to the reduced stress values obtained adopting an anisotropic material model with respect to an isotropic model. Moreover, the

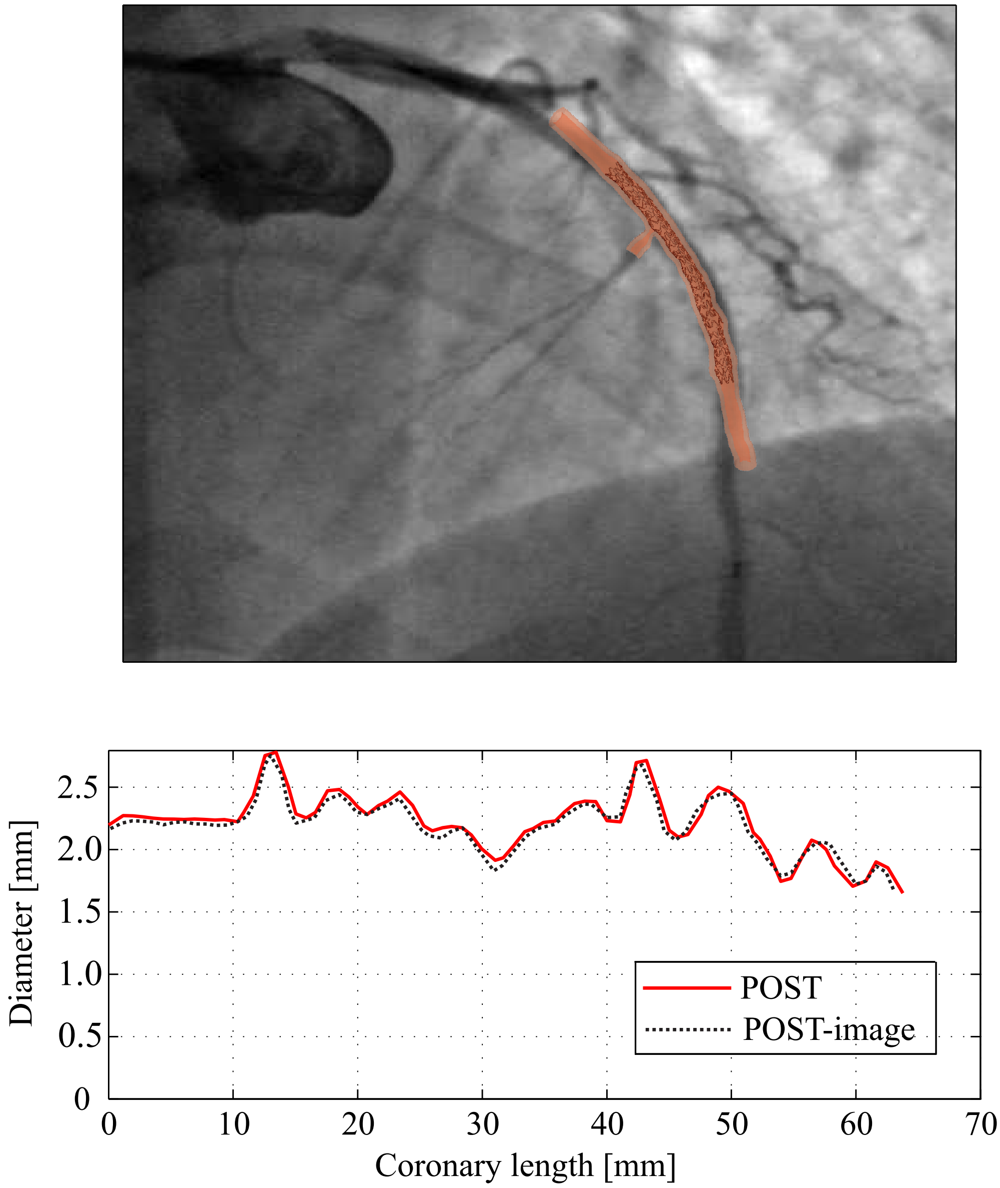

Figure 3.24 *Comparison of the diameter values computed from the X-Ray images acquired after the percutaneous coronary intervention and the coronary model projected in the same plane with respect to the image.*

performed simulations confirm that anisotropic coronary arteries exhibit a smoother, more physiological behaviour, by demonstrating that the choice of the material model represents a tricky issue when performing numerical simulations.

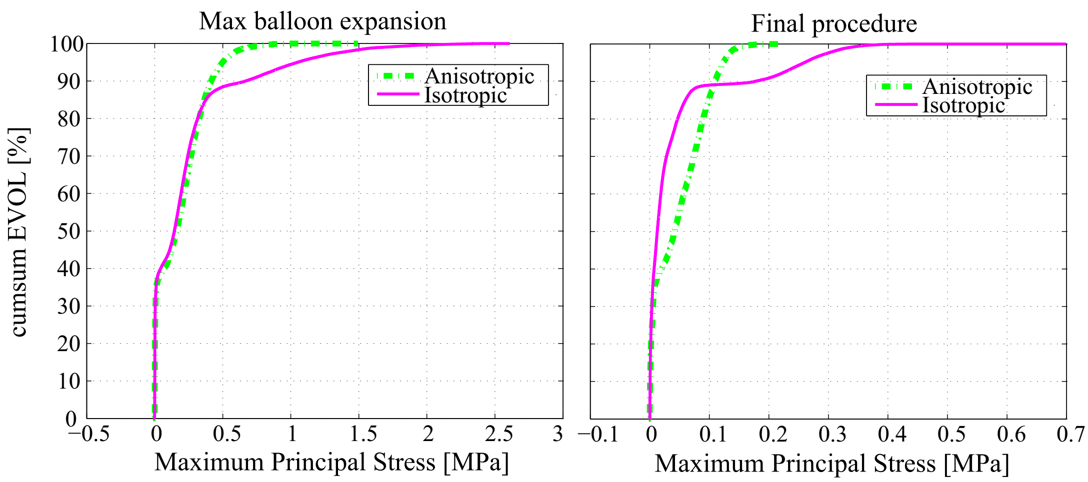

Figure 3.25 *Comparison of the maximum principal stress results at the maximum balloon expansion and at the end of the stenting procedure of one long stent having two different constitutive material model from the patient-specific coronary vessel.*

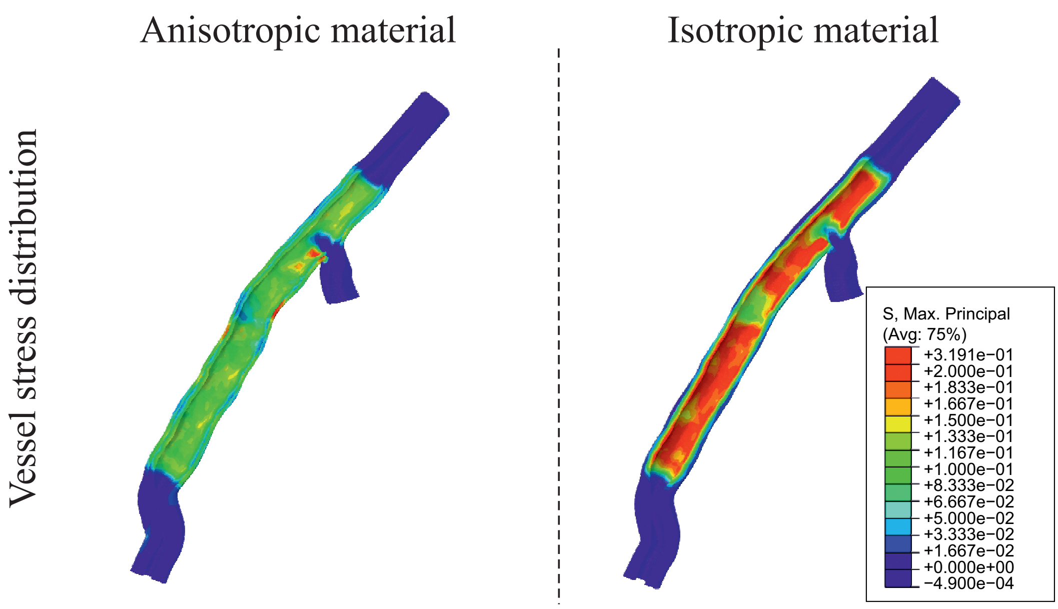

Figure 3.26 *Maximum principal stress in the post-stenting coronary artery with respect to the different constitutive material models implemented in this study.*

Chapter 4

Simulation of long coronary stenting

In this chapter, we focus on the finite element analysis (FEA) of the stenting procedure for a specific coronary artery disease treatment, i.e., the long coronary lesion.
We implement two different stenting techniques used in the clinical practice to provide the surgeon a considerable support to the pre-procedural planning. Indeed, several open issues regarding the long coronary lesions treatment among interventional cardiologists render difficult the choice of the better stenting procedure to be adopt in order to avoid restenosis problems.

4.1 Introduction

Long coronary lesion consists in a significant growth of atherosclerotic plaque that diffuses extensively along the coronary lumen [114].
Nowadays, the treatment of the long coronary lesions represents the 20% of the percutaneous coronary interventions (PCIs) and the suitable surgical strategy to adopt is still limited and not clear in the clinical practice.
Hence, coronary long lesion constitutes a challenge for interventional cardiology [115].
Although the introduction of drug-eluting stents has reduced the occurrence of restenosis intra-stent in coronary arteries with respect to the bare metal stent [114, 116], it remains a problem in the long lesions treatment due to several problems that occur after the PCIs, such as the wrong apposition of the stent strut at the coronary wall, which increases the thrombosis risk due to the contact lack of the stent strut on the vessel wall have been highlighted by Intra Vascular Ultra Sound (IVUS) and Optical Computed Tomography (OCT) analyses [117, 118].
Generally, such a problem is caused by the choice of the diameter size of the stent, which could fit unevenly due to the not constant lumen diameter. For this reason the measure of the distance between stent strut and lumen occurs after the PCI as predictive factor of stenting success rate [119].
Nowadays, for the long coronary lesions treatment, two main stenting strategies are adopted: one long stent or two/more overlapping short stents. The last one could remove the problem of the wrong apposition of the stent by choosing different stent diameters to better adapt the stent strut to the coronary wall. Such a procedure consists in the apposition of a first short stent in the distal part of the coronary lumen, i.e., the coronary portion farthest from the aortic valve, then, the subsequent short stent/stents in the proximal coronary part. Nevertheless, this procedure could involve the alteration of the blood flow in the overlapping area of the stents, preferring, thus, the choice of

a long stent for this specific coronary treatment. But the impact of the long stenting implant to the treatment of the long coronary lesions on the in-stent restenosis is not clear [116].
Moreover, clinical studies report controversial data about the stenting strategies adopted for coronary long treatment. Some investigators higlighted that the use of multiple short stents in long lesions shows similar outcomes with respect to that of single long stent [120, 121, 122, 123]. On the other hand, some studies reported the efficacy of the long stent implantation with respect to the other strategies, as shown by Kastrati et al. [124]. In the clinical study of Tsagalou et al. [125] is reported that the implantation of multiple long overlapping stents in patients with diffuse disease in left anterior descending artery are relatively safe. Raber et al. [126] have compared the clinical outcomes of patients with the implantation of one long stent, of multiple stents with and without overlapping. This study demonstrates that the major adverse cardiac events are more common in patients with stent overlapped rather to the other groups at the follow-up. Nevertheless, the intervention of long lesions remains a complicated issue in cardiological interventions because the efficacy of a possible strategy, i.e., one long stent versus two/more stents, is not still proven.
Such aspects indicate a significant need to develop dedicated tools for procedure planning in order to improve this specific coronary treatment and to standardize the treatment with a correct strategy. In the last decade, several structural finite element analyses of coronary stenting have been performed [14, 47, 49, 50, 127, 128]. If we focus our attention on recent studies addressing stenting of coronary bifurcation, the study of Mortier et al. [49] represents the starting point of a dramatic increase of simulation complexity and its capability to reflect the reality. In fact, Authors use FEA to evaluate the impact of different new-generation stent designs on the same vessel anatomy, reconstructed from angiographic data imposing also a layer-specific anisotropic mechanical response; the simulations include the geometry of the folded balloon model and the stent models based on high-resolution micro-CT of a real device.
Following this direction, FEA of coronary stenting can be considered nowadays an effective tool to perform virtual implants as proved also by Morlacchi et al. [50], which have recently described the implementation of a patient-specific model that uses image-based reconstruction of coronary bifurcations and is able to replicate real stenting procedures following clinical practice. In particular, the study investigates two real clinical cases treated with provisional side branch stenting. The numerical simulations embed realistic models of stent, balloon and patient-specific coronary vessel meshes generated from the medical image analysis.
Unfortunately, at the best of our knowledge none of the current FEA-based studies, addressing the coronary stenting simulations, focus on the treatment of long coronary lesions. In the present study, we use FEA to evaluate the performance of two strategies of stenting implant for long lesion treatment: application of one long stent versus two overlapping short stents in a patient-specific coronary artery with a coronary lesion, i.e., a left anterior descending artery (LAD). The study is organized as follows:

- we generate a patient-specific coronary artery model based on DICOM images of X-Ray coronary angiography;

- we consider two stenting strategies from a specific stent design, i.e., Xience Prime in different configurations, in terms of diameter and length size;

- for each strategy, we simulate the insertion and the deployment of the stent in the patient-specific coronary artery;
- we analyze the simulation results in terms of stress and strain with respect to the volume elements of the models, comparing also the pre- and post-stenting vessel geometry to evaluate the lumen gain and vessel straightening.

4.2 Materials and Methods

In this work, we perform two FEA-based simulations, that is one for each stenting strategy. Each simulation embeds several models (stent, artery, balloon and introducer) and is composed by two main analyses, i.e., (i) stent crimping and insertion and (ii) stent deployment. Table 4.1 details the simulation of every stent implant, which can be considered both for long stent and for each short stent.
Since the study focuses on the stenting strategy, we consider the same coronary anatomy generating a patient-specific model from angiographic images regarding the left anterior descending coronary artery (LAD) and the same stent design, i.e., Xience Prime. Although the stent design is fixed, we vary the size and configurations to accomplish the two stenting strategies under investigation: (i) one long stent, i.e., 3x38mm; (ii), two short stent, i.e., one 3x23mm stent (distal position) plus one 3x18mm stent (proximal position)[1].
The numerical analyses are clearly non linear, involving large deformations and contact. We use Abaqus/Explicit as finite element solver to perform such numerical simulations.

Analysis	Step	Description	Models
Stent crimping and insertion	Crimping	Outer diameter of the stent, mounted onto the balloon, is reduced through the radial decrease of the introducer diameter	Stent Balloon Introducer
	Positioning	The system balloon-stent is gradually bent and positioned within the artery model through the contact with the rigid surface of the introducer, which deforms to resemble the lumen centerline	Stent Balloon Introducer
Stent deployment	Balloon inflation	Stent expansion through balloon inflation	Stent Balloon Coronary
	Balloon deflation	Balloon deflation and stent recoil	Stent Balloon Coronary

Table 4.1 *Schematic description of the two analyses, each of them comprises of two steps, to simulate every stent deployment.*

[1]The different lengths of the Xience Prime stents are available in commerce.

4.2.1 Coronary artery model

3D bifurcated patient-specific coronary model has been reconstructed from two single-plane X-Ray angiographic views. Every angographic view is defined by the flat detector orientation in terms of the left or the right anterior oblique angle and the caudal or cranial angle with respect to the iso-center point, where the C-arm of the angiography rotates (see Section 3.2.1, *Chapter 3*).
In this study, we consider an heterogeneous and anisotropic behaviour of the coronary artery referring to the model proposed by the work of Gasser et al. [7], which considers the fibers symmetrically oriented with respect to the circumferential direction. The constitutive modelling has been amply discussed and the material coefficients used in the numerical simulation used in this Chapter are illustrated in Table C.2 (see Appendix C).

4.2.2 Stenting system model

Although in the clinical practice the stenting system is composed of several components, i.e., stent, balloon, catheter, tip, guide-wire etc., in our study we consider only few parts to reduce the computational cost of the procedure. Hence, we consider the following parts: 1) stent; 2) balloon. Moreover, for the sake of simulation strategy, we include another part in the global model, i.e., a cylindrical rigid surface, in the following labelled as *introducer*, which is used in the numerical analysis to position the stent within the vessel, as described in the Section 4.2.3.

Stent Model

The coronary stent selected for this study is the Xience Prime, which is a cobaltum-cromium stent crimped on a trifolded balloon. Three different nominal lengths of such a stent are considered in this work: (i) one long stent (3x38 mm); (ii) first short stent (3x23 mm); (iii) second short stent (3x18 mm). The size of every stent refers to the diameter value before the crimping procedure and its length.
The geometry, material and mesh modelling of the Xience Prime stent have been detailed in the Section 3.2.2 of the *Chapter 3*. In Figure 4.1 (a), we show the meshed stent model.

Balloon Model

As previously described, the geometry of the trifolded balloon used in this study has been reconstructed through the high resolution of the images obtained with the micro-CT, which has allowed to capture the balloon size and shape (see Section 3.2.3 of the *Chapter 3*). Every tapered part of the balloon has a length size equal to the stent one, while the non-tapered part one equal to 1.5 mm in both the balloon extremities (see Figure 4.1 (b)). In this study, we choose a thickness value of 0.03 mm for the trifolded balloon mesh.

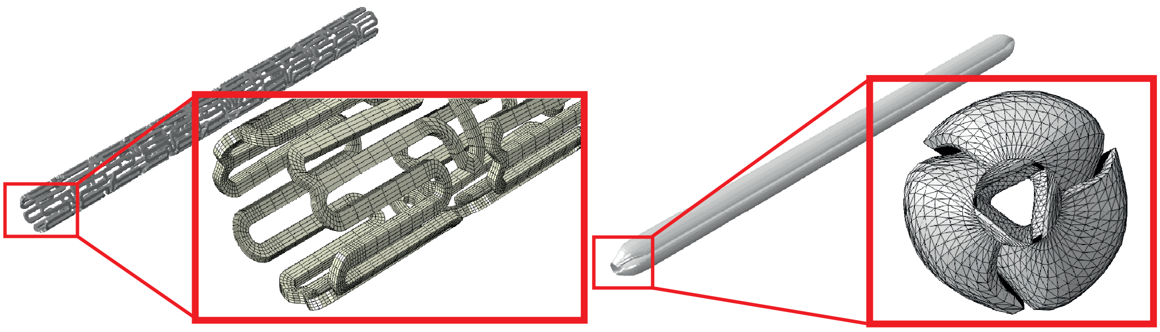

(a) (b)

Figure 4.1 *Mesh models: (a) the stent is discretized with eight-node hexahedral elements; (b) the balloon, having a trifolded configuration, is meshed with three-node triangular membrane elements.*

Introducer

To perform the first analysis of the stenting simulation, we label as introducer the rigid surface which is used to decrease the stent diameter (crimping phase) and to guide the stent model apposition inside the coronary lumen (delivery phase). The introducer is modeled as a rigid body and defined through a surface obtained by sweeping a cylindrical section having a length equal to balloon one. The mesh is realized with 4-node surface elements with reduced integration (SFM3D4R). The use of such a surface within the numerical analysis is discussed in the next section.

4.2.3 Numerical simulation

The numerical simulation of coronary stenting procedure is performed assembling conveniently the components of the stenting system model and the 3D patient-specific coronary model, as illustrated in the previous Table 4.1.

All the analyses have been modelled through a quasi-static Abaqus/Explicit procedure, in which the stable time increment is dependent both from the smallest element dimension of the mesh models and the dilatation wave speed. In such analyses, increasing the physical loading rate is often required to obtain a (computationally) economical solution in the case of explicit dynamic procedure. Hence, we have reduced artificially the computation time increasing the rate whereby the load is applied in the simulation. However, the process could be accelerated, and, thus, the inertial forces may become dominant. Therefore, a time-(in)dependency study has been performed for all the analyses to determine the loading rates at which inertial forces remain insignificant [108]. We detailed the quasi-static analysis regime in Section 3.4.1, *Chapter 3*.

In this study, we consider also the interaction problem between the models of interest for the given analysis, implementing the stable general contact algorithm and the frictional behaviour described by a Coulomb friction model with a static friction coefficient of 0.2 [49]. These contact specifications allow avoiding numerical instabilities in the simulation during the stenting procedure.

Moreover, to damp out dynamic effects and, thus, to reach quasi-static equilibrium in

a minimal number of increments, a viscous pressure loading is applied on the external surface both of the coronary vessel and stent models [50] (for more details see Section 3.4.6, *Chapter 3*).
In the next paragraph, we described the steps of the two main analyses which characterize every stenting strategy: (i) the stent crimping and positioning; (ii) the stent deployment.

Stent crimping and positioning

Crimping. The crimping consists in a gradual decreasing of the introducer diameter to reach the true stent diameter, while a pressure on the inner balloon surface varies in a very small range (0-0.04 N/mm^2) to partially unfold the balloon without transferring the load to the stent. During the crimping step, the balloon nodes at the both extremities are constrained to prevent the movement and shortening problems. Such a procedure has been implemented in the simulation before the insertion of the stent and the balloon inside the coronary artery to simulate the real stent configuration in terms of diameter size.
Equivalent plastic strain (PEEQ) values have been computed at the end of the crimping to evaluate the influence of such a procedure with respect to the initial non-loaded stent configuration. A mean PEEQ value of 10^{-4} order for the 99% of the volume elements has been computed on the stent, proving any influence of the crimping procedure on the non-loaded stent configuration for both the stenting strategies.

Positioning. This procedure allows to the stent and the balloon to be placed inside the stenotic coronary artery of interest through the use of the introducer. The stent and balloon deformation is imposed by the configuration change of the introducer through the application of the displacement boundary conditions (BCs) on its nodes. The BCs are determined as the difference between the starting and final introducer configuration. Particularly, the procedure consists in the bending of whole models: starting from a straight configuration, the introducer is gradually bent accomplishing the vessel centerline and leading to the stent and balloon deformation. Figures 4.2 and 4.3 depict the stent crimping and positioning procedure in the coronary vessel within the relative introducer.

Stent deployment

In this subsection, we describe the procedure to deploy the stent within the inner wall of the coronary artery through the inflation of the balloon. We have included in the finite element analysis also the balloon deflation to analyse the elastic recoil of the stent. Such a numerical analysis has been adopted for both the stenting strategies.

Inflation. The simulation of the balloon expansion for the stent deployment has been achieved by imposing a linear increasing pressure starting from 0 up to 1.824 N/mm^2, which is uniformly applied on the inner surface of the trifolded balloon.
During this step the nodes at the balloon boundaries have been constrained to prevent movement problems, while the stent model has been left free.

Deflation. To simulate the balloon deflation procedure, we have applied, after the previous step, a linear decreasing pressure starting from 1.824 down to 0 N/mm^2 on the inner surface of the balloon.

In the stent deployment analysis, we have verified the quasi-static regime computing the ratio between the kinetic and internal energy, proving that the ratio is lower than 5-10%.
Furthermore, a smoothing amplitude of the loading has been adopted, because the quasi-static analysis requires small changes in terms of acceleration and velocity to ensure that the inertia forces are neglected (for the details see Section 3.4.1, *Chapter 3*). Figures 4.2 and 4.3 depict the stent deployment procedure in both the stenting strategies.

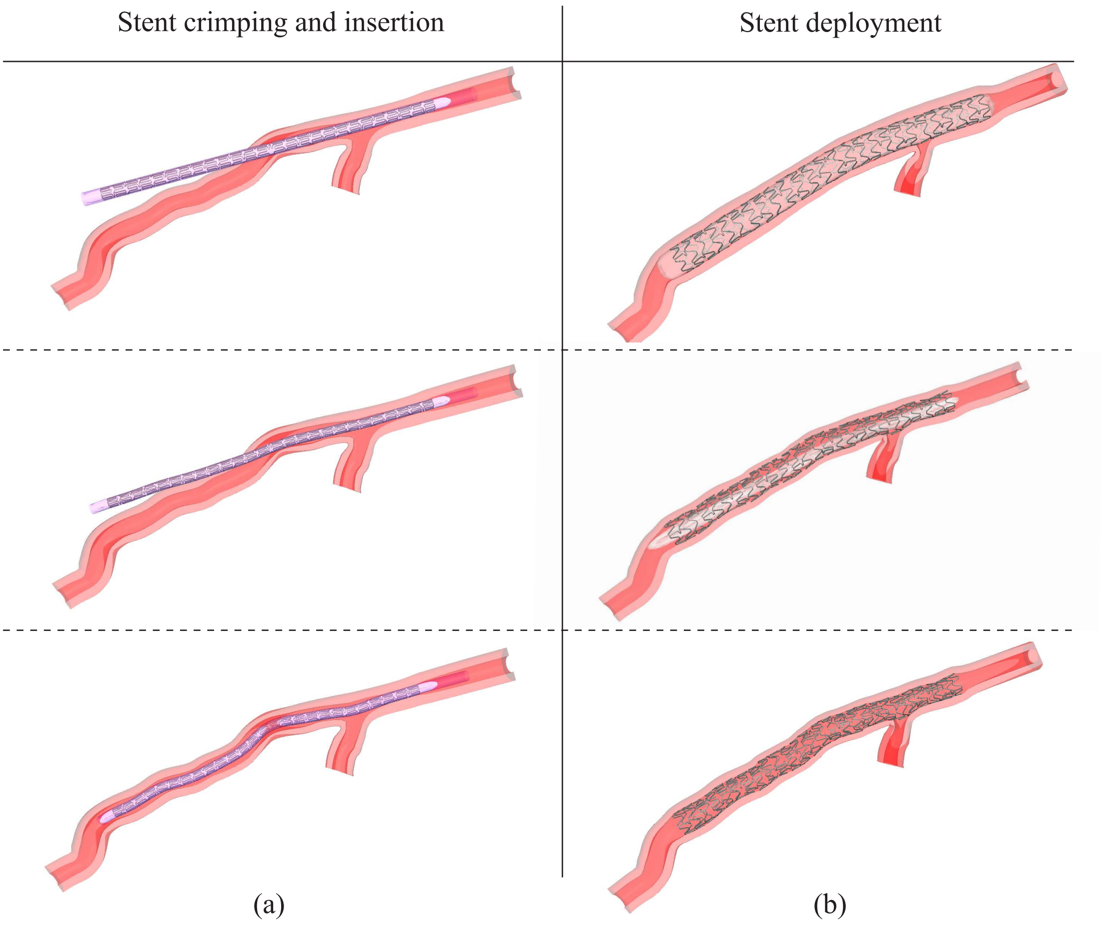

Figure 4.2 *Mapping stenting procedure of the one long stent. (a) Stent crimping and insertion procedure: (i) initial configuration; (ii) crimping and bending procedure of the stent/balloon through the introducer displacement; (iii) final position of the stent/balloon before the balloon inflation. (b) Stent deployment: (i) configuration at the maximum balloon expansion (pressure reaches 1.8214 MPa); (ii) deflation of the balloon at the pressure of 0 MPa; (iii) final configuration of the stent inside the coronary vessel.*

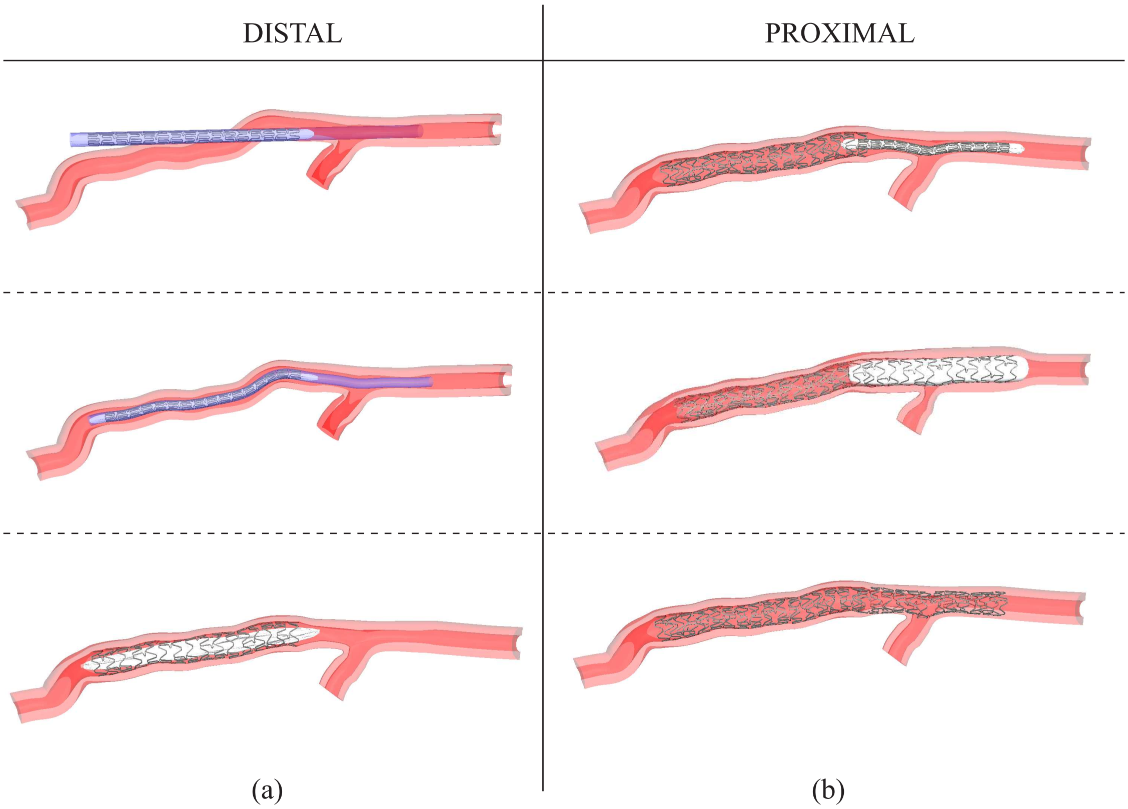

Figure 4.3 *Mapping procedure of two short stents in the distal and proximal part of the coronary artery. (a) Short distal stent: (i) initial configuration of the balloon/stent surrounded by the introducer, (ii) crimping and bending procedure of the stent/balloon to insert the stent/balloon in the distal region, (iii) final position of the short stent after the balloon inflation. (b) Short proximal stent: (i) insertion of the second short stent/balloon in the proximal main vessel after the crimping and bending procedure, (ii) configuration at the maximum balloon expansion, (iii) final position of the second short stent.*

4.2.4 Comparison between the mapping and classical procedure to simulate the first numerical analysis

In our study, we have simulated the stenting positioning using a sort of *mapping* approach as discussed in Section 3.3 of *Chapter 3*. In this section, we want to compare this simulation strategy with a *classical* approach, adopted by Mortier et al. [49] and Morlacchi et al. [50]. Such an approach consists in the insertion of the stent/balloon inside the coronary artery through their movement along a guide-wire. Although the classical approach is more close to the procedure reality than our strategy, it implies higher computational costs and potentially induces undesired inertial effects.
Starting from these considerations, we have simulated the case of one long stent implant using both the approaches; obviously, for the *classical* approach, excluding the rigid surface of the introducer, we have included other two components in the numerical analysis: the catheter shaft, which is a tube placed inside the balloon connected with the balloon extremities, and the guide-wire, which is the rail of the balloon/stent system. Also in this case, the simulation is defined by two main steps:

- crimping, enforced by an increasing pressure on outer surface of the stent while the balloon is slightly pressurised to allow a preliminary contact;

- insertion, driver by an imposed time-dependent displacement at the proximal end of the catheter shaft, which transmits the motion to the balloon/stent system up to reaching to the target position.

The results of simulation adopting the *classical* approach are depicted in Figure 4.4, while our approach has been already discussed in Section 3.3.
If we compare the numerical outputs reported in Tables 4.2 and 4.3, it is possible to conclude that the two simulation approaches are equivalent.

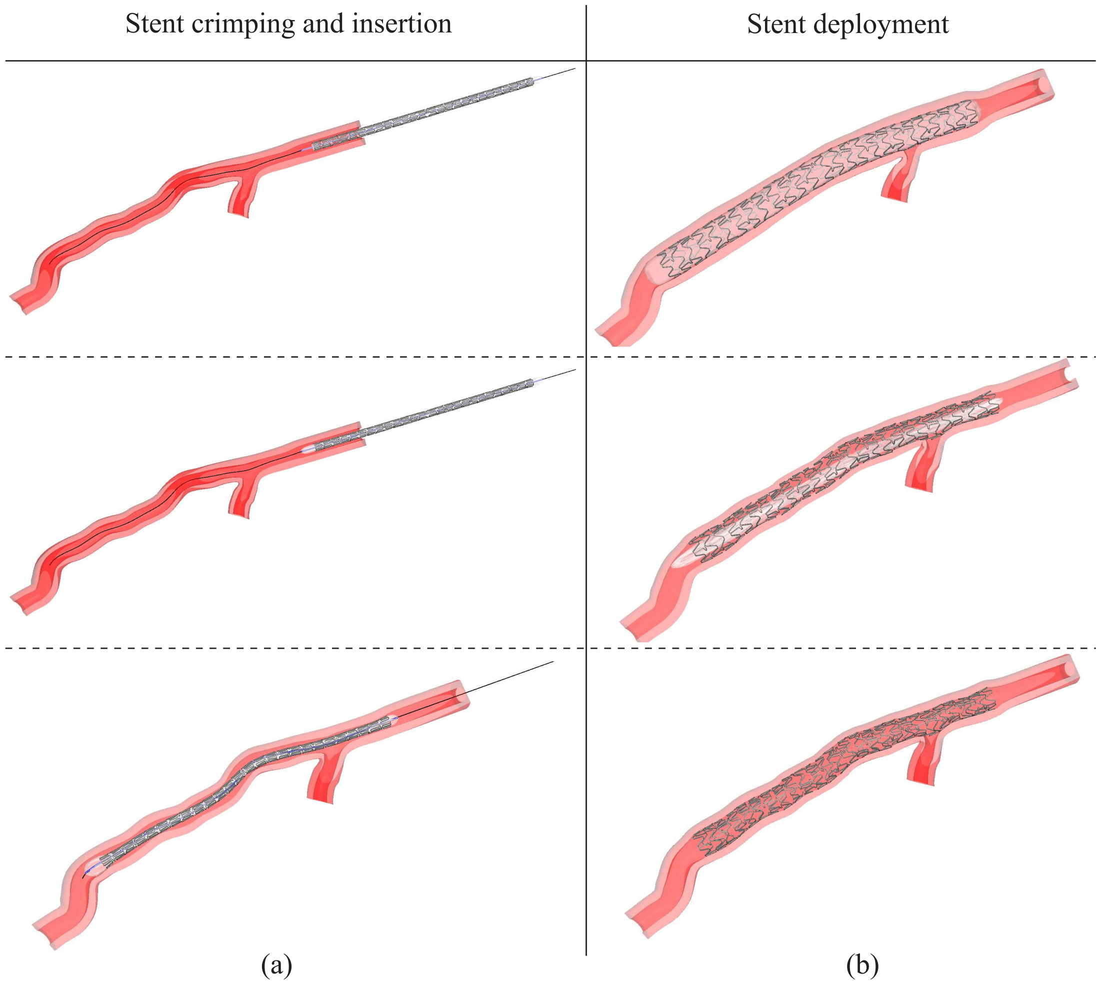

Figure 4.4 *Stenting procedure of the one long stent through classical procedure. (a) Stent crimping and insertion procedure: (i) initial configuration; (ii) crimping and insertion procedure of the stent/balloon and catheter models along the guide-wire; (iii) final position of the models before the balloon inflation. (b) Stent deployment: (i) configuration at the maximum balloon expansion; (ii) deflation of the balloon at the pressure of 0 MPa; (iii) final configuration of the stent inside the coronary vessel.*

Analysis	Coronary stress	Max balloon expansion	Final procedure
classical	Max	1.496 MPa	0.211 MPa
	$< 99\%$	0.689 MPa	0.151 MPa
mapping	Max	1.486 MPa	0.213 MPa
	$< 99\%$	0.693 MPa	0.152 MPa

Table 4.2 *Comparison between classical and mapping approach described in this study in terms of coronary maximum principal stress values at the maximum balloon expansion and at the end of the stenting procedure.*

Analysis	Stent values	PEEQ	Von Mises stress
classical	Max	0.448	835 MPa
	$< 99\%$	0.20	595 MPa
mapping	Max	0.45	834 MPa
	$< 99\%$	0.20	595 MPa

Table 4.3 *Comparison between classical and mapping approach described in this study in terms of stent stress/strain values at the end of the stenting procedure.*

4.3 Results and Discussion

As illustrated by Table 4.1, which depict the result of the several simulation steps for both the stenting strategies, the adopted simulation strategy is able to reproduce the complexity of clinical procedure under investigation, providing a realistic representation of the various stent/artery configurations characterising the implant sequence.
In the following, we analyse the numerical outcomes to evaluate the impact of stenting strategy, i.e., one long stent versus two short stents with respect to different aspects of clinical interest, such as the post-stenting anatomical changes or the level of stent/arterial solicitation level.

4.3.1 Arterial straightening

The implant of one or more stents restores the lumen patency through stenosis enlargement but, at the same time, induces several other changes on the vascular anatomy. Among the others, the post-stenting arterial straightening is a clinically-relevant issue because it is considered a reliable predictor of post-operative adverse cardiac events [109] and restenosis intrastent due to the alteration of the wall shear stress [110]. Moreover, the vessel straightening could be thought as an indirect measure of stent flexibility, already investigated by several numerical studies [49, 111].
Given such considerations, we evaluate also the post-stenting arterial straightening following the approach proposed by previous works [50, 112], which suggest to evaluate this effect through the comparison of the pre- and post-operative tortuosity index (T)[2]. Regarding the long stent deployment, the tortuosity index changes from 0.0574 to 0.0339 (-41%), while after the two short stents deployment, the tortuosity value decreases of

[2]The lumen tortuosity index (T) is defined as: $T = L/L' - 1$, with L, the centerline length, and L', the distance between the extreme points of the vessel [113]; the centerline is computed through the *vmtkcenterlines* module of VMTK library (`http://www.vmtk.org`).

0.0316 (-45%). In the recent study of Morlacchi et al. [50] the tortuosity index is measured before and after the stenting procedure, considering two different coronary patient-specific vessel models; in such a study the index T decreases of 20-30%. In our study, we measure a tortuosity change of 40-45% for the adopted stenting strategies, which is lower than that computed in [50] due to the smaller initial T value of the coronary artery: T has a value equal to zero for a straight vessel and increases with the vessel curvature.
Recent studies regarding the coronary vessel tortuosity suggest that the tortuosity decrease avoids the blood flow alteration resulting in a reduction in coronary pressure distal to the tortuous segment of the coronary artery [129, 130]. Hence, obtaining a significant vessel straightening after the stenting procedure may decrease the clinical problems, such as the intrastent restenosis and the alteration of blood flow.

4.3.2 Elastic recoil

Elastic recoil of the stent consists of its diameter decrease due to the compressive force created by the vessel after the maximum expansion of the balloon to place the stent. After the deployment of the stent, a low elastic recoil value is required to minimize the in-stent restenosis; hence, the stent should be sufficiently rigid to resist the compressive forces of the vessel wall [131]. The measure of elastic recoil is defined as follows: $(R_{load} - R_{unload})/R_{load}$, where R represents the radius of the stented vessel at the maximum balloon inflation (load) and after its deflation (unload).
Given such considerations, we compute the diameters of the coronary lumen at three specific stages of the stenting: before the stenting (Initial), at the maximum balloon inflation (Max) and after the balloon deflation (Final). The results of this analysis for the long stent case are reported in Figure 4.5 (a), while Figure 4.5 (b) depicts the results for the case of two short stents; moreover, a comparison between the two cases is provided in Figure 4.5 (c).
The first consideration regards the pre-operative diameter lumen profile; from the plot of the vessel diameter as function of the coronary length (from proximal to distal end), it is possible to notice that there are two main stenotic regions, i.e., at 20 and 40 mm of the coronary length, where the stenosis degree[3] is 55% and 50%, respectively.
For both the stenting options, we can observe an abrupt change of the lumen diameter profile close the ends of the stenting region due to the stent placement.
For both the cases, we can note that at the maximum balloon expansion the coronary lumen profile is uniform, whereas after the balloon deflation, such a uniformity disappears. This result highlights the vessel/stent configuration variability after the stenting procedure; clearly, such a variability is particularly significant in long coronary lesions with diffused stenosis.
Results highlight that both the stenting strategies are similar in terms of final diameter values of the coronary vessel, as depicted in Figures 4.5 (c). After the long stent deployment, we have computed a mean elastic recoil value of 0.137 ± 0.012 (14%), which reaches the maximum value of 25-30% in the proximal part of the coronary vessel. Whereas, in the case of two short stents deployment, the computed elastic recoil values are equal to 0.126 ± 0.011 (13%) and 0.118 ± 0.008 (12%) in the proximal and in the

[3] The severity of the stenosis degree is computed as $S = [1 - (D_{min}/D_{ref})^2] * 100\%$, where D_{min} is the minimum diameter and D_{ref} is the reference diameter, i.e., healthy mean diameter of the coronary lumen [95].

distal part of the stented coronary vessel, with a maximum elastic recoil value of 26% reached in the proximal coronary segment.
Similar clinical results are highlighted also in previous medical studies [132, 133, 134], which computed the elastic recoil immediately after balloon deflation through medical images analysis. The elastic recoil of coronary stent might be an important component of restenosis rate; hence, a low elastic recoil value is required in the stenting procedure [131].

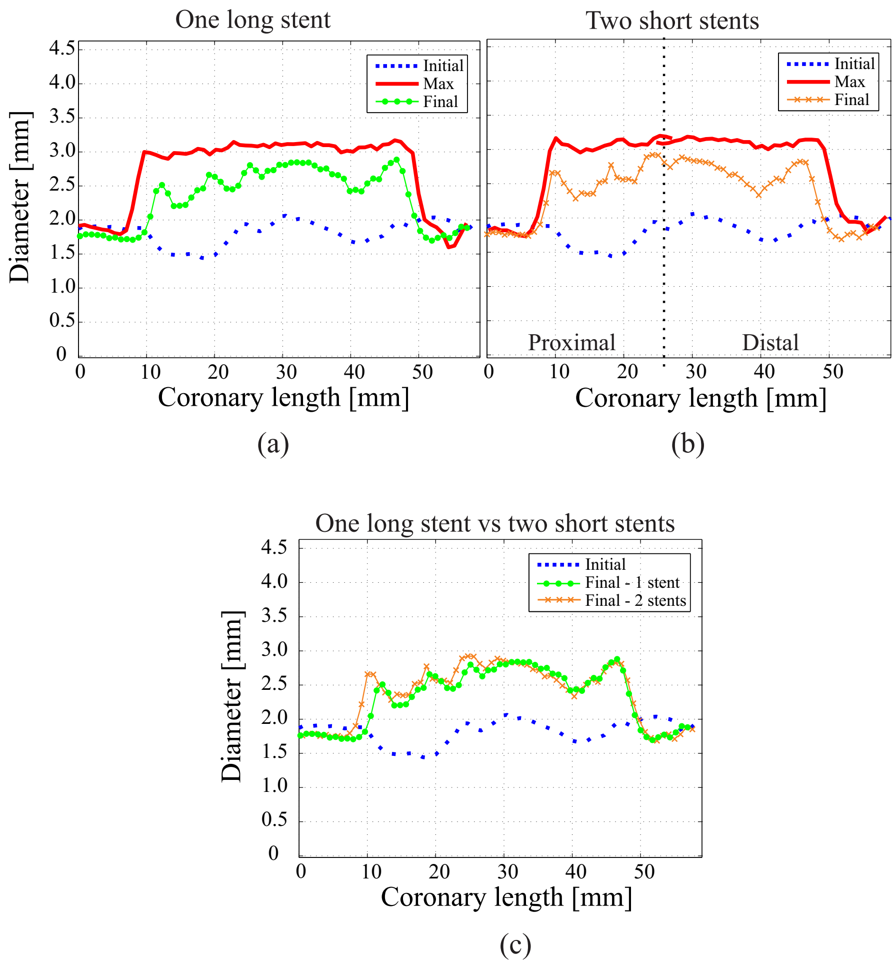

Figure 4.5 *Computed diameter profile of the coronary artery at three specific stages of stenting: before the implant (Initial); at the maximum balloon expansion (Max); after the balloon deflation (Final).*

4.3.3 Post-stenting arterial stress distribution

The simulation of stent deployment allows to calculate the stress distribution along the arterial wall during the different stages of the procedure. We consider the maximum principal stress under the hypothesis that they resemble the circumferential tensional stress of the arterial wall; this hypothesis relies on the mechanism of stenting, it is in fact reasonable that the maximum stress induced by the stent enlargement to the

arterial wall is oriented in circumferential direction, assuming a cylindrical coordinate framework and that the vessel can be considered as a thick-walled tubed.
The maximum principal distribution along the vessel wall for the two considered stenting options is depicted in Figure 4.6. The results indicate that the apposition of one long stent induces a uniform stress distribution along the whole stenting region while, in the case of two short stents deployment, the region of stent overlapping corresponds, as expected, to higher arterial stress. This is due to the mechanical influence of overlapping stents, which is already proven in several clinical studies [120, 125, 135, 136] and in the recent engineering study of Morlacchi et al. [50]. The stress concentration in the overlapping area may cause localized restenosis, preferring thus the choice of the one long stent for the long coronary lesions treatment.
In the following, we describe some clinical and engineering aspects which have been highlighted by results.
Two short stents deployment. In the case of the stenting procedure with two short stents deployment, the coronary vessel is mainly stressed by the proximal stent, in a non-uniform way. This could be attributed to the stenting procedure of the two short stents: in fact, the proximal stent is deployed after the distal stent placement.
Long stent versus short stents deployment. High circumferential stress values are computed in both the adopted strategies at the maximum balloon expansion, as shown in Figures 4.7. In particular, at the maximum balloon expansion in one long stent case, the stress reaches the maximum value of 1.5 MPa in the proximal part of the coronary artery and nearby the bifurcation area. Instead, in the case of two short stents, we can observe that the coronary vessel is doubly stressed due to the two stents deployment: stress values at the maximum balloon expansion in the distal and proximal part of the coronary artery reach the maximum values of 0.75 and 1 MPa, respectively (see Figure 4.7 (a)). High values of stress can cause injuries in the inner of the coronary artery [107] and considering the ultimate stress value of the coronary artery approximatively equal to 1-2 MPa, the stress values computed in both cases are critical.
Figure 4.7 (b) depicts the coronary stress values at the end of the stenting procedure for both the procedures, highlighting different results: the 99% of the discretized coronary volume has a stress value lower than 0.15 MPa, reaching the maximum value of 0.21 MPa, after the one long stent deployment; instead, in the other stenting strategy option, the 99% of the discretized coronary volume has a stress value lower than 0.22 MPa and the maximum value of the stress reaches the 0.33 MPa.
In Figure 4.6, we show the resulting contour plot of the maximum principal stress in both the stenting strategies at the end of the stenting procedure. Regarding one long stent deployment, the stress values are evenly distributed along the coronary vessel, except some small and sparse areas having higher stress values. After the two short stents deployment, we can observe that the higher stress value is more concentrated both nearby the bifurcation area and in the central part of the coronary vessel due to the impact of the two short stents in the overlapping area. Furthermore, the proximal part of the coronary vessel is more stressed than that distal and the stresses distribution is not homogeneous along the vessel; this could modify the mechanical behaviour of the coronary vessel, preferring, thus, the choice of the stenting strategy using one long stent.
Similar results in terms of coronary stress values are reported also in the study of Mortier et al. [49], which adopted an anisotropic constitutive model for the coronary

vessel wall in the numerical stenting procedures.
As already stated, in the present study we have adopted an anisotropic hyper-elastic model to reproduce the mechanical response of the arterial wall as proposed by [49] but, it is worth noting that most of FEA of coronary stenting use an isotropic model [50]. Given such a consideration, we have also performed some numerical tests described in Appendix 3.5.4 to evaluate the impact of the arterial model, i.e., isotropic versus anisotropic, on the final vessel stress distribution. Such results show different bio-mechanical responses between the considered vessel models, highlighting the importance to adopt the anisotropic material to reproduce the real mechanical behaviour of the coronary arteries.

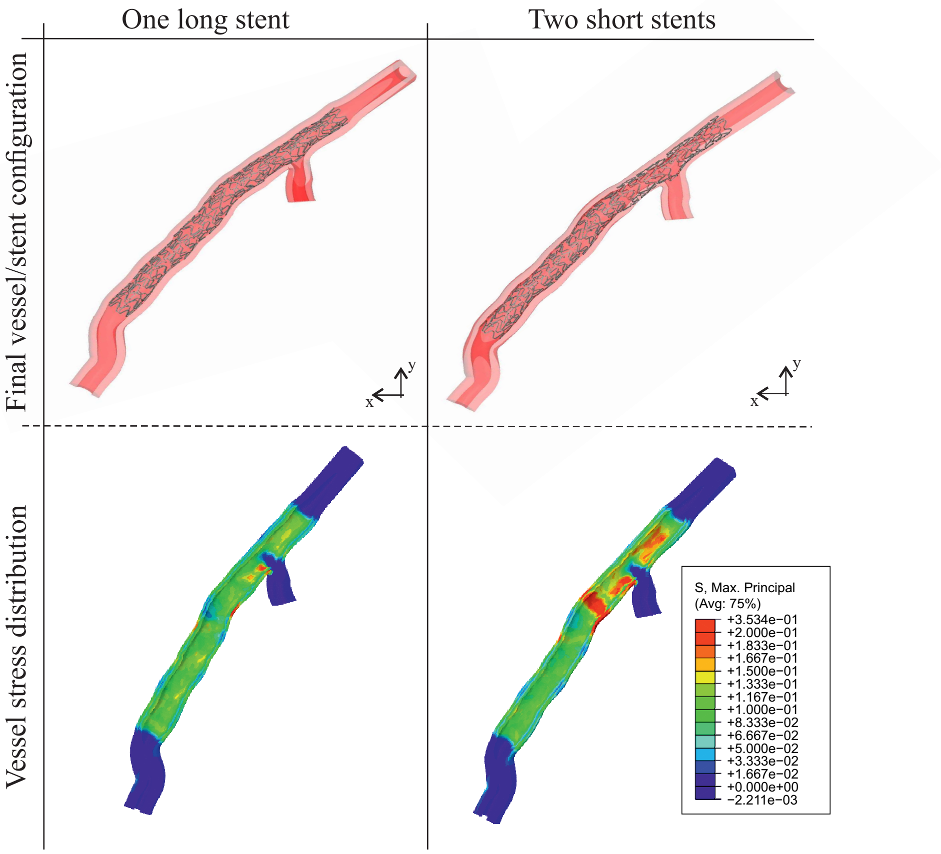

Figure 4.6 *Comparison of the maximum stress distribution [MPa] along the arterial wall for both stenting options. The results corresponds at the end of the stenting procedure, i.e., at the end of balloon deflation.*

4.3.4 Stent and strain distribution in the stent struts

The computation of the stress/strain distribution along the stent frame during the stenting procedure allows to assess the potential risk of structural failure of the device during the procedure. In particular, we have considered the distribution of two scalar

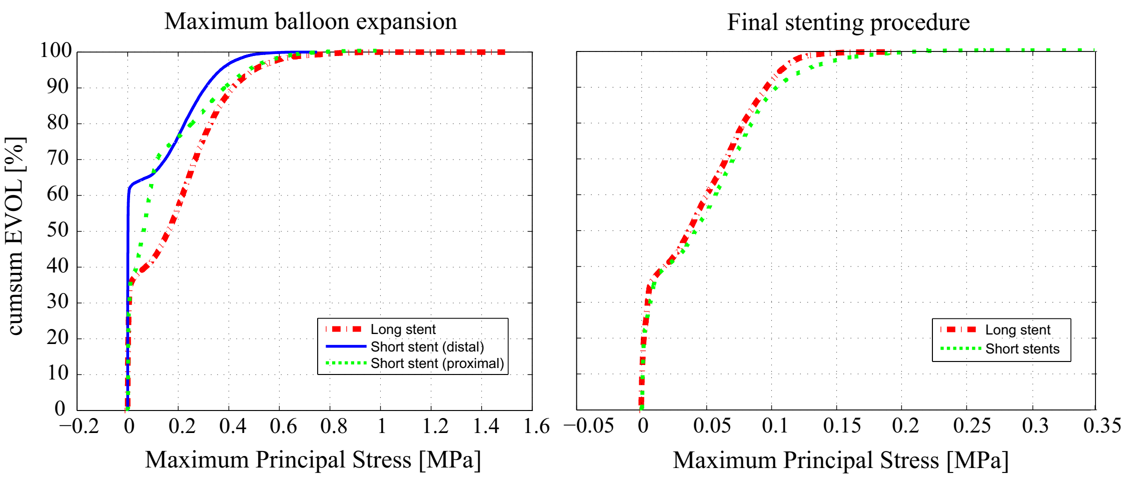

(a) (b)

Figure 4.7 *Comparison of the maximum stress distribution [MPa] of the coronary vessel. (a) Stress values at the maximum balloon inflation in three different cases: (red) one long stent deployment, (blue) short distal stent and (green) short proximal stent deployment. (b) Stress values computed at the end of the stenting procedure for both the stenting strategies.*

indexes: the von Mises stress (VMS)[4] and the plastic equivalent strain (PEEQ)[5], at two stages of the stenting procedure, i.e., at maximum balloon inflation and at the end of balloon deflation.
Figure 4.8 (a), depicting the VMS distribution along the stent frame for the one long stent case, indicates that the higher stress (around 834 MPa) is present at the bended strut and in particular at the intersection point with the inter-ring connectors. A similar result is obtained for the case of the short stents with a more pronounced effect in the overlapping zone; for this case, we have not found a particular difference between the distal and proximal stent, in fact the maximum value of VMS reaches the 853 MPa for the stent deployed in distal part of the coronary artery and the 836 MPa in the proximal one (see Figure 4.8 (b)).
The computed PEEQ values for each case at the end of the procedure show that the inelastic strain is more concentrated in the bended strut as highlighted by Figure 4.9; in both the cases, these values are close to the ultimate tensile strain at the break of the considered material (CrCo), i.e., 0.448 [50]. These results highlight the potential critical situations related to the stents deployment. In fact, in this scenario, the integrity of the stent structure and the deformation areas are also critical for the potential damage of the stent polymer coating as also discussed by the study of Morlacchi et al. [50]. In particular, the overlapping area of the two stent could prevent the emission of the drug, which is in the polymeric coating, and thus, preventing the anti-proliferative and anti-inflammatory processes.

[4] $VMS = \sqrt{\frac{3}{2}S : S}$, where S is the deviatoric stress tensor ($S = \sigma + pI$), with σ the stress and $p = -\frac{3}{2}trace(\sigma)$ the equivalent pressure stress.

[5] $PEEQ = \sqrt{\frac{2}{3}PE_{ij} * PE_{ij}}$, where PE the plastic strain.

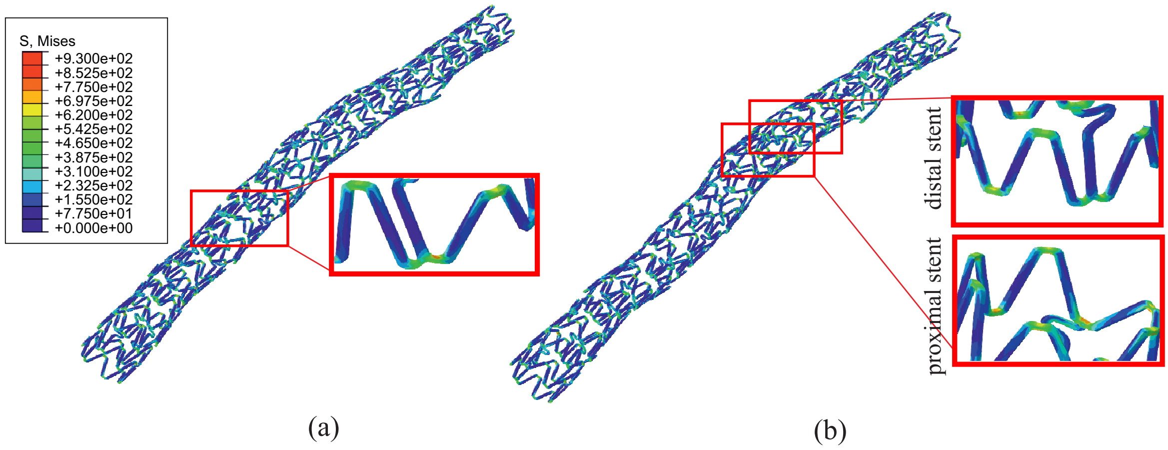

Figure 4.8 *Von Mises stress at the end of the stenting procedure: (a) the use of the one long stent produces an uniform distribution of the stent and remarkable stress results; (b) the application of the two short stents induces a not uniform distribution of the stress and, in particular, the proximal part of the coronary are more stressed than the otherwise.*

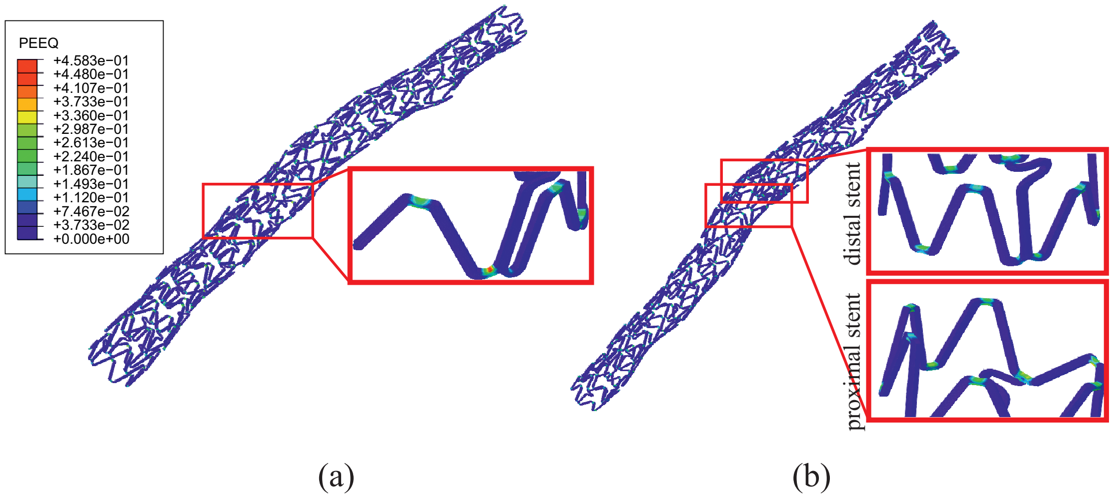

Figure 4.9 *PEEQ at the end of the stenting procedure: (a) PEEQ value at the final procedure, where the maximum PEEQ reaches value of 0.44 at the great bending of the stent strut; (b) PEEQ value at the final procedure, where the maximum PEEQ reaches value of 0.40 and 0.37 at the great bending of the distal and proximal stent strut, respectively.*

4.3.5 Evaluation of the stent apposition

Nowadays, the imaging techniques, such as the Optical Coherence Tomography (OCT) and Intra Vascular Ultra Sound (IVUS), allow to visualize *in-vivo* the geometrical configuration and distribution of the stent struts inside the vessel after the implant; unfortunately, these techniques are not always available and not easy to elaborate [106]. In this context, FEA simulations can provide quantitative information and a comprehensive visualization of the (predicted) final stent/vessel configuration [137]. For these reasons, we have quantitatively evaluated the distance between the stent surface and the lumen surface using the *vmtksurfacedistance* module of VMTK library (`http://www.vmtk.org`). As expected, the results suggests that in both stenting op-

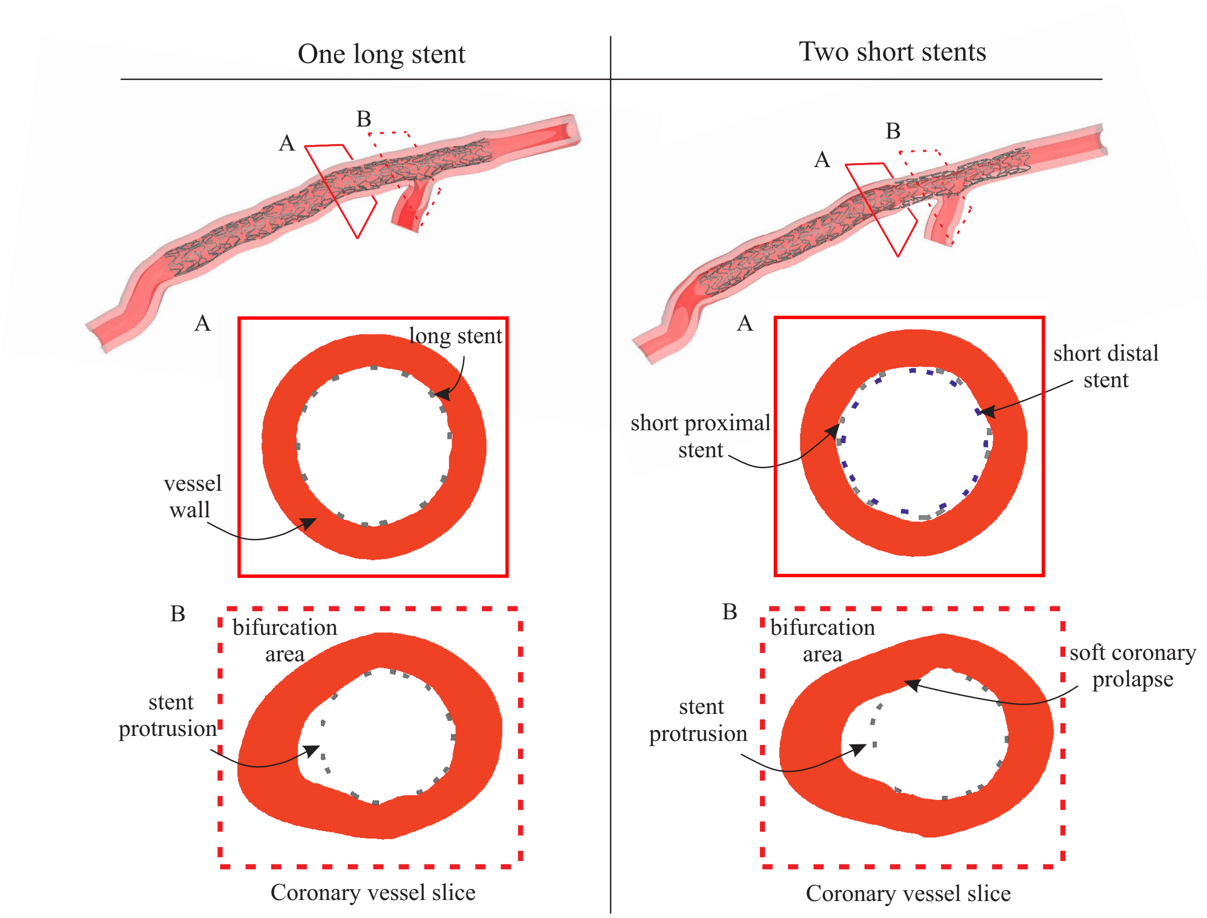

Figure 4.10 *Crossing slices of the stented coronary vessel (red) in the two stenting procedures to qualitatively evaluate the apposition inside the coronary lumen of the long stent (grey), the short proximal stent (blue) and the short distal stent (grey).*

tions the mean stent/lumen distance is negligible ($< 0.08mm$), except for the bifurcation area where the stent protrudes in the lumen of the coronary branch (see Figure 4.10 - B crossing slice). The stent configuration in this area at the end of the stenting procedure might cause hemodynamic problems due to the resistance offers to blood flow, as discussed also in [20, 41, 138].
The stent apposition proves to be an important measure index to quantitatively investigate for clinical aspects [139]. Figure 4.10 shows some crossing slices (A, B) of the stented coronary vessel to highlight the circumferential distribution of the stent struts in both the stenting procedures. In particular, in the overlapping zone of the two short stents, we can observe the apposition of the distal and proximal stent struts; whereas in the bifurcation area we can note how the stent protrudes in coronary lumen branch.

Chapter 5

Final Remarks

Within this research work, we have illustrated the dissertation which can be collocated in the area of computational biomechanics, as it exploits methods of computational imaging and mechanics to investigate several aspects of the 3D coronary artery modelling stenting and numerical stenting procedures from the X-Ray angiographic image elaboration.
The application of such a multidisciplinary approach has highlighted the use-fulness of using the simulations for both device evaluation and procedure planning.
In this chapter we briefly resume the obtained results to finally discuss the corresponding further developments.

5.1 Conclusions

Chapter 1 describes the coronary artery disease and the different imaging techniques to detect the atherosclerotic lesions: X-Ray angiography, computed tomography, magnetic resonance, intravascular ultra-sound and optical coherence tomography.
However, we exalt the use of the X-Ray angiographic images for the 3D coronary lumen reconstruction because this technique is the *gold standard* technique for accurately stenosis detection and currently available in clinical practice. Realistic geometrical models obtained from such a diagnostic tool represents the starting point for realistic simulations evaluated in this research work. Some imaging techniques are analyzed to perform the image segmentation and model reconstruction to objectify and quantify the anatomical features of the coronary artery tree.

Chapter 2 proposes a simple framework to generate 3D meshes of coronary bifurcations from a pair of planar angiographic images obtained by X-Ray coronary angiography. As also shown by the application of the framework to three real cases, the proposed approach represents a preliminary step toward the integration of clinical practice and numerical simulation through the generation in a fast and effective manner of the mesh grids, i.e., directly from the medical images used in the clinical practice. Moreover, we perform a tool suitable also to compute automatically some important clinical features, such as the coronary diameters, lumen area and stenosis degree. Finally, two validation tests are verified to show the goodness of the reconstruction approach adopted in this study.

Chapter 3 describes the numerical simulation of the stenting procedure through finite

element analysis from patient-specific coronary vessel models. The stenoted coronary meshes, which present a diffuse narrowed lumen along the left main branch, are generated from the image processing and the 3D reconstruction approach developed in this study. Moreover, material models able to reproduce anisotropy, thus including histological information, as well as physiological boundary conditions have to be considered aiming at virtually mimicking the coronary artery behavior.
Also the stent and the balloon models are performed from the elaboration of the images acquired by micro-CT tomography and modelled appropriately through the use of several softwares, i.e., Rhinoceros, ImageJ, Matlab and Abaqus/CAD.
We describe the numerical procedure and all the features which characterize the finite element analysis. Some considerations and hypotheses are adopted to perform the stenting procedure, such as boundary conditions, loading amplitude, balloon thickness and viscous pressure. Results show that at the end of the stenting procedure the coronary lumen of the vessels increases thanks to the apposition of the stent. It worth noting also several geometrical changes, which constitute important clinical factors because they are considered as reliable predictors of post-operative adverse cardiac events. Also, We focus the attention on the parametric results of the stent stress and strain and the maximum principal stresses of the coronary vessel to ensure that the maximum values reached are lower than threshold values. Hence, in this scenario, the evaluation of the post-stenting procedure through specific stent in a given patient is essential to know the suitable coronary treatment in order to increase the patient-outcome.
Finally, we compare the post-operative results in terms of geometrical changes, i.e., the coronary diameters, and the X-Ray angiographic images obtained after the percutaneous coronary intervention, achieving good and comfortable results.

In **Chapter 4**, we use the FEA to evaluate the performance of two different stenting procedures for long coronary lesions treatment, i.e., the long stent versus the two short stents deployment evaluating the bio-mechanical response of patient-specific coronary model generated by X-Ray angiographic images. We consider the maximum principal stress induced on the vessel wall, the vessel straightening and elastic recoil as measures of stenting impact on the vessel anatomy and finally the evaluation of the stent apposition on the artery wall. Regarding the final configuration of the vascular anatomy and the measured stresses both of the stent and of the vessel, the results suggest that the two analyzed stenting strategies differ considerably.
In particular, the implantation of one long stent has shown good results with respect to those of two short stents deployment: in fact, the stress values observed in the case of one long stent are lower than those measured in the case of two short stents strategy and their distribution is homogeneous along the coronary vessel wall, avoiding the neo-intimal hyperplasia generation, i.e., the abnormal cellular proliferation of the intimal layer. Good results in terms of stent apposition have been proved finally in the one long stent deployment with respect to that two short stents: well apposition of the stent struts avoids possible deposits of extra-cellular material and, thus, inflammatory response of the coronary lumen that contributes to intra-stent restenosis after pecutaneous coronary intervention.
Further, in the case of two short stents deployment the coronary stress values are higher and not homogeneous than the other case and the overlapped area of the two stents is critical during and after the clinical procedure. We have also focused the attention

on the parametric results of the stress and strain of the stent, which may contribute to the damage of polymeric coating of the stent and injury in the coronary lumen when the stent is placed during the balloon expansion. In particular, the higher stress and strain values are computed in the overlapped area of the two short stents.
Even though the investigation is limited to one stent design at different sizes and one coronary vessel anatomy, our study provides important results to compare quantitatively the two different surgical strategies through dedicated numerical simulations based on computational mechanics methods.

5.2 Future works

Although we have approached several aspects regarding the procedure of the bi dimensional segmentation and the three-dimensional reconstruction, this study has still some limitations calling for further developments as discussed in the following.
Flat detector rotation angle. Our approach considers two projected views acquired by varying the LAO/RAO angle, keeping stable the CAUD/CRAN angle, or vice-versa. This limits the degree of freedom of the operator during the image acquisition procedure, but at the same time simplify the 3D reconstruction procedure adopted in this study. For this reason, our approach in its present form could be adopted following a predefined protocol.
Noise spectrum information. Our algorithm implements a filtering procedure for noise removing without any evaluation of the noise spectrum data in the image. Further analyses about this aspect should be assessed to enhance such a topic.
Vessel wall reconstruction. X-Ray angiographic technique does not provide any information about the geometry and the composition of the atherosclerotic plaque or on the vessel wall thickness. Such an information can be derived by other techniques such Optical Coherence Tomography (OCT) and IntraVascular UltraSound (IVUS). In fact, the combination of the X-Ray angiography and OCT/IVUS imaging provides the necessary data both to reconstruct the vessel wall including the plaque and to know the composition of the atheroma [140]. In fact, once the 3D coronary artery is reconstructed from the X-Ray angiographic images, the artery could be registered with the corresponding OCT/IVUS pull-back series by appropriated algorithm based on the distance mapping, as also reported in [36].
Moreover, the procedure to generate the lumen and the vessel wall discussed in Section 2.3.5, does not allow to recreate asymmetric stenosis because the 3D lumen profile is defined by sweeping along the centerline a number of circular cross-sections having constant radius. Also in this case, combining the X-Ray angiography and OCT/IVUS imaging techniques would solve such a limitation, as reported in Schuurbiers et al. [84].
Although we have validated our approach with respect to two test-cases, comparing also the results of the 2D analysis with the data from a QCA workstation, other tests could be taken into account. For example, we can compare the 3D coronary model computed with our framework with the 3D vascular anatomy reconstructed from volumetric CTA images as reported by [63] and [141].
Stenotic palque. In this study the coronary vessel are generated without the plaque modelling but it is also necessary to mention that their inclusion in the vessel wall model requires a number of information that are not embedded in the angiographic

images.
In fact, even if the feasibility to generate patient-specific coronary models with atherosclerotic plaques based on images of *ex-vivo* tissue samples has been proved by Holzapfel et al. [93, 142], our study generates the 3D coronary model from X-Ray angiographic images which do not provide any information on the atherosclerotic plaques and the vessel wall thickness of the coronary arteries. Despite such a limitation, we have decided to keep this input for our vessel modelling because X-Ray angiography is the gold standard technique for lumen stenosis detection and the routine imaging procedure during coronary stenting. This is also the basic motivation why we are not considering for this study other approaches based on more sophisticated imaging techniques as OCT or IVUS, which could be used to assess the shape and size of atherosclerotic plaque within the coronary vessel wall [84]. In particular, combining the 3D profile of the coronary lumen, reconstructed from the X-Ray angiographic images, with OCT/IVUS pull-back series, registered by appropriate algorithms [36], is possible to generate accurate vessel models accounting for the localization of the plaques inside the coronary vessel wall. Unfortunately, such IVUS/OCT are not usually adopted in the clinical practice. Another approach to overcome the limitations imposed by the use of X-Ray angiography, is to add the information derived from coronary Computed Tomographic Angiography (CTA) [38], but the limited use of coronary CTA in the clinical routine limits the extensive use of this approach.
Constitutive model. The constitutive model of the stent has been performed by implementing a standard mechanical behaviour of the Cobalt-Chromium alloy, which is used to fabricate the medical device, because the data about the realistic behaviour of the stent are not provided due to the industrial policy. Hence, the results in terms of stent stress and strain may be considered only in a qualitative way.
Although the highlighted limitations can influenced the final stent/vessel configuration, given the comparative nature of our study, the obtained results are satisfactory. Clearly, future developments are necessary in order to provide more accurate results and further to validate the parameters introduced in the present study.
Boundary conditions. Our study neglects the vessel pressurization, the presence of residual stresses and of the surrounding heart muscle tissues. We are conscious that this modeling issues can certainly have an effect on the final simulation outcomes (e.g., stress distribution in the vessel wall, the straightening degree and the lumen gain) but, given the comparative purpose of this study, we believe that these analyses are acceptable.

5.3 Computational aspects and medical imaging

This research study focuses on clinically relevant problem, accounting for realistic modelling of the coronary stenting procedure from the elaboration of medical images.
The developed topic evaluates the useful of the images as support in the medical decisions and in 3D model reconstruction both to quantify better important clinical features of the complex anatomy of the coronary artery tree and to reproduce the components of the medical device. Such models are the starting point to reproduce numerically the stenting procedure. We model accurately the stent, the folded balloon and the vessel geometry and its mechanical response; moreover, the complexity of the analysis is able

to reproduce the key steps of the real procedure in the case both of the long stent deployment and of two short stents deployment. Our computational study on coronary artery disease propose three main analyses:

1. we consider a patient-specific coronary vessel model to study realist clinic cases of long coronary lesion;
2. we consider the coronary vessel composed of three layers, having an anisotropic mechanical behaviour and assigning the fibers orientation for each of them, and compare it with respect to isotropic behaviour in terms of stress results after the stenting procedure starting from the experimental data;
3. we compare the post-operative results, i.e., stress, straightening effect, stent apposition, elastic recoil of two specific surgical strategies for the long coronary lesions treatment through FEA method providing specific guideline to improve such a treatment.

Our study highlights an engineering approach in biomedical science, in particular for coronary stenting treatment to predict events and final results in order to overcome some clinical uncertainty offered by surgeons in the choice of the best stenting procedure to adopt from a given patient. The obtained results show good approximation of the realistic 3D model reconstruction and of the surgical stenting procedure, which are confirmed by the medical images acquired before and after the intervention. Hence, the analysis wants to encourage the use of the numerical simulation from medical images to investigate patient-specific cases for the coronary lesions treatment.

Appendix A

Gold standard technique for stenosis detection

A.1 Traditional X-Ray Coronary Angiography

Clinical methods to quantify coronary vascular anatomy have been explored in the *Chapter 1.* Each of them provides peculiar outcomes for the coronary artery reconstruction. Nevertheless, the X-Ray coronary angiography represents the sole current technique for lumen and stenosis detection, providing an accurate geometry of coronary anatomy [73, 74]. This technology is widely available, in fact there are many cardiologists well trained in the technique; moreover the image interpretation and the spatial/temporal resolution are unsurpassed and the diagnostic procedure can be easily transitioned into a therapeutic procedure [1, 42].
The number of diagnostic and therapeutic angiographic procedures are increased dramatically during the last several decades. Although it has been widely accepted and used, traditional angiography is limited by its two-dimensional representation of 3D structures and the consequent imaging artefacts that impair the optimal visualization of the images.
In Figure A.1, two projected views of X-Ray angiographic images are shown. It worth noting the multiple limitations of the traditional X-Ray angiography: the vessel segments are poorly visualized due to the overlap with adjacent branches and the true length of a segment could be misrepresented by the phenomenon of foreshorting. Unfortunately, such a technique is not standardized, subjectively chosen and highly depenrdent on the individual operators skills [54]. It has been shown that the visual assessment tends to underestimate coronary stenosis lesions 50% and to overestimate those more 50% [143]. Hence a quantitative assessment of coronary anatomy could allow to compute objectively the coronary features and to decide which specific measures of the device, e.g., balloon or stent, should be chosen for the PCI [32].

A.2 Quantitative Coronary Analysis (QCA)

Since the late 1980s, Quantitative Coronary Angiography (QCA) has been developed in order to objectively quantify the coronary artery disease [144]. It's based on one selected angiogram with the interactively identification of stenotic segment, as shown in Figure A.2, where the plots of diameter and area profiles associated with such a segment are computed automatically by the workstation. These advancements in medical imaging are critical for the continued improvement of patient outcomes in a complex interventions area, in particular for bifurcated coronary artery, as evaluated in several

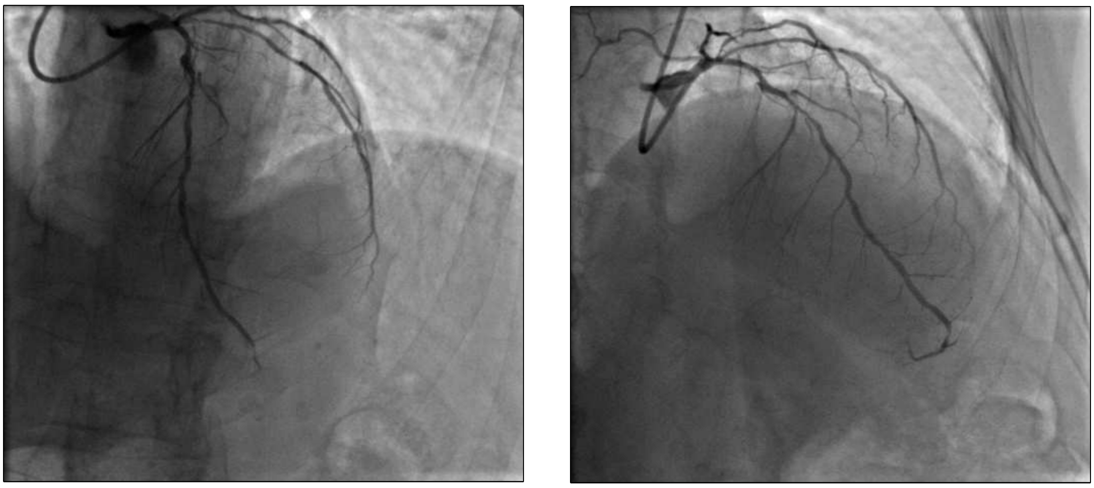

(a) (b)

Figure A.1 *Angiographic images acquired by X-Ray coronary angiography: (a) first and (b) second image represent two different projected views of a coronary tree selected at the same cardiac phase.*

studies [29, 31, 35, 44]. Thus, from a quantitative analysis, a number of techniques to estimate the 3D structure of coronary arteries with computer assistance have been developed.
Currently, 2D QCA is the most commonly used and validated imaging technique in interventional cardiology [42]. From the late decade, X-Ray imaging systems have been improved in terms of instrumentations [145] to increase the image quality. QCA system is able to compute the smaller diameter vessels and analyze both complex lesions and coronary morphology with irregular borders [146]. In the common clinical practice there are different validated computer systems for QCA, among them the most commonly employed are CAAS (PIE Medical, Maastricht, The Netherlands) and QAngio XA (Medis, Leiden, The Netherlands) [42]. Unfortunately, such procedures have still bi-dimensional limitations due to the vessel overlap and foreshorting during image acquisition [43, 85, 96], which are of particular interest in the evaluation of bifurcations owing to their complex geometric configuration. Furthermore, as reported in Di Mario et al. [147], the evaluation of complex geometries, such as long coronary lesions length with severe calcifications and tortuosity or bifurcation lesions, are difficult to be rendered with conventional 2D angiography.
Recently, advanced QCA analyses have been introduced to provide more accurate measurements of coronary vascular tree, evolving in a 3D coronary angiographic technique to overcome the 2D limitations [29, 31, 35, 44], yet facing challenges in the 3D analysis and model reconstruction of complex lesions, as evaluated in Rancharitar et al. [43], Wischgoll et al. [94], Louvard et al. [148].

Nowadays, 3D QCA programs, available in dedicated software, provide information of vessel size, percent diameter stenosis, minimal lumen diameter, bifurcation angle and other QCA values [78, 84]. Comparisons of 3D QCA programs to conventional 2D QCA programs have shown mixed results regarding the accuracy of this technology [35, 43, 78, 84, 149, 150]. The CardiOp-B system is an example of the 3D QCA, which

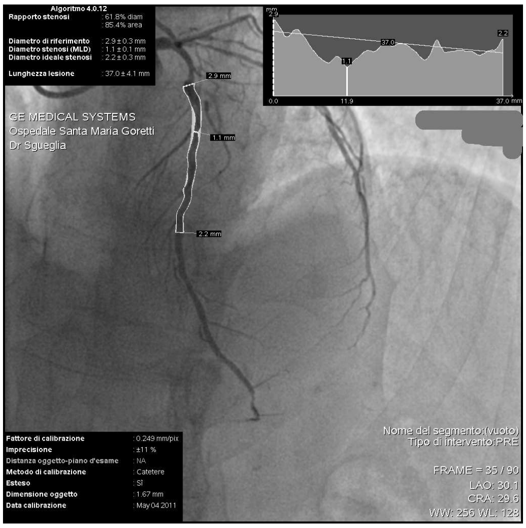

(a)

(b)

Figure A.2 *Projected views acquired by Quantitative Coronary Angiography (QCA): (a) first and (b) second are selected and analyzed to compute the main features.*

has been evaluated in the work of Dvir et al. [35]. Authors have reported a 3D reconstruction success rate of 83%, where the mean stenosis area was significantly smaller in the 3D reconstructions versus 2D images and the mean lesion length was significantly shorter. Such a result is due to the high and complex morphology of coronary vessel, where lesions are not visible. Thus, 3D reconstructions may be considered as an useful tool in coronary procedures to improve assessment of the coronary lesions characteristics [43].

Furthermore, 3D QCA analysis is able to follow the complex arterial curvilinear structure of the bifurcation and to select the most appropriate view to avoid foreshortening in the region of interest. As evaluated in Galassi et al. [45], 3D QCA allows a more appropriate imaging of bifurcation geometry, with respect to the 2D QCA.

Although there are multiple software programs dedicated for 3D QCA, only two software packages are dedicated for bifurcation analysis: the CardiOp-B system [35, 45] and the recent CAAS 5 QCA 3D bifurcation software [151]. As reported in such works, the main issue for the application of QCA in bifurcating segments includes: minimal user interaction in the selection and processing of the coronary segments to be analysed, minimal editing to determine the results, automatically, short analysis time, providing highly accurate and precise results, with small systematic and random errors. However, the 3D QCA techniques are widespread useful in the clinical practice because provide good results in terms of 2D visualization of the projected views and 3D reconstruction of the coronary vessel to quantify the surgical measures.

Appendix B

Medical image processing and elaboration

B.1 Introduction

In this chapter, we focus on some techniques adopted in the image processing, using specific operation yet implemented the software Matlab.
The aim is to describe the main image analyses from the image quality increasing to features computation both qualitatively and quantitatively in order to perform an appropriate reconstruction of the anatomical structures.
Following, we describe the main procedures of the image processing and elaboration for the 2D visualization and 3D modelling:

- image enhancement;
- image segmentation;
- quantification.

B.2 Image Enhancement

Image enhancement techniques improve the image quality and the visibility of its details, facilitating the diagnosis and treatment in clinical practice.
Generally, medical images are often deteriorated by noise due to various sources of interference and other phenomena that affect the measurement processes in imaging and data acquisition systems, as movement artefacts, signal processing etc.. In this scenario, accurate interpretation may become difficult if noise levels are relatively high, in particular where the distinction between normal and abnormal tissue is subtle.
Moreover, although some images are not much affected by noise, they have a limited contrast due to the nature and the superimposition of the soft tissues. Thus, the procedure to exalt or adjust the image contrast is another important aspect to follow.
The application of the image enhancement techniques increases the quality of medical images, improving the interpretation of the physician during the diagnosis and the treatment. Nevertheless, inappropriate techniques may increase noise while improving contrast, or eliminate small details and edge sharpness, or may produce artefacts in general. Indeed, such techniques have be applied carefully, especially in angiographic images that reproduce anatomical regions which are complicated to interpreter, like the anatomy of the coronary artery tree.

The quality of the X-Ray angiographic images depends on three main parameters, i.e., sharpness, contrast and noise: image contrast allows to discern the details in a low luminosity compared to the background, sharpness provides the finer details of the image and noise depends on the image spatial resolution, which is the ability to discern two points near with high-contrast.
The principal image enhancement techniques to elaborate angiographic images are:

- smoothing filter to reduce or delete the image noise with the use of *low pass filters*, which generate a smoothing of the image contours;
- sharpnening filter to improve the image sharpness and reduce the image blurring, with the use of *high pass filter*;
- grey-scale manipulation to improve and exalt the image contrast, with the use of a "windowing techniques", which modify the image histogram.

Smoothing filter. We can take into account two main *low pass filters* for noise removing, i.e., the median and the wiener filter.
The median filter reduces the amount of intensity variation between one pixel and its neighbour: the idea is replaced each pixel value with its median value. Figure B.1 (a) shows the original image of an Angio-CT axial mediastinum slice, where the section of aorta, superior vena cava and other blood vessels are depicted. The application of a mean filter cleans the original image to remove spurious elements into the image, reducing the noise and preserving the edges. In Figure B.1 (b) the median filter (3x3) generates a smoothing of the image contours, exalting some highlighted anatomical structure with respect to the background. The application of a filter n x n, with n increasing, provides an image with a growing smooth, losing, thus, some image information, which belong to the background (see Figures B.1 (c) and (d)).

Sharpening filter. Sharpness filter reduces the image noise and blur, improving the sharpness, but the image loses the principal information at the low frequencies, because the filter is an high pass filter. So for this image analysis, the high pass filter becomes difficulty to be used. In Figures B.2 (a) and (b), an example of the sharpness filter application.

Grey-scale manipulation. One of the characteristics of an image to analyze is the lightness of its pixels, i.e., the image luminosity. Figure B.3 shows the tone steps of the image, which consists in the image histogram, where every pixel belongs to each tone. This histogram has a fixed-height vertical axis, which is setted equal to the tone with the greatest frequency. The heights of the other bars are then setted relatively to the tone with the greatest frequency. Because the steps in this example are equal in size, i.e., they have the same number of pixels, the bars are equal in height. In Figures B.4 (a) and (b), an example of two histograms in a data range of [0 250] HU[1] are depicted: (a) the original image histogram, (b) the manipulated histogram one from a pixel data's saturation percentage (2%) at low and high intensities of the image, which

[1]Hounsfield Unit (HU) is a quantitative scale for describing radiodensity, which is computed as 1000 x $(\mu_x - \mu_{water})/\mu_{water}$, with μ_x is linear attenuation coefficient of the material and μ_{water} is the linear attenuation coefficients of water

(a)

Figure B.1 *CTA images of the mediastinum: (a) original image of a generic axial slice, (b) median filtering (3x3) applied to the original image; (c) median filtering (7x7) and (d) median filtering (9x9).*

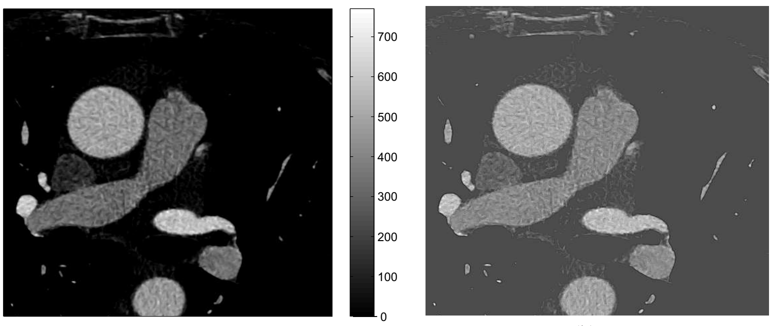

(a) (b)

Figure B.2 *High pass filtering procedure: (a) original image and (b) filtered image through the sharpening filter.*

is the elimination of the outliers. Hence, the window and the window center change in the new values. Such a procedure adopts a filtering method, i.e., *imadjust*, which is already implemented within the Matlab Image Processing Toolbox, showing only a part of the range of grey values of the image to exalt the contrast.

Medical images used in this study have a display range of [0 65535] HU. Hence, every images has an higher tone number depended by the image resolution. Once the image is update to image elaboration, the tool automatically changes the data range from such

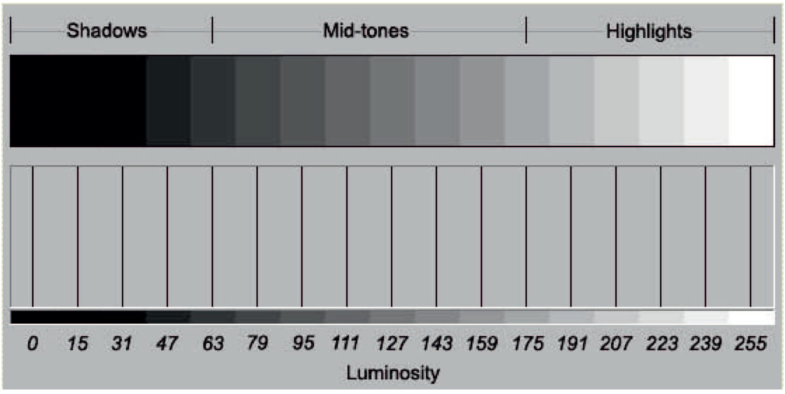

Figure B.3 *Luminosity values range from 0 (black) to 255 (white). Each of the 17 steps contains 2048 pixels, so the height of each bar underneath represents a count of 2048.*

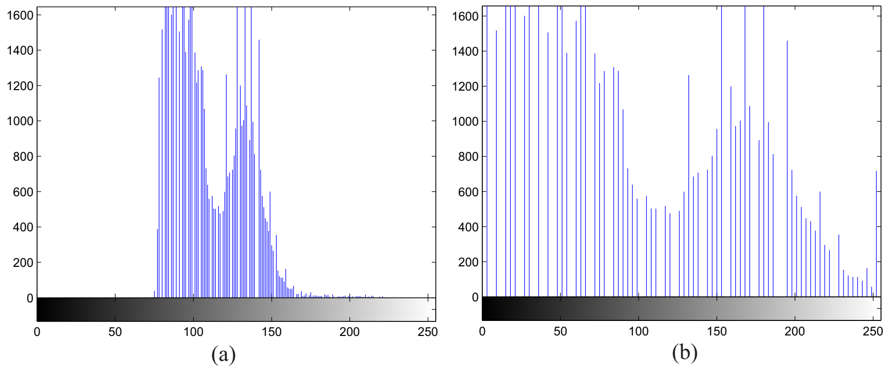

Figure B.4 *Grey-scale manipulation: (a) original image histogram; (b) manipulated histogram by th pixel data's saturation percentage (2%) at low and high intensities of the image.*

a range value to that [0 250] HU, to manipulate the value of the grey scale intensity. Then, at the end of each procedure of scale manipulation, the original range is restored. Figures B.5 (a) and (b) show an X-Ray angiographic image of a coronary artery and its image histogram, respectively, to improve and to exalt the image contrast. The tool *imadjust* enhances the contrast by mapping the intensity values in grey-scale image I to new values, I_c, such that 1% of data is saturated at low and high intensities of I, as shown in Figures B.6 (a) and (b). This increases the contrast of the output image I_c. We can note also the change of the window and the window center values. Finally the tool restores the initial data range, as illustrated in Figure B.6 (c).
In the case saturation's percentage equal to 50%, the image is more contrasted than the first one, as illustrated in Figures B.7 (a) and (b): the pixel number are spread in the all of the original data range, resulting in a strong dilation of the image contrast (Figure B.7 (c)).

B.3 Image Segmentation

The principal goal of the segmentation process is to subdivided the image into regions (also called classes or subsets) that are homogeneous with respect to one or more fea-

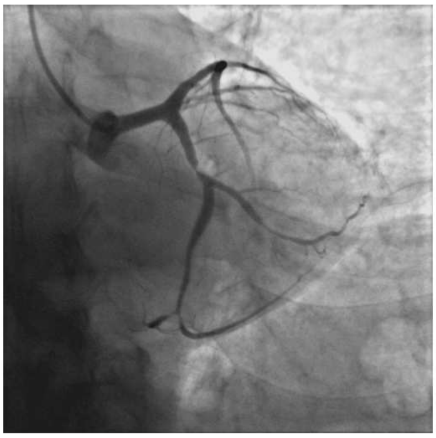

(a)

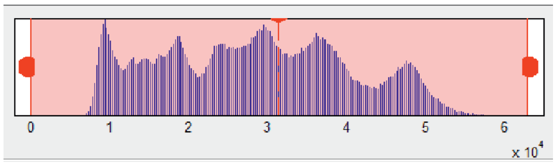

(b)

Figure B.5 *Image enhancement technique: (a) original X-Ray angiographic images of the left coronary artery and its left marginal artery; (b) histogram of the angiographic image.*

tures [152].
Segmentation is an important tool in medical image processing, and it has been useful in many applications, like features extraction, image measurements and image display. The our goal is the coronary contours detection in angiograms for quantitative and qualitative measurement, surgical planning, surgery simulations. In some applications it may be useful to classify image pixels into anatomical regions, such as bones, muscles and blood vessels, while in others into pathological regions, such as cancer, tissue deformities and multiple sclerosis lesions and 3D reconstruction. As an example, in the studies about the brain anatomy, the segmentation could detect different regions, i.e., the white matter, gray matter and cerebrospinal fluid spaces. The most commonly segmentation techniques can be classified into two main categories [153]:

1. region segmentation techniques that look for the regions satisfying a given homogeneity criterion;

2. edge-based segmentation techniques that look for edges between regions with different characteristics.

In this work, a thresholding technique, which is the common region segmentation method, has been chosen to segment the anatomical structures of interest [87]. In this technique, after the selection of a threshold value, the image is divided in groups of pixels having values less than the threshold and groups of pixels with values greater or equal to the threshold.
There are several thresholding methods based on the image histogram or local properties, such as local mean value and standard deviation or local gradient. The most intuitive approach is global thresholding: only one threshold is selected for the entire image, based on the histogram. If the threshold depends on local properties of some image regions, for example, local average gray value, thresholding is called local. If the local thresholds are selected independently for each pixel (or groups of pixels), thresholding is called dynamic or adaptive.

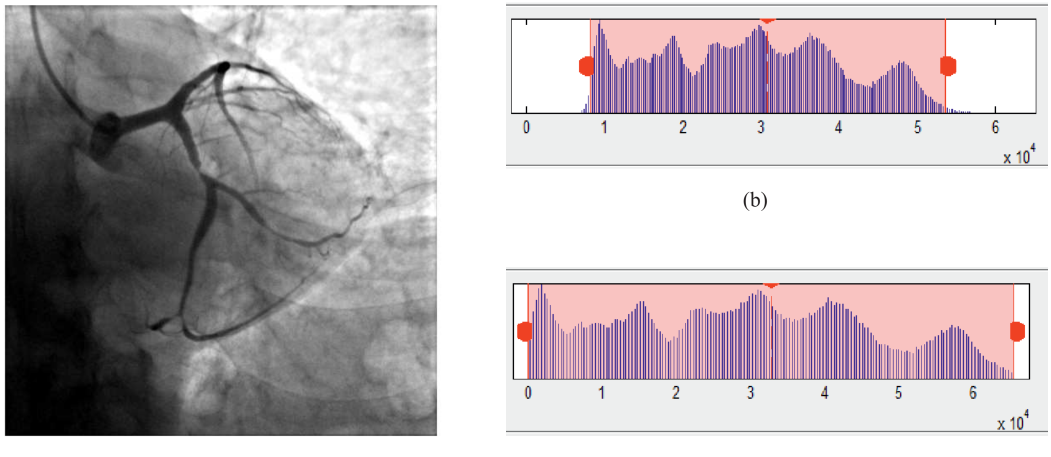

(a) (c)

Figure B.6 *Grey-scale manipulation procedure: (a) angiographic image after the application of the imjust tool to improve the contrast; (b) data saturation of 1% al low and high intensities of the original image; (c) the resulting image histogram.*

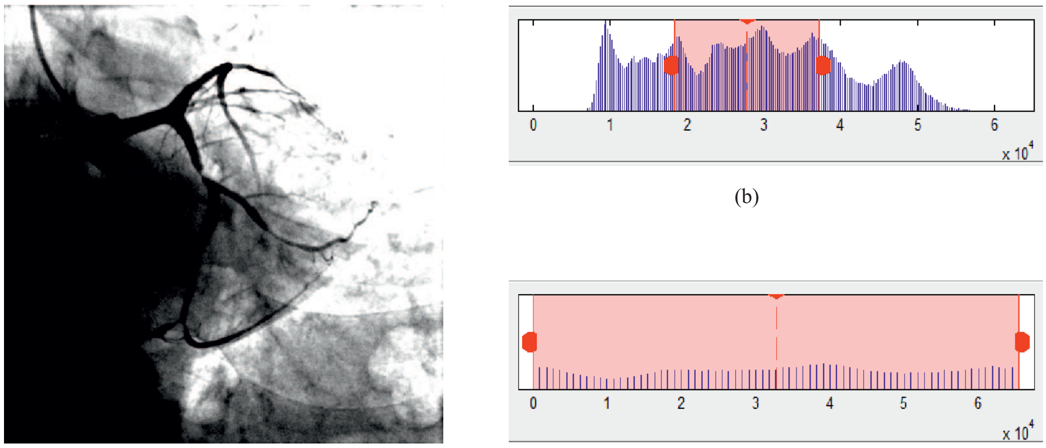

(a) (c)

Figure B.7 *Grey-scale manipulation procedure: (a) angiographic image after the application of the imjust tool to improve the contrast; (b) data saturation of 50% al low and high intensities of the original image; (c) the resulting image histogram.*

- Global thresholding.

Global thresholding is based on the assumption that the image has a bimodal histogram and, therefore, the object can be extracted from the background by a simple operation that compares image values with a threshold value T [88]. Suppose that we have an image f(x,y) with the histogram shown in Figure B.8. The object and background pixels have gray levels grouped in two dominant modes. One obvious way to extract the object from the background is to select a threshold T that separates these modes.

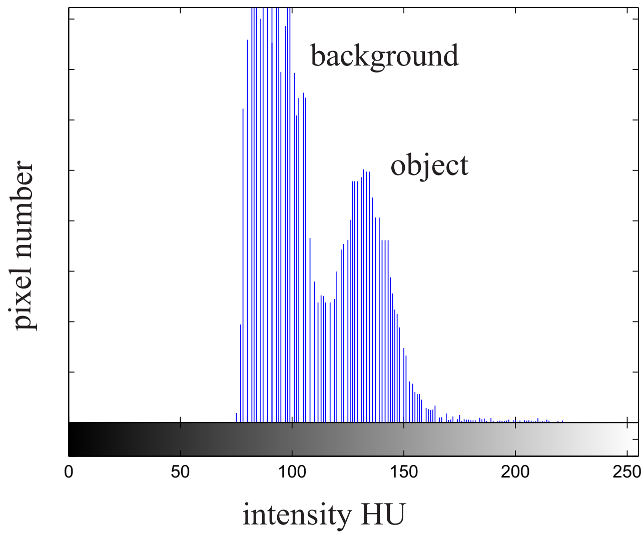

Figure B.8 *An example of bimodal histogram with selected threshold T.*

The thresholded image g(x,y) is defined as:

$$g(x,y) = \begin{cases} 1 & \text{if} \quad f(x,y) > T \\ 0 & \text{if} \quad f(x,y) \leq T \end{cases} \tag{B.3.1}$$

The result of thresholding is a binary image, where pixels with intensity value of 1 correspond to objects, whereas pixels with value 0 correspond to the background. As an example of a global thresholding and the application of the segmentation are shown in Figures B.9: the original image (Figure B.9 (a)) contains white cell on a black background, in a data range of [0 250] HU.

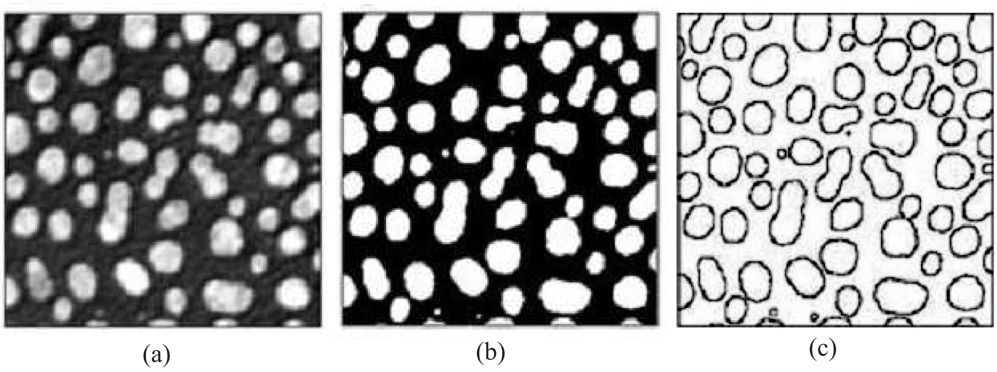

Figure B.9 *An example of global thresholding: original image; (b) result of thresholding with T=127 HU applied to the original image; (c) outline of the white borders after applying a 3x3 laplacian to the image (b).*

The threshold T=127 HU was selected as the minimum value between two modes and the result of segmentation is depicted in Figure B.9 (b), where pixels with intensity values higher than 127 HU are highlighted in white color. In the last step, the edges of the cells were obtained by a 3x3 Laplacian filter [87], which was applied to the

thresholded image to outline the image contours (Figure B.9 (b)).
Global thresholding is computationally simple and fast, working well on the images that contain objects with uniform intensity values on a contrasting background. However, it fails if there is a low contrast between the object and the background intensity varying significantly across the image. Figures B.10 show the result of the global thresholding technique of an Angio-TC image to visualize the carotid vessels, where we can obtain an approximative bimodal histogram.
The original image (Figure B.10 (a)) contains white lumen and other grey object on a black background; the threshold T=1.4 x 10^{-4} HU was selected as the minimum value between false two modes on a histogram in Figure B.10 (b), and the result of segmentation is shown in Figure B.10 (c), where pixels with intensity values higher than T are shown in white color.

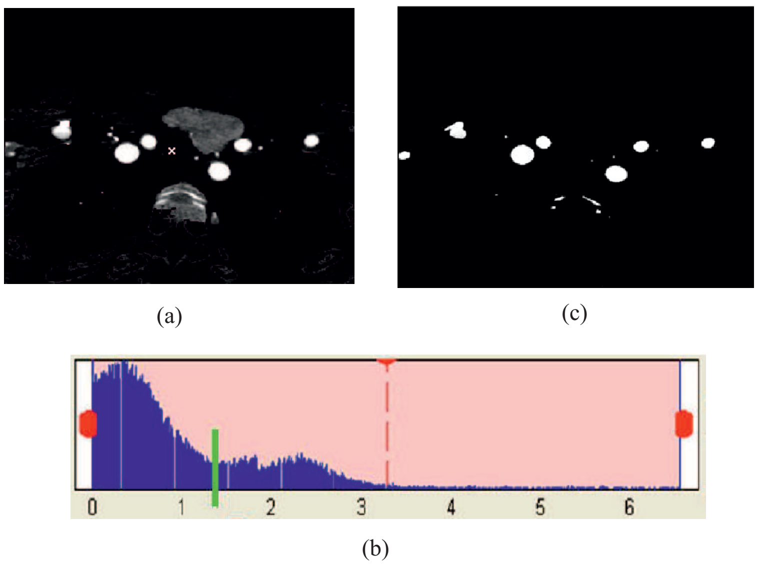

Figure B.10 *(a) Original image: axial slice of angio-CT scan, carotid vessels are shown in the image as a white circles; (b) bimodal histogram of the carotid angio-CT scan; (c) result of the local thresholding application to the original image, where the lumen of the vessel was isolated from the background.*

- Local or adaptative thresholding.

In many applications, a global threshold value cannot be determined from an histogram to provide a good segmentation result over the image due to the low contrast or fuzzy contours. An example is depicted in Figure B.11 (a): the background is not-uniform and the contrast of object is variable across the image. Thresholding technique may work well in one part of the image, but may produce unsatisfactory results in other areas.
Hence, we apply the local (adaptive) thresholding method [154, 155], where the threshold value can be selected using the mean value of the local intensity distribution, through the study of the histogram modes. The histogram modes, which correspond to the different types of regions in an image, may often overlap between them and, thus, the segmentation procedure by thresholding may become difficult. Image preprocessing

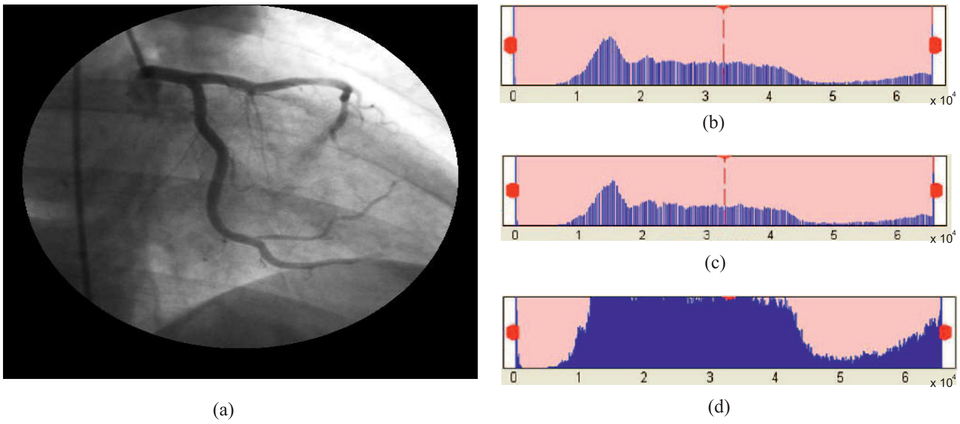

Figure B.11 *(a) Original image: X-Ray angiography scan of the coronary vessel. (b) Histogram of the original image: a non bimodal characterization is shown for the coronary image. (c) Median filter: histogram of the coronary image filtering. (d) Adaptive Filter: histogram of the coronary image filtering.*

techniques can sometimes help to improve the shape of the image histogram, making it bimodal.
Among such techniques, we can find the procedure of image smoothing using the mean or median filter. The mean filter replaces the value of each pixel by the average of all pixel values in a local neighbourhood (usually an N by N window, where N=3,5,7, etc.). In the median filter, the value of each pixel is replaced by the median value calculated in a local neighbourhood, preserving the edge contours without any blurring effect.
Figures B.11 (b)-(c)-(d) illustrate the histograms result of angiographic images processed using a local thresholding for the segmentation procedure. The computed histogram (Figure B.11 (b)) is unimodal: this precludes the selection of an appropriate threshold value. The median and the adaptative filters sharp differently the peaks of the image histogram and allow to select possible threshold values, as depicted in Figure B.11 (c) and (d), respectively; but both the procedures are not easy to implement due to the poor boundaries. Hence, another approach is required to segment the structures, which is based on the edges detection procedures.

- Edge Based Segmentation Technique.

Although the human eye can quickly locate the larger parts of the vessels in the input image, this task is not trivially implemented within the context of a computational model. There are several areas of the image background that, when locally viewed, are not readily distinguishable from vessel segments. For instance, physical objects present in the patient's chest, such as bone and muscle tissue, may appear in the X-Ray projection as artefacts which resemble to the blood vessel when viewed at a local scale.
The image edges or boundaries are discontinuity of the pixels intensity presented in the image. These edges are defined by the local pixel intensity gradient, which is an approximation of the first-order derivative of the image function. For a given image I(x,y), we can calculate the magnitude of the gradient as follows:

$$\nabla f = \begin{bmatrix} G_x \\ G_y \end{bmatrix} = \begin{bmatrix} \dfrac{\partial f}{\partial x} \\ \\ \dfrac{\partial f}{\partial y} \end{bmatrix} \tag{B.3.2}$$

The magnitude of this vector is

$$\nabla f = mag(\nabla \mathbf{f}) = \sqrt{\left[G_x^2 + G_y^2\right]} = \sqrt{\left(\frac{\partial f}{\partial x}\right)^2 + \left(\frac{\partial f}{\partial y}\right)^2} \tag{B.3.3}$$

To simplify the computation of the Equation B.3.3, the ∇f is approximated sometimes omitting the square-root operation, as follows,

$$\nabla f \approx \; G_x^2 + G_y^2 \tag{B.3.4}$$

or using the absolute values

$$\nabla f \approx |G_x| + |G_y| \tag{B.3.5}$$

These approximation still behave as derivatives: they are zero in area of constant intensity and their values are proportional to the degree of intensity which changes in areas whose pixel values are variable. It is common practice refers to the magnitude of the gradient or its approximations simply as "the gradient".
A fundamental property of the gradient vector is that it points in the direction of the maximum change rate of f at coordinate (x,y). The angle at which this maximum change rate occurs is the following

$$\alpha(x, y) = tan^{-}1\left(\frac{Gy}{Gx}\right) \tag{B.3.6}$$

Finally, to compute the image edges, proper function are used to estimate the derivatives G_x and G_y.
Second-order derivatives in image processing are also used to compute the image edges using the Laplacian operator. The Laplacian of a 2D function f(x,y) is the second-order derivatives of the function, which is defined as follows

$$\bigtriangledown^2 f(x, y) = \frac{\partial^2 f(x, y)}{\partial x^2} + \frac{\partial^2 f(x, y)}{\partial y^2} \tag{B.3.7}$$

The Laplacian is used for edges detection, but it is sensitive to noise and its magnitude produces double edges. However, such an operator can be a powerful complement when used in combination with other edge-detection techniques. The main idea to edges detection is to find places in an image where the intensity changes rapidly, using two principal criteria: (i) find the places where the first derivative of the intensity is greater in magnitude than a specified threshold; (ii) find places where the second derivative of the intensity has a zero crossing.
Since the peaks in the first order derivative correspond to zeros in the second order

derivative, the Laplacian operator, which approximates second order derivative, can also be used to detect edges [87, 153].
Hence, the Laplacian is combined with smoothing as a precursor to finding edges via zero-crossings. Consider the function

$$h(r) = -e^{-\frac{r^2}{2\sigma^2}} \tag{B.3.8}$$

where $r^2 = x^2 + y^2$ and σ is the standard deviation. Convolving this function with an image means smoothing the image, with the degree of blurring determined by the value of σ. The Laplacian of h, that is the second derivative of σ with respect to r is

$$\nabla^2 h(r) = -\left[\frac{r^2 - \sigma^2}{\sigma^4}\right] e^{-\frac{r^2}{2\sigma^2}} \tag{B.3.9}$$

This function is commonly known as the Laplacian of Gaussian (LoG) because the Equation B.3.8 is in the form of a Gaussian function. Since, the second derivative is a linear operation, convolving the image with the Gaussian smoothing function of Equation B.3.8 first and, then, computing the Laplacian of the result. Thus, the purpose of the Gaussian function in the LoG formulation is to smooth the image, reducing the noise, and the purpose of the Laplacian operator is to provide an image with zero crossings used to establish the location of the edges.
We want to detail such a procedure as follows: we suppose to have the following signal f(t), with an edge, as highlighted in Figure B.12 (a). If we take the gradient of this signal, which is in one dimension the first derivative with respect to time t, we get the result as shown in Figure B.12 (b).

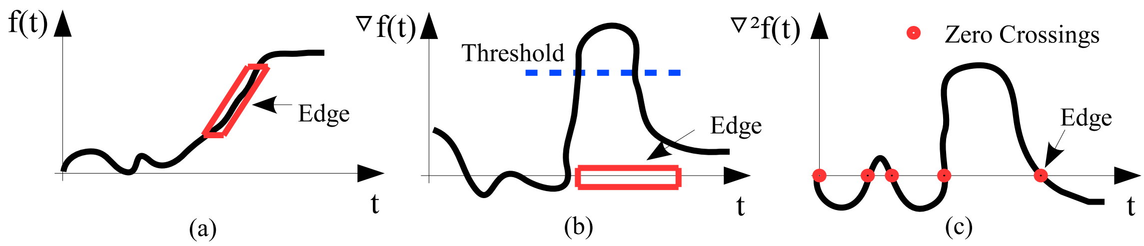

Figure B.12 *(a) One dimensional signal f(t): edge region corresponding to the jump to the slope. (b) The gradient of the Laplacian signal. (c) The localization of the edge at the zero-crossing point.*

Clearly, the gradient has a large peak centred around the edge and comparing the gradient to a threshold value, we can detect an edge whenever the threshold is exceeded. In this case, we have found the edge, but the edge has become *thick* due to the thresholding. However, since we know the edge occurs at the peak, we can localize it computing the Laplacian, which is in one dimension the second derivative with respect to t, and finding the zero crossings, as shown in Figure B.12 (c).
All the edges detection methods use a gradient operator, followed by a threshold operation on the gradient, in order to decide whether an edge has been found [88]. As a result, the output is a binary image, where around the contour line around the borders

are the edges. The general syntax for this function is:

$$[g, t] = edge(f, \texttt{method}, parameters) \tag{B.3.10}$$

where f is the input image, `method` is one of the methods used as edges detector and *parameters* are additional parameters. In this section, we describe three main edges detection operators used in this study to identify the lumen contours of the X-Ray angiographic images: Canny, Laplacian of Gaussian (LoG) and Zero-crossing operator [88].

Canny Edge detector.
The Canny detector is the most powerful edge detector provided by function *edge*. The method can be summarized as follows:

1. the image is smoothed using a Gaussian filter with a specific standard deviation, σ, to reduce the noise;
2. the local gradient $g(x, y)$ and the edge direction $\alpha(x, y)$ are computed at each point: any edge point is defined to be a point whose strength is locally maximum in the direction of the gradient;
3. the edge points computed in (2) give rise to ridges in the gradient magnitude image. Then, the algorithm tracks along the top of these ridges and sets to zero all the pixels that are not actually on the ridge top. The ridge pixels are then thresholded using two thresholds, T_1 and T_2, with $T_1 < T_2$. The ridge pixels with values greater than T_2 are declared as "strong", otherwise as "weak" edge pixels;
4. the algorithm performs edge linking by incorporating the weak pixels to that strong.

The syntax for the Canny edge detector is

$$[g, t] = edge(f, \texttt{canny}, T, \sigma) \tag{B.3.11}$$

where T is the vector $T = (T_1, T_2)$, σ is the standard deviation of the smoothing filter, having the default value equal to 1. If T is not provided, or it is empty, the *edge* chooses the value automatically. Setting T to 0 produces edges that are closed contours, a familiar characteristic of the LoG method.

Laplacian of Gaussian detector.
The LoG operator filters (or convolves) the image with $\nabla h(r)$. The key concept to underlying the LoG operator is that the convolution operator used in this procedure filters first the image with a smoothing function and then compute the Laplacian of the result. Marr and Hildreth (1995) proposed smoothing the image with a Gaussian filter before application of the laplacian [156]; such procedure is called Laplacian of Gaussian, LoG, as depicted in Figure B.13 (b). This approach was used by Goshtasby and Turner (1995) to extract the ventricular chambers in MR cardiac images [80].

Hence, the filter smooths the image reducing the noise and computes the Laplacian locating the edges through the calculation of the zero-crossings. The general calling syntax for the LoG detector is

$$[g, t] = edge(f, \texttt{log}, T, \sigma) \tag{B.3.12}$$

where σ is the standard deviation and the other parameters have been explained previously; the default value for σ is 2. As before, *edge* ignores any edges that are not stronger than T; the other parameters have been explained in the other methods.

Zero-Crossings detector.
This detector is based on the same concept as the LoG method, but the convolution is carried out using a specific filter function, H. The calling syntax is the following

$$[g, t] = edge(f, \texttt{zeroscross}, T, H) \tag{B.3.13}$$

The parameters have been explained for the LoG detector.

Figures B.13 show the results of the edges detectors described previously, which have been applied to the original image of Figure B.11 (a). Such results highlighted the coronary lumen contours including also some background pixels around the major blood vessels. Figure B.13 (a) shows the result of the coronary contours detection using the Canny operator: the filter forms some closed loop in the image, providing also in this case the good lumen contouring of the coronary tree. Figures B.13 (b) and (c) consist in the application of the LoG and Zero-crossing filters: the results are similar and both the filters are able to compute the coronary contours.

At the end of every edges detection procedure, the final result consists in a binary image: it worth noting that the contours are well identified and some small false edges, which are outer to the coronary vessel, are computed due to ripple and texture in the image. After the edges detection, it is possible to extract the morphological features of the coronary boundaries in the medical images through the “quantification procedure”.

B.4 Quantification

Quantification techniques are applied to extract the essential diagnostic information, i.e., shape, texture, size and angles of the arteries. Since the type of measurement and tissue vary considerably in angiographic imaging, numerous techniques that address specific applications have been developed. The quantification in two and three dimensional data, the use of shape transformations to characterize the structures and the arterial tree morphometry are some of the interesting tools to provide clinical information to the physicians.

Furthermore, the effectiveness of quantification depends significantly on the selection of the database and image features and the quantitative measures obtained from medical images are typically used for making decisions regarding the structure or function of the tissue and for the visualization of the anatomical structures.

Figures B.14 show the summarizing framework of the image processing: (a) the image enhancement through proper filters, (b) the edges detection of the coronary lumen

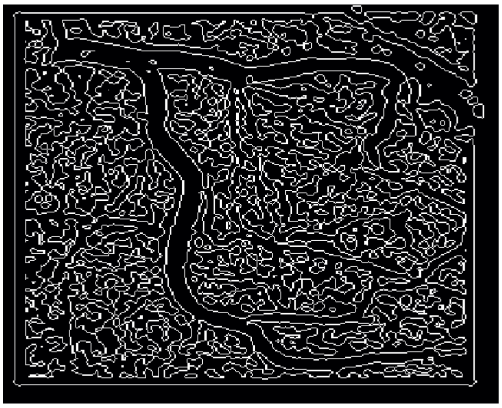

(a)

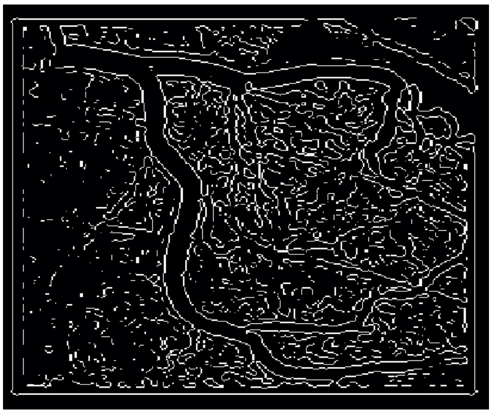

(b)

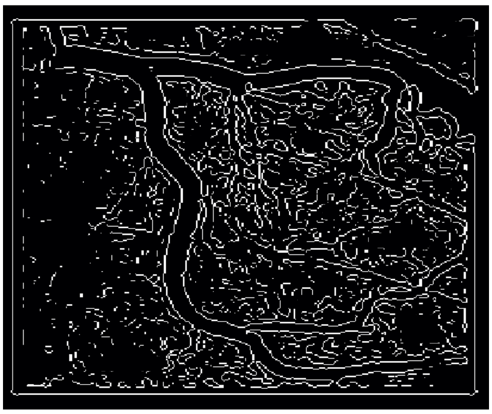

(c)

Figure B.13 *Edge detection of the coronary artery tree applied to the X-Ray angiographic image: (a) Canny, (b) Laplace of Gaussian and (c) Zero-crossing operators.*

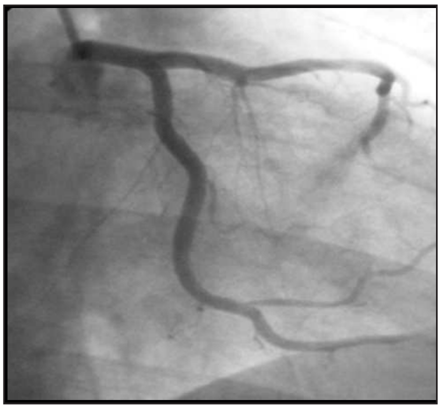

(a)

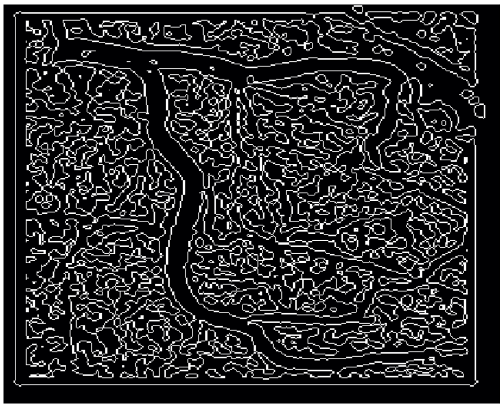

(b)

(c)

Figure B.14 *Image processing of the X-Ray angiographic image to segment the coronary tree: (a) image enhancement to adjust the image contrast and remove the noise, (b) edges detection procedure to find the lumen contours and (c) segmentation procedure to quantify the lumen size.*

contours and (c) finally the segmentation procedure to quantify the morphology of the coronary artery tree. Techniques for coronary artery quantification to compute its morphological and morphometrical aspects for coronary tree are detailed in the *Chapter 2*.

Appendix C

3D coronary artery material modelling

C.1 Introduction

Nowadays, the inclusion of the vessel wall has been recognized as central in coronary stenting modelling as well. The definition of constitutive laws for the vessel wall, including the dissimilar arterial layers, is often based on the work proposed by Holzapfel et al. [93], where results are adopted as a standard for modelling coronary arteries. In such a work, Authors firstly performed an experimental investigation of the passive mechanical properties of arterial strips from each of the three layers of human left anterior descending coronary arteries in both the axial and circumferential directions; secondly, they implemented specific constitutive laws for the description of the mechanical response of each tissue.

In particular, Mortier et al. [49] have reported the definition of constitutive law for the three layers of the coronary vessel wall, based on this work [93] to generate an anisotropic material enforced by two fibres families. Also Gastaldi et al. [47] have implemented a constitutive law for the three layers starting from experimental data, considering, however, the material of each layer as isotropic in a not patient-specific coronary artery model.

Nevertheless, pathological coronary arteries are characterized by the presence of atherosclerotic plaques which could strongly influence the mechanical behaviour of the arteries and the post-stenting structural outcomes [47, 157, 158]. Indeed, the mechanical properties exhibited by plaque tissue components are highly responsible for lumen widening after stent expansion. However, only a few studies involving stenting simulations considered their presence. Commonly, the constitutive laws used to model atherosclerotic plaques are based on the experimental data presented in Loree et al. [159], which found a large variation in the mechanical behaviour within each plaque type (cellular, hypocellular or calcified).

Other numerical studies considering the presence of plaque used isotropic hyperelastic [157, 158] or hyperelastic [47] constitutive models to describe in a simple way a mechanical behaviour that, in reality, is characterized by very complex phenomena such as rupture, plaque shift and delamination.

In the recent study of Morlacchi et al. [50], Authors investigated the clinical stenting options in bifurcated coronary arteries, which are considered as isotropic and homogeneous and the plaque positioning is only hypothesized and modelled as soft cellular plaque.

In this chapter, we describe the constitutive material artery modelling used and implemented in our numerical stenting simulations.

C.2 Constitutive material artery modelling

As discussed above, a main topic in cardiovascular solid mechanics is the mechanical and biological investigation of the coronary artery tissue in healthy and disease conditions to develop appropriate computational models behaviour for finite element analysis improving, thus, the numerical procedures [93].
Performing the constitutive equations of the coronary artery means to know its mechanical properties to achieve realistic numerical simulations, increasing, thus, the procedural planning results. In the last years, finite element analyses of coronary stents have been proposed in the literature from different constitutive models of the coronary arteries. Auricchio et al. [160] have reported the FEA of the stenting procedure considering the hyperelastic isotropic behaviour of the arteries: the numerical data provided by the constitutive model of the artery material proposed in this study have been compared with respect to the experimental data, showing a good approximation of the final results. Lally et al. [161] reported the study of the coronary stenting procedure assigned isotropic material parameters to the coronary artery, which are provided by experimental data of human femoral arterial tissue stress-strain. In the study reported by Gastaldi et al. [47], the material parameters of coronary artery have been computed for each layer, considering the arterial wall as heterogeneous and having anisotropic behaviour. Also, in the study of Mortier et al. [49], the stenting procedure has been investigated from heterogeneous and anisotropic coronary artery: for each layer, Authors reported the family-fiber reinforced model to reproduce carefully the mechanical behaviour of the coronary arteries.
The two-fiber reinforced hyperelasticity model has been developed for the first time in Holzapfel et al. [100] for the artery wall and its extension to fiber dispersion in Gasser et al. [7].
In this study, two different constitutive models have been considered to reproduce the mechanical behaviour of the coronary arteries from the experimental data provided by Holzapfel et al. [93]: **hyperlastic isotropic** and **anisotropic** material.

C.2.1 Biomechanical materials and testing

Experimental tests are fundamental to understand the arterial properties and to collect the parameters for the constitutive equations. A variety of methods have been used to determine the mechanical properties of blood vessels. They include classical tensile tests, inflation tests, torsion tests and pressure-diameter tests of tubular specimens.
In particular, the vessel wall is dissected and each layer is tested separately. However, dissection may cause unpredictable alteration of the vessel mechanical properties. In vitro tests typically focus on the behavior of tissue strips, rings or segments cut from the post mortem arterial wall. While, in vivo tests, which are often made complicated by the vascular anatomy, attempts to look at intact, in *situ* vascular segments, virtually undisturbed by surgical intervention.
From the histological point of view, as explained in Section 1.1 of the *Chapter 1*, the arterial wall is composed of three layers (*intima*, *media* and *adventitia*) and the arteries are surrounded by connective tissue made of elastin, collagen and smooth muscle cells.

In experimental and theoretical studies, under physiological conditions, arteries are regarded as nearly incompressible solids [162, 163]. The physiological range of the stresses in arterial tissue is assumed to be in the order of 50-100 kPa under the mean blood pressure of 100 mmHg [164].
Most of the studies have focused on the mechanical properties of animal coronary arteries [165, 166, 167, 168]. Unfortunately, some important processes of human arteries are not observed in the animals: as for example, in the human coronary, the arterial wall consists of a complex intimal layer that develops rapidly in early years and continues to grow gradually throughout life [169]; the intima has a distinctive organization of collagen fibers and exhibits considerable mechanical strength; the intima axial prestretch is much less for aged human arteries than for animal arteries [170]. Only a few in vitro data on the mechanical properties of human coronary arteries are available in the literature [171, 172, 173].
Furthermore, human coronary arteries with non-atherosclerotic intimal thickening comprise three layers; hence, to better understand the mechanical function of the artery tissue requires a layer-specific experimental approach and a design of constitutive descriptions, which can be implemented in numerical computations.
Vito et. al [174] have been the first to study separate mechanical response data for the media and adventitia from canine aorta from uni-axial strip tests in the axial and circumferential directions. Later, Richardson et al. [175] performed mechanical measurements during uni-axial tests of intima segments from the region between the left circumflex and left anterior descending (LAD) coronary arteries.
Holzapfel et al. [93] have reported the study of the mechanical response about the human coronary arteries to experimentally investigate the passive mechanical properties of the arterial strips from each layer of the human LAD coronary arteries. Authors have proposed an experimental approach for the determination of three-dimensional constitutive models to describe the mechanical response of the tissues. The study has been carried out through the uni-axial tensile of thirteen human coronary specimen which are tested in the axial and circumferential directions.
The coronary arterial wall consists of three layers (*intima*, *media* and *adventitia*) with different composition and structural organization [100, 101, 176, 177]. In each layer, it is possible to identify a double set of helicoidally-oriented collagen fibers immersed in an isotropic (non-collageneous) ground matrix. Such a multi-layer and collagen fiber organization confers to the coronary wall an heterogeneous and orthotropic structure, as highlighted in the experimental data reported in [93].
Constitutive models based on the theory of nonlinear hyper-elasticity are commonly used to describe the mechanical properties of soft biological tissues as the coronary artery tissue [101, 178]. In this context, the constitutive law is obtained by derivations of a strain energy function (SEF), Ψ, with respect to strain deformation tensors.
For isotropic material, the strain energy function depends on the change of configuration only through the deformation gradient $\boldsymbol{F}$. Material frame indifference satisfaction implies that SEF is a function of $\boldsymbol{F}$ only through the right Cauchy-Green tensor $\boldsymbol{C}$, i.e., $\Psi = \Psi(\boldsymbol{C})$ with $\boldsymbol{C} = \boldsymbol{F}^T\boldsymbol{F}$.
Following Spencer [179, 180], the strain energy function Ψ may be expressed as function of the three isotropic invariants of $\boldsymbol{C}$, i.e., I_1, I_2, I_3 defined as:

$$I_1 = \mathrm{tr}\boldsymbol{C}, \qquad I_2 = \frac{1}{2}[I_1^2 - \mathrm{tr}C^2], \qquad I_3 = \det \boldsymbol{C}. \tag{C.2.1}$$

$$\tag{C.2.2}$$

Then, we can write $\Psi = \Psi(I_1, I_2, I_3)$. If the material is assumed incompressible, i.e., $I_3 = det\boldsymbol{C} = 1$, the strain-energy function may be written as:

$$\Psi = \Psi(I_1, I_2) - p(I_3 - 1), \tag{C.2.3}$$

with p a Lagrange multiplier accounting for the incompressibility assumption.
For anisotropic material, the strain energy function Ψ besides depending on $\boldsymbol{C}$ depends on the collagen fibers trough the dyadic product $\boldsymbol{a}_0^i \otimes \boldsymbol{a}_0^i$ (the so-called *structural tensor*), where the unit vector $\boldsymbol{a}_0^i$ denotes the orientation of the ith fiber family in the reference configuration. In the particular case of two fiber families, we have $\Psi = \Psi(\boldsymbol{C}, \boldsymbol{a}_0^1 \otimes \boldsymbol{a}_0^1, \boldsymbol{a}_0^2 \otimes \boldsymbol{a}_0^2)$.
Following the invariant theory proposed by Spencer [179, 180], two additional anisotropic invariants are introduced for each fiber family. In particular, for the first fiber-family, the anisotropic invariants are:

$$I_4 = \boldsymbol{C} : \boldsymbol{a}_0^1 \otimes \boldsymbol{a}_0^1, \qquad I_5 = \boldsymbol{C^2} : \boldsymbol{a}_0^1 \otimes \boldsymbol{a}_0^1 \tag{C.2.4}$$

$$I_6 = \boldsymbol{C} : \boldsymbol{a}_0^2 \otimes \boldsymbol{a}_0^2, \qquad I_7 = \boldsymbol{C^2} : \boldsymbol{a}_0^2 \otimes \boldsymbol{a}_0^2 \tag{C.2.5}$$

It is worth noting that I_4 and I_6 represent the square of the stretch along the corresponding preferred direction, whereas I_5 and I_7 register shear deformations [181, 182]. Finally, a coupling invariant I_8 related to the pair of the two preferred directions ($\boldsymbol{a}_0^1$, $\boldsymbol{a}_0^2$) is defined:

$$I_8 = \boldsymbol{a}_0^1 \cdot \boldsymbol{a}_0^2[\boldsymbol{C} : sym \;\; \boldsymbol{a}_0^1 \otimes \boldsymbol{a}_0^2] \tag{C.2.6}$$

with the term $\boldsymbol{a}_0^1 \otimes \boldsymbol{a}_0^2$ included in Equation C.2.6 to ensure that I_8 is not affected by reversal of either a_0^1 or a_0^2. Merodio and Ogden [183] evidenced that the coupling invariant I_8 have a destabilizing effect on the stress-deformation and ellipticity of the governing equations, so that it should be considered carefully in the construction of constitutive models.
Moreover, as explained firstly by Humphrey and Yin [184] and later by Holzapfel and Ogden [185], if all the invariants are included in the SEF it is difficult to describe the most common features of anisotropic materials. In order to overcome this drawback, the invariants not strictly needed are omitted from the constitutive law.
For biological materials the influence on the strain energy of the matrix is described by the invariant I_1, whereas the influence of fibers is frequently assumed to be described by the fiber stretches, i.e., the invariants I_4 and I_6 [185, 186].

C.2.2 Strain energy functions

In this study, we consider a specific isotropic SEF and a specific anisotropic SEF commonly used to describe the passive mechanical behavior of arteries.

Regarding the **isotropic model**, we use a polynomial function of the sixth order depending on the invariants I_1, as follows:

$$\Psi_{iso} = \sum_{i=1}^{n} \boldsymbol{C_{i0}}(I_1 - 3)^i \tag{C.2.7}$$

where C_{i0} are material constants and $C_{00} = 0$.
Particularly, the expression of Equation C.2.7 refers to the reduced polynomial model (Yeoh) also reported in the Abaqus Documentation.
Regarding the **anisotropic model**, we use the strain energy function Ψ proposed by Gasser *et al.* [7] which is split into an isotropic part $\Psi_{iso}(I_1)$ associated to the elastin matrix and to an anisotropic part $\Psi_{aniso}(I_4, I_6)$ associated to the collagen fibers embedded in the matrix.

$$\Psi = \Psi_{iso}(I_1) + \Psi_{aniso}(I_4, I_6) - p(I_3 - 1), \tag{C.2.8}$$

The isotropic part is modelled by the neo-Hookean potential:

$$\Psi_{iso} = \frac{\mu}{2}(I_1 - 3) \tag{C.2.9}$$

with μ the shear modulus of the matrix.
The anisotropic part is modelled by an extended form of the exponential function of Tong and Fung [187], taking into account the fiber dispersion:

$$\Psi_{aniso} = \frac{k_1}{2k_2} \sum_{i=4,5} \left\{ \exp\left[k_2(\kappa I_1 + (1 - 3\kappa)I_i - 1)^2 \right] - 1 \right\} \tag{C.2.10}$$

with $k_1 > 0$ a stress-like parameter, $k_2 > 0$ a dimensionless parameter, and $\kappa \in [0, 1/3]$ the fiber distribution parameter. The limit $\kappa = 0$ and $\kappa = 1/3$ correspond to fibers perfectly aligned and to fibers randomly distributed, respectively.

C.2.3 Optimization method

Once an arterial model is defined, the correct identification of the material parameters involved in its expression represents the next step in constitutive modelling. The process of identification requires experimental data obtained usually from mechanical tests and the solution of an inverse problem using optimization algorithms [188].
The two investigated strain-energy functions are calibrated with respect to the experimental data, based on atherosclerotic human coronary arteries, reported in the work described in Holzapfel et al. [93]. In the present work, we refer to the experimental data of IX specimen for the adventitia, media and intima layers. Such a study [93] refers to uniaxial tensile tests performed on specimens of human coronary arteries excised in the circumferential and longitudinal directions.
With respect to the uniaxial tests the measured kinematic quantities are:

- traction in circumferential direction: λ_1, λ_2 from $\sigma_{22}(\lambda_1, \lambda_2)$=0, $\lambda_3 = \lambda_1^{-1}\ \lambda_2^{-1}$;
- traction in longitudinal direction: λ_2, λ_1 from $\sigma_{11}(\lambda_2, \lambda_1)$=0, $\lambda_3 = \lambda_1^{-1}\ \lambda_2^{-1}$;

We start from the non-zero components of the Cauchy stress tensor, σ_{11} and σ_{22}, which are given by:

$$\sigma_{11} = 2\Psi(\lambda_1^2 + (\lambda_1^2\lambda_1^2)^{-1}) + 2\Psi_4\lambda_1^2, \qquad \sigma_{22} = 2\Psi(\lambda_2^2 + (\lambda_1^2\lambda_1^2)^{-1}) \tag{C.2.11}$$

Noting that the Lagrange multiplier $p = 2\Psi(\lambda_1\lambda_2)^{-2}$ has been determined from the plain stress condition $\sigma_3 = 0$. Since we are considered the uni-axial tensile test and the stress $\sigma_{22} = 0$, it follows from the Equation C.2.11 that $\lambda_2 = \lambda_1^{-1/2}$ and, thus, the only one-zero stress component is σ_{11}, which is equal to $\sigma_{11} = 2\Psi(\lambda_1^2 + \lambda_1^{-1})) + 2\Psi_4\lambda_1^2$.

Assuming that the two fiber classes are mechanically equivalent such that $\psi_1 = \psi_2$, the non-zero components of the Cauchy stress tensor, σ_{11} and σ_{22}, the model prediction stresses are computed as follows:

- circumferential direction:

$$\sigma_{11}^{\psi} = 2\Psi_1(\lambda_1^2 + (\lambda_1^2\lambda_1^2)^{-2}) + 2\Psi_4\lambda_1^2 cos^2\theta, \qquad \sigma_{22}^{\psi} = 0 \tag{C.2.12}$$

  with $\psi_a = \dfrac{\partial\psi}{\partial I_a}(a = 1, 2, 4, 6)$

- longitudinal direction:

$$\sigma_{11}^{\psi} = 0, \qquad \sigma_{22}^{\psi} = 2\Psi_1(\lambda_2^2 + (\lambda_1^2\lambda_1^2)^{-2}) + 2\Psi_4\lambda_1^2 sin^2\theta \tag{C.2.13}$$

The directly measured static quantities are the stresses σ_{11}^{exp}, σ_{22}^{exp}, with $\sigma_{33}^{exp} = 0$ for the plane stress condition. The superscript "exp" stands for experiment. Usually, the measured quantities are considered free of errors.
The standard minimization technique requires the definition of the objective function χ^2 as squared sum of the residual, i.e., the squared sum of the difference between the experimental stress data and the corresponding theoretical values:

$$\chi^2 = \sum_{i=1}^{N}[w_1(\sigma_{11}^{exp} - \sigma_{11}^{\Psi})_i^2 + w_2(\sigma_{22}^{exp} - \sigma_{22}^{\Psi})_i^2] \tag{C.2.14}$$

with N the number of the data point, w_1 and w_2 are weighting factors, introduced to scale properly the term, which are referred to the circumferential and longitudinal experimental tests.
The minimization problem becomes:

$$\begin{cases} \min\limits_{\kappa} \chi^2(\kappa), \\ \text{subjected to:} \quad \kappa \in \mathcal{K}, \end{cases} \tag{C.2.15}$$

with $\kappa = \kappa : \kappa^- \leq \kappa \geq \kappa^+$ the solution space and κ^- and κ^+ the lower and the upper bounds for the material parameters, respectively. We have developed a simple code to implement the objective function C.2.14, whereas the minimization problem C.2.15

has been solved using a standard function within Matlab. The quality of the fitting procedure is evaluated computing the normalized mean square root error (NRMSE) proposed by Holzapfel et al. [93], as follows:

$$NRMSE = \sqrt{\frac{\chi^2}{p-q}}.\frac{1}{\sigma_{ref}} \tag{C.2.16}$$

with q the number of parameters and p the number of the data points. The value σ_{ref} is the sum of the all Cauchy stress for each data point divided by the number of all data points:

$$\sigma_{ref} = \frac{1}{p}\sum_{a=1}^{p}(\sigma_{11}^{exp} + \sigma_{22}^{exp}) \tag{C.2.17}$$

The five independent parameters, μ, k_1, k_2, κ and β, are computed minimizing an objective function χ^2.

The material parameters related to isotropic and anisotropic SEF are summarized in Tables C.1 and C.2, respectively.

C.2.4 Fiber orientation for anisotropic material

In this section, we describe the adopted procedure to assign an appropriate local coordinate system to each element of the coronary vessel mesh as required for the implementation of the anisotropic hyperelastic model available in Abaqus.

The implementation of the considered anisotropic model requires the definition of the fibers orientation for each element of the coronary arterial mesh. In the present work, such orientations are defined with respect to a proper local coordinate system.

If we consider the artery as a cylindrical tube, its geometry can be described by using a cylindrical coordinate system defined by three unit vectors e_1, e_2, e_3 which represent the radial, the circumferential and the axial direction, respectively. Under this idealization, collagen fibers are supposed to be symmetrically and helically disposed with respect to the circumferential direction [100, 189]: in the undeformed configuration, the fiber orientations are locally defined by two unit vectors a_{01} and a_{02} lying in the plane tangent to the cylindrical surface defined by the circumferential and the axial directions, e_2 and e_3. In this plane, the unit vectors a_{01} and a_{02} form constant angles $\pm\beta$ with respect to the circumferential direction. For this particular case, the components of the unit vectors a_{01} and a_{02} with respect to the cylindrical coordinate system (e_1, e_2, e_3) are:

$$a_{01} = (0, cos\beta, sin\beta), \qquad a_{02} = (0, cos\beta, -sin\beta) \tag{C.2.18}$$

Therefore, the definition of the fiber orientation is related to the definition of the local coordinate system e_1, e_2, e_3 and β.

According to the previous considerations, we can generalize the adopted approach to more complex geometries such as the coronary bifurcation (see Figure C.1 (a)). In view of the problem at hand, we define the vessel centerline as a sequence of segments, k, (see Figure C.1 (b)).

In the following, we summarize the approach by sixth steps:

1. the k-th centerline segment is assumed to be the local axis e_3;

2. identifying element i set and assembling to segment k ;
3. for each segment k of the centerline find the middle point M_k;
4. for each element i of the mesh find the barycentre G_i;
5. for each element i of the mesh compute the distance $\overline{G_i M_k}$;
6. assign element i to element set k which corresponds to the minimum of $\overline{G_i M_k}$.

Then, for each element i of element set k, the local basis e_1, e_2, e_3 is defined as follows:

- axial axis, e_3: this vector has the same orientation of the segment k defined by the points a_k and b_k of the centerline;
- radial axis, e_1: this vector lies in the plane defined by points G_i, a_k, b_k and is perpendicular to e_3; thus, e_1 has the direction of the segment $\overline{G_i H_k}$;
- tangential axis, e_2: this vector is obtained by computing the vector product e_2 x e_3.

Clearly, the three vectors e_1, e_2, e_3 are defined orthogonal and then normalized. Finally, the basis e_1, e_2, e_3 is properly rotated according the orientation of the element (see Figure C.1 (c)); this procedure is iteratively applied to identify a local cylindrical coordinate system for each element of the mesh (see Figure C.1 (d)). Given the local basis, the fiber orientation for each element is given by Equation C.2.18.
We implement the procedure for brick-like elements or 4-nodes planar elements but it can easily be adapted to triangular or tetrahedral meshes. Other procedures to automatically define the distribution of collagen fibers for models of vascular structures have been reported by Hariton et al. [190], Kiousis et al. [191] and Mortier et al. [49].

C.2.5 Verification of the implemented arterial model

In this section, we verified the good correspondence of model's predicted curves with respect to the experimental data by Holzapfel et al. (2005) for each layer of the coronary arterial wall. Such analyses are performed both for the isotropic and for anisotropic vessel material.

Isotropic material.

The material coefficients of the isotropic SEF of the coronary vessel model are computed through a polynomial strain energy function of the sixth order from the experimental data of the coronary artery's IX specimen provided by Holzapfel et al. [93].
The material parameters and the error measure are listed in Table C.1. The model's predicted curves are plotted in Figure C.2, highlighting a good correspondence with the experimental data.

Anisotropic material.

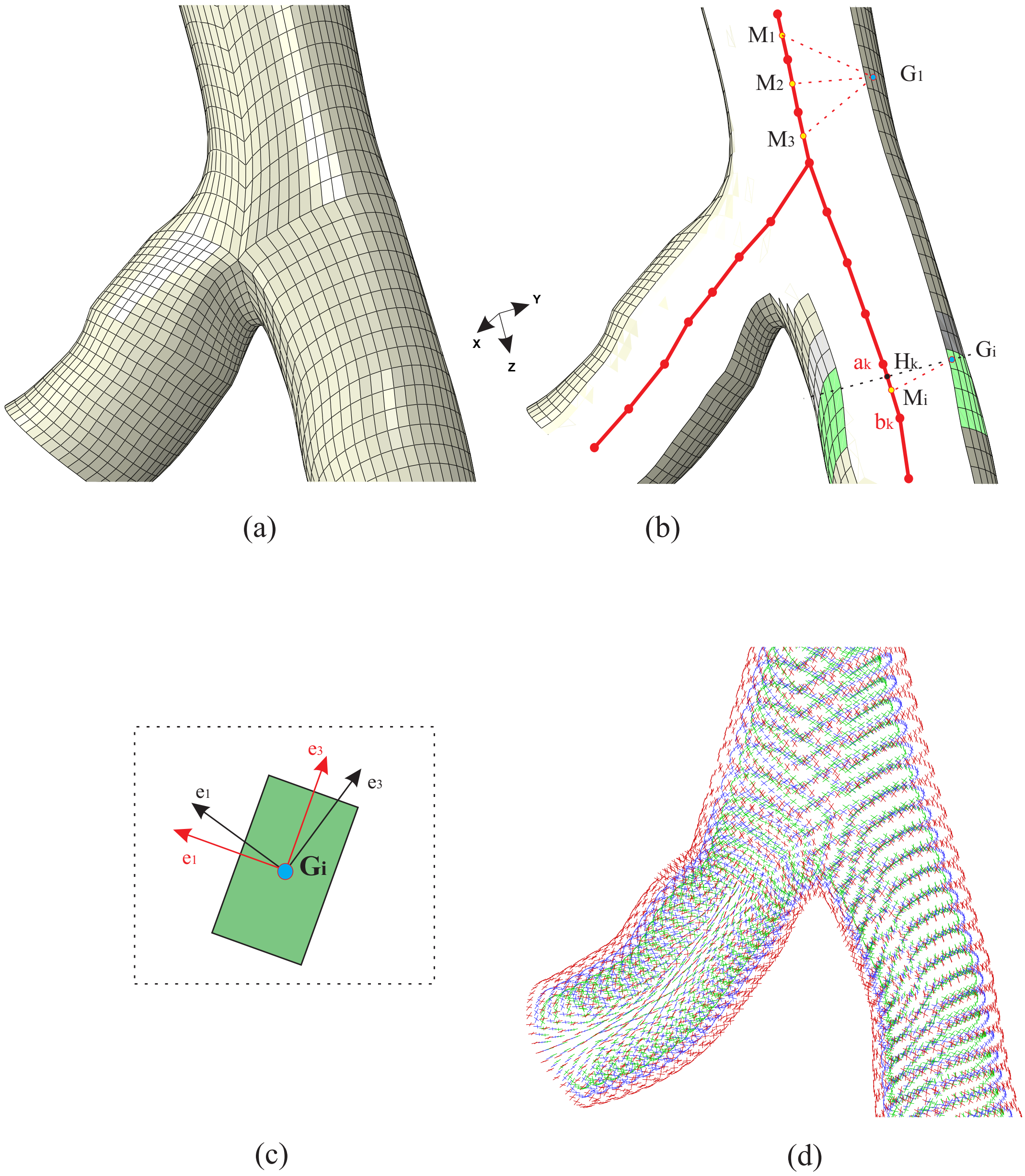

Figure C.1 *Fiber orientation for anisotropic material: (a) mesh of bifurcated coronary model; (b) example of local coordinate system definition; (c) local cylindrical coordinate system rotation to accomplish element orientation; (d) obtained collagen fiber distribution at bifurcation for intima (green crosses), media layer (blue crosses) and adventitia layer (red crosses).*

The results of the fitting procedure and the parameters used in this study from the IX specimen are depicted in Figure C.3 and illustrated in Table C.2: for each layer of the arterial wall, we highlight a good correspondence with the experimental data.
Then, we have computed the normalized mean square root error (NRMSE) to evaluated the fittings quality, following the Equation C.2.17.
Finally, the results of the simulated axial and the circumferential deformation in terms of Cauchy stress vs stretch show a good correlation for every layers with respect to the experimental curves provided by [93], which confirms the accuracy of the implemented

Layer	Material parameters						RMSE
	C_{10} (kPa)	C_{20} (kPa)	C_{30} (kPa)	C_{40} (kPa)	C_{50} (kPa)	C_{60} (kPa)	
I(IX)	34.7	95	1310	−34400	443000	−1370000	0.0034
M(IX)	1.27	22.5	−37.2	49.7	337	−337	0.000945
A(IX)	18.1	166	−2450	22900	−8430	0	0.0044

Table C.1 *Material coefficients the polynomial strain energy function (sixth order) obtained fitting the experimental data of human coronary artery (IX specimen) reported in Holzapfel et al. [93], for isotropic model.*

Layer	Material parameters					RMSE
	μ (kPa)	k_1 (kPa)	k_2 (-)	β (°)	κ (kPa)	
I(IX)	25.11	6812.60	3173.50	35.8	0.245	0.0251
M(IX)	2.80	70.78	85.58	34.5	0.282	0.0212
A(IX)	6.10	794.98	1502.30	53.4	0.251	0.0263

Table C.2 *Material parameters of human coronary artery (IX specimen) provided by the model proposed by Gasser et al. [7] from the experimental data of Holzapfel et al. [93] for anisotropic model.*

constitutive model adopted in this study.

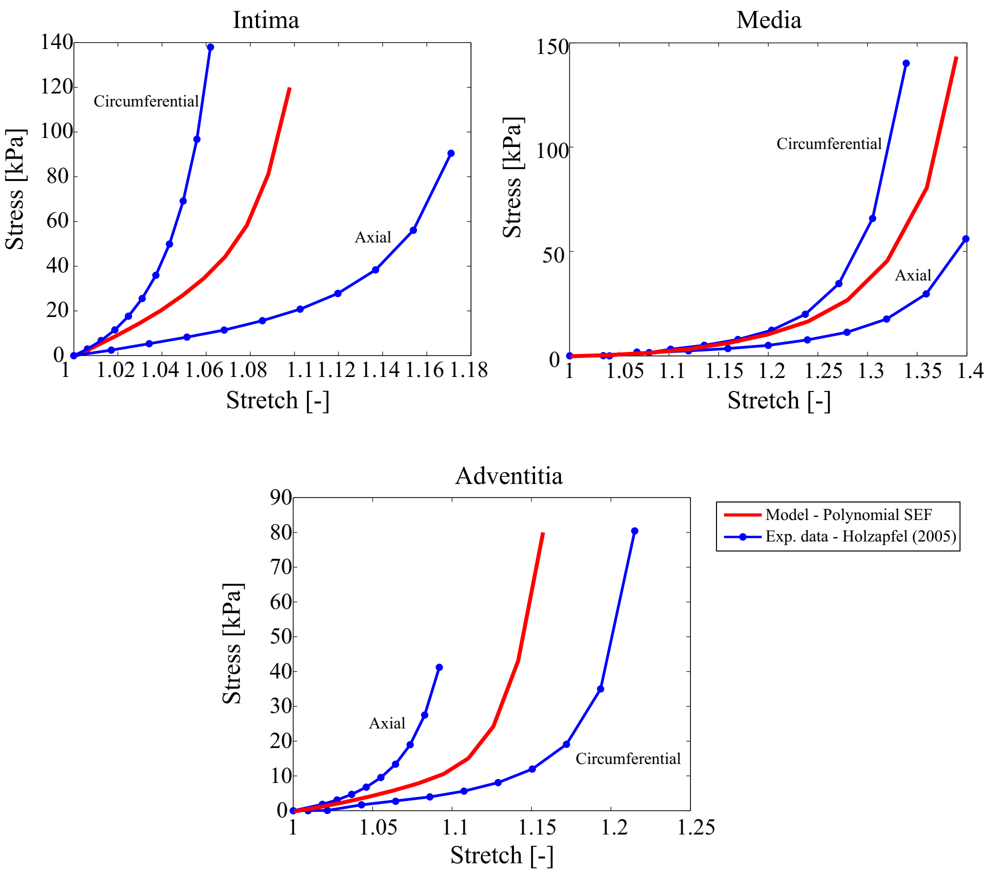

Figure C.2 *Circumferential and axial stress-stretch response of human coronary artery (IX speciem) reported by Holzapfel (2005) compared with respect to the isotropic model adopted in this study for the three layers.*

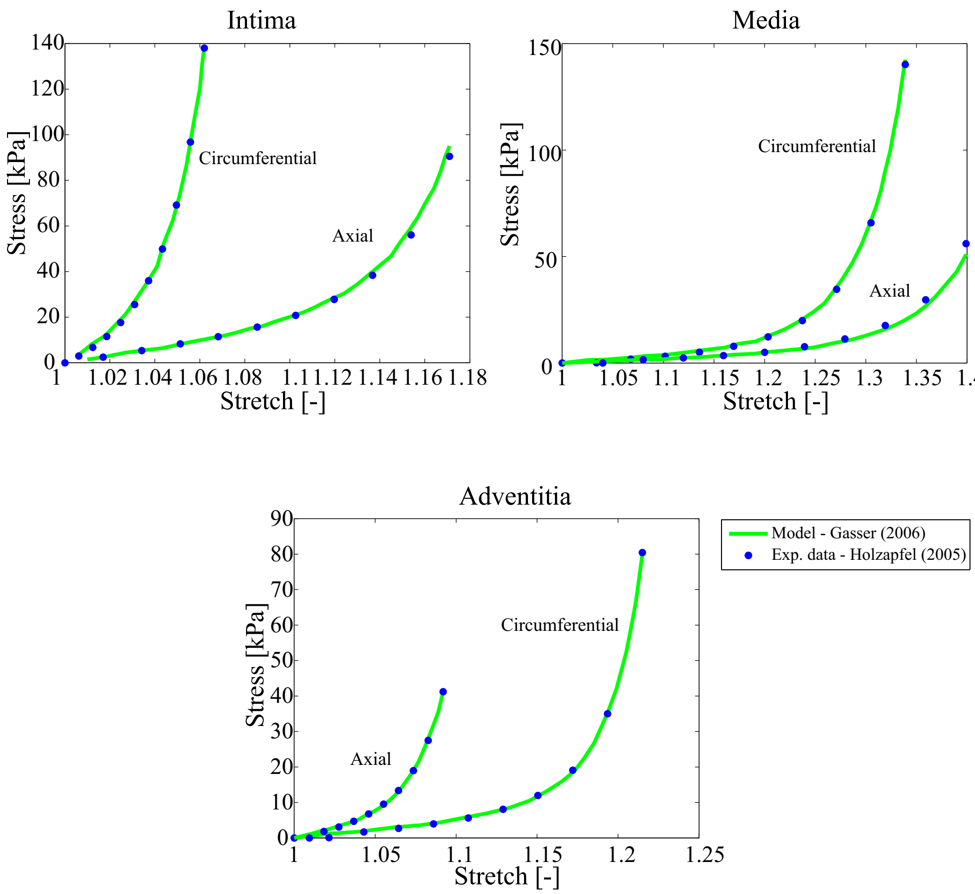

Figure C.3 *Circumferential and axial stress-stretch response of human coronary artery (IX speciem) reported by Holzapfel (2005) compared with respect to the models proposed by Gasser (2006) and implemented in this study for the three layers.*

List of Figures

List of Tables

Bibliography

[1] V.L. Roger, A.S. Go, D. M. Lloyd-Jones, R. J. Adams, J. D. Berry, T. M. Brown, M. R. Carnethon, S. Dai, G. de Simone, E. S. Ford, C. S. Fox, H. J. Fullerton, C. Gillespie, K. J. Greenlund, S. M. Hailpern, J. A. Heit, P. M. Ho, V. J. Howard, M. K. Brett, S. J. Kittner, D. T. Lackland, J. H. Lichtman, L. D. Lisabeth, D. M. Makuc, G. M. Marcus, A. Marelli, D. B. Matchar, M. M. McDermott, J. B. Meigs, C. S. Moy, D. Mozaffarian, M. E. Mussolino, G. Nichol, N. P. Paynter, D. Rosamond, P.D. Sorlie, R.S. Stafford, T. N. Turan, M. B. Turner, N. D. Wong, and J. Wylie-Rosett. Heart disease and stroke statistics 2011 update. a report from the american heart association. *Circulation*, 123:18–209, 2011.

[2] Elaine Nicpon. Marieb. *Human Anatomy & Physiology.* ISBN 0805354638. 6th edition, 2003.

[3] MedicaLook. Medicalook.com., editor. *Heart.* 05-03 2010.

[4] Pearson, editor. *Emergency Medical Responder: A Skills Approach.* Number ISBN 9780135004852. 3rd canadian edition, 2010.

[5] T. N. Wight. The extracellular matrix and atherosclerosis. *Current Opinion in Lipidology*, 6(5): 326–334, 1995.

[6] G. A. Holzapfel and R. W. Ogden. *The cardiovascular system: anatomy, physiology, and cell biology.*, volume Biomechanics of Soft Tissue in Cardiovascular Systems. J. D. Humphrey AND A. D. McCulloch., CISM, Udine., 2001.

[7] T. C. Gasser, R. W. Ogden, and G. A. Holzapfel. Hyperelastic modelling of arterial layers with distributed collagen fibre orientations. *Journal of the Royal Society Interface*, 3:15–35, 2006.

[8] B. M. Learoyd and M. G. Taylor. Alterations with age in the viscoelastic prop-erties of human arterial walls. *Circulation Research*, 18:278–292, 1966.

[9] H. Wolinsky and S. Glagov. Structural basis for the static mechanical properties of the aortic media. *Circulation Research*, 14:400–413, 1964.

[10] B. V. Shekhonin, S. P. Domogatsky, V. R. Muzykantov, G. L. Idelson, and V. S. Rukosuev. Distribution of type i, iii, iv and v collagen in normal and atheroscle-rotic human arterial wall: immunomorphological characteristic. *Collagen and Related Research*, 5:355–368, 1985.

[11] R. W. Ogden and C. A. J. Schulze-Bauer. *Phenonenological and structural as-pects of the mechanical response of arteries.* ASME., New York, 2000.

[12] Porth Study Guide. *Disorders of Blood Flow and Blood Pressure.* Chapter 18., 2012.

[13] G. A. Sgueglia, D. Todaro, and E. Pucci. Complexity and simplicity in percutaneous bifurcation interventions. *EuroIntervention*, 6(5):664–5, 2010.

[14] M. De Beule, P. Mortier, S. G. Cailer, B. Verhegghe, R. Van Impe, and P. Verdonck. Realistic finite element-based stent design: the impact of balloon folding. *Journal of Biomechanics*, 41: 383–389, 2008.

[15] G. De Santis, M. Conti, B. Trachet, T. De Schryver, M. De Beule, J. Degroote, J. Vierendeels, F. Auricchio, P. Segers, P. Verdonck, and B. Verhegghe. Haemodynamic impact of stent-vessel (mal)apposition following carotid artery stenting: mind the gaps! *Computer Methods in Biomechanics and Biomedical Engineering*, 2011.

[16] B. Balakrishnan, A. R. Tzafriri, P. Seifert, A. Groothuis, C. Rogers, and E.R. Edelman. Strut position, blood flow, and drug deposition, implications for single and overlapping drug-elunting stents. *Cuirculation*, 111:2958–2965, 2005.

[17] R. Balossino, F. Gervaso, F. Migliavacca, and G. Dubini. Effects of different stent designs on local hemodynamics in stened arteries. *Journal of Biomechanics*, 41(5):1053–1061, 2008.

[18] E. Cecchi, C. Giglioli, S. Valente, C. Lazzeri, G.F. Gensini, R. Abbate, and L. Mannini. Role of haemodynamic shear stress in cardiovascular disease. *Atherosclerosis*, 214(2):249–256, 2011.

[19] C. Chiastra, S. Morlacchi, S. Pereira, G. Dubini, and F. Migliavacca. Computational fluid dynamics of stented coronary bifurcations studied with a hybryd discretization method. *European Journal of Mechanichs - B/Fluid*, 35:76–84, 2012.

[20] E. Cutri, P. Zunino, S. Morlacchi, C. Chiastra, and F. Migliavacca. Drug delivery patterns for different stenting techniques in coronary bifurcations: a comparative computational study. *Biomechanics and Modeling in Mechanobiology*, 12:657–669, 2013.

[21] M. Lederlin, J.B. Thambo, V. Latrabe, O. Corneloup, H. Cochet, M. Montaudon, and F. Laurent. Coronary imaging techniques with emphasis on ct and mri. *Pediatric Radiology Journal*, 41(12): 1516–1525, 2011.

[22] P. Campadelli, E. Casiraghi, S. Pratissoli, and G. Lombardi. *Automatic abdominal organ segmentation from CT images.* PhD thesis, Department of Computer Science, Universita' degli studi di Milano., 2009.

[23] P. Schoenhagen, R.D. White, S.E. Nissen, and E.M. Tuzcu. Coronary imaging: angiography shows the stenosis, but ivus, ct, and mri show the plaque. *Cleveland Clinic Journal of Medicine*, 70(8):713–719, 2003.

[24] M.J. Budoff, S. Achenbach, and A. Duerinckx. Clinical utility of computed tomography and magnetic resonance techniques for noninvasive coronary angiography. *Journal American College of Cardiology*, 42(11):1867–1878, 2003.

[25] M.G. Friedrich. Current status of cardiovascular magnetic resonance imaging in the assessment of coronary vasculature. *Canadian Journal of Cardiology*, 26 Suppl A:51–55, 2010.

[26] http://www.osirix-viewer.com/.

[27] M. Prompona, C. Cyran, K. Nikolaou, K. Bauner, M. Reiser, and A. Huber. Contrast-enhanced whole-heart coronary mra using gadofosveset 3.0 t versus 1.5 t. *Academic Radiology*, 17(7): 862–870, 2010.

[28] S. J. Chen and J. D. Carroll. Coronary angiography. *Practical Signal and Image Processing in Clinical Cardiology, Springer-Verlag London Limited, Goldberger J.J. and Ng J., Chapter 13*, pages 157–185, 2010.

[29] S. J. Chen and D. Schaper. Three-dimensional coronary visualization, part i: Modelling. *Cardiology Clinics.*, 27:433–452, 2009.

[30] C. Blondel, G. Malandain, and R. Vaillant. Reconstruction of coronary arteries from a single rotational x-ray projection sequence. *IEEE Transactions on Medical Imaging*, 25:653–63, 2006.

[31] G. Schoonenberg, A. Neubauer, and M. Grass. Three-dimensional coronary visualization, part ii: 3d reconstruction. *Cardiology Clinic*, 27:453–465, 2009.

[32] T. Hirai and Y. Korogi. Pseudostenosis phenomenon at volume-rendered three-dimensional digital angiography of intracranial arteries: frequency, location, and effect on image evaluation. *Radiology*, 232:882–887, 2004.

[33] C.V. Bourantas, S. Garg, K.K. Naka, A. Thury, A. Hoye, and L.K. Michalis. Focus on the research utility of intravascular ultrasound - comparison with other invasive modalities. *Cardiolovascular Ultrasound*, 9(1):2, 2011.

[34] S.K. Zimmerman and J.L. Vacek. Imaging techniques in acutecoronary syndromes: a review. *ISRN Cardiology*, 359127, 2011.

[35] D. Dvir, H. Marom, and A. Assali. Bifurcation lesions in the coronary arteries: Early experience with a novel 3 dimensional imaging and quantitative analysis before and after stenting. *EuroIntervention*, 3:95–99, 2007.

[36] S. Tu, N. R. Holm, G. Koning, Z. Huang, and J. H. Reiber. Fusion of 3d qca and ivus/oct. *International Journal of Cardiovascular Imaging*, 27(2):197–207, 2011.

[37] C. J. Slager, J. J. Wentzel, J. C. Schuurbiers, J. A. Oomen, J. Kloet, R. Krams, C. von Birgelen, W. J. van der Giessen, P. W. Serruys, and P. J. de Feyter. True 3-dimensional reconstruction of coronary arteries in patients by fusion of angiography and ivus (angus) and its quantitative validation. *Circulation*, 102(5):511–516, 2000.

[38] R. Cardenes, J. L. Diez, I. Larrabide, H. Bogunovic, and A. F. Frangi. 3d modeling of coronary artery bifurcations from cta and conventional coronary angiography. *Medical Image Computing and Computer- Assisted Intervention*, 14:395–402, 2011.

[39] D. A. Steinman. Image-based computational fluid dynamics modeling in realistic arterial geometries. *Annals of Biomedical Engineering*, 30:483–497, 2002.

[40] C. A. Taylor and D. A. Steinman. Image-based modeling of blood floow and vessel wall dynamics: applications, methods and future directions. *Annals of Biomedical Engineering: sixth International Bio-Fluid Mechanics Symposium and Workshop, March 28-30, 2008 Pasadena, California.*, 38(3):11188–1203, 2010.

[41] J. Ormiston, M. Webster, S. Jack, D. MacNab, and S. Simpson Plaumann. The ast petal dedicated bifurcation stent: first in human experience. *Chateterization and Cadiovascular Interventions*, 70:335–340, 2007.

[42] P. Garrone, G. Biondi Zoccai, and I. Salvetti. Quantitative coronary angiography in the current area: principles and applications. *Journal of Interventional Cardiology*, 22:527–536, 2009.

[43] S. Rancharitar, Y. Onuma, J. P. Aben, C. Consten, B. Weijers, M. A. Morel, and P.W. Serruys. A novel dedicated quantitative coronary analysis methodology for bifurcation lesions. *EuroIntervention*, 3:553–557, 2008.

[44] D. Dvir, A. Assali, E. Lev, I. Ben Dor, A. Battler, and R. Kornowski. Percutaneous intervention in unprotected left main lesions: novel three-dimensional imaging and quantitative analysis befor and after intervention. *CardioVascular Revascularization Medicine*, 11:236–240, 2010.

[45] A.R. Galassi, S.D. Tomasello, and D. Capodanno. A novel 3d reconstruction system for the assessment of bifurcation lesions treated by the mini-crusch technique. *Journal of Interventional Cardiology*, 23:46–53, 2010.

[46] Y. Onuma, C. Girasis, J.P. Aben, G. Sarno, N. Piazza, C. Lokkerbol, M.A. Morel, and P.W. Serruys. A novel dedicated quantitative coronary analysis methodology for bifurcation lesions. Technical report, EuroIntervention, 2011.

[47] D. Gastaldi, S. Morlacchi, R. Nichetti, C. Capelli, G. Dubini, L. Petrini, and F. Migliavacca. Modeling of provisional side-branch stenting approach for the treatment of atherosclerotic coronary bifurcations: effects of stent positioning. *Biomechanics and Modeling in Mechanobiology*, 9: 551–561, 2010.

[48] F. Auricchio, M. Conti, S. Marconi, A. Reali, J. L. Tolenaar, and S. Trimarchi. Patient-specific aortic endografting simulation: From diagnosis to prediction. *Computers in Biology and Medicine*, 43:386–394, 2013.

[49] P. Mortier, G. A. Holzapfel, M. De Beule, D. Van Loo, Y. Taeymans, P. Segers, P. Verdonck, and B. Verhegghe. A novel simulation strategy for stent insertion and deployment in curved coronary bifurcations: comparison of three drug-eluting stents. *Annals of Biomedical Engineering*, 38: 88–99, 2010.

[50] S. Morlacchi, S.G. Colleoni, R. Cardenes, C. Chiastra, J.L. Diez, I. Larrabide, and F. Migliavacca. Patient-specific simulations of stenting procedures in coronary bifurcations: two clinical studies. *Medical Engineering and Physics*, 35(9):1272–1281, 2013.

[51] L. Goubergrits, E. Wellnhoufer, U. Kertzscher, K. Affels, C. Petz, and H.C. Hege. Coronary artery wss profling using a geometry reconstruction basedon biplane angiography. *Annals of Biomedical Engineering*, 37:682–691, 2009.

[52] G. De Santis, P. Mortier, M. De Beule, P. Segers, P. Verdonck, and B. Verhegghe. Patient-specific computational fluid dynamics: structured mesh generation from coronary angiography. *Medical and Biological Engineering and Computing*, 48:371–380, 2010.

[53] S. Salles, F. P. Salvucci, and D. Craiem. A reconstruction platform for coronary arteries, finite element mesh generation and patient specific simulations. In SABI, editor, *Journal of Physics*, number 012048 in 332. IOP Publishing Ltd, 2011.

[54] E.J. Topol and S. E. Nissen. Our preoccupation with coronary luminology. the dissociation between clinical and angiographic findings in ischemic heart disease. *Circulation*, 92:2333–2342, 1995.

[55] L. Antiga. *Patient-specific modelling of geometry and blood flow in large arteries.* PhD thesis, Politecnico di Milano, 2002.

[56] F. J. Gijsen, F. Migliavacca, S. Schievano, L. Socci, L. Petrini, A. Thury, J. J. Wentzel, A. F. van der Steen, and P. W. Serruys. Simulation of stent deployment in a realistic human coronary artery. *Biomedical Engineering*, 7:23, 2008.

[57] N. Gonzalo, H. M. Garcia-Garcia, E. Regar, P. Barlis, J. J. Wentzel, Y. Onuma, J. Ligthart, and P. W. Serruys. In vivo assessment of high-risk coronary plaques at bifurcations with combined intravascular ultrasound and optical coherence tomography. *JACC Cardiovascular Imaging*, 2(4): 473–482, 2009.

[58] A.G. van der Giessen, M. Schaap, F. J. Gijsen, H. C. Groen, T. van Walsum, N. R. Mollet, J. Dijkstra, F. N. van de Vosse, W. J. Niessen, P. J. de Feyter, A. F. van der Steen, and J. J. Wentzel. 3d fusion of intravascular ultrasound and coronary computed tomography for in vivo wall shear stress analysis: a feasibility study. *International Journal of Cardiovascular Imaging*, 26(7):781–796, 2010.

[59] C.P. Pellot, A. Herment, and M. Sigelle. A 3d reconstruction of vascular structures from two x-ray angiograms using an adapted simulated annealing algorithm. *IEEE Transaction Medical Imaging*, 13(1):49–60, 1994.

[60] T. V. Nguyen and J. Sklansky. Reconstructing the 3-d medial axes of coronary arteries insingle-view cineangiograms. *IEEE Transactions on Medical Imaging*, 13:61–73, 1994.

[61] K. Sprague, M. Drangova, G. Lehmann, P. Slomka, D. Levin, B. Chow, and R. deKemp. Coronary x-ray angiographic reconstruction and image orientation. *Medical Physics*, 33:707–718, March 2006.

[62] K. Haris, N. Serafim Efstratiadis, N. Maglaveras, and Costas Pappas. Model-based morphological segmentation and labeling of coronary angiograms. *IEEE Transactions on Medical Imaging*, 18: 1003–1015, 1999.

[63] J. Messenger, J. Chen, D. Carroll J.E.B. Burchenal, K. Kioussopoulos, and B. Groves. 3d coronary reconstruction from routine single-plane coronary angiograms: Clinical validation and quantitative analysis of the right coronary artery in 100 patients. *The International Journal of Cardiac Imaging*, 16:413–427, 2000.

[64] P. Radeva, R. Toledo, C. Von Land, and J. Villanueva. 3d vessel reconstruction from biplane angiograms using snakes. *Computing in Cardiology*, pages 773–776, 1998.

[65] M. Garreau, J.L. Coatrieux, and R. Collorec. A knowledge-based approach for 3d reconstruction and labeling of vascular networks from biplane angiographic projections. *IEEE Transaction Medical Imaging*, 10(2):122–31, 1991.

[66] J. Christianens, R. Van de Walle, P. Gheeraert, Y. Taeymans, and I. Lemahieu. Determination of optimal angiographic viewing angles for qca. In *International Congress Series.*, 2001.

[67] C. V. Bourantas, I. C. Kourtis, M. E. Plissiti, D. I. Fotiadis, C. S. Katsouras, M. I. Papafaklis, and L. K. Michalis. A method for 3d reconstruction of coronary arteries using biplane angiography and intravascular ultrasound images. *Computerized Medical Imaging and Graphics*, 29:597–606, December 2005.

[68] G. Tommasini, P. Rubartelli, and M. Piaggio. A deterministic approach to automated stenosis quantification. *Chateterization and Cadiovascular Interventions*, 48:435–445, 1999.

[69] I. Liu and Y. Sun. Fully automated reconstruction of 3d vascular tree structures from two orthogonal views using computational algorithms and production rules. *Optical Engineering*, 31 (10):197–207, 1992.

[70] R. Kemkers, J. De Beek, and H. Aerts. 3d-rotational angiography: first clinical application with use of a standard philips c-arm system. *Proceedings Computer Assisted Radiology and Surgery*, pages 182–187, 1998. Tokyo.

[71] J. Moret, R. Kemkers, and J. Beek. 3d rotational angiography: clinical value in endovascular treatment. *Medicamundi*, 42(3):8–14, 1998.

[72] A.B. Merle, G. Finet, J. Lienard, and I.E. Magnin. 3d reconstruction of the deformable coronary tree skeleton from two x-ray angiographic views. *Computers in Cardiology*, pages 756–760, 1998.

[73] S.Y.J. Chen and J.D. Carroll. On-line 3d reconstruction of coronary arterial tree for optimization of visualization strategy using a single-plane imaging system. *IEEE Transactions on Medical Imaging*, 19(4):318–36, 2000.

[74] S. J. Chen and J. D. Carroll. 3-d reconstruction of coronary arterial tree to optimize angiographic visualization. *IEEE Transactions on Medical Imaging*, 19:318–336, 2000.

[75] R. Gradaus, K. Mathies, G. Breithardt, and D. Bocker. Clinical assessment of a new real time 3d quantitative coronary angiography system: Evaluation in stented vessel segments. *Catheterization and Cadiovascular Interventions*, 68:44–49, 2006.

[76] Y. Xu, H.Zhang, H. Li, and G. Hu. An improved algorithm for vessel centerline tracking in coronary angiograms. *Computer Methods and Programs in Biomedicine*, 88:131–143, 2007.

[77] Qin Li, H. Shui, X. Hu, Y. Liu, and Y. Wang. How to reconstruct 3d coronary arterial tree from two arbitrary views. In *3rd International Conference on Bioinformatics and Biomedical Engineering*, 2009.

[78] K. Tsuchida, W. van Giessen, M. Patterson, S. Tanimoto, H. Garcia, A. M. Maugenest, J. Wentzel, and P. Serruys. In vivo validation of a novel three-dimensional quantitative coronary angiography system (cardiop-b): comparison with a conventional two dimensional system (caas ii) and with special reference to optical coherence tomography. *EuroIntervention*, 3:100–108, 2007.

[79] J. Brien, J.F. O Brien, and N.F. Ezquerra. Automated segmentation of coronary vessels in angiographic image sequences utilizing temporal, spatial and structural constraints. In *Spatial and Structural Constraints in Proceedings of SPIE Visualization in Biomedical Computing.*, 1994.

[80] A. Goshtasby and D.A. Turner. Segmentation of cardiac cine mr images for extraction of right and left ventricular chambers. *IEEE Transaction Medical Imaging*, 14:56–64, 1995.

[81] S. Chroeder, A.F. Kopp, A. Baumbach, C. Meisner, A. Kuettner, C. Georg, B. Ohnesorge, C. Herdeg, C.D. Claussen, and K.R. Karsch. Non invasive detection and evaluation of atherosclerotic coronary plaques with multislice computed tomography. *Journal of the American College of Cardiology*, 37:1430–1435, 2001.

[82] A. Radaelli and J. Peiro'. On the segmentation of vascular geometries from medical images. *International Journal for Numerical Methods in Biomedical Engineering*, 26:3–34, 2010.

[83] D. Schafer, J. Borget, V. Rasche, and M. Grass. Motion-compensated and gated cone beam filtered back-projection for 3d rotational x-ray angiography. *IEEE Transaction Medical Imaging*, 25(7):898–906, 2006.

[84] J. C. Schuurbiers, N. G. Lopez, J. Ligthart, F. J. Gijsen, J. Dijkstra, P. W. Serruys, A. F. Van der Steen, and J. J. Wentzel. In vivo validation of caas qca 3d coronary reconstruction using fusion of angiography and intravascular ultrasound (angus). *Catheterization and Cadiovascular Interventions*, 73:620–626, 2009.

[85] S. Y. J. Chen, K. R. Hoffmann, and J. D. Carroll. Three-dimensional reconstruction of coronary arterial tree based on biplane angiograms. *Proc. SPIE 2710, Medical Imaging 1996: Image Processing*, 103, April 1996. doi: 10.1117/12.237914.

[86] S. Y. J. Chen and C. E. Metz. Improved determination of biplane imaging geometry from two projection images and its application to 3d reconstruction of coronary arterial trees. *Medical Physics*, 24(5):633–654, 1997.

[87] R. C. Gonzales and R. E. Woods. *Digital Image Processing.* MA Addison Wesley Publishing Company Reading., 2002.

[88] M. Sonka, V. Hlavac, and R. Boyle. *Image Processing Analysis and Machine Vision.* PWS Publishing., CA, 1999.

[89] M. Schaap, C. T. Metz, T. O. van Walsum, A. G. van der Giessen, A. C. Weustink, N. R. Mollet, C. Bauer, H. Bogunovic, C. Castro, X. Deng, E. Dikici, T. O Donnell, M. Frenay, O.Friman, M. H. Hoyos, P. H. Kitslaar, K.Krissian, C. Kunhel, M. A. Luengo Oroz, M. Orkisz, O. Smedby, M. Styner, Y. Zhang, G. P. Krestin, S. K. Warfield, and S. Zambal. Standardized evaluation methodology and reference database for evaluating coronary artery centerline extraction algorithms. *Medical Image Analysis*, 13:701–714, 2009.

[90] D. Lesage, E. D. Angelini, I. Bloch, and G. Funka Lea. A review of 3d vessel lumen segmentation techniques: Models, features and extraction schemes. *Medical Image Analysis*, 13:819–845, 2009.

[91] V. Farooq, B.D. Gogas, T. Okamura, J. Ho Heo, M. Magro, J. Gomez-Lara, Y. Onuma Y., M.D. Radu, S. Brugaletta, G. van Bochove, R.J. van Geuns, and H.M. García Garcí a. Tree-dimensional optical frequency domain imaging in conventional percutaneous coronary intervention: the potential for clinical application. *European Heart Journal*, doi:10.1093/eurheartj/ehr409, 2011.

[92] U. Jandt, D. Schaper, M. Grass, and V. Rascher. Automatic generation of 3d coronary artery centerline using rotational x-ray angiography. *Medical Image Analysis*, 13:846–858, 2009.

[93] G. A. Holzapfel, G. Sommer, C.T.Gasser, and P. Regitnig. Determination of layer-specific mechanical properties of human coronary arteries with nonatherosclerotic intimal thickening and related constitutive modeling. *Heart and Circulatory Physiology*, 289:2048–2058, 2005.

[94] T. Wischgoll, J. S. Choy, and G. S. Kassab. Extraction of morphometry and branching angle of porcine coronary arterial tree from ct images. *American Journal Physiology - Heart and Circulatory Physiology*, 297:1949–1955, 2009.

[95] H. Yan, B. Zheng, Z. Wu, J. Wang, H. Zhao, L. Song, and Y. Chi. Two-stent strategy for renal artery stenosis with bifurcation lesion. *Journal of Zhejiang University-SCIENCE B (Biomedicine & Biotechnology)*, 11(8):561–567, 2010.

[96] Claire Chapolin, Gerard Finet, and Isabelle E. Magnin. Modeling of the 3d coronary tree for labeling purposes. *Medical Image Analysis*, 5:301–315, 2001.

[97] J. Lee, P. Beighley, E. Ritman, and N. Smith. Automatic segmentation of 3d micro-ct coronary vascular images. *Medical Image Analysis*, 11:630–647, 2007.

[98] A. Zifan, P. Liatsis, P. Kantartzis, M. Gavaises, N. Karcanias, and D. Katritsis. Automatic 3d reconstruction of coronary artery centerlines from monoplane x-ray angiogram images. *Interventional Journal of biological in Life Sciences*, 4:44–50, 2008.

[99] R. Ponzini, M. Lemma, U. Morbiducci, F.M. Montevecchi, and A. Redaelli. Doppler derived quantitative flow estimate in coronary artery bypass graft: a computational multiscale model for the evaluation of the current clinical procedure. *Medical Engineering and Physics*, 30(7):809–816, 2008.

[100] G. A. Holzapfel, T. C. Gasser, and R. W. Ogden. A new constitutive framework for arterial wall mechanics and a comparative study of material models. *Journal of Elasticity*, 61:1–48, 2000.

[101] J. D. Humphrey. *Cardiovascular solid mechanics. Cells, tissue and organs.* Springer-Verlag., 2002.

[102] F. Auricchio, M. Conti, A. Ferrara, S. Morganti, and A. Reali. Patient-specific finite element analysis of carotid artery stenting: a focus on vessel modeling. *Numerical Methods in Biomedical Engeenering*, 29(6):645–654, 2013.

[103] F. Auricchio, M. Conti, M. Ferraro, and A. Reali. Evaluation of carotid stent scaffolding through patient-specfic finite element analysis. *International Journal for Numerical Methods in Biomedical Engineering*, 28:1043–1055, 2012.

[104] P. Crook. *Cobalt and Cobalt Alloys. Materials Handbook: Properties and Selection: Nonferrous Alloys and Special-Purpose Materials.* ASM International: Materials Park, OH., 2000.

[105] M. De Beule, P. Mortier, S. G. Carlier, B. Verhegghe, R. Van Impe, and P. Verdonck. Realistic finite element-based stent design: the impact of balloon folding. *Journal of Biomechanics*, 41(2): 383–389, 2008.

[106] P. Mortier, M. De Beule, G. Dubini, Y. Hikichi, Y. Murasato, and J. A. Ormiston. Coronary bifurcation stenting: insights from in vitro and virtual bench testing. *EuroIntervention*, 6:53–60, 2008.

[107] P. Mortier, M. De Beule, D. Van Loo, B. Verhegghe, and P. Verdonck. Finite element analysis of side branch access during bifurcation stenting. *Medical Engineering and Physics*, 31:434–440, 2009.

[108] F. Migliavacca, F. Gervaso, M. Prosi, P. Zunino, S. Minisini, L. Formaggia, and G. Dubini. Expansion and drug elution model of coronary stent. *Computer Methods in Biomechanics and Biomedical Engineering*, 10:63–73, 2007.

[109] M. Gyongyosi, P. Yang, A. Khorsand, and D. Glogar. Longitudinal straightening effect of the stents in an additional predictor for major adverse cardiac events. *Journal of the American College of Cardiology*, 35:1580–1589, 2000.

[110] J.J. Wentzel, W. J. Whenal, H. M. van der Giessen, I. A. van Beusekom, P.W. Serruys, C. J. Slager, and R. Kramns. Coronary stent implantation changes 3d vessel geometry and 3d shear stress distribution. *Journal of Biomechanics*, 33:1287–1295, 2000.

[111] F. Migliavacca, L. Petrini, M. Colombo, F. Auricchio, and R. Pietrabissa. Mechanical behavior f coronary stents investigated through the finite element method. *Journal of Biomechanics*, 35: 803–811, 2002.

[112] F. Auricchio, M. Conti, M. De Beule, G. De Santis, and B. Verhegghe. Carotid artery stenting simulation: From patient-specific images to finite element analysis. *Medical Engineering and Physics*, 33:281–289, 2011.

[113] J. Thomas, L. Antiga, S. Che, J. Milner, D.H. Steinman, J. Spence, B. Kutt, and D.A. Steinman. Variation in the carotid bifurcation geometry of young versus older adults: implications for geometric risk of atherosclerosis. *Stroke*, 36:2450–2456, 2005.

[114] H. Joeng, J.T. Luu, and A.J. Minisi. Treatment of diffuse coronary artery disease with long lengths (¿ 30 mm) of intracoronary stents. *Interventional Medicine and Applied Science*, 3(4): 189–194, 2011.

[115] M.H. Jim, K.H. Yiu, H.H. Ho, W.L. Chan, A.K. Yan, C.W. Siu, and W.H. Chow. Angiographic and clinical outcomes of everolimus-eluting stent in the treatment of extra long stent stenosis (aeetes). *Journal of Interventional Cardiology*, 2006. doi: 10.1111/Joic.

[116] S.H. Chang, C.C. Chen, M.J. Hsieh, C.Y. Wang, C.H. Lee, and I.C. Hsieh. Lesion length impacts long term outcomes of drug-elunting stents and bare metal stents differently. *PLoS One*, 8(Iusse 1):53207, 2013.

[117] J. Schmitt, D. Kolstad, and C. Petersen. Intravascular optical coherence tomography opens a window onto coronary artery disease. *Optics and Photonics News*, 15:20–25, 2004.

[118] A.K. Hassan, S.C. Bergheanu, T. Stijnen, B.L. van der Hoeven, J.D. Snoep, J.W. Plevier, M.J. Schalij, and J. W. Jukema. Late stent malapposition risk is higher after drug-eluting stent compared with bare-metal stent implantation and associates with late stent thrombosis. *European Heart Journal*, 31:1172–1180, 2010.

[119] P. Mortier, H. M.M. van Beusekom, M. De Beule, I. Krabbendam Peters, B. Van Der Smissen, G. De Santis, J. M. Ligthart, B. Verhegghe, and W.J. van der Giessen. Improved understanding of stent malapposition using virtual bench testing. *Interventional Cardiology Review*, 6(2):106–109, 2011.

[120] S.H. Lee, Y. Jang, S.J. Oh, K.J.Park, Y.S. Moon, J. W. Min, J.Y. Yang, and G.J. Jang. Overlapping vs. one long stenting in long coronary lesions. *Catheterization and Cadiovascular Interventions*, 62:298–302, 2004.

[121] I.K. De Scheerder, K. Wang, K. Kostopoulus, J. Dens, W. Desmet, and J.H. Piessens. Treatment of long dissections by-pass use of a single long or multiple shorts stents: clinical and angiographic follow-up. *American Hear Journal*, 136:345–351, 1998.

[122] M. Pan, J.S. de Lezo, A. Medina, M. Romero, S. Gonzales, J. Segura, D. Palvovic, M. Rodrigez, J. Munoz, S. Ojeda, E. Hernandez, E. Callabero, A. Delgado, and F. Melian. Influence of stent treatment strategies in the long term-outcome of patients with long diffusive coronary lesions. *Catheterization and Cadiovascular Interventions*, 58:293–300, 2003.

[123] R. Hoffmann, G. Herrmann, S. Silber, P. Braun, G.S. Werner, B. Hennen, H. Rupprecht, J. vom Dahl, and P. Hanrath. Randomized comparison of success and adverse event rates and cost effectiveness of one long versus two short stents for tretment of long coronary narrowing. *American Journal of Cardiology*, 90:460–464, 2002.

[124] A. Kastrati, S. Elezi, J. Dirshinger, M. Hadamitzky, F.J. Neumann, and A. Shoming. Influence of lesion length on restenosis after coronary stent placement. *American Journal of Cardiology*, 83:1617–1622, 1999.

[125] E. Tsagalou, A. Chieffo, I. Iakovou L. Ge, G. M. Sangiorgi, N. Corvaja, F. Airoldi, M. Montorfano, I. Michev, and A. Colombo. Multiple overlapping drug-eluting stents to treat diffuse disease of the left anterior descending coronary artery. *International Cardiology*, 45(10): doi:10.1016/j.jacc.2005.01.049, 2005.

[126] L. Raber, P. Juni, L. Loffel, S. Wandel, S. Cook, P. Wenaweser, M. Togni, R. Vogel, C. Seiler, F. Eberli, T. Luscher, B. Meier., and S. Windecker. Impact of stent overlap on angiographic and long-term clinical outcome in patients undergoing drug-eluting stent implantation. *Journal of the American College of Cardiology*, 55(12), 2010. doi: 10.1016/j.jacc.2009.11.052.

[127] S. Morlacchi, C. Chiastra, D. Gastaldi, G. Pennati, G. Dubini, and F. Migliavacca. Sequential structural and fluid dynamic numerical simulations of a stented bifurcated coronary artery. *Journal of Biomechanical Engineering*, 133:121010–11, 2011.

[128] N. Foin, R. Torii, P. Mortier, M. De Beule, N. Viceconte, P.H. Chan, J.E. Davies, X.Y.Xu, R. Kramns, and C. di Mario. Kissing balloon or sequential dilation of the side branch and main vessel for provisional stenting of bifurcations: lessons from micro-computed tomography and computational simulations. *JAAC cardiovascular Interventions*, 5:47–56, 2012.

[129] E.S. Zegers, B.T.J. Meursing, E.B. Zegers, and A.J.M. Oude Ophuis. Coronary tortuosity: a long and winding road. *Netherlands Heart Journal*, 15(5):191–195, 2007.

[130] L. Caiying, L. Qingxiao, G. Zuojun, Z. Lixia, Z. Shuang, and S. Peng. Quantitative analysis of correlation between coronary tortuosity and coronary heart disease using 256-slice spiral ct angiography. *Philips CT Clinical Science*, 2013.

[131] P. Barragan, R. Rieu, V. Garitey, P.O. Roquebert, J. Sainsous, and M. Silvestri G. Bayet. Elastic recoil of coronary stents: a comparative analysis. *Chateterization and Cadiovascular Interventions*, 50(1):112–119, 2000.

[132] Y. Somitsu, Y. Ikari, K. Ui, M. Nakamura, K. Hara, F. Saeki, T. Degawa, T. Tamura, S. Yabuki, and T. Yamaguchi. Elastic recoil following percutaneous transluminal coronary angioplasty and palmaz-schatz stent implantation. *Journal of Invasive Cardiology*, 7(6):165–172, 1995.

[133] Y. Yamamoto, D.L. Brown, T.A. Ischinger, A. Arbab-Zadeh, and W.F. Penny. Effect of stent design on reduction of elastic recoil: a comparison via quantitative intravascular ultrasound. *Chateterization and Cadiovascular Interventions*, 47(2):251–257, 1999.

[134] K. Battikh, R. Rihani, and J. M. Lemahieu. Acute stent recoil in the left main coronary artery treated with additional stenting. *The Journal of Invasive Cardiology*, 15(2), 2003.

[135] G. Di Sciascio, G. Patti, G. Nasso, A. Manzoli, A. DÁmbrosio, and A. Abbate. Early and long-term results of stenting of diffuse coronary artery disease. *The American Journal of Cardiology*, 86(11):1166–1170, 2000.

[136] S.E. Kassaian, M. Salarifar, M. Raissi Dehkordi, M. Alidoosti, E. Nematipour, H.R. Poorhosseini, A.M. Hajizeinali, D. Kazemisaleh, A. Sharafi, M. Mahmoodian, N. Paydari, and A.V. Farahani. Outcomes of stenting with overlapping drug-eluting stents versus overlapping drug-eluting and bare-metal stents for the treatment of diffuse coronary lesions. *Cardiovascular Journal of Africa*, 21(6):311–315, 2010.

[137] P. Mortier, M. De Beule, P. Segers, P. Verdonck, and B. Verhegghe. Virtual bench testing of new generation coronary stents. *EuroIntervention*, 7(3):369–376, 2011.

[138] A. Colombo, J. W. Moses, M. C. Morice, J. Ludwig, Jr. D. R. Holmes, V. Spanos, Y. Louvard, B. Desmedt, C. Di Mario, and M. B. Leon. Randomized study to evaluate sirolimus-eluting stents implanted at coronary bifurcation lesions. *Circulation*, 109(10):1244–1249, 2004.

[139] Y. Ozaki, M. Okumura, T.F. Ismail, H. Naruse, K. Hattori, S. Kan, M. Ishikawa, T. Kawai, Y. Takagi, J. Ishii, F. Prati, and P.W. Serruys. The fate of incomplete stent apposition with drug-eluting stents: an optical coherence tomography-based natural history study. *European Heart Journal*, 31:1470–1476, 2010.

[140] C. J. Slager, J. J. Wentzel, J.C. Schuurbiers, J. A. Oomen, J. Kloet, R. Krams, C. von Birgelen, W. J. van der Giessen, P. W. Serruys, and P. J. de Feyter. True 3-dimensional reconstruction of coronary arteries in patients by fusion of angiography and ivus (angus) and its quantitative validation. *Circulation*, 102:511–516, 2000.

[141] G. Girasis, J. C. H. Schuurbiers, Y. Onuma, P.W. Serruys, and J.J. Wentzel. Novel bifurcation phantoms for validation of quantitative coronary angiography algorithm. *Catheterization and Cadiovascular Interventions*, 77:790–797, 2011.

[142] G.A. Holzapfel, M. Stadler, and T.C. Gasser. Changes in the mechanical environment of stenotic arteries during interation with stents: computational assessment of parametric design. *Journal of Biochemical Engeenering*, 127:166–180, 2005.

[143] R.M. Fleming, R.L. Kirkeeide, and R.W. Smalling. Patterns in visual interpretation of coronary arteriograms as detected by quantitative coronary arteriography. *Journal American College of Cardiology*, 18:945–951, 1991.

[144] P. W. Serruys, J.H.C. Reiber, and W. Wijns. Assessment of percutaneous transluminal coronary angioplasty by quantitative coronary angiography: Diameter versus densitometric area measurements. *American Journal of Cardiology*, 54:482–488, 1984.

[145] M. Spahn, V. Heer, and R. Freytag. Flat-pannel detectors in x-ray system. *Radialogy*, 43:340–350, 2003.

[146] P.L. Van Herck, L. Gavit, and P. Gorissen. Quantitative coronary arteriography on digital flat-panel system. *Chateterization and Cadiovascular Interventions*, 63(2):192–202, 2004.

[147] C. DiMario, G.S. Werner, G. Sianos, A. R. Galassi, J. Buttner, D. Dudek, B. Chevalier, T. Lefevre, J. Schofer, J. Koolen, H. Sievert, B. Reimers, J. Fajadet, A. Colombo, A. Gershlick, P.W. Serruys, and N. Reifart. European perpective in the recanalisation of chronic total occlusion (cto): consensus document from the euro cto club. *EuroIntervention*, 3:30–43, 2007.

[148] Y. Louvard, M. Thomas, V. Dzavik, D. Hildick Smith, A. R. Galassi, M. Pan, F. Burzotta, M. Zelizko, D. Dudek, P. Ludman, I. Sheiban, J. F. Lassen, O. Darremont, A. Kastrati, J. Ludwig, I. Iakovou, P. Brunel, A. Lansky, D. Meerking, V. Legrand, A. Medina, and T. Lefevre. Classification of coronary artery bifurcation lesion and treatments: time for a consensus! *Chateterization and Cadiovascular Interventions*, 71:175–183, 2008.

[149] D. Meerkin, H. Marom, and O. C. Biton. Three-dimensional vessel analyses provide more accurate length estimations than the gold standard qca. *Journal Interventional Cardiology*, 23:157–165, 2010.

[150] S. Tu, G. Koning, and W. Jukema. Assessment of obstruction length and optimal viewing angle from biplane x-ray angiograms. *International Journal of Cardiovascular Imaging*, 26:5–17, 2010.

[151] Y. Onuma, C. Girasis, J. P. Aben, G. Sarno, N. Piazza, C. Lokkerbol, M. A. Morel, and P. W. Serruys. A novel dedicated three-dimensional quantitative analysis methodology for bifurcation lesions. *EuroIntervention*, 7(5):629–635, 2011.

[152] N. P. Thrasyvoulos. An adaptive clustering algorithm for image segmentation. *IEEE TRANSACTIONS ON SIGNAL PROCESSING*, 40(4), April 1992.

[153] K. R. Castleman. *Digital Image Processing.* Upper Saddle River Prentic Hall., 2005.

[154] J. Bersen. Dynamic thresholding of gray level images. In *Image thresholding techniques.*, pages 1251–1255, October 1986.

[155] A. Kundu. Local segmentation of biomedical images. *Computerized Medical Imaging and Graphics*, 14:173–183, 1990.

[156] D. Marr and E. Hildreth. Theory of edge detection. *Royal Society London*, 27:753–763, 1996.

[157] I. Pericevic, C. Lally, D. Toner, and D. J. Kelly. The infuence of plaque composition on underlying arterial wall stress during stent expansion: the case for lesionspecific stents. *Medical Engineering and Physics*, 31(4):428–433, 2009.

[158] S. Zhao, L. Gu, and S. Froemming. Finite element analysis of the implantation of a self-expanding stent: impact of lesion calcification. *Journal of Medical Devices*, 6:021001–1, 2012.

[159] H. M. Loree, A. J. Grodzinsky, S. Y. Park, L. J. Gibson, and R. T. Lee. Static circumferential tangential modulus of human atherosclerotic tissue. *Journal of Biomechanics*, 27:195–204, 1994.

[160] F. Auricchio, M. Di Loreto, and E. Sacco. Finite-element analysis of a stenotic revascularization through a stent insertion. *Computer Methods in Biomechanics and Biomedical Engineering*, 4: 249–264, 2001.

[161] C. Lally, F. Dolanb, and P.J. Prendergast. Cardiovascular stent design and vessel stresses: a finite element analysis. *Journal of Biomechanics*, 38:1574–1581, 2005.

[162] T. E. Carew, R. N. Vaishnav, and D. J. Patel. Compressibility of the arterial wall. *Circulation Research*, 23:61–68, 1968.

[163] C. J. Chuong and Y. C. Fung. Compressibility and constitutive equation of arterial wall in radial compression experiments. *Journal of Biomechanics*, 17:35–40, 1984.

[164] G. A. Holzapfel, M. Stadler, and C. A. J. Schulze-Bauer. A layer-specific 3d model for the simulation of balloon angioplasty using mr imaging and mechanical testing. *Annals of Biomedical Engineering*, 30(6):753–767, 2002.

[165] S.J. Bund and A.A. Oldham. *Mechanical properties of human atherosclerotic lesions.* Pathology of human atherosclerotic plaques., 1990.

[166] T. Kang, J. Resar, and J. D. Humphrey. Heat-induced changes in the mechanical behavior of passive coronary arteries. *Journal of Biomechanical Engineering*, 117:83–93, 1995.

[167] X. Lu ANDJ. Yang, J. B. Zhao, H. Gregersen, and G. S. Kassab. Shear modulus of porcine coronary artery: contributions of media and adventitia. *American Journal Physiology - Heart and Circulatory Physiology*, 285:1966–1975, 2003.

[168] X. Lu, A. Pandit G.S., and Kassab. Biaxial incremental homeostatic elastic moduli of coronary artery: two-layer model. *American Journal Physiology - Heart and Circulatory Physiology*, 287: 1663–1669, 2004.

[169] C. Velican and D. Velican. Study of coronary intimal thickening. *Atherosclerosis*, 56:331–334, 1985.

[170] C.A.J. Schulze-Bauer and G.A. Holzapfel. Determination of constitutive equations for human arteries from clinical data. *Journal of Biomechanics*, 36:185–169, 2003.

[171] G.V.R. Born and P.D. Richardson. *Mechanical properties of human atherosclerotic lesions.* Pathology of Human Atherosclerotic Plaques., 1990.

[172] D.V. Carmines, J. H. McElhaney, and R. Stack. A piece-wise non-linear elastic stress expression of human and pig coronary arteries tested in vitro. *Journal of Biomechanics*, 24:899–906, 1991.

[173] C.J. Van Andel, P.V. Pistecky, and C. Borst. Mechanical properties of porcine and human arteries: implications for coronary anastomotic connectors. *Annals of Thoracic Surgery*, 76:58–65, 2003.

[174] R. P. Vito and H.A. Demiray. Two-layered model for arterial wall mechanics. *Annual Conference onEngineering in Medicine and Biology Society*, 1982.

[175] P.D. Richardson and S.M. Keeny. *Anisotropy of Human Coronary Artery Intima.* Worcester MA., 1989.

[176] J. G. Rhodin. *Architecture of the vessel wall, in: D. F. Bohr, A. D. Somlyo, H. V. Sparks (Eds.), Handbook of Physiology. The Cardiovascular System. Volume 2: Vascular Smooth Muscle.* American Physiological Society, Bethesda., 1980.

[177] H. Demiray and R. P. Vito. A layered cylindrical shell model for an aorta. *Journal of Biomechanics*, 5:309311, 1991.

[178] R. W. Ogden. *Non-linear elastic deformation.* Dover, New York., 1997.

[179] A.J.M. Spencer. *Deformation of fiber-reinforced materials.* Oxford University Press, 1982.

[180] A.J.M. Spencer. *Continuum theory of the mechanics of fibre-reinforced composites.* New York., 1984.

[181] J. Merodio and R. W. Ogden. Instabilities and loss of ellipticity in fiber-reinforced compressible non-linearly elastic solids under plane deformation. *International Journal of Solids Structural*, 40:4707–4727, 2003.

[182] J. Merodio and R.W. Ogden. On tensile instabilities and ellip-ticity loss in fiber-reinforced incompressible non-linearly elastic solids. *Mechanical Research Comunity*, 32:290–299, 2005.

[183] J. Merodio and R.W. Ogden. The influence of the invariant i8 on the stress-deformation and ellipticity characteristics of doubly fiber-reinforced non-linearly elastic solids. *International Journal of Non-linear Mechanics*, 41:556–563, 2006.

[184] J.D. Humphrey and F.C.P. Yin. On constitutive relations and finite deformations of passive cardiac tissue: I. a pseudostrainñenergy function. *Journal of Biomechanical Engineering*, 109: 298–304, 1987.

[185] G.A. Holzapfel and R.W. Ogden. On planar biaxial tests for anisotropic nonlinearly elastic solids a continuum mechanical framework. *Mathematical Mechanics and Solids*, 14:474–489, 2009.

[186] G.A. Holzapfel, T.C. Stadler, and M. Gasser. A structural model for the viscoelastic behavior of arterial walls: continuum formulation and finite element analysis. *European Journal of Mechanics - A/Solids*, 21(3):441–463, 2002.

[187] P. Tong and Y. C. Fung. The stress-strain relationship for the skin. *Journal of Biomechanics*, 7: 649–657, 1974.

[188] G.A. Holzapfel and H.W. Weizsacker. Biomechanical behavior of the arterial wall and its numerical characterization. *Computers in Biology and Medicine*, 28(4):377–392, 1998.

[189] G.A. Holzapfel, G. Sommer, and P. Regitnig. Anisotropic mechanical properties of the tissue components in human atherosclerotic plaques. *Journal of Biomechanical Engineering*, 126:657–665, 2004.

[190] I. Hariton, G. deBotton, T.C. Gasser, and G.A. Holzapfel. How to in-corporate collagen fibers orientations in an arterial bifurcation? In *Proceeding of 3rd IASTED International Conference on Biomechanics.*, 2005.

[191] D. Kiousis, S.F. Rubinigg, M. Auer, and G.A. Holzapfel. A methodology to analyze changes in lipid core and calcification onto fibrous cap vulnerability: the human atherosclerotic carotid bifurcation as an illustratory example. *Journal of Biomechanical Engineering*, 131(12):121002, 2009.